TRANSITION METAL OXIDE AND PHOSPHATE-BASED/CARBON COMPOSITES AS SUPERCAPACITOR ELECTRODES

HO MUI YEN

Thesis submitted to the University of Nottingham

for the Doctor of Philosophy degree

July 2016

Acknowledgement

I would like to convey my deepest appreciation to my supervisor, Prof. Dr. Khiew Poi Sim, for his constant encouragement, invaluable guidance, patience and understanding throughout the whole period of my PhD candidature. This project had been a tough but enriching experience for me in research. I would like to express my heartfelt thanks to Prof. Dr. Khiew Poi Sim also for his guidance on writing scientific papers including this PhD thesis.

It's my pleasure to work with a group of brilliant, warmhearted and lovely people, Prof Dr.Dino Isa, Dr. Chiu Wee Siong, Dr.Chia Chin Hua, Dr. Nafisah Naim, Dr. Dr.Joanna Chia, Mr. Tan Thian Khoon, Ms. Maxine Yee, Ms. Low Sze Shin and Mr. Ejikeme Raphael Ezeigwe.

Particular acknowledgement goes to Andrew, Fareez, Filzah, Fatihah, Elyas, Asyraf and Khairani for their kind supports in materials characterization and research laboratory equipment arrangement.

In addition, I want to express my sincerest appreciation to the Department of Materials Engineering, Tunku Abdul Rahman University College for offering me chance to further my PhD study at University of Nottingham with sponsorship.

Finally, I would like to express my heartfelt thanks to my family, particular thanks to my husband. Without their boundless love, encouragement and support, this research could not have been completed successfully.

Table of Contents

Acknowledgement i

Table of Contents ii

Abstract……..vi

Nomenclature…….viii

List of Tables…….....ix

List of Figures……..... xi

List of Publications xx

CHAPTER 1: Introduction 1

1.1 Background 1

1.2 Historical background and industry developments 3

1.3 Rationale and research objectives 9

1.4 Structure of this thesis 10

CHAPTER 2: Literature Review 15

2.1. Introduction 15

2.2. Principle of supercapacitor 17

2.3 Electrode materials 20

2.3.1 Carbon-based materials 21

2.3.2 Transition metal oxides 31

2.3.3 Conducting polymer 45

2.3.4. Composites 48

2.4.5 New materials: Lithium -ion capacitor 72

2.5 Electrolyte 75

CHAPTER 3: Experimental Techniques 93

3.1 Reagents and apparatus 93

3.2 Preparation of metal oxide-based materials 94

3.2.1 Preparation of metal-oxide/activated carbon composite electrodes ... 94

3.2.2 Synthesis of graphene 95

3.2.3 Preparation of SnO_2-graphene composites 96

3.2.4 Preparation of MoO_3-graphene composites 96

3.2.5 Preparation of electrodes for electrochemical characterization 96

3.3 Characterization techniques 97

3.3.1 Field Emission Scanning Electronic Microscopy (FESEM) 97

3.3.2 Energy Dispersive X-Ray (EDX) 101

3.3.3 Transmission electron microscopy (TEM) 101

3.3.4 X-Ray Diffraction (XRD) 102

3.3.5 Brunauer-Emmett-Teller (BET) 105

3.3.6 Raman spectroscopy 108

3.3.7 Thermogravimetric analysis (TGA) 109

3.4 Electrochemical Characterisation 109

3.4.1 Cyclic Voltammetry (CV) 111

3.4.2 Galvanostatic Charging- Discharging (GCD) 113

3.4.3 Electrochemical Impedance Spectroscopy (EIS) 115

CHAPTER 4: Electrochemical Performance of Nano Fe_3O_4 - Activated Carbon Composites in Symmetric Supercapacitors 119

4.1 Introduction 119

4.2 Characterisation of Fe_3O_4-AC composites 121

4.3 The electrochemical performance of the composite electrodes 126

4.3.1 Cyclic Voltammetry (CV) 126

4.3.2 Galvanostatic Charge-Discharge (GCD) 133

4.3.3 Electrochemical Impedance Spectroscopy (EIS) 136

4.3.4 Ragone Plot and Cyclability Analysis 140

4.5 Summary 143

CHAPTER 5: Electrochemical Studies on Calcined TiO_2-Activated Carbon and ZnO-Activated Carbon Composite Electrodes for Aqueous Supercapacitors 149

5.1 Introduction 149

5.2 Characterisation of TiO_2-AC and ZnO-AC composites 151

5.2.1 Effect of heat treatment 151

5.2.2 Effect of metal oxide loading 157

5.3 The electrochemical performance of TiO_2-AC and ZnO-AC composite electrodes 160

5.4 Summary……..…….169

CHAPTER 6: Charge Storage Performance of Lithiated Iron Phosphate - Activated Carbon Composite as Symmetrical Electrode for Electrochemical Capacitor 173

6.1 Introduction 173

6.2 Results and Discussion 175

6.2.1 X-Ray Diffraction (XRD) 175

6.2.2 Scanning Electron Microscopy (SEM) 176

6.2.3 Brunauer-Emmett-Teller (BET) 178

6.2.4 Cyclic Voltammetry (CV) 179

6.2.5 Galvanostatic Charge-Discharge (GCD) 183

6.2.6 Electrochemical Impedance Spectroscopy (EIS) 187

6.3.7 Ragone Plot and Cyclability 190

6.4 Summary 193

CHAPTER 7: Glucose-assisted tin oxide-graphene composites via green and facile solvothermal approach for supercapacitor application 197

7.1. Introduction 197

7.2 Results and Discussion 199

7.2.1 X-Ray Diffraction (XRD) 199

7.2.2 Raman Spectroscopy 200

7.2.3 Scanning Electron Microscopy (SEM) 201

7.2.4 Cyclic Voltammetry (CV) 204

7.2.5 Galvanostatic Charge-Discharge (GCD) 206

7.2.6 Electrochemical Impedance Spectroscopy (EIS) 208

7.3 Summary 210

CHAPTER 8: Ethylene glycol assisted molybdenum oxide-graphene composite electrodes via green and facile solvothermal approach for aqueous supercapacitor application 215

8.1. Introduction 215

8.2 Results and Discussion 219

8.2.1 X-Ray Diffraction (XRD) 219

8.2.2 Raman Spectroscopy 220

8.2.3 Scanning Electron Microscopy (SEM) 221

8.2.4 Cyclic Voltammetry (CV)..... 224
8.2.5 Galvanostatic Charge-Discharge (GCD) 227
8.2.6 Electrochemical Impedance Spectroscopy (EIS) 229
8.3 Summary..... 231
CHAPTER 9: Conclusions and Recommendations..... 238
9.1. Conclusions 238
9.2 Recommendations..... 241

Abstract

Electrochemical capacitors, also known as supercapacitors, have attracted considerable attention over the past decades owing to their higher power density, long cycle life and moderate energy density compared. A high-performance supercapacitor integrates innovative electrode materials with desirable properties coupled with low cost and sustainability. In this thesis, a series of low cost transition metal oxide-activated carbon composite materials, lithium iron phosphate-activated carbon composite materials as well as metal oxide-graphene composite materials were prepared, characterized and evaluated as supercapacitor electrodes.

Iron oxide (Fe_3O_4) – activated carbon (AC), zinc oxide (ZnO) – AC and titanium oxide (TiO_2) – AC nanocomposites were prepared by using simple mechanical mixing method. The charge storage capabilities of these metal oxide-based composites with different loading ratios were evaluated in both mild aqueous 1 M Na_2SO_3 and 1 M Na_2SO_4 electrolytes. The incorporation of small amount of metal oxides onto AC could effectively enhance the capacitive performance of pure AC electrodes. It is believed that the presence of metal oxide nanoparticles can provide favourable surface adsorption sites for sulphite anions (SO_3^{2-}). Nevertheless, bulk increasing of the metal oxide content is found to distort the capacitive performance and deteriorate the specific surface area of the electrode, mainly due to the aggregation of the metal oxide particles within the composite. On the other hand, composite materials consisting of lithium iron phosphate ($LiFePO_4$) and AC exhibit high specific capacitance of 112.41 F/g in 1 M Na_2SO_3 with the incorporation of 40 wt % of $LiFePO_4$. The synergistic effect between the faradaic battery type materials and the EDLC-based materials is greatly demonstrated. The intercalation and extraction of Li^+ ions in $LiFePO_4$ lattices are responsible for the reversible Faradaic reaction on top of the adsorption and de-adsorption of SO_3^{2-} anions from Na_2SO_3 electrolyte.

In the preparation of SnO_2-graphene and MoO_3-graphene nanocomposites, low-temperature solvothermal method using mild reducing agents was adopted. The preparation steps do not require high pressure or extreme synthetic condition and do not involve the usage of hazardous reactants. The electrochemical results of SnO_2-graphene

composite electrodes demonstrate that the composite electrodes possess a high specific energy (14 Wh/kg) with 93 % capacitive retention after 1500 cycles while MoO_3-graphene composite electrodes yield an enhanced specific energy (16.3 Wh/kg) which is 28 % higher than that of pure MoO_3 (11.8 Wh/kg). A maximum specific capacitance of 99 F/g was obtained from the optimized SnO_2-graphene composite electrodes while a high average specific capacitance of 148 F/g was achieved for MoO_3-graphene composites at a scan rate of 5mV/s in neural 1 M Na_2SO_3 electrolyte. The incorporation of graphene onto both SnO_2 and MoO_3 respectively, can promote the electrochemical utilization of metal oxides as well as the electrical conductivity of the electrodes. The graphene sheet serves as a good support in promoting effective charge transfer for redox reactions of MoO_3. Additionally, deposition of metal oxides on graphene sheets prevents the graphene sheets from agglomeration, resulting in facile ion transportation pathway for electrolyte to access the surface of active material.

Nomenclature

AC	Activated carbon
BET	Brunauer-Emmett-Teller
CNT	Carbon nanotube
CPE	Constant phase element
CV	Cyclic voltammetry
DI	Deionized
EC	Electrochemical capacitor
EDLC	Electrical double layer capacitor
EDCC	Electric double-cylinder capacitor
EDX	Energy Dispersive X-Ray
ESA	Electrode separator assembly
EIS	Electrochemical impedance spectroscopy
ESR	Equivalent series resistance
EWCC	Electric wire-in-cylinder capacitor
FESEM	Field emission scanning electron microscopy
Fe_3O_4	Iron oxide
GCD	Galvanostatic charge/discharge
GO	Graphene oxide
IHP	Inner Helmholtz plane
ILs	Ionic liquids
$LiFePO_4$	Lithium iron phosphate
$LiSO_4$	Lithium sulphate
$(NH_4)_6Mo_7O_{24}\cdot 4H_2O$	Ammonium molybdate tetrahydrate
MWNT	Multi-walled carbon nanotubes
MoO_3	Molybdenum oxide
Na_2SO_3	Sodium sulphite
$NaSO_4$	Sodium sulphate
NMP	N-methyl-2-pyrrolidinone
OCP	Open-circuit potential
OHP	Outer Helmholtz plane
PVDF	Polyvinylidene fluoride
PTFE	Polytetrafluoroethylene
RGO	Reduced graphene oxide
SEM	Scanning electron microscopy
$SnCl_2$	Tin chloride
SnO_2	Tin oxide
SWNT	Single-walled carbon nanotubes
TEM	Transmission electron microscopy
TGA	Thermogravimetric Analysis
TiO_2	Titanium oxide
XRD	X-ray Diffraction
ZnO	Zinc oxide

List of Tables

Table 1.1. The basic characteristics of conventional capacitors, supercapacitors and batteries [8].

Table 1.2. Historical developments of supercapacitor.

Table 1.3. Summary of world-wide commercially available supercapacitor.

Table 2.1. Comparison of specific capacitance, surface area, pore volume and average pore size of ACs [19].

Table 2.2. Specific capacitance obtained by cyclic voltammetry at various scan rates for $RuO_2.xH_2O$ [74].

Table 2.3. Relationship between MnO_2 crystal structures, BET surface areas and the specific capacitances measured at scan rate of 5 mV/s in 0.1 M K_2SO_4 [85].

Table 2.4 Summary of the single electrode materials investigated.

Table 2.5. Theoretical and experimental specific capacitance of various conducting polymers [94].

Table 2.6. Specific capacitance and BET surface area as a function of ruthenium loading [14].

Table 2.7. Recent research works that were carried out in relation to the symmetric composite electrodes, including different combinations of material, various fabrication/synthesis techniques as well as different electrolytes employed.

Table 3.1. Chemical/reagents used for the preparation of various electrode materials.

Table 3.2. General apparatus used for the preparation of electrode materials.

Table 3.3. Different mass percentage of materials in the various metal oxide-activated carbon electrodes.

Table 3.4. Different solvothermal reaction times for electrode materials.

Table 4.1. BET surface area of carbon black, AC_LSA, Fe_3O_4 and their nanocomposites.

Table 4.2. Effects of electrolyte and Fe_3O_4 loading on specific capacitance of Fe_3O_4-AC composite electrodes, at the scan rate of 10 mV/s.

Table 4.3. Comparison of specific capacitances and ESR values between AC, 4Fe-AC_LSA, 20Fe-AC_LSA, 60Fe-AC_LSA composite electrodes.

Table 4.4. Simulated Values of L. R_Ω, R_{CT}, CPE, W, n from the Equivalent Circuit in Figure 4.13.

Table 5.1 Physical appearance of Ti-AC and ZnO-AC composite materials thermally treated at various temperatures.

Table 5.2 Weight loss for 4TiO-AC and 4Zn-AC in various heat treatment temperatures.

Table 5.3 Weight loss for AC, CB, TiO_2 and ZnO after heat treatment at 400 ^oC.

Table 5.4. The variation of BET specific surface area of TiO_2-AC and ZnO-AC with different compositions of the composite materials.

Table 6.1. BET surface area of $LiFePO_4$-AC composite electrodes.

Table 6.2. Comparison of specific capacitances and ESR values between AC, 4 wt %, 20 wt% and 60 wt % $LiFePO_4$-AC composite electrodes.

Table 8.1. Specific capacitance of GM12 as a function of scan rate.

Table 9.1 Comparative table summarises different types of composite electrodes in relation to their electrochemical performance in 1 M Na_2SO_3.

List of Figures

Figure 1.1. A simplified Ragone plot [9].

Figure 2.1. Ragone plot showing the specific power against specific energy for various electrical energy storage systems [2].

Figure 2.2. Simplified schematic of double layer [7].

Figure 2.3. The basic structure model of EDLC.

Figure 2.4. Taxanomy of supercapacitors [13].

Figure 2.5. Schematic diagram of (a) a negatively charged mesopores with solvated cations approaching the pore wall to form an electric double-cylinder capacitor (EDCC); (b) a negatively charged micropore of radius b with cations lining up along the pore axis to form an electric wire-in-cylinder capacitor (EWCC) [24].

Figure 2.6. SEM image of the CNT film electrode, showing the well-entangled and interconnected porous structure [34].

Figure 2.7. Schematic depiction of the conventional “stacked geometry” versus “in-plane geometry” [45].

Figure 2.8. Cyclic voltammogram of RuO_2 thin film for different scan rates (a) 20, (b) 50, (c) 100 mV/s. Inset shows plot of specific capacitance with scan rates [76].

Figure 2.9. Cyclic voltammetric curves of MnO_2 in various electrolytes at a concentration of 0.1 M [50].

Figure 2.10. Comparison of the specific capacitance, ionic conductivity and BET surface area of various MnO_2 structures [87].

Figure 2.11. A schematic of proposed strategy for enhancing the capacitive behavior of a NiO film with open macropores [81].

Figure 2.12. CVs of the deposited nickel oxide film in 1 M KOH and 1 M Na_2SO_4 solutions, respectively, at a scan rate of 25 m/V[67].

Figure 2.13. Specific capacitance of the deposited NiO film measured at various scan rates and scanned potential ranges [67].

Figure 2.14. Effect of carbon black content on BET surface area of Fe_3O_4-based electrode. (□) is calculated BET surface area; (∇) is measured BET surface area. The theoretical values are based on the assumption of unchanged surface area of carbon black as well as non-porous and non-agglomerated Fe_3O_4 [56].

Figure 2.15. Molecular structures of oxidized and reduced forms of PEDOT. A^- represents the counter-anions [90].

Figure 2.16. Specific capacitance of composite electrodes (C_{sp}) demonstrated by mesoporous carbon and RuO_2 active materials and specific capacitance of ruthenium component (C_{sp}^{Ru}) as a function of ruthenium loading [83].

Figure 2.17. Surface morphologies of the oxides deposited in the MnO_2 with addition of (a) 0, (b) 0.03, (c) 0.05, (d) 0.06, (e) 0.08, and(f) 0.15 M $FeCl_3$ [115].

Figure 2.18. Impedance spectra of (a) NiO/RuO_2-based composite electrode and (b) pure NiO electrode [118].

Figure 2.19. EIS spectra of pure MWNT-MWNT symmetric electrodes, MWNT-Fe_2O_3 asymmetric composites and MWNT-Fe_2O_3/MWNT asymmetric composites [104].

Figure 2.20. Effect of calcination temperature on the specific capacitance of Fe_3O_4/carbon nanocomposites in 1 M Na_2SO_4. [122].

Figure 2.21. AC impedance plots of graphene-ZnO, graphene-SnO_2 and pure graphene electrodes [35].

Figure 2.22. Total specific capacitance of TiO_2/AC composite electrodes as a function of TiO_2 content in 1 M H_2SO_4 [135].

Figure 2.23. SEM images for (a) pure AC electrode and (b) TiO_2/AC composite electrode [135].

Figure 2.24. Nyquist plots of $TiO_{2:}$AC (1:3), TiO_2:AC (1:3), TiO_2:AC (1:3) composite electrodes [136].

Figure 2.25. Capacitance calculated from CV curves of CrO_3/SWNTs and pure SWNT-based electrodes carried out in 1 M H_2SO_4 using two-electrode measurement [144].

Figure 2.26. Images showing the colour scheme changes when the smart composite electrodes ($W_{18}O_{49}$-PANI) are charged and discharged at varying levels. The electrode is fully charged (100 %) at 0.8 V while it is at discharged state (0 %) at -0.5 V [147].

Figure 2.27. Comparison of voltage profile for a hybrid lithium-ion capacitor consists of activated carbon cathode and $Li_4Ti_5O_{12}$ and a AC/AC conventional EDLC [183].

Figure 2.28. Ragone plot comparing lithium-ion batteries, carbon-coated $Li_4Ti_5O_{12}$/AC lithium-ion capacitors and AC/AC conventional EDLCs [184].

Figure 2.29. Ragone plot showing AC/$LiMn_2O_4$ hybrid capacitor with higher specific energy and power densities compared to those of AC/AC conventional EDLC in Li_2SO_4 [189].

Figure 3.1. Schematic diagram of a FESEM [7].

Figure 3.2. The regions from which SE, BSE and X-rays can be detected in FESEM interaction volume [7].

Figure 3.3. Reflection of X-ray at planes of atoms occurred in XRD [13].

Figure 3.4. Basic features of XRD experiment setup [2].

Figure 3.5. Typical BET plot [16].

Figure 3.6. Different types of isotherm [18].

Figure 3.7. A simplified schematic of a potentiostat [22].

Figure 3.8. Two-electrode cell configuration [25].

Figure 3.9. A typical cyclic voltammogram showing the characteristic symmetrical peaks of a reversible single electrode transfer reaction [24].

Figure 4.1. XRD patterns of carbon black, AC_LSA, Fe_3O_4 and their nanocomposites.

Figure 4.2. BET plots for (a) 4Fe-AC_LSA and (b) 60Fe-AC_LSA.

Figure 4.3. Scanning electron micrographs of different Fe_3O_4 loading in AC_LSA electrodes: (a) AC_LSA, (b) 4Fe-AC_LSA, (d) 20Fe-AC_LSA, (e) 60Fe-AC_LSA, at magnification of 2500x.

Figure 4.4. Cyclic voltammograms for different compositions of Fe_3O_4 loaded in AC_LSA electrodes, scanned at 10 mV/s, in 1 M Na_2SO_3.

Figure 4.5. Cyclic voltammograms for different compositions of Fe_3O_4 loaded in AC_LSA electrodes, scanned at 10 mV/s, in 1 M Na_2SO_4.

Figure 4.6. Specific capacitance of Fe_3O_4-AC_LSA composite electrodes as a function of Fe_3O_4 loading, in 1 M Na_2SO_3 and 1 M Na_2SO_4 respectively, at the scan rate of 10 mV/s between 0 to 1 V.

Figure 4.7. Cyclic voltammogram of (a) 4Fe-AC_LSA in 1 M Na_2SO_3 under different scan rates.

Figure 4.8. Cyclic voltammograms of AC_LSA electrodes in 1 M Na_2SO_3 under different scan rates.

Figure 4.9. Variation of specific capacitance of (a) 4Fe-AC_LSA composite electrode and (b) AC_LSA electrode at different scan rates in 1 M Na_2SO_3.

Figure 4.10. Charge-discharge curves of (a) AC_LSA electrode, (b) 4Fe-AC_LSA, (c) 20Fe-AC_LSA, (d) 60Fe-AC_LSA composite electrodes obtained at the constant density of 10 mA/cm^2.

Figure 4.11. Variation of specific capacitance of (a) 4Fe-AC__LSA composite electrode and (b) AC electrode at different current densities in 1 M Na_2SO_3.

Figure 4.12: Nyquist plots obtained for composite electrodes with different Fe_3O_4 loading: (a) AC_LSA, (b) 4Fe-AC_LSA, (c) 20Fe-AC_LSA, (d) 60Fe-

AC_LSA, at 0 V over the frequency range of 100 kHz – 0.01 Hz in 1 M Na_2SO_3.

Figure 4.13. The equivalent circuit used to fit the Nyquist spectra using NOVA equivalent circuit editor.

Figure 4.14. CV profile comparison of AC electrodes with lower surface area (AC_LSA), AC electrodes with higher surface area (AC_HSA) and their composite electrodes at 10 mV/s in 1 M Na_2SO_3.

Figure 4.15. Ragone plot of 4Fe-AC_HSA composite electrodes.

Figure 4.16. Cycle stability of 4Fe-AC_HSA composite electrodes in aqueous Na_2SO_3 electrolyte at scan rate of 10 mV/s between 0 and 1 V.

Figure 4.17. CV profile comparison of 4Fe-AC_HSA composite electrodes between 100^{th} cycle and 1000th cycle at 10 mV/s in 1 M Na_2SO_3.

Figure 5.1. TGA plot for 4TiO-AC composite materials.

Figure 5.2. TGA plot for 4ZnO-AC composite materials.

Figure 5.3. XRD patterns of (a) pure AC, 4TiO-AC composites calcined at temperature of (b) 25, (c) 100, (d) 200, (e) 300, (f) 400 °C.

Figure 5.4. XRD patterns of (a) pure AC, 4ZnO-AC composites calcined at temperature of (b) 25, (c) 100, (d) 200, (e) 300, (f) 400 °C.

Figure 5.5. SEM images of (a) AC, (b) 4TiO-AC, (c) 20TiO-AC, (d) 60TiO-AC, (e) 80TiO-AC, at magnification of 2500x.

Figure 5.6. SEM images of (a) AC, (b) 4ZnO-AC, (c) 20ZnO-AC, (d) 60ZnO-AC, (e) 80ZnO-AC, at magnification of 2500x.

Figure 5.7. Cyclic voltammograms for AC electrodes with different TiO_2 nanomaterials loading in 1 M Na_2SO_3 at a scan rate of 10 mV/s.

Figure 5.8. Cyclic voltammograms for AC electrodes with different ZnO nanomaterials loading in 1 M Na_2SO_3 at a scan rate of 10 mV/s.

Figure 5.9. Correlation between specific capacitance, crystallinity and BET surface are on TiO_2-AC composite electrodes.

Figure 5.10. Correlation between specific capacitance, crystallinity and BET surface are on ZnO-AC composite electrodes.

Figure 5.11. Galvanostatic CD profiles of (a) AC, (b) 4TiO-AC and (c) 4ZnO-AC electrodes in 1 M Na_2SO_3 electrolytes at a current density of 5 mA/cm^2.

Figure 5.12. (i) Nyquist plots obtained for (a) AC, (b) 4TiO-AC and (c) 4ZnO-AC electrodes at 0 V over the frequency range of 100 kHz – 10 mHz in 1 M Na_2SO_3. (ii) Randles equivalent circuit representing the circuit elements that are used to fit the experimental Nyquist spectrum of 4ZnO-AC electrode using the software Nova.

Figure 5.13. Cycling stability of 4TiO-AC composite electrodes in aqueous Na_2SO_3 electrolyte at scan rate of 10 mV/s between 0 and 1 V.

Figure 5.14. Cycling stability of 4ZnO-AC composite electrodes in aqueous Na_2SO_3 electrolyte at scan rate of 10 mV/s between 0 and 1 V.

Figure 5.15. Ragone plot of 4TiO-AC composite electrodes.

Figure 5.16. Ragone plot of 4ZnO-AC composite electrodes.

Figure 6.1. XRD patterns of AC electrode and various $LiFePO_4$-AC composite electrodes.

Figure 6.2. Scanning electron micrographs of different $LiFePO_4$ loading in AC: (a) AC, (b) 4LFP-AC, (c) 20LFP-AC, (d) 40LFP-AC, (e) 60LFP-AC, (f) EDX results indicating the elements detected on the 40LFP-AC composite materials, at magnification of 20000x.

Figure 6.3. BET plot for 40LFP-AC composite materials.

Figure 6.4. Cyclic voltammograms for different compositions of $LiFePO_4$ loaded in AC electrodes, scanned at 10 mV/s, in 1 M Na_2SO_3.

Figure 6.5. Cyclic voltammograms for different compositions of $LiFePO_4$ loaded in AC electrodes, scanned at 10 mV/s, in 1 M Li_2SO_4.

Figure 6.6. Specific capacitance of $LiFePO_4$- AC composite electrodes as a function of $LiFePO_4$ loading, in 1 M Na_2SO_3 and 1 M Li_2SO_4 respectively, at the scan rate of 10 mV/s.

Figure 6.7. Charge-discharge curves of $LiFePO_4$-based composite electrodes with various compositions: (a) AC, (b) 4LFP-AC, (c) 20LFP-AC, (d) 40LFP-AC, (e) 60LFP-AC, obtained at the constant density of 5 mA/cm^2.

Figure 6.8. Galvanostatic charge-discharge curves of 40LFP-AC composite electrodes at different current densities in 1 M Na_2SO_3: (a) 2, (b) 3, (c) 5, (d) 10 mA/cm^2.

Figure 6.9. Specific capacitance of 40LFP-AC in Na_2SO_3 in the function of current densities.

Figure 6.10. (a) Nyquist plots obtained for composite electrodes with different Fe_3O_4 loading at 0 V over the frequency range of 100 kHz – 10 mHz in 1 M Na_2SO_3: (a) AC, (b) 4LFP-AC, (c) 20LFP-AC, (d) 40LFP-AC, (e) 60LFP-AC.

Figure 6.11. (a) The fitting of the impedance expressions (▬) obtained from the equivalent circuit to the experimental Nyquist spectra (■); (b) Randles equivalent circuit representing the circuit elements that are used to fit the experimental Nyquist spectra using the software Nova.

Figure 6.12. Ragone plot of 40LFP-AC composite electrodes.

Figure 6.13. CV profile comparison of 40LFP–AC composite electrodes between initial cycle and 1000th cycles at 10 mV/s in 1 M Na_2SO_3.

Figure 6.14 Cycling life of 40LFP–AC composite electrodes in aqueous Na_2SO_3 electrolyte at scan rate of 10 mV/s between 0 and 1 V.

Figure 7.1. A schematic illustration for the synthesis of the SnO_2-graphene composite materials.

Figure 7.2. XRD patterns of graphite and SnO_2-graphene composites.

Figure 7.3. Raman spectra of graphene and SnO_2-graphene composites.

Figure 7.4 FESEM micrographs of (a) graphene, (b) SnO_2, (c)GS6, (d) GS12, (e) GS24, TEM images of (f) graphene , (g) GS24, ,(h) HRTEM of GS24 and (i) EDX spetrum of GS24.

Figure 7.5. CV curves of SnO_2, GS6, GS12 and GS24 electrodes at a scan rate of 5 mV/s.

Figure 7.6. Galvanostatic charging/discharging curves of various electrode materials at a current density of 2 A/g in 1 M Na_2SO_3 electrolyte.

Figure 7.7. Ragone plot of (a) SnO_2-graphene (GS24) and (b) SnO_2 at various scan rates (100, 50, 20, 10, 5 mV/s).

Figure 7.8. Cycle performance of SnO_2-graphene (GS24) composite electrodes.

Figure 7.9. (a) Nyquist polts for SnO_2-graphene (GS24) composite electrodes and SnO_2 electrodes; (b) Fitting of the impedance for GS24 composite electrodes; Randles equivalent circuit representing the circuit elements that are used to fit the experimental Nyquist spectra of (c) GS24 and (d) SnO_2.

Figure 8.1. Schematic representation of the MoO_3-graphene composite materials prepared via green and facile EG-assisted solvothermal synthesis.

Figure 8.2. XRD patterns of graphite and MoO_3-graphene composites.

Figure 8.3. Raman spectra of graphene and MoO_3-graphene composites.

Figure 8.4. SEM micrographs of (a) graphene, (b) MoO_3, (c) GM6, (d) GM12, (e) GM24, (f) EDS spetrum of GM12, TEM images of (g) graphene and (h) GM12.

Figure 8.5. CV curves of MoO_3, GM6, GM12 and GM24 electrodes at a scan rate of 5 mV/s in 1 M Na_2SO_3 electrolyte. (b) CV curves of GM12 composite electrodes at different scan rates of 5, 10, 20, 50 and 100 mV/s.

Figure 8.6. Charge-discharge curves of MoO_3, GM6, GM12 and GM24 electrodes at a current density of 2 A/g.

Figure 8.7. Ragone plot of GM12 and MoO_3 at various scan rates (a) 5, (b) 10, (c) 20, (d) 50, (e) 100 mV/s.

Figure 8.8. Cycling stability of MoO_3-graphene (GM12) composite electrodes at a current density of 2 A/g up to 1600 cycles.

Figure 8.9. Nyquist plots for (a) MoO_3, (b) GM6, (c) GM12, (d) GM24, (e) the fitting of the impedance expressions (━) obtained from the equivalent circuit to the experimental Nyquist spectra (●) and (f) Randles equivalent circuit representing the circuit elements that are used to fit the experimental Nyquist spectra using the software Nova.

List of Publications

Papers published in international referred journals

1. M.Y. Ho, P.S. Khiew, D. Isa, T.K. Tan , W.S. Chiu, C.H. Chia, M.A.A. Hamid and R. Shamsudin, "Nano Fe_3O_4 - Activated Carbon Composites for Aqueous Supercapacitors," Sains Malaysiana 43(2014) 885–894.

2. M.Y. Ho, P.S. Khiew, D. Isa, T.K. Tan , W.S. Chiu, C.H. Chia, " A Review of Metal Oxide Composite Electrode Materials for Electrochemical Capacitors," Nano 9 (2014) 1430002-25.

3. M.Y. Ho, P.S. Khiew, D. Isa, T.K. Tan , W.S. Chiu, "Electrochemical studies on nanometal oxide-activated carbon composite electrodes for aqueous supercapacitors," Functional Materials Letters 7 (2014) 1440012 -4.

4. M.Y. Ho, P.S. Khiew, D. Isa, T.K. Tan , W.S. Chiu, C.H. Chia, "Charge storage performance of lithiated iron phosphate/activated carbon composite as symmetrical electrode for electrochemical capacitor," Current Applied Physics 14 (2014) 1564-1572.

Papers presented in international conference

1. 4th International Conference on Advanced Materials Research (ICAMR 2014), 22-23 January 2014 in Macau.

2. 2nd Asia Conference on Mechanical and Materials Engineering (ACMME 2014), 28-29 July 2014 in Taipei, Taiwan.

3. International Conference on Materials Science and Nanotechnology (ICMSNT 2016), 12-14 May 2016 in Seoul National University, Korea.

CHAPTER 1
Introduction

1.1 Background

Global warming, air-pollution emission, rising oil prices and diminishing supply of fossil fuel have been increasingly driving the world towards the development of clean and environmentally friendly high power energy resources [1]. Transforming natural energy from sustainable and renewable resources such as the sun, ocean tides and wind could yield high electricity energy output. However, man has limited control over natural phenomena because the optimum energy harvesting performances from these renewable resources are greatly dependent on the environmental and geographical factors such as climate, location or the gravitational attraction of the moon and the sun upon the earth. For example, solar harvesting activity is almost impossible during the winter time for some countries when the sun is hardly to appear in the day time. With these climate/geographical constraints, energy storage technology appears as one of the most promising options in tackling the problem since renewably-generated electrical energy can be stored during the optimum production period for future use.

Of the available electrical energy storage devices, batteries have been the technology of choice for most applications as they can store large amounts of energy and provide suitable levels of power for many applications [2]. However, the charge and discharge processes in batteries often involve irreversible redox reactions of species at the electrode-electrolyte interfaces, which in turn change the molecular structure of the electrode materials. For this reason, the cycle-life of batteries is usually limited to several thousand charge-discharge cycles only and serious performance distortion is encountered thereafter [3]. Conversely, the electrode materials in supercapacitors do not participate in redox reactions; therefore there are no major chemical and phase changes in electrode materials during cycling. As a result, an almost unlimited cyclability, typically between 10^5 and 10^6 times cycle lifetimes are frequently obtained in this highly reversible storage mechanism [4]. In addition, much higher-power delivery can be achieved for short times in supercapacitors because the charge storage mechanism employed in supercapacitors is

much faster than the faradaic processes in batteries [5]. Furthermore, supercapacitors can be charged and discharged in few seconds or less whereas rechargeable batteries require at least several minutes or more to release their energy and recharge [6]. Nevertheless, the main drawback of supercapacitors is their relatively low energy density compared to batteries [7]. Table 1.1 summarises the inherent differences between supercapacitors and batteries as well as the conventional capacitors [8].

Table 1.1. The basic characteristics of conventional capacitors, supercapacitors and batteries [8].

Factors	Conventional Capacitors	Supercapacitors	Batteries
Charge time	10^{-6} ~ 10^{-3} s	1 ~ 30 s	0.3 ~ 3 h
Discharge time	10^{-6} ~ 10^{-3} s	1 ~ 30 s	1 ~ 5 h
Specific power (W/kg)	10,000	1000 ~ 2000	50 ~ 200
Specific energy (Wh/kg)	< 0.1	1 ~ 10	20 ~ 100
Cycle life (cycle)	> 500,000	> 100,000	500 ~ 2000
Charge-discharge efficiency (%)	~ 100 %	90 % ~ 95 %	70 % ~ 85 %

A simplified Ragone plot (Figure 1.1) which presents the power densities of various energy storage devices versus their energy densities, discloses that the fuel cells and batteries have high energy but with a limited power density whereas supercapacitors can yield moderate energy and high-power densities. It should be noted that no single energy source can match all power and energy regions. Supercapacitors are likely filling the gaps between the conventional capacitors and batteries [9]. Additionally, a more recent application in low-emission hybrid electric vehicles has shown that supercapacitors are of equal importance to batteries for future energy storage systems. These hybrid energy systems couple the supercapacitors that possess high power capabilities and rapid charge/discharge rate with the primary high-energy batteries [13].

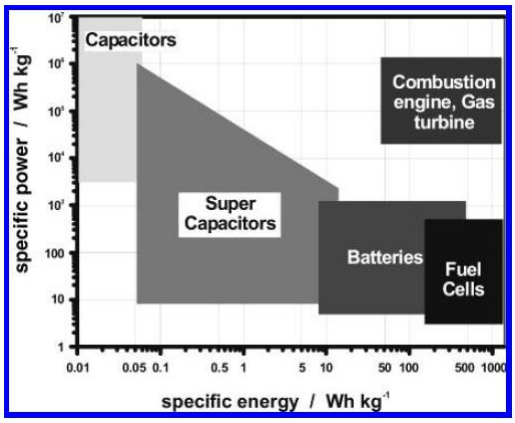


Figure 1.1. A simplified Ragone plot [9]

1.2 Historical background and industry developments

Supercapacitors have evolved through several generations of designs since 1978 [14]. The conventional supercapacitor design technology, which is better known as Electrical Double layer Capacitor (EDLC), employs two identical polarisable electrodes (carbon electrodes) that typically rely on the adsorption of ions onto the high surface area of the electrodes [15]. Second generation symmetric devices were introduced in the 1980s, which used a non-aqueous electrolyte (organic electrolyte) to increase the cell operating voltage. The symmetric technology is also applied to the arrangement where both composite electrodes that are made of metal oxides/conducting polymers and carbon materials [16]. The third generation supercapacitors incorporate both polarisable (carbon) electrode and a non-polarisable electrode (metal oxide or conducting polymer) within a same electrochemical system [15]. This design is referred to as hybrid capacitor. This new technology offers a number of advantages over the standard symmetric design including: improved safety; higher specific energy; more stable operating voltage; lower materials and manufacturing costs and voltage self-balancing in high-voltage strings of capacitor cells [17].

The principle of charge separation and charge storage characteristics was discovered by both Dutch physicist Pieter van Musschenbroek and German experimenter Ewald G. von Kleist when they invented and developed a Leyden jar independently in the middle of 1800s [18]. The discovery of the Leyden jar was of fundamental importance in

the many early electrical research and experiments. It was the first device capable of storing electric charge, which consisted of glass jar with conducting metal foil coating on inner and outer surfaces. The inner and outer surfaces of the jar was separated by the insulating glass which stored equal but opposite charges when an electric generator was connected to the inner surface while the outer was grounded. Subsequently, the concept of electric double layer capacitance was described by Helmholtz in 1853 as a simple capacitor based on a physical model in which a single layer of ions was adsorbed at the surface. It is proposed that the double layer is formed as the solvated ions are accumulated at the electrode-electrolyte interface when an electrode is immersed into an electrolyte solution [19]. This would create a separation of oppositely charged layers along the interface in which the excess charge on the electrode surface is compensated by an accumulation of excess ions of the opposite charge in the solution.

The Helmholtz model was later refined by Gouy and Chapman by introducing a diffuse model of the electric double layer, from which the electric potential decreases exponentially away from the surface to the fluid bulk in the early 1900's [12]. However, the assumption made in the Gouy-Chapman model had its limitation in the calculation of the double layer capacitance which only approached true values near the point of zero charge [12]. Consequently, Stern proposed the combination of the Helmholtz and the Gouy-Chapman models, thereafter named the Stern-Grahame model in 1924, incorporating the compact layers and the diffuse layer [20]. Grahame then divided the compact layer into inner Helmholtz plane (IHP) and outer Helmholtz plane (OHP). In 1963, Bockris and co-workers suggested a model that included the action of the solvent in double layer system [8]. This model which proposed the presence of a single layer of water within the IHP is currently widely accepted.

The practical use of double-layer capacitors began in 1957, when a patent was placed by General Electric for an electrolytic capacitor using porous carbon electrodes [21]. In the patent, it was noted that "it is not positively known exactly what takes place when the device was used", but it was believed that the energy was stored in the pores of porous carbon which enabled the capacitor to exhibit an "exceptionally high capacitance." Later in 1966, Standard Oil Company of Ohio (SOHIO) patented a device that stored energy at the double layer interface, which forms the basis for the hundreds of subsequent

patents and thousands of journal articles later [6]. It was claimed in the patent that the energy storage was achieved through the ionic adsorption within the energy storage sites at the inter-phase boundaries between the carbon electrodes and the aqueous solution, under the electrostatics field induction [22]. In addition, it was also suggested that the reversible electrochemical reactions occurring at the inter-phase boundaries further enhanced the energy storage capability of the device [22].

In 1970, SOHIO patented a disc-shaped capacitor incorporating a carbon paste electrodes with a separator soaked in an electrolyte [23]. The separator was believed to serve as an insulator to electrons but which permitted the movements of ions. In the patent, it was also explained that the carbon paste electrodes were fabricated from the finely divided carbon particles blended with an electrolyte followed by compression and drying processes [23]. However, the subsequent lack of sale had made SOHIO to abandon their research on the low voltage electrolytic capacitor in 1971 [24]. Following the first commercially introduction of double-layer capacitor, supercapacitors have evolved through several generations of designs since 1978 [6]. "SuperCapacitor" which was developed by NEC under license from SOHIO had low voltage but high internal resistance. The Matsushita Electric Industrial Co. (which is now known as Panasonic) introduced the 'Gold capacitor' by 1980 [25]. In 1987, ELNA has started manufacturing a double-layer capacitor called "Dynacap" [26]. The "PRI Ultracapacitors" utilising metal-oxide electrodes were the first high-power double-layer capacitors and were designed for military applications under the invention of PRI [27]. Subsequently, a study on double-layer capacitor for the application of hybrid electric vehicles was embarked by the United State Department of Energy (DoE) at the Maxwell Laboratories in 1992 [26]. Table 1.2 presents some historical landmarks of discoveries and development of supercapacitor.

Table 1.2. Historical developments of supercapacitor.

Date	Landmark	Source	Reference
1800	Discovery of the Leyden jar- principle of charge separation and charge storage characteristics.	Pieter van Musschenbroek and Ewald G. von Kleist	[18]
1853	Discovery of first double layer capacitance model – Helmholtz double layer model.	Helmholtz	[19]
1910	Introduction of a diffuse model of the double layer - Gouy-Chapman diffusion model.	Gouy and Chapman	[12]
1924	Introduction of Guoy-Chapman-Stern model by combining the Helmholtz compact layer and the Gouy-Chapman type diffuse layer.	Stern	[20]
1947	Introduction of the Grahame model which proposed the existence of three regions: IHP, OHP and diffuse layer.	Grahame	[28]
1957	First patent of electrolytic capacitor using porous carbon electrodes.	General Electric	[21]
1963	Introduction of a single layer of water molecules within IHP at the surface of the metal electrode – current model.	Bockris, Devanathan and Muller	[8]
1966	Patent of a device that stored energy at the double layer interface.	SOHIO	[6]
1970	First attempts to market: a disc-shaped capacitor incorporating a carbon paste electrodes with a separator soaked in an electrolyte.	SOHIO	[23]
1971	Research on the low voltage electrolytic capacitor was abandoned due to lack of sale.	SOHIO	[24]
1978	First commercially introduction of double-layer capacitor named “SuperCapacitor”	NEC	[6]
1980	Introduction of “Gold capacitor”.	Matsushita Electric Industrial Co. (Panasonic)	[25]
1982	First high-power double-layer capacitors designed for military applications called “PRI Ultracapacitors”.	PRI	[27]
1987	First manufacturing of a double-layer capacitor called “Dynacap”	ELNA	[26]
1992	Study on double-layer capacitor in the application of hybrid electric vehicles at the Maxwell Laboratories	DoE	[26]

At present, with an increased demand for the expansion power quality needs and the emerging energy management/conservation such as mobile electronics, transportation, renewable energy production and space industries, there are a number of companies around the world that continues actively engaging in the research and development of supercapacitor, namely, Cooper, Evans, AVX, Maxwell and IOXUS in United States, Tavrima in Canada, Cornell Dubilier in UK, Saft in France, WIMA in Germany, Cellergy in Israel, NEC and Panasonic in Japan, Cap-XX in Australia, Nesscap and Vinatech in Korea, and ESMA in Russia. Current markets address a large majority of their supercapacitors using symmetric activated carbon electrode materials and an acetonitrile electrolyte [12]. The performance characteristics of several commercial supercapacitors currently available from various manufacturers are summarised in Table 1.3.

As a result of low cost, easy availability, large active area and good electric conductivity, carbon-based materials currently dominate the market as core electrode materials [46]. However, the exploitation of pseudocapacitive effects to enhance double-layer capacitance seems to be an alternative means to develop the next generation of high-power and high-energy supercapacitors. Nesscap has produced one of the first commercially available pseudocapacitors that store more than twice the energy of a standard EDLC [44]. However, this type of supercapacitor frequently suffers a number undesirable shortcoming including charge storage instability, an increased resistance, short life cycle and higher manufacturing cost if compared to those of carbon-based electrodes [2].

Table 1.3. Summary of world-wide commercially available supercapacitor.

Company	Product Name	Country	Volatge Range (V)	Capacitance Range (F)	ESR range (mΩ)	Reference
Cooper Bussmann	Powerstor	US	2.5 – 5.5	0.07 – 100	20 – 100000	[29]
Evans	Capattery	US	5.5, 11	0.47 – 1.5	0.60 – 4	[30]
AVX	Bestcap	US	3.6 – 16	0.010 – 1	25 – 600	[31]
Maxwell	Boostcap	US	2.2 – 125	1 – 3000	0.29 – 700	[32]
IOXUS	Ultracapacitor Cell	US	2.3 – 16	58 – 5000	0.25 – 45	[33]
IOXUS	Hybrid Capacitor	US	1 – 2.3	220 – 1000	7 – 25	[33]
Tarvima	ESCap	Canada	14 – 300	2 – 160	9.9 – 300	[34]
Cornell Dubilier	CDE	UK	2.1 – 5.5	0.022 – 70	10 – 200000	[35]
SAFT-ESMA	Saft Nickel Capacitor	France	7 – 29	500 – 1200	2 – 6	[36]
WIMA	Supercap	Germany	2.5, 2.7	110 – 6500	11	[37]
Cap-xx	Cap-xx	Australia	2.3 - 5.5	0.09 – 120	14 – 200	[38]
Cellergy	Cellery	Israel	2.1 – 12	0.01 – 0.12	65 – 1200	[39]
Panasonic	Gold Capacitor	Japan	2.1 - 5.5	0.015 – 70	100 – 150000	[40]
NEC/Tokin	Supercapacitor	Japan	2.7 - 12	0.01 – 100	700 – 300000	[41]
Elna	Dynacap	Japan	2.5 – 5.5	0.047 – 100	-	[42]
Nichicon	Evercap	Japan	2.5, 2.7	0.47 – 4000	1.8 – 4000	[43]
Nesscap	EDLC	Korea	2.3 – 2.7	5 – 60	14 – 123	[44]
Nesscap	Pseudocapacitor	Korea	2.3	50 – 300	12 – 14	[44]
VINATECH	HY-CAP	Korea	2.3 – 5.4	0.75 – 800	3 – 330	[45]

Recent developments of composite materials which integrate carbon-based materials with either metal oxide or conducting polymer have demonstrated the improved capacitive performance and cycle life through the synergistic effect of both EDLC and pseudocapacitance mechanisms. Carbon-based materials provide a high-surface area backbone that increases the contact between the deposited active materials and electrolyte while pseudocapacitive materials enhance the capacitance of composite electrode through

Faradaic reactions. Similar to this concept, hybrid capacitor-battery designs utilizing battery-type and supercapacitor-type electrodes are reported to obtain significantly higher energy storage than currently available commercial supercapacitors [17]. Efforts to commercialize asymmetric hybrid capacitors are currently being pursued by IOXUS and Saft-Esma signifying their capability to compete with the lithium-ion hybrid and asymmetric nickel-carbon supercapacitors that are currently available in the market [17].

1.3 Rationale and research objectives

Recently, there have been great interests in transition metal oxide-based composite materials for supercapacitors. However, large scale production of these hybrid capacitors still remains challenging due to their high cost and relatively low energy density. Thus, there is an urgent demand to utilize cost-effective electrode materials and develop cost-saving automated fabrication methods, which offer flexible alternatives in cost reduction [2]. With the advantages of low cost, natural abundance, easy availability and environmental friendly unique features, iron oxide (Fe_3O_4), zinc oxide (ZnO), titanium oxide (TiO_2), molybdenum oxide (MoO_3) and tin oxide (SnO_2) have been investigated as the candidates of electrode materials for supercapacitors. Additionally, the incorporation of carbon-based materials (activated carbon and graphene) into metal oxide –based electrodes has been proven to be an effective method to combine the good conductivity, high capacitive performance and excellent cycle stability of composites. On top of advanced electrode materials, to exploit green and suitable electrolytes is another key driver to develop high-performance supercapacitors. Organic electrolytes and ionic liquids with broad operating windows offer relatively higher energy density. However, organic electrolytes with poor electrical conductivity are not environmentally friendly while ionic liquids are cost-ineffective, leading to both types of electrolytes being undesirable in practical applications. In view of environmental concerns and cost, neutral and non-toxic aqueous electrolytes are desirable by configuring smart supercapacitors with appropriate electrode materials. In fact, fabrication methods also remain equally important for any practical purpose, where a simple, cost effective and direct procedure is required for commercial purpose.

With these considerations, this thesis aims to design and develop a series of transition metal oxide-based composite materials with enhanced electrochemical performance for neutral aqueous supercapacitor. The specific research objectives in this project are to:

- synthesize and characterize cost effective metal oxide – activated carbon nanocomposite electrodes for superior electrochemical charge storage performance in different electrolytes.
- develop lithium iron phosphate and activated carbon ($LiFePO_4$-AC) materials with enhanced electrochemical performance.
- develop a facile, green and cost-effective solvothermal route for the preparation of metal oxide – graphene nanocomposite electrodes for supercapacitor application.

1.4 Structure of this thesis

Beginning from a brief introduction to supercapacitors in Chapter 1, Chapter 2 presents a comprehensive literature review on the working principles of supercapacitors, the commonly used techniques for evaluating the electrochemical properties of supercapacitors and the electrode materials used for supercapacitors. Presented in Chapter 3 are the chemicals, reagents and experimental methods used in this thesis. Chapter 4 discusses the preparation, characterization and electrochemical properties of iron oxide (Fe_3O_2) – activated carbon (AC) composite electrodes with an emphasis on the effect of Fe_3O_4 loading on the electrochemical performance of composite electrodes in Na_2SO_3 and Na_2SO_4, respectively. Chapter 5 reports the comparative research results of composite materials of zinc oxide (ZnO) – AC and titanium oxide (TiO_2) - AC in neutral Na_2SO_3 electrolyte. Chapter 6 describe the investigation on the novel phosphate-based electrode, consisting of lithium iron phosphate ($LiFePO_4$) and AC material, emphasizing the effect of compositions on electrochemical performances in different electrolytes. Chapter 7 summarises the results of preparation of tin oxide (SnO_2) – graphene composite electrodes using glucose and their electrocapacitive performance. Chapter 8 discusses the experimental data of ethylene glycol assisted molybdenum oxide-graphene

composite electrodes via green and facile solvothermal approach. Finally, Chapter 9 outlines the main conclusions drawn from this thesis and recommendations for future work.

Reference

[1] A. D. Pasquier, I. Plitz, J. Gural, S. Menocal, and G. Amatucci, "Characterisitcs and Performance of 500 F Asymmetric Hybrid Advanced Supercapacitor Prototypes," Journal of Power Sources 113 (2003) 62-71.

[2] A. Burke, "Ultracapacitor-Why, How and Where is the Technology," Journal of Power Sources 91 (2000) 37-50.

[3] P. J. Hall, M. Mirzaeian, S. I. Fletcher, F. B. Sillars, A. J. R. Rennie, G. O. Shitta-Bey, G. Wilson, A. Cruden, and R. Carter, "Energy storage in electrochemical capacitors: designing functional materials to improve performance," Energy & Environmental Science 3 (2010) 1238.

[4] A.K.Shukla, S.Sampath, and K.Vijayamohanan, "Electrochemical Supercapacitors: Energy Storage Beyond Battery," Current Science 79 (2000) 1656-1661.

[5] H. D.Abruna, Y. Kiya, and J. C.Henderson, "Battery and Electrochemical Capacitors," American Institute of Physics (2008).

[6] J. R. Miller, A. F.Burke, "Electrochemical Capacitors: Challenges and Opportunity for Real-World Applications," The Electrochemical Society Interface, (2008).

[7] M.Jayalakshmi and K.Balasubramanian, "Solution Combustion Synthesis of Fe_2O_3/C, Fe_2O_3-SnO_2/C, Fe_2O_3-ZnO/C Composites and Their Electrochemical Characterisation in Non-Aqueous Electrolyte for Supercapacitor Application," International Journal of Electrochemical Science 4 (2009) 878-886.

[8] M. V. Kiamahalleh, S. H. S. Zein, G. Najafpour, S. A. Sata, and S. Buniran, "Multiwalled Carbon Nanotubes Based Nanocomposites for Supercapacitors: A Review of Electrode Materials," Nano 07 (2012) 1230002.

[9] M. S.Halper and J. C.Ellenbogen, "Supercapacitor: A Brief Overview," MITRE (2006).

[10] K. W. Leitner, B. Gollas, M. Winter, and J. O. Besenhard, "Combination of redox capacity and double layer capacitance in composite electrodes through immobilization of an organic redox couple on carbon black," Electrochimica Acta 50 (2004) 199-204.

[11] T. Brousse, P.L. Taberna, O. Crosnier, R. Dugas, P. Guillemet, Y. Scudeller, Y. Zhou, F. Favier, D. Bélanger, and P. Simon, "Long-term cycling behavior of asymmetric activated carbon/MnO_2 aqueous electrochemical supercapacitor," Journal of Power Sources 173 (2007) 633-641.

[12] A. Davies and A. Yu, "Material advancements in supercapacitors: From activated carbon to carbon nanotube and graphene," The Canadian Journal of Chemical Engineering 89 (2011) 1342-1357.
[13] P. Simon, Y. Gogotsi, "Materials for Electrochemical Capacitors," Macmillan Publishers Limited (2008).
[14] J. R.Miller, "Capacitor Energy Storage for Stationary-Power Applications."
[15] N. W. Duffy, W. Baldsing, and A. G. Pandolfo, "The nickel–carbon asymmetric supercapacitor—Performance, energy density and electrode mass ratios," Electrochimica Acta, 54, (2008) 535-539.
[16] M. Winter and R. J.Brodd, "What Are Batteries, Fuel Cells and Supercapacitors?," American Chemical Society 104 (2004) 4245-4269.
[17] J. Ledge, "Saft and ESMA to cooperate on supercapacitor development, production and commercialisation," Saft Press Release (2009).
[18] B. E. Conway, V.Birss, and J.Wojtowicz, "The role and utilization of pseudocapacitance for energy storage by supercapacitors " Journal of Power Sources 66 (1997) 1-14.
[19] A. Nishino, "Capacitors: Operating Principles, Current Market and technical Trends," Journal of Power Sources 60 (1994) 137-147.
[20] M. Sharon, V. Khairnar, and C.C. Hu, "Chapter 15: Electric Double Layer Capacitor and Carbon Nano Materials," in Carbon Nano Forms and Applications, M. S. Madhuri Sharon, Ed., ed. New York City, US: Mc Graw Hill (2009) 230-246.
[21] Howard I. Becker et al, "Low voltage electrolytic capacitor," U.S. Patent 2800616 (1957).
[22] R. A. Rightmire et al, "Electrical energy storage apparatus," (1966).
[23] Donald L. Boos et al, "Electrolytic capacitor having carbon paste electrodes,"(1970).
[24] M.Endo et al, "High power electric double layer capacitor (EDLC's); from operating principle to pore size control in advanced activated carbons," Carbon science 1 (2001) 117-128.
[25] A. Yoshida, K. Imoto, A. Nishino, and H. Yoneda, "An electric double layer capacitor with high capacitance and low resistance," presented at the 41st Electronic Components and Technology Conference, Atlanta, GA, USA (1991).
[26] J.G.Zhu. (2012) Supercapacitors [Online]. Available: http://services.eng.uts.edu.au/cempe/subjects_JGZ/eet/SuperCap_1_11_05.pdf [access in Jan 2012].
[27] G.L.Bullard et al, "Operating principles of the ultracapacitor," IEEE Transactions on Magnetics 25 (1988) 102-106.

[28] Electric Double Layers and Capacitance Response [Online]. Available: http://uqu.edu.sa/files2/tiny_mce/plugins/filemanager/files/27/08_Appendix.pdf[access in Jan 2012].
[29] C. Bussmann. (2012). PowerStor Supercapacitors [Online]. Available: http://www.cooperindustries.com/content/public/en/bussmann/electronics/products/powerstor_supercapacitors.html[access in Jan 2012].
[30] E. C. Company. (2012). Evans Capacitor Company Products [Online]. Available: http://www.evanscap.com/evans_capacitor_products.htm[access in Jan 2012].
[31] A. Corporation. (2012). AVX Prodinfo [Online]. Available: http://www.avx.com/prodinfo_catalogview.asp?prxID=10[access in Jan 2012].
[32] M. Technologies. (2012). Boostcap Ultracapacitor [Online].Available: http://www.maxwell.com/products/ultracapacitors/product.aspx?pid=PC10-SERIES[access in Jan 2012].
[33] IOXUS. (2012). IOXUS Data Sheets [Online]. Available: http://www.ioxus.com/data-sheets.html[access in Jan 2012].
[34] Tavrima. (2012). Products [Online]. Available: http://www.tavrima.com/products.htm[access in Jan 2012].
[35] C. Dubilier. (2012). Catalog Listing [Online]. Available: http://www.cde.com/catalog/listing/[access in Jan 2012].
[36] Saft. (2012). Nickel-Carbon Capacitor [Online]. Available: http://www.saftbatteries.com/Technologies_Nickel_NiCcapacitor_455/Language/en-US/Default.aspx[access in Jan 2012].
[37] WIMA. (2012). SuperCapacitors [Online]. Available: http://www.wima.de/EN/products_super.htm[access in Jan 2012].
[38] Cap-xx. (2012). Products [Online]. Available: http://www.cap-xx.com/products/products.php[access in Jan 2012].
[39] Cellergy. (2012). Products Overview [Online].Available: http://www.cellergycap.com/index.php?option=com_content&view=article&id=11&Itemid=1 [access in Jan 2012].
[40] Panasonic. (2012). Industrial Devices [Online]. Available: http://industrial.panasonic.com/www-ctlg/ctlg/qABC0000_WW.html[access in Jan 2012].
[41] NEC/Tokin. (2012). Product List [Online].Available: http://www.nec-tokin.com/english/product/product_list.html[access in Jan 2012].
[42] ELNA. (2012). Capacitors [Online]. Available: http://www.elna.co.jp/en/capacitor/double_layer/index.html[access in Jan 2012].
[43] Nichicon. (2012). 2012 Electronic Components [Online]. Available: http://www.nichicon.co.jp/english/products/evercap/pict_f.htm[access in Jan 2012].

[44] Nesscap. (2012). Product Overview [Online]. Available: http://www.nesscap.com/product/overview.jsp[access in Jan 2012].
[45] VINATECH. (2012). Product Information [Online]. Available: http://www.vina.co.kr/new_html/eng/product/info.asp?cate1=10&cate2=16&cate3=[access in Jan 2012].
[46] A. G. Pandolfo and A. F. Hollenkamp, "Carbon properties and their role in supercapacitors," Journal of Power Sources 157 (2006) 11-27.
[47] L.L.Zhang and X.S.Zhao, "Carbon-based materials as supercapacitor electrodes," The Royal Society of Chemistry 38 (2009) 2520-2531.

CHAPTER 2
Literature Review

2.1. Introduction

Demand for energy consumption has significantly increased due to the rapid growth of population and global economy. Based on the surveys conducted by Energy Information Administration (EIA), fossil fuels (petroleum, coal, natural gas etc.) make up the bulk of the world's current primary energy sources [1]. Excessive dependence on fossil fuels has resulted in increasing greenhouse gas emission, rising oil prices and fossil fuel depletion which consequently lead to global economic crisis and environmental issues. Therefore, transforming natural energy from sustainable and renewable resources such as the sun, ocean tides and wind could help meet increased energy needs. However, man has limited control over natural phenomena due to the climate/geographical constraints. For these reasons, energy storage technology appears as one of the most promising options in harvesting renewably-generated electrical energy during the optimum production period for future use.

Of the available electrical energy storage devices, fuel cells, batteries and capacitors have been the technology of choice for most applications. Each of these system exhibits different characteristics in terms of specific energy and power, as shown in the Ragone plot (Figure 2.1). In general, batteries can store the highest specific energy ranges from 120 to 200 Wh/kg with relatively low specific power, ranging from 0.4 to 3 kW/kg. On the other hand, conventional capacitors deliver relatively very low specific energy (< 0.1 Wh/kg). Comparatively, the electrochemical capacitors have much higher specific power (from 5 to 55 kW/kg) and reasonable specific energy (4 to 8 Wh/kg), which are likely to bridge the function for the energy/power gap between the conventional capacitors and batteries [2].

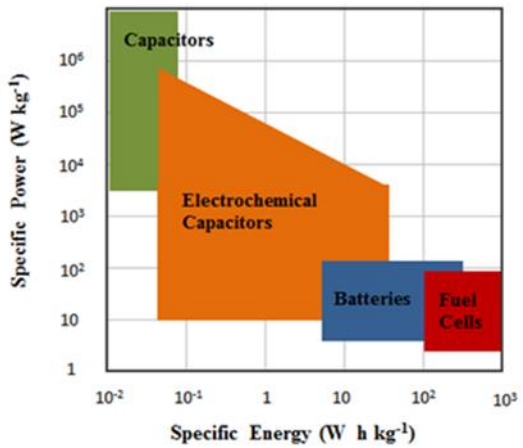


Figure 2.1. Ragone plot showing the specific power against specific energy for various electrical energy storage systems [2].

Generally, there are two main categories of supercapacitor mechanisms. The first category is the electrical carbon layer capacitors (EDLCs), which store energy non-Faradaically via the pure electrostatics charge accumulated at the electrode-electrolyte interface. Carbon-based materials, ranging from activated carbons (ACs) to carbon nanotubes (CNTs) and graphene, have become the most extensively examined electrode materials in EDLCs, owing to the large surface area, high electronic conductivity, sufficient chemical stability and low costs [3].

In contrast to EDLCs, the second category of supercapacitor utilizes the fast and reversible faradaic properties of pseudocapacitive materials to store energy, involving adsorbed and electro-active species at the electrode-electrolyte interface. A good example of pseudocapacitive material is ruthenium oxide (RuO_2). Due to its intrinsic reversibility for various surface redox couples and high conductivity, RuO_2 offers an alternative means to enhance the energy density through faster and highly reversible faradaic charge storage mechanism. However, its impractical high cost and toxicity have impeded its commercial acceptance for supercapacitor applications [4]. While conducting polymers including polyaniline, polypyrrole and polythiophene can also offer the advantages of cost-effective and high conductivity due to their fast doping/dedoping abilities, these materials often possess a lack of stability from mechanical stress or by undergoing soluble transition states during charge/discharge [5].

In view of these limitations, there has been a progressive exploration towards the cost-effective and non-toxic electrode materials. The continuous development of nanostructured materials has led a remarkable progress towards supercapacitor technologies. Nanocomposite, emerging as a new class of electrode materials for supercapacitor applications, is known as hybrid nanostructured material which utilizes both non-Faradaic and Faradaic charge storage mechanisms [6]. Depending on the different combinations of carbon-based materials, transition metal oxides or conducting polymers, these hybrid materials are categorized into three electrode configurations: symmetric, asymmetric and battery-type respectively.

Based on previous literatures, the key factors that affect the selection of electrode materials for supercapacitors are the following [7, 8]:

- high accessible surface area to increase the contact area between electrode and electrolyte for charge storage;
- surface wettability to enhance pore flooding, improving the specific surface area utilized
- good electrical conductivity to reduce the loss in power from internal resistance
- narrow pore size and pore distribution to facilitate ion mobility, accessibility and reduction in diffusion path length.
- long and stable life cycle ($>10^5$) with high mechanical integrity and chemical stability;
- low internal electric resistance which leads to fast charging-discharging and low ohmic resistance;
- low volume and weight;
- low cost;
- environmental friendly materials;

2.2. Principle of supercapacitor

Supercapacitors differ from conventional capacitors by storing charge using the double layer concept. Relative permittivity which initially represents the dielectric constant of the insulating material in the conventional capacitor is now replaced with the

dielectric constant of the charged species of the electrolyte which form the electric double layer. The term *d* which represents the separation distance between the electrodes in the conventional capacitor, is now referring to the effective thickness of the double-layer at the solid/electrolyte interface (Figure 2.2). The separation of the charges at the interface typically is only in the order of few Angstroms, depending on the electrolytes used. As a result of high internal surface area of the electrodes and nanometre scale thickness of the double layer, the capacitances obtained in supercapacitors are several orders of magnitude higher than those of conventional capacitors of the same size [5].

Figure 2.3 shows the basic structure model of supercapacitor. The active material is usually pressed or coated onto the current collector and immersed in the electrolyte. The separator prevents the two electrodes from short- circuiting each other, but is ion-permeable allowing ionic charge transfer to take place [7].

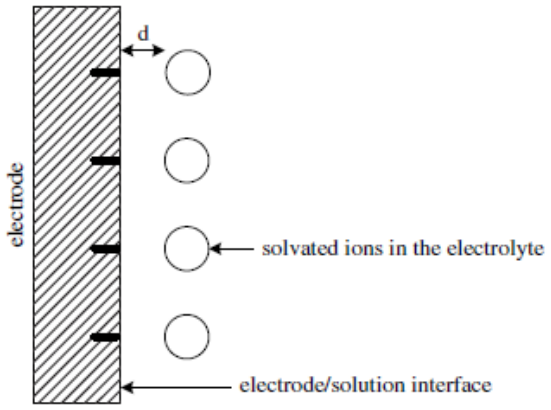


Figure 2.2. Simplified schematic of double layer [7].

Supercapacitors can be explained via two types of charge storage mechanism:

(a) Electrical double layer capacitor (EDLC) utilises a non-faradaic process to store energy through ion adsorption [9]. The double layer capacitance is measured using the following equation:

$$C_{dl} = \frac{\varepsilon_0 \varepsilon_r}{d} A \qquad \text{Eq.(2.1)}$$

where ε_0 is the space permittivity and ε_r is the relative permittivity, A is the surface area of an electrode, and d is the effective thickness of the double layer.

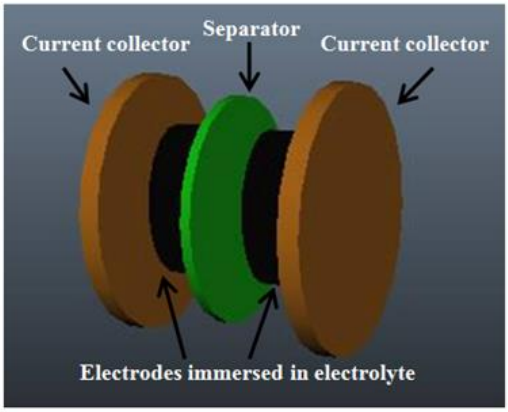


Figure 2.3. The basic structure model of EDLC.

(b) Pseudocapacitor stores energy faradaically via fast and reversible redox reactions between the electrolyte and electroactive species on the electrode surface [9]. The pseudocapacitance arises from the following equation:

$$C_{pc} = q(\frac{d\theta}{dV}) \qquad \text{Eq.(2.2)}$$

where q is the faradaic charge required for adsorption/desorption of ions, dθ is the change of surface coverage by adsorbed species and dV is the change of voltage [10].

The energy stored (E) in a capacitor is directly proportional to its capacitance (C) and the square of applied voltage (V^2) according to equation [3]:

$$E = \frac{1}{2} CV^2 \qquad \text{Eq.(2.3)}$$

It is evident that the decomposition voltage of the electrolyte determines the operating voltage of the cell which in turn contributes different magnitudes of energy density [11]. Thus, a great number of research have been conducted and focused on

studying highly conductive and stable electrolytes with a wide operating voltage for a variety of applications.

In general, supercapacitors can discharge the electrical energy stored rapidly in order to produce high power density. The power density (P) is proportional to the square of applied voltage (V^2) and is limited by the resistance R [4]:

$$P = \frac{V^2}{4 \text{ x } R} \qquad \text{Eq.(2.4)}$$

R is the equivalent series resistance (ESR) which is comprised of the electrode resistance, electrolyte resistance and resistance due to the diffusion of ions in the electrode porosity. Electrolyte conductivity, the size of electrolyte ions and the porosity of electrode materials are among the key factors affecting on the ESR of the cell, which in turn determine its power output [12].

2.3 Electrode materials

As discussed in section 2.2, capacitance, operating voltage and inner resistance of electrochemical capacitors are greatly dependent on electrode materials. By further exploring and developing new materials with improved performance relative to current electrode materials in the market, is the most effective approach to make electrochemical capacitors become very competitive choices for energy storage applications. A graphical taxonomy of supercapacitors is demonstrated in Figure 2.4 [13]. In relation to the recent trends of research and development, supercapacitors can be classified into three main categories: (i) electric double layer capacitors (EDLCs) such as carbon-based materials, (ii) pseudocapacitors including transition metal oxides and conducting polymers, and (iii) hybrid capacitors. Carbon-based materials including activated carbons (ACs), carbon nanotubes (CNTs) and graphene have been extensively investigated as promising EDLC electrodes due to their high surface areas and electrochemical stability [3]. Transition metal oxides and conducting polymers are examples of pseudocapacitors which might be able to contribute up to 10-100 times more than that of EDLCs due to their fast and reversible surface redox reactions [14]. Hybrid capacitors utilise both EDLC and

pseudocapacitance mechanisms to store charge, achieving greater energy and power densities than pure EDLCs or pseudocapacitors. Three different types of hybrid capacitors become the focus of the current research, depending on their electrode configuration: composite, asymmetric and battery-type respectively. Combination of EDLCs, pseudocapacitors with the latest generation of lithium electrodes has brought the energy density of supercapacitors closer to that of batteries [3].

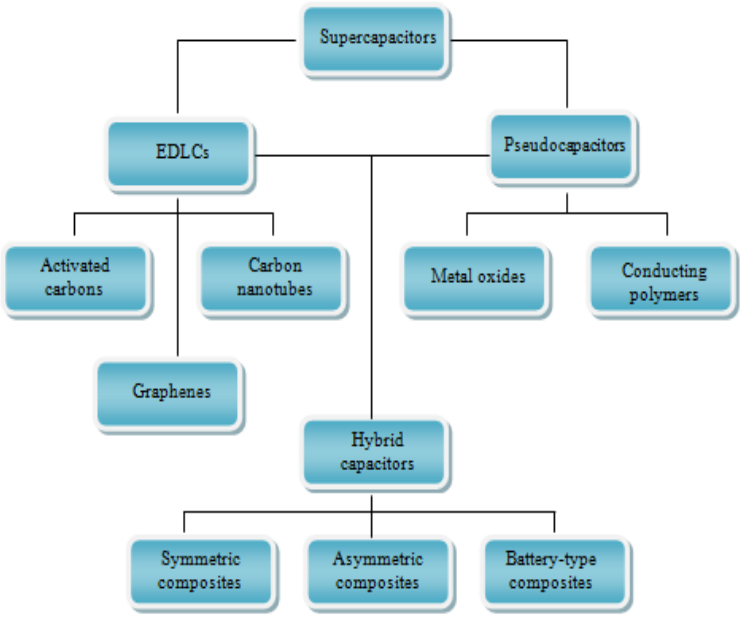


Figure 2.4. Taxanomy of supercapacitors [13].

2.3.1 Carbon-based materials

Since initial commercialization of supercapacitors in 1978, carbon has been widely used as an electrode material for EDLC [12]. From the substantial amount of published literatures available on carbon electrode materials, it is clear that the attraction of carbon as supercapacitor electrode material arises from the distinctive chemical and physical properties, namely [15, 16]: (i) high surface area (~100 to > 2000 m^2/g), (ii) good corrosion resistance, (iii) high temperature stability, (iv) controlled pore structure, (v) relatively high conductivity, (vi) processability and compatibility in composite materials.

On top of the unique combination of chemical and physical properties, great abundance, easy availability and low cost are some of the attractive merit points of carbon for supercapacitor applications. However, carbonaceous compound suffers from the major drawback of high resistivity due to the contact resistance between carbon particles which gives rise to a high internal series resistance [12]. Carbons are available with a specific surface area of up to 2500 m^2/g in the form of activated carbon (AC), carbon black (CB), carbon aerogel, carbon fiber cloth, powdered graphite, graphite cloth, glassy carbon, carbon nanotube (CNT) and graphene [17]. Among the carbon-based materials, AC, CNT and graphene have been extensively studied.

2.3.1.1 Activated carbon (AC)-based materials

Activated carbons (ACs) are generally produced from the pyrolysis of biomass precursors such as wood, coal, peat, coconut and other agricultural waste products which are subjected to activation followed by carbonization processes in order to increase the available surface area and pore accessibility by electrolyte [11]. Generally, chemical and physical activations are employed to improve the specific surface area of AC electrodes by introducing micropores in order to enhance the capacitance performance [12]. In the chemical activation process, carbonization and activation are carried out by thermal decomposition of the precursor impregnated with a chemical activating agent such as KOH, HNO_3 or H_3PO_4. Physical activation involves gasification of the carbon produced from carbonization with an oxidizing gas at elevated temperature [11]. AC utilises a complex porous structure composed of differently sized micropores (< 2 nm wide), mesopores (2-50 nm) and macropores (> 50nm) to achieve the high surface area [13]. Based on the storage mechanism of EDLCs, the specific surface area of AC electrode material is directly proportional to the specific capacitance. Theoretically, it is proposed that the higher specific surface areas would strongly correlate to the improved capacitive performance. However, practical situations are more complicated for a wide variety of ACs as this trend is not perfectly followed [18].

The results shown in Table 2.1 reveal that the capacitance values are non-linear to the BET surface area. It is explained that the narrow micropores may not contribute to the

total double layer capacitance due to a sieving effect which is greatly dependent on the size of the electrolyte ions [19]. Another similar study conducted by Qu (1998) also demonstrated that the measured capacitance of activated carbons did not have a linear relationship with their surface area [20]. In fact, some activated carbons with smaller surface area had larger specific capacitance than those with a larger surface area. With these observations, the authors have identified two primary reasons for the observed phenomenon. Firstly, a wide variety of ACs made from different types of precursors through activation processes and subsequent treatments yield inconsistent double layer capacitance. Secondly, not all the BET surface areas are electrochemically accessible when in contact with electrolyte. It is believed that small diameter micropores may not be accessible to electrolyte solution, especially for those large solvated ions, which are too big to enter those micropores [5]. However, some experimental results have challenged that these findings do not hold. Chmiola et al. (2006) produced ACs with micropore sizes ranged from 0.6 to 2.25 nm, demonstrating that charge storage in pores smaller than the size of solvated electrolyte ions will lead to enhanced ionic transport in porous media [21]. Another similar investigation on the important contribution of micropores, suggested that partial desolvation of hydrated ions has enhanced the overall capacitance [22]. Very recently, Simon and Gogotsi (2008) investigated the capacitive performance on carbon electrodes with pore size less than 1 nm and reported the maximum EDL capacitance was achieved when the electrode pore size was very close to the size of the electrolyte ion [3].

In general, the capacitance values of ACs range from 100 to 200 F/g in aqueous medium, and from 50 to 150 F /g in organic medium [23]. The higher capacitance values in aqueous electrolyte are attributed to a smaller size of solvated ions and a higher dielectric constant. In contrast, organic electrolytes with larger ion sizes which cannot penetrate the pore volume to an equivalent extent, exhibiting poorer capacitive performance. It is proposed that microporous carbon with a high specific surface area is effective for higher energy densities with a relatively slow charge–discharge [13]. On the other hand, in order to obtain higher power densities, carbon electrodes should contain a large amount of mesopores as relatively larger pore size allows improved ion accessibility and diffusion. Macropores generally make insignificant contribution to the

surface area of porous carbon and they act as transport avenues into the interior of carbon particles [12].Thus, it has conclusively been shown that the optimized pore size is crucial for high capacitive performance. As a result, the pore size distributions of ACs as well as the use of distinct electrolytes have become the major areas of research in EDLC design [7, 8, 13].

Table 2.1. Comparison of specific capacitance, surface area, pore volume and average pore size of ACs [19].

Carbon	Specific capacitance (F/g)	BET (m^2/g)	Pore volume (cc/g)	Pore size (Å)
M-10	55.95	1370	0.500	9.12
M-14	57.20	1223	0.561	9.60
M-15A	78.10	1800	0.629	9.17
M-15B	55.80	1624	0.563	9.37
M-15C	63.34	1518	0.600	9.79
M-20	100.00	2130	0.709	14.73
M-30	62.90	2571	1.230	14.95
A-10	35.3	1150	0.424	-
A-20	41.20	2012	0.902	14.23
SACF-20	48.80	1839	0.699	9.74
SACF-25	27.90	2371	0.977	11.93

Recently, a similar research done by Feng and co-workers also proposed that the capacitive behaviour is dependent on the size of the pore [24]. The authors suggested that the pore curvature should be taken into consideration on the overall capacitance of nanoporous carbon-based electrodes. In their approach, they proposed an electric double-cylinder capacitor (EDCC) model for modelling mesoporous carbon electrodes while they used an electric wire-in-cylinder capacitor (EWCC) model to describe microporous carbon electrodes, as illustrated in Figure 2.5. From the two proposed models, the capacitance estimations are given in Eq. (2.5) for the EDCC model and Eq. (2.6) for the EWCC model, respectively:

$$C = \frac{\varepsilon_r \varepsilon_0}{b \ln[b/(b-d)]} A \qquad \text{Eq. (2.5)}$$

$$C = \frac{\varepsilon_r \varepsilon_0}{b \ln(b/a_0)} A \qquad \text{Eq. (2.6)}$$

where b is the pore radius, d is the distance of approaching ions to the surface of the carbon electrode; a_0 is the effective size of the counterions (that is, the extent of electron density around the ions).

With the Eq. (2.5) and (2.6), the authors were able to make a good fits of mathematical results obtained to experimental data, regardless of the types of carbon materials and electrolytes employed. When the pores are large enough until the pore curvature is no longer significant, the EDCC model can be reduced naturally to the traditional planar EDL model given in Eq. (2.2) [25]. However, an in-depth understanding of the charge storage mechanism in micropores and mesopores need to be undertaken for future EDLC development.

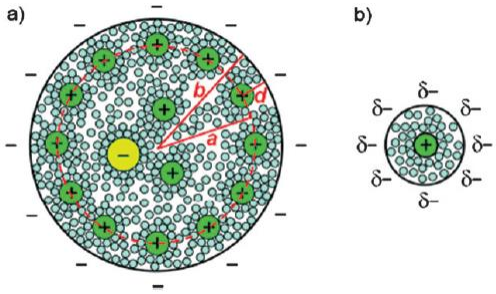


Figure 2.5. Schematic diagram of (a) a negatively charged mesopores with solvated cations approaching the pore wall to form an electric double-cylinder capacitor (EDCC); (b) a negatively charged micropore of radius b with cations lining up along the pore axis to form an electric wire-in-cylinder capacitor (EWCC) [24].

On top of the porous structure of ACs, the surface functionalities also play important roles on the carbon-based electrode performance. The functional groups attributed from electrolyte ions, surfactant ions or acid treatment will affect the wettability of the carbon surface, contributing additional pseudocapacitance [25]. A

recent research producing the low porosity of AC electrode (BET specific surface area = 270 m^2/g) with the presence of oxygen-functional groups, has demonstrated a high energy density of 10 Wh/kg and high power density of 10 kW/kg in acidic electrolyte [26]. On the other hand, some other studies reported that the aging of AC electrodes in organic electrolytes is caused by the active surface of carbon. Pandolfo and co-worker (2006) observed the instability of electrodes, an increase of series resistance and the decomposition of organic electrolyte due to the presence of active surface oxides and a trace of amount of water that were trapped on the electrode [12]. The authors proposed that pure ACs without heteroatoms and water might be better for usage in an organic electrolyte system. In fact, to attain enhanced energy density of supercapacitors without deteriorating their high power density and cycle life, it is desirable to have AC electrode with narrow pore size distribution (with respect to the size of electrolyte ions), an interconnected pore structure, short pore length and controlled surface chemistry [25].

Very recent year, Huang and co-workers (2014) synthesized sulfurized AC by coating the AC surface with thiophenic sulphur functional groups [95]. The sulphur-modified AC exhibits enhanced specific capacitance which is 40 % higher than that of pure AC. It is believed that the sulphur not only could introduce redox reaction on AC but also improve the electrical conductivity of the carbon network.

2.3.1.2 Carbon nanotube (CNT)-based materials

Carbon nanotubes (CNTs), which were first discovered in 1991, have significantly advanced the science and engineering of carbon materials [25]. With excellent electrical conductivity, high thermal stability and good mechanical integrity, CNTs have been studied to offer a new possibility for carbon electrodes for many applications such as batteries, hydrogen storage, flat panel displays, chemical sensors etc. [17]. In addition, the high accessible surface area, narrow pore size distribution and unique pore structure has also led to CNTs being extensively researched as materials for supercapacitor electrodes [11]. CNTs are used as three dimensional supports for active materials owing to their unique morphology and extended graphitic layers. The open mesoporous network formed by the entanglement of nanotubes not only allows the ions

to diffuse easily to the active surface of the composite components but also made the electrodes adapt to the volumetric changes during charge and discharge (Figure 2.6). These properties are essential to improve the cycling performance and enhance the power density of the device [23].

CNTs are generally observed in one of the two forms, multiwalled or single-walled, which were found in 1991 and 1993, respectively. Single-walled carbon nanotubes (SWNTs) have cylindrical walls with diameters ranging between 1 and 3 nm. The structure of a SWNT can be conceptualized by wrapping a one-atom thick layer of graphite called graphene into a seamless cylinder. Multiwalled carbon nanotubes (MWNTs) consist of multiple rolled layers of graphene separated by spacing (0.34 nm) that is close to the interlayer distance in graphene [27]. The first reported MWNT supercapacitor electrodes have been prepared by Niu et al (1997) via the filtration of a dispersed CNT solution, showing specific capacitance of 113 F/g in H_2SO_4 solution [28]. Frackowiak et al (2000) investigated the electrochemical characteristics of multi-walled carbon nanotube (MWNT) pellet electrode with the maximum specific capacitance of 135 F/g in 6 M KOH [29]. Zhang et al. (2001) prepared MWNT electrodes by moulding CNTs with a binder and reported a specific capacitance of 18.2 F/g in an organic electrolyte system [30]. Kim and co-workers (2006) demonstrated a binder-free CNT film electrode using the electrostatic spray deposition (ESD) technique, yielding the specific capacitance of 108 F/g [17].

It is noteworthy that recent studies have shown that entangled CNTs are less efficient in facilitating fast ionic transportation in comparison to aligned CNTs, as a result of the irregular pore structures and high entanglement of the CNT structure in the former electrode [31]. Therefore, the use of aligned CNT would be more beneficial for enhancing power performance of supercapacitors. A densely packed aligned SWNT solid was first fabricated by Futaba et al. (2006) by using the zipping effect of liquids, which allowed the bulk materials to retain the intrinsic properties of SWNTs [32]. The enhanced rate capability and energy density observed from the study showed the importance of the aligned tubular structures in preserving the intrinsic CNT properties on the capacitive performance of CNT electrodes [25]. Additionally, it has been proposed that the capacitance of CNTs can be enhanced via pseudocapacitive effect due to the

functionalization by hot nitric acid (HNO_3) [33]. Research on increasing specific surface area of CNTs via chemical potassium hydroxide (KOH) activation has also shown an encouraging outcome for improving energy density [12].

In spite of having excellent properties, high manufacturing cost has restricted the use of CNTs as bulk active material in EDLC electrodes [18]. Therefore, the recent developments for the use of CNTs in supercapacitor applications are as conductivity enhancers which replace carbon blacks. The study on changing acetylene black to CNTs in EDLC electrodes resulted in a 90% reduction in ESR [11]. The unique architecture of entangled nanotube electrode yields the range of specific capacitance between 80 to 130 F/g [33]. Recent research has also been undertaken to improve specific capacitance of CNT electrodes by modification of CNTs with pseudocapacitive materials such as metal oxides and conducting polymers via faradaic processes. In recent work, Wang and co-workers (2012) have successfully prepared nickel cobalt oxide ($NiCo_2O_4$)/SWCNT ternary nanocomposite for supercapacitor applications [34]. This novel material not only exhibits a remarkable specific capacitance of 1642 F/g, but also demonstrates an excellent cycling stability of 94.1% retention after 2000 cycles. They concluded that the highly conductive SWCNT and $NiCo_2O_4$ have helped to reduce the interfacial resistance of the nanocomposite. However, the authors offer no explanation for the enhanced cycling stability of this ternary composite.

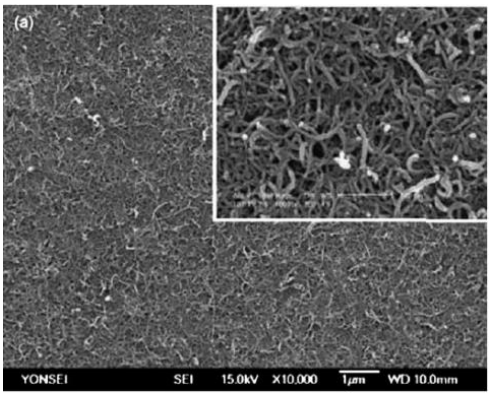


Figure 2.6. SEM image of the CNT film electrode, showing the well-entangled and interconnected porous structure [34].

2.3.1.3 Graphene-based materials

In recent years, a considerable attention has been shifted from AC and CNT to graphene in making composite electrodes due to its good conductivity, superior chemical stability, high elastic and mechanical strength, large surface area, suitable pore size distribution and rapid heterogeneous electron transfer [35]. Graphene, which was studied extensively by Geim's group since 2004, is a single layer of carbon atoms densely packed into a honeycomb structure [36]. Since Vivekchand et al. (2008) [37] and Stoller et al. (2008) [38] pioneered graphene-based electrochemical capacitors, these unique and novel materials have been extensively investigated as possible electrodes for electrochemical energy storage device applications. Unlike the current electrochemical capacitors fabricated with AC and CNT, the high effective specific surface of graphene does not depend on the distribution of pores [39]. Rather the effective surface area of graphene materials is dependent highly on the layers, that is, single or few layered graphene, which have a lower degree of agglomeration. In most recent reports, the chemically modified graphene sheets have demonstrated a very large surface area which is fully accessible to the electrolyte ions while maintaining the high electrical conductivity and good mechanical properties.

Recently, Wang and co-workers (2009) have successfully fabricated the graphene-based electrochemical capacitor that exhibiting remarkable results with specific capacitance of 205 F/g, energy density of 28.5 Wh/kg and power density of 10 kW/kg in KOH [41]. It was followed by the great achievement by Liu and co-workers (2010) who have reported graphene-based supercapacitor using ionic liquid as electrolyte with substantially high specific energy density of 85.6 Wh/kg. [42]. These outstanding findings prove that graphene-based electrochemical capacitors exceeded the specific energy of 21.4 – 42.8 Wh/kg, which is comparable to that of a modern nickel metal hydride battery used in a hybrid vehicle [43]. An interesting phenomenon was observed by Cheng et al. (2011) after charging and discharging graphene electrode galvanostatically for about 1300 cycles in 1 M KCl [39]. Surprisingly, the specific capacitance increased significantly instead of degrading as seen in typical cycling trend of electrochemical capacitors. Authors claimed this observation as electro-activation of graphene sheets in which long charging-discharging process may help electrolyte ions

intercalate into the spaces between graphene layers, fully utilizing the effective surface area of electrode materials. CV curves after about 1300 cycles also revealed that the specific capacitance of 245 F/g is much higher than those of CNT-based electrodes because graphene nanosheets can adapt different sizes of electrolyte ion by physical sheet movement [39]. A very recent research using an in-plane fabrication approach for the preparation of an ultrathin capacitor comprised of pristine graphene and multilayer reduced graphite oxide (RGO) was reported by Yoo et al (2011) [45]. Figure 2.7 presents the schematic depiction of the conventional "stacked" geometry versus the "in-plane geometry". In a "stacked" geometry, the random orientation of the graphitic carbon-based materials with respect to the current collectors resulted in incomplete utilization of effective surface area. On the other hand, the high surface area of graphene layers which was fully utilized, allows the electrolyte ions to penetrate inside the graphitic layers in the "in-plane" design, exhibiting a substantially high specific capacitance of 247.3 F/g.

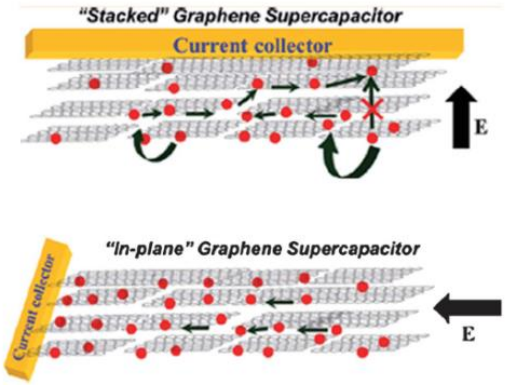


Figure 2.7. Schematic depiction of the conventional "stacked geometry" versus "in-plane geometry" [45].

Very recently, a novel nanocomposite of RGO sandwiched with two Ni_3S_2 nanosheets through a facile one-step hydrothermal approach was developed [66]. Owing to its unique structural features, this Ni_3S_2/RGO/Ni_3S_2 nanocomposite exhibits a superior specific capacitance up to 3234.62 F/g at a current density of 20 mA/cm^2 and 90% retention of the initial capacitance after 1000 cycles at the high rate of 100 mA/cm^2.

2.3.2 Transition metal oxides

Over the past decades, literature review of supercapacitors highlights that a considerable number of metal oxides have been studied intensively. These include ruthenium oxide [46, 47, 48], manganese oxide [49, 50, 51, 52, 53, 54, 55], iron oxide [56, 57, 58, 59], nickel oxide [60, 61, 62, 63, 64, 65] etc.

2.3.2.1 Ruthenium oxide (RuO_2)

RuO_2 in either a crystalline or amorphous hydrous form have been studied extensively in acidic solutions in the past 30 years because of their high specific capacitance and high conductivity characteristics [3]. Owing to its unique properties of three accessible distinct oxidation states, this metal oxide has become the favoured electrode materials in early supercapacitors system for space or military applications [13]. In 1971, Trasatti and Buzzanca firstly used RuO_2 as supercapacitor electrodes and recognized that the almost 'rectangular' current response of RuO_2 films in aqueous H_2SO_4 over a range of potentials from 0.05 to 1.4 V (SHE) was similar to that of EDLC [68]. However, the shape of the cyclic voltammogram (CV) is not a consequence of pure double-layer charging. Rather, it is attributed to a successive electron transfer at redox centres (Ru^{2+}, Ru^{3+}, Ru^{4+}), balanced by the conversion of OH^- to O^{2-} sites in the oxide structure by proton transfer. The energy storage/delivery process within $RuO_x.nH_2O$ generally obeys the following equation:

$$RuO_2 + nH^+ + ne^- \rightleftharpoons RuO_2.n(OH)_n \qquad \text{Eq.(2.7)}$$

According to Lokhande and co-workers (2010), four steps were proposed to determine the capacitive performance of $RuO_x.nH_2O$ [69]:

(i) electron hopping within $RuOx.nH_2O$ particles;

(ii) electron hopping between particles;

(iii) electron hopping between electrode materials and current collectors; and

(iv) proton diffusion within $RuOx.nH_2O$ particles.

Although crystallization of RuO_2 can reduce the intraparticle electron hopping resistance of $RuO_x.nH_2O$ particles, Gujar and co-workers (2007) claimed that the crystalline nature of RuO_2 electrodes limits capacitive performance through an increase

in the diffusion barrier of proton within the rigid lattice of crystalline structure [70]. In fact, literature survey of supercapacitors shows that recent research focus on amorphous hydrous $RuO_x.nH_2O$ thin film based supercapacitor via various methods including sol-gel, cyclic voltammetric deposition, anodic deposition, spray deposition, hydrothermal synthesis, oxidative synthesis etc. [69, 70, 71]. The advantages of amorphous hydrous ruthenium oxides ($RuO_x.nH_2O$) include high specific capacitance, high conductivity, and good electrochemical reversibility [72]. As reported in a literature [73], hydrous $RuO_2.0.5H_2O$ exhibits high capacitance value (~900F/g). However, the capacitance decreased to 29 F/g when the water content was reduced to $RuO_2.0.3H_2O$. Similarly, another report [74] also demonstrated that the importance of hydrous regions which can allow appreciable protonic conduction for high energy and high-power electrochemical capacitors (Table 2.2). Zheng et al. (1995) prepared hydrous $RuO_x.nH_2O$ by the sol-gel method and obtained a high specific capacitance value of 720 F/g with a careful control of the annealing process [75]. Another study on amorphous RuO_2 using spray pyrolysis method presented that a specific capacitance of 551 F/g was obtained in 0.5 M H_2SO_4 electrolyte [70].

Table 2.2. Specific capacitance obtained by cyclic voltammetry at various scan rates for $RuO_2.xH_2O$ [74].

Scan rate (mV/s)	Specific capacitance (F/g)		
	RuO_2	$RuO_2.0.3H_2O$	$RuO_2.0.5H_2O$
2	24	124	342
5	22	112	331
20	19	93	316
50	18	82	304
200	16	68	280
500	15	61	256

The maximum specific capacitance of 1190 F/g was reported for the amorphous $RuO_2 \cdot xH_2O$ that was anodic deposited on stainless steel substrate [76]. The experimental

results show that the RuO_2 film thickness and uniformity can be precisely controlled via electrodeposition method. Figure 2.8 shows the effect of scan rate on anodically deposited RuO_2 on stainless steel substrates. It is observed that the cyclic voltammograms are almost rectangular and symmetrical even at the high scan rate of 100 mV/s. This can be explained that the oxidation and reduction processes at electrode-solution interface are highly reversible, which is an essential requirement for supercapacitor applications. From the graph (inset), the decrease in capacitance at higher scan rate is observed, suggesting that the inner active sites of the electrode surface are inaccessible at high charging-discharging rate [76].

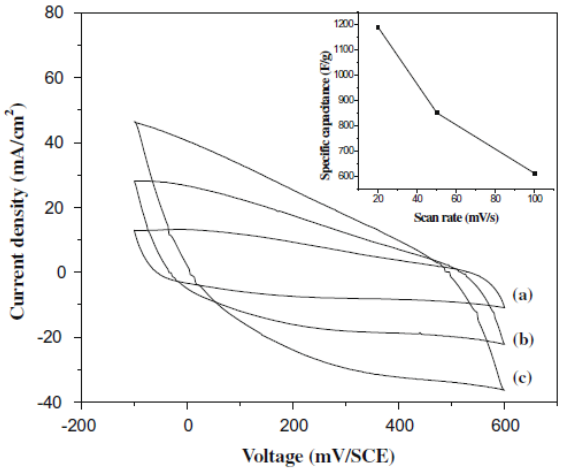


Figure 2.8. Cyclic voltammogram of RuO_2 thin film for different scan rates (a) 20, (b) 50, (c) 100 mV/s. Inset shows plot of specific capacitance with scan rates [76].

Most of the review articles of RuO_2-based supercapacitors have focused on the capacitive performance of electrodes mainly in the concentrated sulphuric acid (H_2SO_4) [69]. Some researchers claimed that conducting metal oxides such as RuO_2 are only suitable for aqueous electrolytes, suggesting that high capacitance value and fast charging are the pseudocapacitance contribution from surface reaction between ruthenium ions and protons (H^+). Hence, a strong acid is therefore necessary to provide good ionic conductivity [13]. However, it should be noted that the cycling performance of metal oxide electrodes will be deteriorated because electrodes tend to dissolute rapidly in the highly concentrated acidic electrolyte [77].

2.3.2.2 Manganese oxide (MnO_2)

The intense interest in MnO_2 for energy storage applications is driven by their low cost and low toxicity characteristics, particularly when compared to other metal oxides such as ruthenium, nickel- and cobalt-oxides [55]. In general, the pseudocapacitance of MnO_x is believed to be predominantly attributed to the redox transitions associated between Mn(III)/Mn(II), Mn(IV)/Mn(III) and Mn(VI)/Mn(IV) [79]. Several techniques have been employed to prepare manganese oxides with controlled morphologies and structures, including nanocasting, sonochemical method, thermal decomposition method, hydrothermal synthesis method, sol–gel route, co-precipitation method and electrochemical deposition method [80].

In comparison to the studies of RuO_2-based supercapacitor, milder aqueous solutions such as KCl and Na_2SO_4 [69] have therefore been adopted for MnO_2 electrode. The first studies on faradaic pseudocapacitive behaviour of nano MnO_2 by Lee and Goodenough in 1998 [49] have shown that mild KCl aqueous solution can replace strong acid such as H_2SO_4 as the electrolyte. Based on the experiment, the electrode materials containing amorphous $MnO_x \cdot nH_2O$ and acetylene black showed a specific capacitance of 200 F/g. After the breakthrough of MnO_2 in mild KCl and Na_2SO_4 is reported, a variety of electrolytes have hence been studied for MnO_2 electrode.

With regards to this, Wang and co-workers (2008) have studied the effect of lithium acetate (LiAc) – magnesium sulphate ($MgSO_4$) mixed solution on the capacitive performance of MnO_2-based electrodes [77]. The experimental results showed that the superior specific capacitance of 205 F/g and good cyclic stability in the mixed solution were observed. It is claimed that the addition of appropriate amount of $MgSO_4$ to the LiAc can inhibit the corrosion of the foamed nickel current collector. However, the study fails to explain the corrosion inhibition mechanism of $MgSO_4$ in LiAc.

Similarly, Liang and Hwang (2010) studied the effect of electrolyte cations on the capacitive performance of electrodeposited MnO_x [82]. Figure 2.9 reveals the maximum capacitance of 284 F/g was obtained in $MgSO_4$ electrolyte, followed by Na_2SO_4 (244 F/g), K_2SO_4 (212 F/g) and Na_3PO_4 (115 F/g). The higher specific capacitance observed in Mg^{2+} solution could be attributed to its higher charge and smaller ionic radii. It is also important to note that the use of non-aqueous electrolyte in several studies of MnO_2 have

successfully proved that metal oxides are not only suitable in aqueous electrolytes but also in organic electrolytes for charge storage application [50]. Brousse et al. (2006) conducted the first systematic study comparing the capacitive properties of MnO_2 powders with various crystal structures [85]. The relationship between the crystal structure, BET surface area and specific capacitance is summarized in Table 4. The different crystalline structure can be described by the size of tunnels which in turns determine the extent of counter-ion intercalation [86].

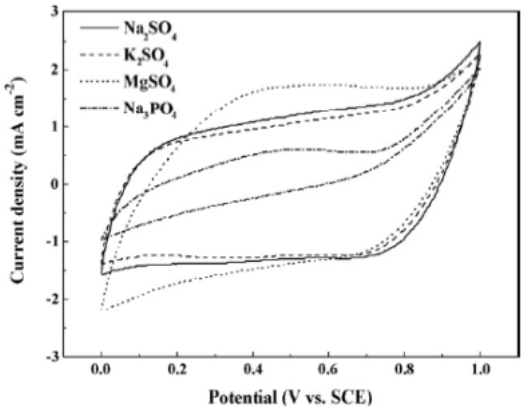


Figure 2.9. Cyclic voltammetric curves of MnO_2 in various electrolytes at a concentration of 0.1 M [50].

Based on Table 2.3, it was found that the capacitance is strongly dependent on the crystalline structure but not BET surface area. Interestingly, both α-MnO_2 and Birnessite δ-MnO_2 demonstrated relatively high specific capacitances even with low BET surface areas.

Table 2.3. Relationship between MnO_2 crystal structures, BET surface areas and the specific capacitances measured at scan rate of 5 mV/s in 0.1 M K_2SO_4 [85].

Structure	BET surface area (m^2/g)	Specific capacitance (F/g)
α-MnO_2	200	150
α-MnO_2	208	150
α-MnO_2	8	125
λ-MnO_2	35	70
γ-MnO_2	41	30
β-MnO_2	1	5
Birnessite δ-MnO_2	17	110
Birnessite δ-MnO_2	89	105
Birnessite δ-MnO_2	3	80

More recently, a similar study reporting the microstructural effects on charge-storage properties of MnO_2-based supercapacitors was published by Ghodbane et al in 2009 [87]. The findings show that the 3D-type spinel exhibited the highest capacitance, followed by the 2D layer birnessite-type MnO_2 and 1D structures including pyrolusite and Ni-todorokite, as shown in Figure 2.10. Furthermore, it was demonstrated that the electrochemical performance of MnO_2-based electrodes was not dependent on the specific surface area but on the ionic conductivities, which is obviously related to the microstructure of MnO_2. Pang et al. (2000) has demonstrated a specific capacitance of 700 F/g for very thin MnO_2 films that prepared by sol–gel techniques [53]. The ultrathin MnO_2 film electrodes exhibit excellent specific capacitance which could be due to the fact that the thinner films possess considerable lower contact resistance between film matrix and current collector which could provide a shorter proton diffusion path length. Broughton and Brett (2004) also have observed a specific capacitance of 700 F/g in thin MnO_2 films prepared by anodic oxidation [55].

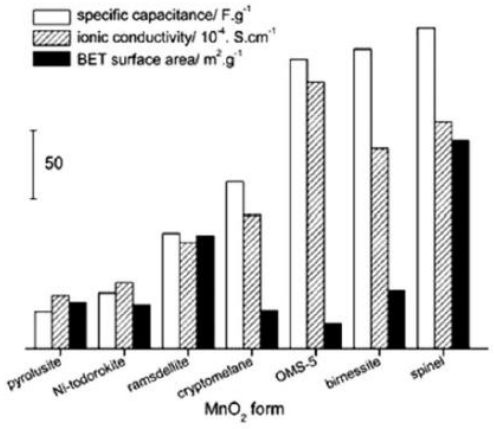


Figure 2.10. Comparison of the specific capacitance, ionic conductivity and BET surface area of various MnO_2 structures [87].

2.3.2.3 Nickel oxide (NiO)

Nickel oxide (NiO) is being considered as one of the promising potential electrode materials for supercapacitors with an anticipation that it could serve as a low-cost alternative of noble oxide RuO_2-based supercapacitor, owing to its easy availability, environmental benign nature and cost effectiveness [60, 61, 62, 63, 64, 65]. Nickel has shown excellent resistance to alkaline electrolytes due to the formation of protective oxide/hydroxide surfaces, making them suitable for application in alkaline batteries, such as nickel-metal hydride and nickel-cadmium batteries [63]. In view of these, NiO has been widely investigated as electrode materials in alkaline electrochemical capacitors.

Xing and co-workers (2004) successfully synthesized a mesoporous nickel oxide with a very high surface area, which not only favour the OH^- ion transfer in the mesopores, but also increase the NiO-electrolyte interfacial area for high charge storage capability [92]. Compared to previous studies, this unique mesoporous NiO can be used to fabricate electrodes for capacitors in a much larger mass (~10 mg) and at the same time, maintain a high value of specific capacitance (~124 F/g). Recently, Wu et al. (2010) has successfully synthesized the porous nickel oxide film with interconnected nanoflakes and open macropores by anodic electrodeposition [81]. The nanoflakes are believed to be beneficial to the capacitance enhancement of NiO due to their high surface area and shortened diffusion path in solid phase. On top of the nanoflakes, a porous film with open macropores also plays an important role in electrolyte penetration and migration. Figure

2.11 reflects that a porous film with macropores may facilitate the electrolyte penetration, leading to an increase in specific capacitance of NiO (351 F/g).

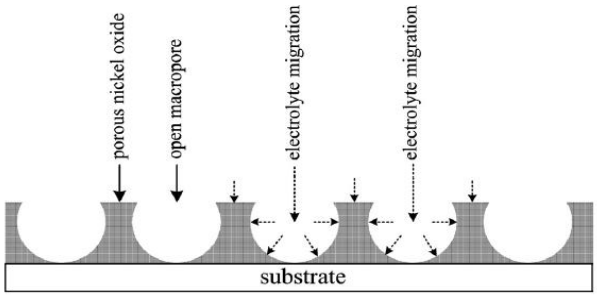


Figure 2.11. A schematic of proposed strategy for enhancing the capacitive behavior of a NiO film with open macropores [81].

Beside the control of surface morphology of electrode materials, optimum heat treatment conditions are also considered as one of the most important design parameters for making an electrochemical capacitor. The effect of heat treatment on the electrochemical properties of electrodeposited nickel hydroxide is studied using cyclic voltammetry (CV) [96]. It is shown that both annealing time and temperature are critical factors in the optimization of the capacitance of the deposit as both parameters alter water content and crystallinity which in turn affect the electrochromic properties of the thin-film system. When the annealing time is prolonged at a high temperature, the pseudocapacitive behavior of the film becomes pronounced. The authors claimed that the capacitance of the thin film is maximized at 300-320℃ between 3 to 3.5 annealing hours and the surface redox reaction accounts for the pseudocapacitance of nickel oxide film, instead of large surface area.

Wu et al. (2007) first demonstrated the comparative studies on the deposited NiO film in 1 M KOH and 1 M Na_2SO_4 solutions, respectively [67]. Figure 2.12 shows two redox peaks observed at 0.41 V (oxidation) and 0.32 V (reduction) vs Ag/AgCl reference electrode in 1M KOH solution. The authors claimed that the following redox couple results in high capacitance of NiO in alkaline solution:

$$NiO + OH^- \leftrightarrow NiOOH + e^- \quad \text{Eq.(2.8)}$$

In contrast, no significant peaks were observed for the deposited nickel oxide film in 1 M Na_2SO_4 solution, suggesting that the solution has a much lower concentration of OH^- in comparison to 1 M KOH solution. Consequently, the current response in Na_2SO_4 solution mainly comes from the electrical double-layer capacitance of the deposited nickel oxide film rather than the contribution from redox reaction.

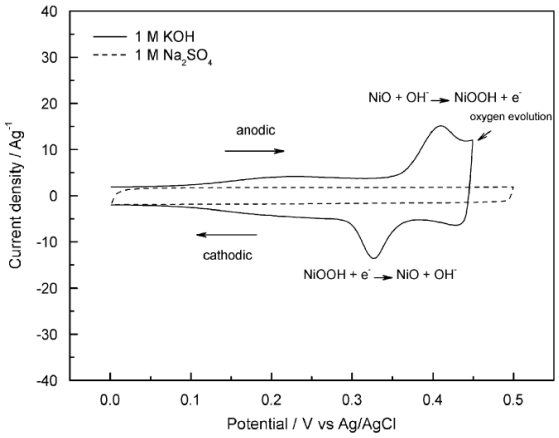


Figure 2.12. CVs of the deposited nickel oxide film in 1M KOH and 1M Na_2SO_4 solutions, respectively, at a scan rate of 25 mV/s [67].

The relationship between the specific capacitance at various scan rates and scan potential ranges are shown in Figure 2.13. Obviously, the deposited NiO film demonstrates a high capacitance at low scan rate (10 mV/s) in all scanned potential ranges. Additionally, it can be seen that the lower the upper limit potential, the higher the capacitance retention even at high scan rate (100 mV/s). These findings show that the double-layer effect, which depends slightly on the scan rate, is responsible for the high capacitance retention at high scan rate [67].

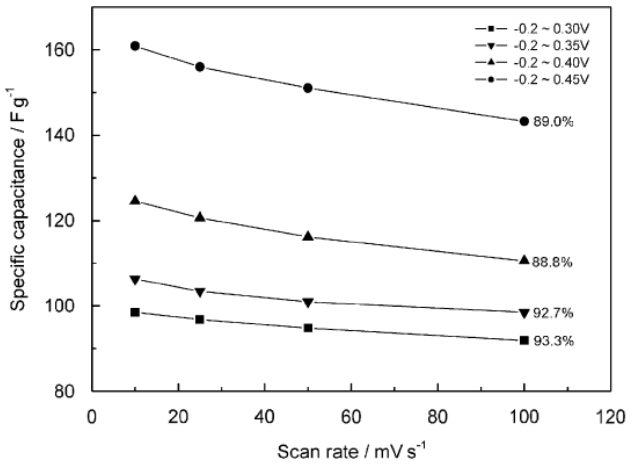


Figure 2.13. Specific capacitance of the deposited NiO film measured at various scan rates and scanned potential ranges [67].

2.3.2.4 Iron oxide (Fe_3O_4)

Fe_3O_4 has been identified as potential electrode material in view of the low-cost and environmentally friendly nature. Several literatures have shown that the capacitive performance of Fe_3O_4 is strongly dependent on the nature of anions and surface area of Fe_3O_4 nanoparticles [57, 59]. In addition, the preliminary evaluations revealed that the relatively low electrical conductivity of Fe_3O_4 requires the introduction of conductive additive such as carbon black (CB) and acetylene black (AB) in order to increase its conductivity and boost its capacitance [56].

Wu and his co-workers (2003) first compared the capacitive performance of Fe_3O_4-CB electrodes using both mechanical grinding and co-precipitation methods in sodium sulphite (Na_2SO_3) [56]. The highest capacitance of 38 F/g in a voltage range from -0.8 to 0.4 V was achieved using co-precipitation method. The poorer capacitive performance for mechanical mixed electrode indicates the limited dispersion of Fe_3O_4 nanoparticles within CB matrix during mechanical grinding. The authors also claimed that the BET surface areas of Fe_3O_4 electrodes increase with the increasing of CB content, as shown in Figure 2.14. This is due to the fact that the presence of CB not only reduces agglomeration of Fe_3O_4 nanoparticles but also provides an additional conductive pathway for the metal oxide electrodes. Nevertheless, further adding CB content until over 75 wt % produces no further increase in the specific capacitance of the mechanical mixed

electrodes. It should be noted that very low Fe_3O_4 loading on supercapacitor electrodes has limitation in the high-power applications.

The study also reveals that sodium sulphate (Na_2SO_4), sodium chloride (NaCl), sodium phosphate (Na_3PO_4) and potassium hydroxide (KOH) electrolytes system only exhibited the capacitance values between 5 to 7 F/g. It was concluded that the specific capacitance of Fe_3O_4 is heavily dependent on the nature of anions and the surface area of electrodes [56, 59]. Similarly, Brousse and co-workers (2003) synthesized Fe_3O_4 nanopowders with high surface area (115 m^2/g) and reported a specific capacitance value of about 75 F/g in 0.1 M K_2SO_4 [103]. It was suggested that the potential which is below -0.8 V vs Ag/AgCl could lead to a drastic structural and microstructural modification of Fe_3O_4 electrode, resulting in a subsequent capacity loss upon cycling.

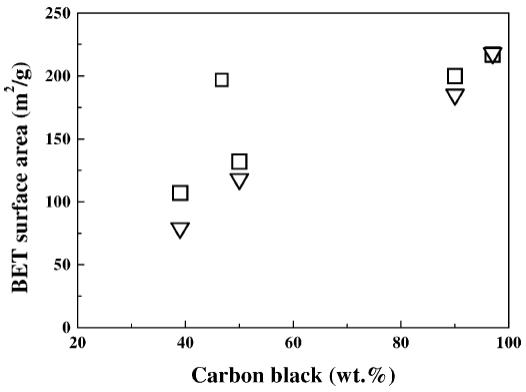


Figure 2.14. Effect of carbon black content on BET surface area of Fe_3O_4-based electrode. (□) is calculated BET surface area; (∇) is measured BET surface area. The theoretical values are based on the assumption of unchanged surface area of carbon black as well as non-porous and non-agglomerated Fe_3O_4 [56].

Fe_3O_4 thin film is currently being investigated for applications in supercapacitor, catalysis and magnetic devices [101]. Conventional pressed pellet or thick films make the devices too bulky until they cannot meet the requirements of flexibility and lightweight in modern energy storage systems [104]. Wang et al. (2006) investigated the capacitance mechanism of electroplated Fe_3O_4 thin-film electrodes in Na_2SO_3, Na_2SO_4, and KOH aqueous solutions [59]. Experimental results indicate that Fe_3O_4 electrodes in Na_2SO_3 exhibit the highest specific capacitance value (170 F/g), followed by Na_2SO_4 (25 F/g) and KOH (3 F/g). The authors suggested that significant improvement on the capacitive

performance in Na_2SO_3 is attributed from the synergy effect of both EDLC and the pseudocapacitance which involves successive reduction of the adsorbed sulphite anions. In contrast, the capacitive current is attributed to EDLC only in Na_2SO_4. Surface oxidation of the oxide electrode in KOH results in a significantly low capacitance.

A two-step anodic electrochemical method has been adopted for the fabrication of cellular Fe_3O_4 films [105]. The cellular Fe_3O_4 films provide high electrochemical accessibility and a fast diffusion rate of the electrolyte, showing the specific capacitance of 105 F/g in 1 M Na_2SO_4. This study highlighted the importance of the porosity of Fe_3O_4 films, which creates a volume for the diffusion of electrolyte and provides a high surface area for the electrode reactions. Chen et al. (2005) have successfully prepared Fe_3O_4 thin films using hydrothermal process [101]. A high specific capacitance of 118 F/g was observed from galvanostatic charge-discharge test for this Fe_3O_4-thin film supercapacitor in 1 M Na_2SO_3. The charge capacity of the system was still retained at 88.75% even after 500 cycles. In recent year, cathodic electrodeposition method has been developed for the fabrication of iron oxide films, containing chitosan additive as a binder [106]. The iron oxide films exhibited specific capacitance as high as 210 F/g with the potential window of -0.9 to -0.1 V vs SCE in 0.25 M Na_2SO_3 solution. It was claimed that the films fabricated without chitosan exhibited low adhesion while the incorporation of chitosan to the precursors enhanced the adhesion and reduced film cracking during cathodic electrodeposition.

Table 2.4 summarises the recent research works that were carried out in relation to the metal oxide-based electrode materials, including the different method of synthesis as well as the type of electrolyte employed within the systems.

Table 2.4 Summary of the single electrode materials investigated.

Electrode Material	Synthesis/Fabrication Method	Electrolyte	Specific Capacitance (F/g)	Year of Publication	Reference
RuO_2	-	H_2SO_4	-	1971	[68]
RuO_2	Sol-gel	H_2SO_4	720	1995	[75]
MnO_2	Mix-roll-press	2 M KCl	200	1998	[49]
MnO_2	Sol-gel	0.1 M Na_2SO_4	700	2000	[53]
MnO_2	Sol-gel	0.1 M $LiClO_4$	720	2000	[51]
NiO	Hydrolysis	3 wt % KOH	124	2002	[62]
Fe_3O_4	Co-precipitation	1 M Na_2SO_3	38	2003	[56]
Fe_3O_4	Emulsion	0.1 M K_2SO_4	75	2003	[103]
Fe_3O_4	Anodic electrochemical	1 M Na_2SO_4	105	2005	[105]
RuO_2	Electrodeposition	0.5 M H_2SO_4	1170	2005	[76]
RuO_2	Spray pyrolysis	0.5 M H_2SO_4	551	2006	[70]
Fe_3O_4	Cathodic electrodeposition	0.24 MN_2SO_3	210	2006	[106]
NiO	SBA-15 replication	2 M KOH	120	2006	[64]
NiO	Electrodeposition	1 M KOH	167	2007	[67]
MnO_2	Liquid-phase deposition	1 M LiAc-$MgSO_4$	205	2008	[77]
RuO_2	Electrodeposition	0.5 M H_2SO_4	786	2008	[69]
Fe_3O_4	Electroplating	1 M Na_2SO_3	170	2008	[59]
Fe_3O_4	Electroplating	1 M Na_2SO_4	25	2008	[59]
Fe_3O_4	Electroplating	1 M KOH	3	2008	[59]

Fe_3O_4	Hydrothermal	1 M Na_2SO_3	118	2009	[101]
RuO_2	Electrodeposition	0.5 M H_2SO_4	1190	2009	[76]
NiO	Electrophoretic deposition	0.5 M KOH	112	2009	[81]
MnO_2	Hydrothermal	0.1 M Mg SO_4	284	2010	[82]
MnO_2	Hydrothermal	0.1 M Na_2SO_4	244	2010	[82]
MnO_2	Hydrothermal	0.1 M K_2SO_4	212	2010	[82]
MnO_2	Hydrothermal	0.1 M Na_3PO_4	115	2010	[82]
NiO	Electrophoretic deposition	1 M KOH	351	2010	[65]
NiO	Chemical bath deposition	1 M KOH	130	2011	[84]
NiO	Electrophoretic deposition	0.5 M KOH	210	2011	[63]
NiO	Ammonia evaporation	1 M KOH	232	2012	[61]
NiO	Hydrazine hydrate reduction	1 M KOH	417	2012	[88]
NiO	Chemical precipitation	6 M KOH	1124	2012	[60]

2.3.3 Conducting polymer

Conducting polymers are promising materials for a redox supercapacitor because they can be readily converted between oxidized (doped) and reduced (dedoped) states by switching the applied potentials [90]. The conductivity of conducting polymer was first reported in 1963 by Weiss and co-workers [92]. They exhibit the pseudocapacitive and conductive behaviour via electron delocalization in conjugated chemical bond system along the polymer backbone. Typically, conducting polymers are formed either through chemical oxidation or electrochemical oxidation of the monomer in which they are p-doped with anions when oxidised and n-doped with cations when reduced. The simplified equations for these two charging processes are as follows [94]:

$$Cp \rightarrow Cp^{n+}(A^-)_n + ne^- \qquad \text{(p-doping)} \qquad \text{Eq.(2.9)}$$

$$Cp + ne^- \rightarrow (C^+)_n\, Cp^{n-} \qquad \text{(n-doping)} \qquad \text{Eq.(2.10)}$$

Conductive polymer based supercapacitors can be classified into three configurations. Type I is a symmetric system using the same p-dopable conductive polymer for electrodes. Type II is an asymmetric system based on two different p-dopable conducting polymers with a different range of electroactivity. Type III is a symmetric system using the same polymer for both electrodes with the p-doped form used as the positive electrode and the n-doped form used as the negative electrode [94]. In fact, many conducting polymers can only p-doped because a purified electrolyte or a room temperature ionic liquid with a wide electrochemical window particularly at negative potentials, is required for n-doping polymer electrode [94].

Conducting polymers can offer relatively cost-effective alternative to the conventional electrode materials as a result of their fast doping/dedoping capabilities, excellent electrochemical reversibilities and high conductivity in a doped state [97]. It is proposed that these pseudocapacitive materials should increase the energy stored and reduce self-discharge, in which EDLCs can achieve a power density of 3-4 kW/kg and an energy density of 3-5 Wh/kg while a conducting polymer-based supercapacitor can achieve a slightly lower power at 2 kW/kg but double the energy density (10 Wh/kg) [107].

Nevertheless, one significant drawback of these materials is the relatively low power or lower rate of charge–discharge due to the slow diffusion of ions within the bulk of the electrode. In addition, conducting polymer-based supercapacitors exhibit lower cycle life due to volume change or swelling as a result of the doping (intercalation)/de-doping (de-intercalation) of ions [107]. Interestingly, the study on the conducting polymer supercapacitors with electrolytes using ionic liquids shows that the electrodes perform better with greater lifetimes where doping and undoping of ions into the polymer is required for the shape changes [108].

Among various conducting polymers, polyaniline (PANI), polypyrrole (PPy), polythiophene (PTh), poly(3, 4-ethylenedioxythiophene) (PEDOT) and poly(styrene sulfonate) (PSS) are most commonly studied for use in supercapacitors. Table 2.5 summaries both theoretical and experimental specific capacitance of various conducting polymers [94].

Table 2.5. Theoretical and experimental specific capacitance of various conducting polymers [94].

Conducting polymer	Molecular weight (g/mol)	Theoretical specific capacitance (F/g)	Measured specific capacitance (F/g)
PANI	93	750	240
PPy	67	620	530
PTh	84	485	-
PEDOT	142	210	92

PANI has been studied extensively as a supercapacitor or battery electrode material because it exhibits high electroactivity, excellent stability and a high specific capacitance of 400–500 F/g in an acidic medium [107]. A major disadvantage of PANI is that it requires acidic solution or ionic liquid for charging or discharging process to occur effectively [94]. It has been reported that the cycle-life of PANI for a Li-doped positive electrode was over 5000 cycles, during which the specific capacitance dropped from 100 to 70 F/g [109]. In another study, PANI doped with $LiPF_6$ achieved a specific capacitance

of 107 F/g but decreased to 84 F/g after 9000 cycles [110]. PPy offers a greater degree of flexibility in electrochemical processing than most other conducting polymers. It has been used to fabricate an all solid-state-supercapacitor with a PVA-based polymer electrolyte which yielded up to 84 F/g capacitance at a specific energy of 12Wh/kg [94].

In particular, PEDOT is a good candidate for a supercapacitor because of its high stability among the other conducting polymers. In addition, its high charge mobility results in fast electrochemical kinetics attributed to its high surface area coupled with high conductivity [90]. However, the major disadvantage of this polymer is its relatively low specific capacitance because of its large molecular weight and a doping level of around 0.33 [94]. Lota et al. (2004) claimed a capacitance of 180 F/g is possible with PEDOT [111]. Li et al (2005) enhanced the specific capacitance of PEDOT (100 F/g) using sponge-like structures synthesized under ultrasonic irradiation [112]. In a recent study, Liu and co-workers (2008) have demonstrated that the thin-walled PEDOT-nanotube-based supercapacitor could maintain high energy density of 5.6 Wh/kg and specific capacitance of 120 F/g even at high power density of 25 kW/kg. [90]. The high power capability is attributed to the fast charge/discharge of nanotubular structures. The pseudocapacitance behaviour of PEDOT is originated from diffusion of charged counter-ions, as shown in Figure 2.15. The hollow nanotubular structures enable counter-ions to penetrate and access PEDOT internal surfaces easily while the thin wall provides a short diffusion distance to facilitate the ion transport.

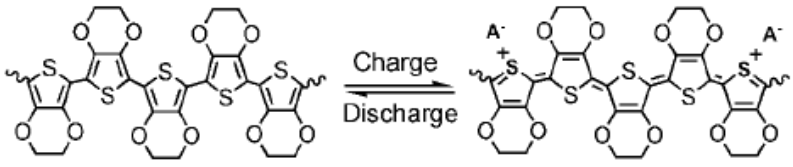


Figure 2.15 Molecular structures of oxidized and reduced forms of PEDOT. A^- represents the counter-anions [90].

2.3.4. Composites

The most widely investigated metal oxide is ruthenium oxide because of its excellent pseudocapacitive behaviours, good reversibility and high conductivity. However, the high cost of this precious metal oxide hinders its practical applications [80]. Consequently, relatively low-cost metal oxides such as iron oxide, manganese oxide, nickel oxide, zinc oxide, copper oxide, etc have been explored as possible electrode materials for electrochemical supercapacitors working in aqueous solution [7, 52, 59, 78, 91]. Although these transition metals exhibit higher specific capacitance than EDLCs, they usually do not possess high conductivity, leading to low power density from industrial point of view [25]. New trends are devoted to the application of materials with pseudocapacitance properties, which store energy through fast and reversible faradaic reactions, especially metal oxides and their composites with carbon-based materials [31].

Another group of pseudocapacitive material, conducting polymer with fast kinetics of doping- undoping mechanisms and good electrical conductivity appears to be promising pseudocapacitive materials [89]. However, its inadequacies of poor mechanical stability and a narrow operating potential window limit their application as an effective electrode material. In order to retain electrochemical advantages of individual component and be complementary to each other, incorporation of conducting polymer into carbon or/and metal oxides is expected to achieve optimised electrochemical properties [113].

Over the past decades, carbon-based materials such as AC, carbon black, CNTs and graphene have been utilized to support various metal oxides or conducting polymers for making composite electrode materials. While carbonaceous materials offer the advantage of excellent electrical conductivity, the observed enhancement of electrochemical performance becomes more pronounced when only a small amount of metal oxide is loaded on the electrode. However, for practical applications such as hybrid electric vehicle (HEV), high mass loading of total active materials with metal oxides are highly demanded [113].

Conversely, when the loading of metal oxides is too high, metal oxide particles become agglomerated with dense morphology and limited accessible surface area of the electrolyte. As a result, these lead to high resistance and a comparatively low specific

capacitance which eventually hinder the electrode materials to be applied in supercapacitor. Therefore, the low-energy density caused by the limited loading of cost-effective metal oxides still remains a major problem. Extensive efforts are still needed to improve the electrochemical utilization of these metal oxides, especially in the cases where high metal oxide loading is needed. In order to tackle with these limitations, composite electrodes fabricated from different configurations including binary and ternary composites have been attempted.

2.3.4.1 Ruthenium oxide (RuO_2)-based composites

RuO_2 is widely studied because it is conductive and has three accessible distinct oxidation states. The pseudo-capacitive behaviour of RuO_2 in acidic solutions has been the focus of research in the past 30 years [14]. In order to reduce the cost of materials while maintain its high charge storage performance, extensive works have focused on the development of combining RuO_2 with carbonaceous materials to form bulk composite electrodes.

The studies of RuO_2/activated carbon nanocomposites with various Ru contents were reported by Sato et al (2000) [40] and Kim et al. (2001) [71] respectively. Both studies revealed that when ruthenium content increases, the specific capacitance and BET surface area of the composites decrease gradually. This is mainly due to the blockage of the mesopores in activated carbon by large RuO_2 particles (Table 2.6). However, the correlation between amount of ruthenium loaded and the specific capacitance of composite electrodes is interesting because the RuO_2-based composite electrodes at high ruthenium loading (80 wt %) demonstrate the highest specific capacitance (599 F/g). These findings are unexpected and differ from some published studies which show the deterioration of charge storage capability at high loading of ruthenium over 60 wt% in the compound [69]. The authors explained that the decrease in charge utilisation of RuO_2 at high ruthenium content is owing to the aggregation of RuO_2 particles.

Table 2.6. Specific capacitance and BET surface area as a function of ruthenium loading [14].

Amount of Ru loaded	BET surface area (m^2/g)	Specific capacitance of the composite electrodes (F/g)
Vulcan XC-72 (carbon black)	248	27
20 wt % Ru	228	221
40 wt % Ru	201	407
60 wt % Ru	114	526
80 wt % Ru	75	599

Hu and Chen (2004) investigated the effect of substrates on the capacitive performance of 10 wt % hydrous RuO_2/AC composites [72]. The results indicate that there is significant contact resistance at the interface between composite electrodes and the stainless steel (SS) current collector due to the poor adhesion of composite nanoparticles on SS meshes. In contrast, the contact resistance at RuO_2/AC-graphite current collector is very low, indicating the good adhesion of the composite on graphite. In order to further enhance the contact resistance between the composites and SS meshes, the authors proposed to deposit a gold (Au) thin film on the SS meshes and a very high specific capacitance of 1450 F/g were observed. The significant improvement in the contact is possibly attributed to the better smearing of RuO_2/AC composites on the Au-coated SS meshes. Based on all the comparisons, the contact resistance at the interface between active materials and current collectors is concluded to be a key factor determining the capacitive performance of the composite electrodes [72]. Nevertheless, the findings would have been more convincing if the ohmic voltage drop or ESR of the composites were further verified by galvanostatic charging-discharging measurements.

Previous studies have demonstrated capacitance enhancement by adding a hydrous ruthenium oxide into the carbon-based electrode. However, one of the major factors that need to be considered is that the extent of ruthenium utilization as pseudocapacitor is dependent heavily on the loading of RuO_2 [83]. In fact, a maximum utilization rather than high loading is desirable. In the study of the capacitive performance for hydrous RuO_2/mesoporous carbon composite electrodes, Jang et al

(2003) addressed that the unloaded mesoporous carbon exhibited a specific capacitance of 100 F/g, but increases to 243 F/g with 54.3 wt % RuO_2 loading, as shown in Figure 2.16. It should be pointed out that, the capacitance increase with ruthenium loading is likely counterbalanced by an increase in the ohmic voltage drop or ESR. The possible explanation of the ESR enlargement with increasing RuO_2 loading is that the hindered ionic motion which is caused by a pore narrowing has increased the electrolyte resistance within the narrowed pores [83].

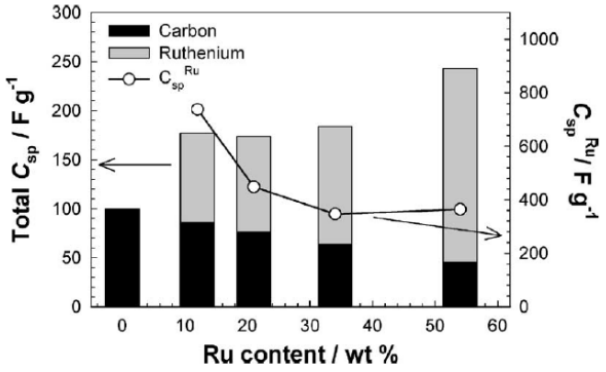


Figure 2.16. Specific capacitance of composite electrodes (C_{sp}) demonstrated by mesoporous carbon and RuO_2 active materials and specific capacitance of ruthenium component (C_{sp}^{Ru}) as a function of ruthenium loading [83].

2.3.4.2 Manganese oxide (MnO_2)-based composites

The capacitive performance and power characteristics of MnO_2 electrode are limited by its poor conductivity [77]. Introduction of conductive, porous and high surface area carbon-based materials is a feasible route to enhance the charge-storage capability by shortening electron transport distance [86]. The study on nanosized Mn_2O_3 particles incorporated in ordered graphitic mesoporous carbon found that the mesoporous carbon is an effective electrode to facilitate fast ion and electron transportations, which the characteristics are highly desirable for high power supercapacitors [93]. Another research which focused on MnO_2/CNT nanocomposites showed good capacitive behaviour, with the highest specific capacitance of 356 F/g is reported. In addition, the results also indicated that the samples containing CNT showed significantly lower resistance compared to the sample without CNT, suggesting that the porous microstructure of CNTs

has facilitated the access of electrolyte ions to the active material [114]. Besides, the author also proposed that the added acetylene black can form a macroscopic conductive network while CNTs act as microscopic conductors, providing good electronic conduction paths between active material particles and current collector [77]. Cheng and co-workers (2011) have successfully fabricated binderless supercapacitors using MnO_2-coated graphene to provide a high specific capacitance of 328 F/g. It is suggested that the MnO_2 nano-flowers are consisted of tiny rods that can provide short-diffusion path length to both ions and electrons [39].

Lee et al. (2007) conducted a study on the effect of Fe addition upon capacitive behaviour of MnO_2-based electrode, suggesting that the addition of 0.05 M $FeCl_3$ exhibited the optimum specific capacitance of the composite electrodes (212 F/g) [115]. The authors also revealed that the Fe addition significantly affects the surface morphology of the MnO_2 electrodes, as shown in Figure 2.17. As seen from the SEM images, surface roughness of the deposited oxides gradually increases with increasing $FeCl_3$ concentration in the plating solution up to 0.05 M. However, after which, the surface began to be smoother as the $FeCl_3$ addition was further increased. On top of their poor electronic conductivity, the electrochemical cyclability is another important issue for MnO_2 electrodes [86]. Zhang et al. (2012) achieved promising result from PANI-MnO_2 composites with the maximum specific capacitance of 320 F/g compared to that of pure MnO_2 (125 F/g). In addition, the specific capacitance retains approximately 84% of the initial value after 10,000 cycles, indicating the good cycle stability of the composite electrode [97]. With excellent conductivity and mechanical stability, PANI polymers enhanced the electrochemical and mechanical properties of the composites. Another study on MnO_2-based electrode with the addition of PPy showed that there was improved specific capacitance of the MnO_2-PPy nanocomposite (290 F/g) if compared to that of pure MnO_2 electrode (221 F/g). The enhancement is attributed to a combination of the improved conductivity effect and the high specific capacitance of PPy [86].

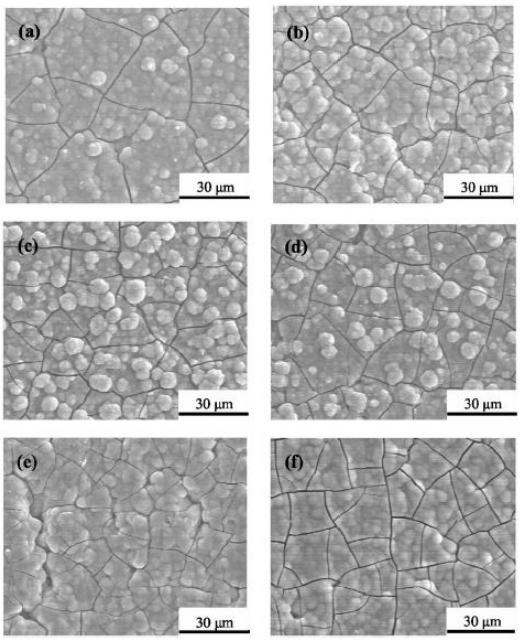


Figure 2.17. Surface morphologies of the oxides deposited in the MnO_2 with addition of (a) 0, (b) 0.03, (c) 0.05, (d) 0.06, (e) 0.08, and(f) 0.15 M $FeCl_3$ [115].

2.4.3.3 Nickel oxide (NiO)-based composites

NiO is one of the most widely investigated metal oxides for supercapacitor applications due to its inexpensive, pseudocapacitive and highly electronic conductive behaviours [55]. Yuan et al. (2005) studied the electrochemical behaviour of activated carbon loaded with NiO [44]. It is somewhat surprising that although the BET surface area was decreased from 1332 to 1232 m^2/g by the loading of 4 wt % NiO onto AC, the capacitance was increased from 175 to 194 F/g. This phenomenon has not previously been described. A possible explanation for this might be that the capacitance of the NiO/AC composite electrode is mainly relying on pseudocapacitance contribution from the redox reaction of the NiO. Although, the BET surface area decreased, it has little effect since the contribution from the double layer charging was relatively small. Another study on the NiO/CNT nanocomposite shows that the incorporation of CNTs improve the capacity up to 160 F/g, revealing the presence of CNT network in the NiO significantly enhanced (i) the electrical conductivity of the host NiO by the formation of conducting network of CNTs and (ii) the active sites for the redox reaction of the metal oxide by increasing its specific surface area [116].

A composite electrode consisted of MnO_2/NiO mixed oxides were successfully prepared by Kim and Popov (2003) and the electrode was exhibiting high specific capacitance of 172 F/g at 20% carbon loading [117]. The introduction of RuO_2 is also helpful to improve the electrochemical performance and pseudocapacitive behaviour of NiO-based composite electrodes. A maximum specific capacitance of 210 F/g was obtained for NiO electrode that was loaded with 10 wt % RuO_2 in 1 M KOH [118]. In addition, the energy density of NiO/RuO_2 composite was found to be 14.2 Wh/kg while the energy density of pure NiO electrode was only 2.6 Wh/kg. The high energy density of the composite electrode is due to the operating voltage extension obtained by the incorporation of RuO_2. Figure 2.18 shows the impedance spectra of NiO/RuO_2 composite electrode and pure NiO electrode. The major difference in the spectra is that the semicircle of NiO/RuO_2 composite electrode was smaller than that of pure NiO electrode, indicating that its charge-transfer resistance is smaller and also revealing that the introduction of RuO_2 had enhanced the conductivity of the composite electrode.

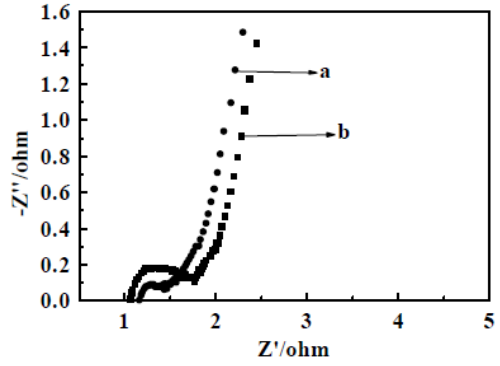


Figure 2.18. Impedance spectra of (a) NiO/RuO_2-based composite electrode and (b) pure NiO electrode [118].

2.4.4.4 Iron oxide (Fe_3O_4)-based composites

In view of low cost, low environmental impact and relatively high theoretical capacity previously demonstrated in Li-ion batteries, iron oxide-based composites have been proposed to have great potential for large-scale applications [104,119]. Wu (2002) firstly reported that Fe_3O_4-SnO_2 composite electrode can achieve a specific capacitance of 33 F/g in 1.0 M Na_2SO_4 aqueous solution [120]. It was suggested that the low

conductivity of Fe_3O_4 combined with other conductive materials such as SnO_2 is essential to obtain large capacitance. However, the main weakness of the study is that the failure to address the optimal loading of SnO_2 nanopowders into the Fe_3O_4 electrodes. Furthermore, the study would have been more persuasive if the author had included the galvanostatic charging/discharging and AC impedance analysis on the composite electrodes. The binder-free MWNT/Fe_2O_3 thin-film composite electrodes were first fabricated by Zhao et al. (2009) using spray deposition technique. The authors highlighted that the hybrid supercapacitor achieved a very high specific energy density of 50 Wh/kg at a specific power density of 1 kW/kg [104]. To compare the ion diffusion and charge-transfer resistances between pure MWNT-MWNT symmetric electrodes, MWNT-Fe_2O_3 asymmetric composites and MWNT-Fe_2O_3/MWNT asymmetric composites, the authors performed the electrochemical impedance spectroscopy (EIS) measurements, as shown in Figure 2.19. In their analysis, the semicircle at high frequencies for the MWNT-Fe_2O_3 hybrid composites was much larger compared to that of pure MWNT electrodes, revealing higher charge-transfer resistance at the electrode due to the low conductivity of Fe_2O_3. In addition, the MWNT-Fe_2O_3 composites plot exhibited 45˚ phase angle, corresponding to the Warburg region and indicating a high ion diffusion resistance. The incorporation of MWNT into Fe_2O_3 electrodes reduced both charge-transfer and ion diffusion resistance effectively.

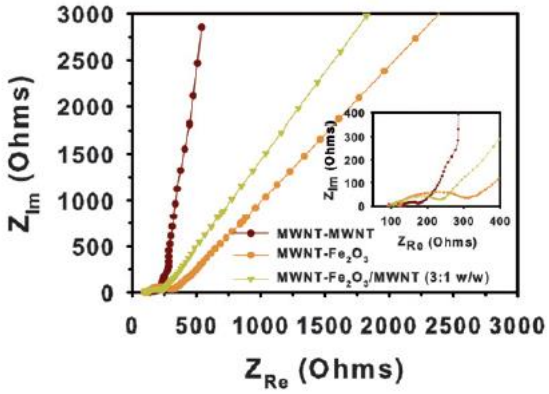


Figure 2.19. EIS spectra of pure MWNT-MWNT symmetric electrodes, MWNT-Fe_2O_3 asymmetric composites and MWNT-Fe_2O_3/MWNT asymmetric composites [104].

In 2010, Mansour et al. utilized the electroless deposition method to fabricate nanoscale iron oxide coating onto carbon nanofoams [102]. The resulting iron oxide-carbon nanofoams composite electrodes demonstrated high specific capacitance (85 F/g) in relative to the pure carbon nanofoam (31 F/g) in 2.5 M Li_2SO_4. It was believed that the additional charge-storage capacity arises from faradaic pseudocapacitance of the iron oxide coating. A composite supercapacitor containing Fe_3O_4 nanoparticles dispersed in multiwalled carbon nanotubes (MWNTs) was reported by Kim & Park (2011) [121]. The Fe_3O_4-MWNTs composite electrode exhibits specific capacitance of 165 F/g in 1 M Na_2SO_3, which this value is almost 3-fold enhancement if compared to the pure MWNT electrode (58 F/g). Dubal et al. (2009) have studied the electrochemical properties of the amorphous nanostructured Fe-doped MnO_2 electrodes via galvanostatic deposition [57]. From the results, it was found that the capacitive performance increases with the Fe doping concentration and achieved a maximum of 173 F/g at 2 at% Fe doping in 1 M Na_2SO_4. It was suggested that the addition of Fe significantly alters the surface morphology and leads to an increase in porosity, which ultimately improves the pseudocapacitive performance of MnO_2.

In the work by Pang et al. (2011), they reported the capacitive characteristic of Fe_3O_4/carbon nanocomposite thin film in 1 M Na_2SO_4 solution [122]. In their study, sago starch was chosen as the carbon source as well as a surfactant to control aggregation of Fe_3O_4 nanoparticles and the effect of calcination temperature on the specific capacitance of the nanocomposites was investigated. Figure 2.20 shows that the specific capacitance increases substantially with increasing calcination temperatures up to 300℃ but starts to decrease at above 300℃. The maximum specific capacitance (124 F/g) is obtained for the nanocomposites which exhibit the highest specific area at 300℃. It is thus believed that the densification of films up to 300℃ could lead to enhanced electronic conductivity. However, the reduction in specific capacitance at above 300℃ could be attributed to the reduction in total surface area caused by grain coarsening [122]. These findings support the earlier observation by Wu (2002) which found the similar trend of the correlation between the calcination temperature and the capacitance of SnO_2 electrodes [120]. The author explained that the rise in the capacitance of the SnO_2 electrodes with increasing calcination temperature is attributed to the reduction in defect density and an increase of

crystallinity. This explanation is consistent with the Mott-Schottky relationship which predicts an increase interfacial capacitance with increasing of the carrier density of the semiconductor [120].

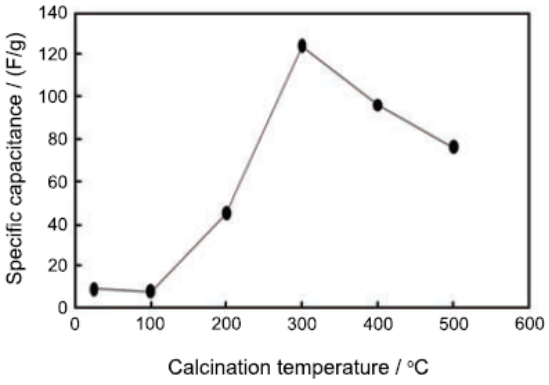


Figure 2.20. Effect of calcination temperature on the specific capacitance of Fe_3O_4/carbon nanocomposites in 1 M Na_2SO_4. [122].

2.3.4.5 Zinc oxide (ZnO)-based composites

ZnO has received a great deal of attention in the application of electronics and optoelectronics such as battery active materials, solar cells, gas sensors, and light-emitting diodes due to its good electrochemical activity, well-known surface conductivity, high electron mobility, wide band gap and eco-friendly nature [78]. However, zinc oxides have a serious drawback on the formation of dendrite growth during consecutive cycling which leads to decrease in cycle life [123]. With a view to improve both capacitive and cycling performances of ZnO, Selvakumar et al. (2010) studied the electrochemical performance of ZnO/AC composite materials in 0.1 M Na_2SO_4 as the electrolyte. The ZnO/AC nanocomposite electrode showed the specific capacitance of 160 F/g. The specific capacitance of the electrodes decreased with the increasing of ZnO content. These findings also support the idea that there was a synergistic effect from ZnO and carbon materials in controlling the dendrite formation and thus maintaining stable specific capacitance of composite electrodes [78].

A comparative evaluation of ZnO/carbon with pure ZnO showed that the removal of carbon reduced the specific capacitance from 21.7 F/g to 7.38 F/g, indicating the significant role of carbon in enhancing the capacitance [124]. These findings suggested

that cations and anions from metal oxides and aqueous electrolyte such as Zn^{2+} Na^{+}, K^{+}, H^{+}, SO_4^{2-} and OH^{-} can occupy some pores within the high-surface-area carbon electrodes and then participate in the formation of the electrochemical double layer [123]. Another group has developed ZnO/CNT supercapacitor cells that achieved a high capacitance of 324 F/g. The study showed that the capacitance of CNT-ZnO is higher than that of pure CNT cells in 1 M KCl aqueous electrolyte. The presence of ZnO is the main cause in the increase of the total capacitance as the redox reactions occur on the composite electrode/electrolyte interface through the electrochemical conversion of Zn^{2+} to other valence states. However, the large amount of ZnO accumulated in the network structure of CNT matrix lowers the specific surface area of CNTs and thus decrease the adsorption of charge carriers such as protons and electrons on the surface of the electrodes [125]. Lu and co-workers (2010) have developed ZnO/graphene for supercapacitor applications [35]. The specific capacitances of ZnO/graphene and graphene electrodes that calculated from the study are 62 F/g and 39 F/g respectively. The EIS conducted on ZnO/graphene and pure graphene electrodes shows that pure graphene electrode exhibited the higher charge-transfer resistance (2.5 Ω) than ZnO/graphene (0.6 Ω) (Figure 2.21). These comparative results show that the ZnO/graphene composite electrodes exhibit better capacitive performance if compared to the pure graphene electrodes.

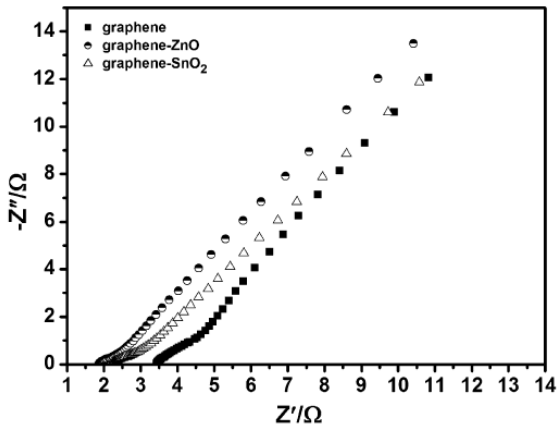


Figure 2.21. AC impedance plots of graphene-ZnO, graphene-SnO_2 and pure graphene electrodes [35].

2.3.4.6 Titanium oxide (TiO_2)-based composites

TiO_2 is considered an environment friendly n-type metal oxide semiconductor because it can be utilized to decompose harmful organic and inorganic pollutants that present in air and aqueous system under sunlight or indoor fluorescent irradiation. [127]. However, the poor conductivity of TiO_2 restricts its application as electrode material for electrochemical capacitors (EC) application [128]. Although TiO_2 nanomaterials are not suitable to be used as the core electrode material for electrochemical capacitors, many research studies revealed that it can enhance the homogeneity of other metal oxides or hydrous oxide within the electrode mixture [129]. It is important to control the dispersion behaviour of fine particles in various solvents in the field of supercapacitor because the dispersibility of fine particles affects the electrochemical performance of the charge storage devices [130].Therefore, several researchers have used TiO_2 nanotubes as a solid support to improve the dispersibility of some metal oxides including RuO_2 as the pseudocapacitor electrodes. [131, 132, 133, 134].

The CV curves obtained from the study of RuO_2 deposited on TiO_2 substrates were close to a rectangular shape and none of sharp oxidation or reduction peaks were observed. This indicates that the TiO_2 substrate does not exhibit pseudo-capacitive performance but contributes only as an EDLC platform in a charge-discharge process, by improving the electrolyte ion adsorption and desorption process on the surface of electrode substrate. Hence, the accessible surface area of RuO_2 and the proton interaction with RuO_2 can be intensively improved using TiO_2 nanotube array as an electrode substrate [132]. In another study, RuO_2/TiO_2 nanotubes composite was prepared by loading RuO_2 on TiO_2 nanotubes. The results show that the asymmetric supercapacitor based on RuO_2/TiO_2 nanotube positive electrode combined with an activated carbon (AC) negative electrode, exhibited higher working voltage (hence higher specific energy) if compared to the symmetrical supercapacitor that based on RuO_2/TiO_2 composite solely [134].

Ahn et al. (2007) found that further heat treatment of the TiO_2 at 800°C under nitrogen can greatly improve the electrochemical performance of the RuO_2 electrodes, especially at fast charge-discharge rates [131]. In addition, the charge storage performance of RuO_2/TiO_2 nanotubes was found to be significantly enhanced, mainly

attributed to the highly accessible surface areas of RuO_2. The loading of RuO_2 in TiO_2 nanotubes can improve the proton interaction with RuO_2, which in turn promote the electrochemical capacitor performance and the cyclic stability [132]. Very recently, Seo and Park (2010) conducted a study on the effect of nanosized TiO_2 on the electrochemical characteristics of AC electrodes in 1 M H_2SO_4 [135]. Figure 2.22. demonstrates the effect on the specific capacitance of TiO_2/AC composite electrodes with various compositions of TiO_2. The optimised content of TiO_2 in the composites was found to be 10 wt %, in which the specific capacitance of the composite electrode has been improved from 100 to 155 F/g compared to that of pure AC electrode.

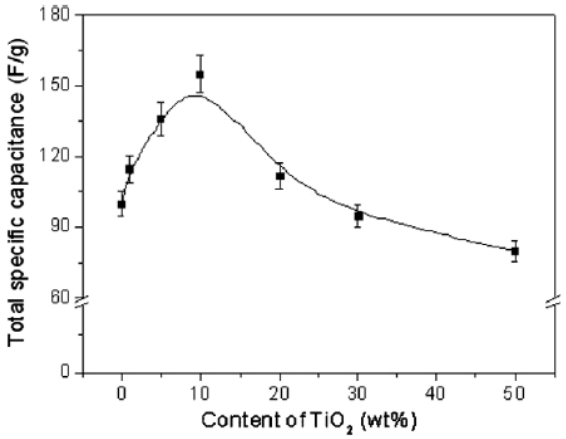


Figure 2.22. Total specific capacitance of TiO_2/AC composite electrodes as a function of TiO_2 content in 1 M H_2SO_4 [135].

AC electrodes are polarisable and thus could lead to the reduction of ions accumulation on the double layer. The polarization of activated carbon can be reduced through the modification with nanosized TiO_2 since there are more charges on the surface of TiO_2 than other regions, as a result of the attractive contribution of positively charged depletion region. It is believed that the improved capacitance of electrochemical double layer capacitors (EDLC) is attained if the ion concentration on the double layer of activated carbon is increased. This is because some of the activated carbon pores are likely to be filled by hydrous TiO_2 after impregnation with TiO_2 and thus reduce the polarization of activated carbon [135]. The SEM results (Figure 2.23) reveal another explanation in which the capacitance enhancement mainly originates from the interaction between ACs and TiO_2. The very small cluster of TiO_2 attached to large AC granules

provide preferential nucleation sites on the AC surfaces. In 2012, Selvakumar and Bhat successfully prepared nanostructured TiO_2:AC composite electrodes in three different compositions of 1:1, 1:2 and 1:3 by using microwave-assisted approach [136]. Figure 2.24 shows the Nyquist plot for these three different composite electrodes, indicating that the charge transfer resistance (size of semicircle) of the composite electrodes was estimated to be about 70 Ω, 50 Ω and 20 Ω for 1:1, 1:2 and 1:3 respectively. The observed highest capacitance (92 F/g) was achieved for the electrode with 1:3 composition.

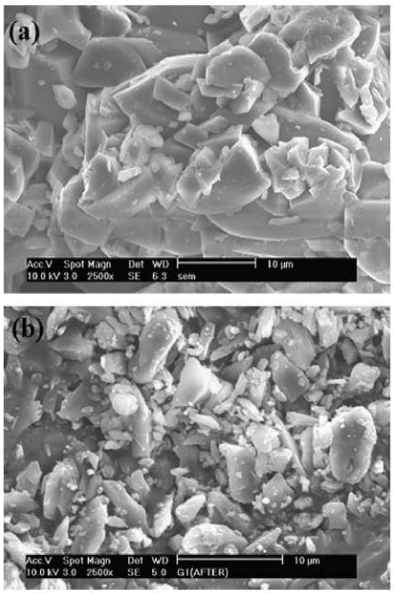


Figure 2.23. SEM images for (a) pure AC electrode and (b) TiO_2/AC composite electrode [135].

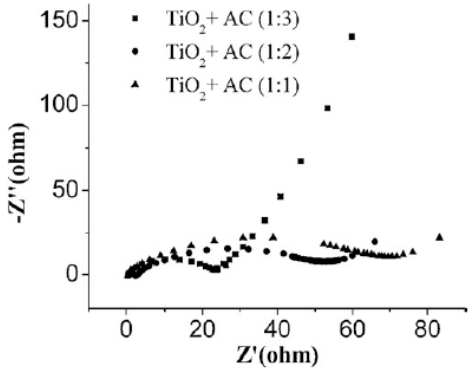


Figure 2.24. Nyquist plots of TiO2:AC (1:3), TiO_2:AC (1:3), TiO_2:AC (1:3) composite electrodes [136].

2.3.4.7 Cobalt oxide (Co_xO_y) -based composites

Co_3O_4 materials have the main drawback of poor cyclability as a result of large volume expansion/contraction which could be overcome by coupling Co_3O_4 nanoparticles with graphene in 6 M KOH [137]. The study reveals that the specific capacitance of 415 F/g was attained when Co_3O_4 nanoparticles intercalated into the spaces within graphene nanosheets, keeping the sheets from restacking while maintaining their high effective surface area. Similarly, another study on the graphene/Co_3O_4 nanocomposite in 6 M KOH exhibited specific capacitance of 243 F/g and 95.6% capacitance retention after 2000 cycles, indicating graphene not only acts conductive agent but also as a buffer to prevent the volume change in Co_3O_4 electrodes. A novel system consisting of conductive carbon fibre paper coated with Co_3O_4 nanowire network demonstrates high specific capacitance (1124 F/g) with remarkable durability up to 5000 cycles. Obviously, such unique electrode design has facilitated stress relaxation during cycling and enhanced ion/electron diffusion with improved kinetics of redox reactions. The authors suggested that the similar concept is possibly applied on MnO_2 and V_2O_5 for high- performance electrode materials [138]. Another new approach of designing superior pseudocapacitive nanocomposites is to fabricate mesoporous CoO nanowire and coupled with highly conductive conducting polymer PPy, which demonstrated outstanding specific capacitance (2223 F/g) and excellent cyclability (~20000 times) [139].

2.3.4.8 Other metal oxide-based composites

Many other metals oxides such as copper oxide (CuO), tin oxide (SnO_2), molybdenum oxide (MoO_3), chromium oxide (CrO_3), lead oxide (PbO), tungsten oxide ($W_{18}O_{49}$) and vanadium oxide (V_2O_5) have been explored as potential composite electrode materials. Kim and co-workers (2012) have prepared CuO/CNT composites which exhibit 60 F/g in 6 M KOH [140]. Graphene/SnO_2 composite electrodes were prepared by screen-printing approach show the capacitance value of 42.7 F/g in 1 M KCl [35]. Hu and co-workers (2008) demonstrated that the complementary properties of SnO_2 nanoparticles embedded within PANI exhibited excellent capacitance of 305 F/g with a specific energy density of 42 Wh/kg. The enhancement of the capacitive performance is

suggested to be attributed to the presence of SnO_2 nanoparticles embedded within PANI chains, increasing the electrode-electrolyte interfacial area for insertion and extraction of ions [126]. Very recently, Kang and co-workers (2014) adopted facile approach of electrochemical polarisation to fabricate the low-cost nanoporous Ni-Mn based oxy-hydroxide in 1 M $(NH_4)_2SO_4$ solution, paving new way for the next generation of high-performance electrochemical capacitors [141].

Sugimoto and co-workers (2001) first investigated MoO_3/AC composite electrodes in 1 M NaOH and 0.5 M H_2SO_4, respectively [142]. The study demonstrates that an increase in specific capacitance from 132 to 177 F/g was obtained when 1.4 wt% MoO_3 was incorporated onto AC in 1 M NaOH. In 0.5 M H_2SO_4, this composite electrode exhibits 176 F/g, which is 29 % higher than that of AC (136 F/g). Very recently, Aravinda et al. (2013) have successfully deposited MoO_3 on MWCNTs using magnetron sputtering method [143]. This nanocomposite electrodes exhibit the specific capacitance of 70 F/g in 1 M Na_2SO_4, measured with two-electrode configuration. The specific capacitance was almost constant up to 800 cycles and decreased to 82 % gradually from its initial value at the end of 1000^{th} cycle**.** Lota et al. (2007) have studied the electrochemical performance of CrO_3/SWNT in 1 M H_2SO_4 and 6 M KOH, respectively using two-electrode measurement [144]. These composite electrodes exhibit better capacitive behaviour in acidic electrolyte (~50 F/g) than in alkaline solution. A nearly good shape of CV curve of CrO_3/SWNT composite electrode 1 M H_2SO_4 (Figure 2.25) shows no redox peaks, explaining that redox transformation of chromium compounds responsible for faradaic reactions could not be predicted in two-electrode cell measurement. Similar implication was made by Stroller (2010) when they reviewed the test methods of both two- and three- electrode cells [145].

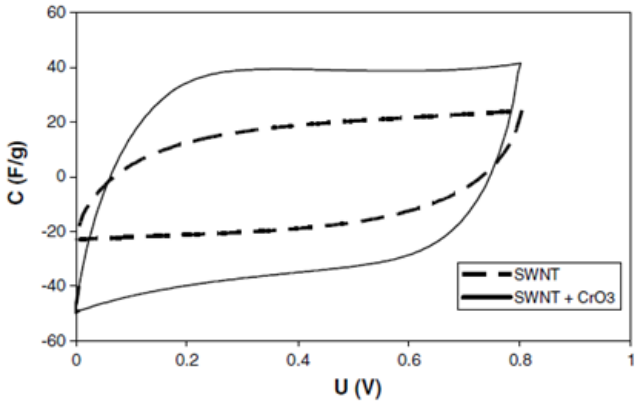


Figure 2.25. Capacitance calculated from CV curves of CrO_3/SWNTs and pure SWNT-based electrodes carried out in 1 M H_2SO_4 using two-electrode measurement [144].

Recently, the investigation on PbO_2/AC hybrid capacitor has been carried out using two-electrode cell configuration in 5.3 M H_2SO_4 [146]. The study showed that a specific capacitance of 101 F/g was recorded on this hybrid capacitor and the system also exhibited the excellent stability in concentrated H_2SO_4 after 2600 cycles. Tian and co-workers (2014) have reported a novel smart electrochemical capacitor which delivers new functionalities compared to conventional energy storage devices, employing $W_{18}O_{49}$ and conducting polymer PANI as composite materials. The composite was able to display multiple colour change in response to varying levels of stored energy in aqueous solution of H_2SO_4. As can be shown from Figure 2.26, when the smart composite electrode was fully charged to 0.8 V, the logo on the electrode (SINANO) was transparent on the blue background. On contrary, the logo becomes blue in colour on a transparent background as the electrochemical capacitor was discharged at -0.5 V. These additional features have brought an important breakthrough in next generation of energy storage technology [147]. Lee and co-workers (2015) reported a facile method for the synthesis of V_2O_5 – graphene nanocomposite using a low-temperature hydrothermal process [98]. It is believed that graphene oxide (GO) played a vital role as a mild oxidizing agent for the formation of nanowires, as well as enhanced the conductivity of the nanocomposite. The maximum specific capacitance of 288 F/g was achieved for this V_2O_5 –graphene nanocomposite in 1 M Na_2SO_4.

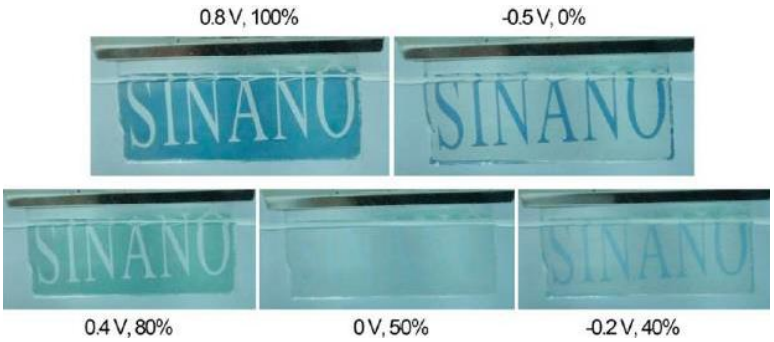


Figure 2.26. Images showing the colour scheme changes when the smart composite electrodes ($W_{18}O_{49}$-PANI) are charged and discharged at varying levels. The electrode is fully charged (100 %) at 0.8 V while it is at discharged state (0 %) at -0.5 V [147].

2.3.4.9 Ternary composites

Electron conductivity and mechanical stability of electrode material have always been limitations that hinder the practical applications of electrochemical capacitors. To overcome these problems, combination of three components in a single electrode materials have been attempted recently. A comparative evaluation on nano SnO_2-Al_2O_3, SnO_2-Al_2O_3-carbon and SnO_2-V_2O_5-CNT composites were conducted by Jayalakshmi et al. (2006) for electrochemical capacitor applications [148]. The study shows that there is an increasing order of specific capacitance measured from cyclic voltammogram at 100 mV/s: SnO_2-V_2O_5-CNT composite (121.40 F/g) > SnO_2-Al_2O_3 mixed oxide (88.90 F/g) > SnO_2-Al_2O_3- carbon composite (69.30 F/g), revealing that ternary composites could be more superior than binary composites if the optimal compositions were achieved. In recent work, Wang and co-workers (2012) have successfully prepared nickel cobalt oxide ($NiCo_2O_4$)/SWCNT ternary nanocomposite for electrochemical capacitor applications [34]. This novel material not only exhibits a remarkable specific capacitance of 1642 F/g, but also demonstrates an excellent cycling stability of 94.1% retention after 2000 cycles. They concluded that the highly conductive SWCNT and $NiCo_2O_4$ have helped to reduce the interfacial resistance of the nanocomposite. However, the authors offered no explanation for the enhanced cycling stability of this ternary composite.

Recently, Yan et al (2012) successfully synthesized a novel MnO_2/PANI/carbon ternary composite in 1 M H_2SO_4 [150]. With the 12 % MnO_2 loading, the maximum specific capacitance of 695 F/g and the 88% capacitance retention are achieved after 1000 cycles. This study shows that the protective PANI nanolayer enables MnO_2/carbon composites to be operated in acidic electrolyte. Similar study on ternary composite of MnO_2/CNT/poly (3,4-ethylenedioxythiophene) - poly (styrenesulfonate) or PEDOT-PSS by Hou et al. (2010) reported that the specific capacitance of the ternary composite reaches 200 F/g with only less than 1% decay in specific capacitance after 1000 cycles cyclic analysis [151]. They suggested that the good conductive CNTs provide high surface for the deposition of highly porous MnO_2 nanospheres and improve the mechanical stability of the composite. In addition, PEDOT/PSS can act as an effective dispersant and binder for improving the adhesion to the substrate and the connection among MnO_2/CNTs particles. Similarly, Cheng and co-workers (2012) adopted novel approach of fabricating ternary nanocomposites of graphene-MnO_2-CNTs via direct growth of MnO_2 nanoparticles and CNTs on graphene substrate. CNTs which provide electronic conductivity and mechanical reinforcement in combination with highly electrochemically active MnO_2 nanoparticles and high-surface-area graphene produced the synergetic effects for superior performance of the nanocomposite electrodes. These flexible electrodes successfully deliver high specific capacitance of 372 F/g without the need of current collectors and binders [152].

Another research group has reported on a novel PANI/TiO_2/graphene oxide (GO) composite which demonstrated the highest specific capacitance of 1020 F/g can be achieved accordingly [153]. TiO_2 nanoparticles serve as avenue for electrode to penetrate to three dimensional graphene oxide-PANI networks, facilitating the faradaic reactions of PANI. To improve its processability, polystyrenesulfonate (PSS) is added and this results in an aqueous dispersion of PEDOT/PSS as PEDOT has good compatibility with polar group polymers. A study on PEDOT/PSS-SWNT composite material has demonstrated that the specific capacitance of 104 F/g is obtained for the 40 % SWNT compositions in the polymer matrix [154]. Huang et al. (2006) have claimed an impressive 1409 F/g for the PEDOT/PSS/RuO_2 composite [155]. While this device shows very promising

performance, ruthenium-based starting materials however are too expensive for the large scale production of commercially viable electrochemical capacitors.

Zhang and co-workers (2013) reported an electrode of $NiCo_2O_4$ mesoporous nanosheets grown on conductive Ni foam which demonstrated an excellent electrochemical performance. The highly porous $NiCo_2O_4$ nanosheets with increased electroactive sites have greatly facilitated the ionic and electronic transport. Moreover, the new concept of direct grown $NiCo_2O_4$ nanosheets on conductive substrate has ensured good electric contact and good mechanical adhesion for high-performance electrodes [156]. Similarly, another novel design of composite electrodes has been realised by facile coating nanometer-thick redox active MnO_2 thin film to highly electronic conductive Zn_2SnO_4 nanowires which are directly grown on flexible carbon mircofibers in 1 M Na_2SO_4. In such a composite, the maximum specific capacitance of 642 F/g is achieved through the synergetic contributions from MnO_2, Zn_2SnO_4 and carbon microfibers [157]. Wei's research group (2014) described a combination of freeze drying and hydrothermal synthesis method for preparation of 3D mesoporous $NiCo_2O_4$/graphene nanoarchitectures [158]. High specific capacitances of 778 F/g and 374 F/g were obtained at current densities of 1 A/g and 80 A/g, respectively. Nanohoneycomb – like $CoMoO_4$ decorated on 3D graphene sheets has been successfully produced and is being used as long-life supercapacitor electrodes [159]. The hybrid electrodes displayed an excellent specific capacitance of 2329 F/g at current density of 2.43 A/g. Even under very high current density of 400 A/g, the $CoMoO_4$/graphene hybrid electrodes still exhibited a superior stable specific capacitance of 440 F/g and high capacitive retention (~ 96 %) after 100000 cycles. The impressive results were attributed to the positive synergistic effects of the mixed metal oxides and graphene.

Very recently, Tang and co-workers (2015) developed a novel ternary composite consisting of vanadium/single-walled carbon nanotubes (SWCNTs)/carbon nanofibers which exhibited a high specific capacitance of 367 F/g in 6 M KOH. The results show that simultaneously adding vanadium and SWCNTs can greatly enhance the conductivity, capacitive performance and stability. Another novel ternary composite MnO_2 nanoflake/ polyaniline (PANI) nanorod hybrid nanostructures on reduced graphene oxide (RGO) were successfully synthesized for flexible supercapacitor electrode application [192].The

MnO_2/PANI/RGO composite shows a large specific capacitance of 636.5 F/g at 1.0 A/g in 1.0 M Na_2SO_4 electrolyte and excellent cycling stability (85% capacitance retention after 10^4 cycles). It is speculated that the optimized ternary composite structure is achieved with more electroactive sites, fast ion and electron transfer, and strong structural integrity. Chee et al. (2015) prepared a ternary composite made from the combination of polypyrrole (PPy), graphene oxide (GO) and zinc oxide (ZnO) [193]. This PPy/GO/ZnO nanocomposites deposited on nickel foam demonstrate a specific capacitance of 94.6 F/g at a current density of 1 A/g in 1 M Na_2SO_4.

A new ternary composite, RGO/SnO_2/PANI composite, has firstly and facilely been synthesized via chemical reduction of GO by $SnSO_4$ [99]. Meanwhile SnO_2 nanoparticles were deposited on the surface of RGO sheets while the PANI nanofibers were coated on the surface of the graphene-SnO_2. The graphene/SnO_2/PANI composite exhibits excellent electrochemical performance (913 F/g) in 1 M H_2SO_4.

Table 2.7 summarises the recent research works that were carried out in relation to the symmetric composite electrodes, including different combinations of material, various fabrication/synthesis techniques as well as different electrolytes employed. It should be noted that fabrication and material costs continue as major challenges to the mass production of electrochemical capacitors particularly for high-performance applications. With this regards, the recent development of cost-effective electrode materials as well as green and facile synthesis methods are underway by a number of researchers. With the synergic effect from novel advanced materials, continual effort is still worth in developing of composite electrode, owing to its feasibility, availability and compatibility for next-generation electrochemical capacitor.

Table 2.7. Recent research works that were carried out in relation to the symmetric composite electrodes, including different combinations of material, various fabrication/synthesis techniques as well as different electrolytes employed.

Composite Electrode	Configuration	Electrolyte	Specific Capacitance (F/g)	Year of Publication	Reference
RuO_2/carbon	Metal oxide/carbon	1 M H_2SO_4	407	2001	[163]
RuO_2/carbon paper	Metal oxide/carbon	1 M H_2SO_4	620	2002	[164]
Fe_3O_4/SnO_2	Mixed oxides	1 M Na_2SO_4	33*	2002	[120]
RuO_2/Sb-doped SnO_2	Mixed oxides	1 M H_2SO_4	930*	2003	[165]
RuO_2/AC	Mixed oxides	0.1 M H_2SO_4	185	2004	[162]
RuO_2/NiO	Mixed oxides	1 M KOH	210	2004	[161]
SnO_2/Al_2O_3	Mixed oxides	0.1 M NaCl	119	2005	[166]
SnO_2/Al_2O_3/carbon	Mixed oxides/carbon	0.1 M NaCl	90	2005	[166]
NiO/AC	Metal oxide/carbon	6 M KOH	194	2005	[167]
NiO/CNT	Metal oxide/carbon	2 M KOH	160*	2005	[168]
RuO_2/SnO_2	Mixed oxides	1M H_2SO_4	690	2007	[149]
RuO_2/ TiO_2	Metal oxide/carbon	0.5 M H_2SO_4	687	2007	[131]
V_2O_5/SnO_2/CNT	Mixed oxides/carbon	1 M KCl	121	2007	[148]
MnO_2/CNT	Metal oxide/carbon	1 M LiAc-$MgSO_4$	205	2007	[77]
SnO_2/PANI	Metal oxide/polymer	1 M H_2SO_4	305	2008	[89]
MnO_2/CNT	Metal oxide/carbon	0.5 M Na_2SO_4	356	2009	[114]
ZnO/CNT	Metal oxide/carbon	1 M KCl	324	2009	[125]

MnO_2/carbon	Metal oxide/carbon	6 M KOH	600	2009	[170]
TiO_2/AC	Metal oxide/carbon	1M H_2SO_4	155	2010	[135]
ZnO/AC	Metal oxide/carbon	0.1 M Na_2SO_4	160	2010	[78]
ZnO/graphene	Metal oxide/carbon	1 M KCl	62	2010	[35]
SnO_2/graphene	Metal oxide/carbon	1 M KCl	43	2010	[35]
RuO_2/ graphene	Metal oxide/carbon	1 M H_2SO_4	570	2010	[160]
MnO_2/CNT/PEDOT-PSS	Metal oxide/carbon/polymer	1 M Na_2SO_4	200	2010	[113]
MnO_2/graphene	Metal oxide/carbon	1 M KCl	328*	2011	[39]
Fe_3O_4/MWNT	Metal oxide/carbon	1 M Na_2SO_3	165	2011	[171]
CuO/SWCNT	Metal oxide/carbon	6 M KOH	62	2011	[91]
CuO/AC	Metal oxide/carbon	6 M KOH	210	2011	[91]
MnO_2/Zn_2SnO_2/carbon	Mixed metal oxides/carbon	1 M Na_2SO_4	642	2011	[157]
Ag/CuO	Mixed oxides	6 M KOH	689	2012	[91]
CuO/CNT	Metal oxide/carbon	6 M KOH	60	2012	[140]
PANI/MnO_2	Metal oxide/polymer	1 M Na_2SO_4	320	2012	[97]
PANI/MnO_2	Metal oxide/polymer	0.5 M Na_2SO_4	262	2012	[172]
MnO_2/PANI/carbon	Metal oxide/polymer/carbon	1M H_2SO_4	695*	2012	[150]
TiO_2/PANI/graphene	Metal oxide/polymer/carbon	1M H_2SO_4	1020	2012	[153]
Co_3O_4/graphene	Metal oxide/carbon	6 M KOH	415	2012	[137]
$NiCo_2O_4$/CNT	Mixed oxides/carbon	2 M KOH	1642	2012	[34]
MnO_2/Mn/MnO_2	Metal oxide/metal/metal oxide	1 M Na_2SO_4	937	2012	[173]
Co_3O_4/carbon fiber paper	Metal oxide/carbon	-	1124	2012	[138]

Graphene/MnO_2/CNT	Carbon/metal oxide/carbon	1 M Na_2SO_4	372	2012	[152]
PANI/MoO_3/RGO	Polymer/metal oxide/carbon	1 M H_2SO	553	2012	[174]
PANI/MoO_3/RGO	Polymer/metal oxide/carbon	1 M Na_2SO_4	363	2012	[174]
ZnO/graphene	Metal oxide/carbon	1 M KCl	109	2013	[175]
CoO/PPy	Metal oxide/polymer	3 M NaOH	2223	2013	[139]
$NiCo_2O_4$/Ni	Metal oxides/metal	2 M KOH	1743	2013	[156]
ZnO/RGO	Metal oxide/carbon	2 M KOH	314	2014	[169]
$NiCo_2O_4$ /graphene	Mixed oxides/carbon	2 M KOH	778	2014	[158]
$CoMoO_4$/graphene	Mixed oxides/carbon	2 M KOH	2329	2014	[159]
$W_{18}O_{49}$/PANI	Metal oxide/polymer	H_2SO_4	Smart electrode	2014	[147]
PEDOT/MWCNT/graphene	Polymer/mixed carbon	5 M KOH	225	2014	[119]
PANI/RGO/ZrO_2	Polymer/carbon/metal oxide	1 M H_2SO_4	1360	2014	[100]
Ni_3S_2/RGO/Ni_3S_2	Metal sulphide/carbon	2 M KOH	3235	2015	[66]
Fe_2O_3/RGO	Metal oxide/carbon	1 M KOH	268	2015	[176]
V_2O_5/SWCNT/Carbon	Metal oxide/mixed carbon	6 M KOH	367	2015	[190]
MnO_2/PANI/RGO	Metal oxide/polymer/carbon	1 M Na_2SO_4	637	2015	[192]
PPy/RGO/ZnO	Polymer/carbon/metal oxide	1 M Na_2SO_4	95*	2015	[193]
V_2O_5/RGO	Metal oxide/carbon	1 M Na_2SO_4	288	2015	[98]
RGO/SnO_2/PANI	Carbon/metal oxide/polymer	1M H_2SO_4	913	2015	[99]
PPy/MoO_3/RGO	Polymer/metal oxide/carbon	0.5 M K_2SO_4	175	2016	[177]

* Measurement using two-electrode cell configuration.

2.4.5 New materials: Lithium -ion capacitor

The new generation of hybrid capacitor-battery designs utilizing battery-type and electrochemical capacitor-type electrodes are found to have higher energy storage than currently available commercial electrochemical capacitors [178]. The use of the lithium metal oxides in hybrid capacitor results in excellent cyclability and rate capability, offering alternatives for the lifespan limitations associated with batteries as well as unsatisfactory energy density of capacitors [179]. Amatucci el al (2001) first proposed the $Li_4Ti_5O_{12}$/AC hybrid energy storage system which is able to achieve more than 10 Wh/kg in acetonitrile solution [180]. Following to this work, other systems have been designed, coupling a negative lithiated compound to a positive AC at low voltage [181]. The non-aqueous asymmetric hybrid capacitors utilizing lithium-intercalated compounds ($Li_4Ti_5O_{12}$) negative electrode and AC positive electrode was introduced by Telcordia Technologies in 2002 [182]. These 500 F devices were made in the same technology as Li-ion batteries, demonstrating specific energy of 11 Wh/kg in 2 M $LiBF_4$. Additionally, the cycle-life of this lithiated electrode is more superior as compared to Li-ion batteries, approaching that of electrochemical capacitors. Nevertheless, this novel study shows that the internal resistance of the device increases during the course of discharge as a result of the delithiation of the $Li_4Ti_5O_{12}$ anode and subsequently becomes less conductive. Similarly, Naoi and co-workers (2011) have developed another nanohybrid capacitor consists of a faradaic $Li_4Ti_5O_{12}$ negative electrode combined with a AC positive electrode in 1 M $LiBF_4$ organic electrolyte [183]. The study demonstrates that this configuration of hybrid electrochemical capacitor exhibits a higher energy density in comparison to that of a conventional (AC/AC) electrochemical capacitor due to its larger working voltage and higher capacitance, as shown in Figure 2.27. Very recently, Jung and co-workers (2013) have developed a novel high energy density hybrid capacitor consisting carbon-coated $Li_4Ti_5O_{12}$ (LTO) negative electrode and AC positive electrode in 1 M $LiPF_6$ [184]. As seen in Figure 2.28, this advanced hybrid capacitor system with the improved electronic conductivity carbon coating on $Li_4Ti_5O_{12}$ electrodes, offers the maximum specific energy of 35.5 Wh/kg which is higher than that achieved by AC/AC conventional EDLC. In the study, the authors proposed that the Li^+ cations are intercalated into the carbon-coated $Li_4Ti_5O_{12}$ negative electrode whereas the PF_6^- anions are adsorbed onto the high surface

area AC positive electrode during charging while both anions and cations are then released during discharging.

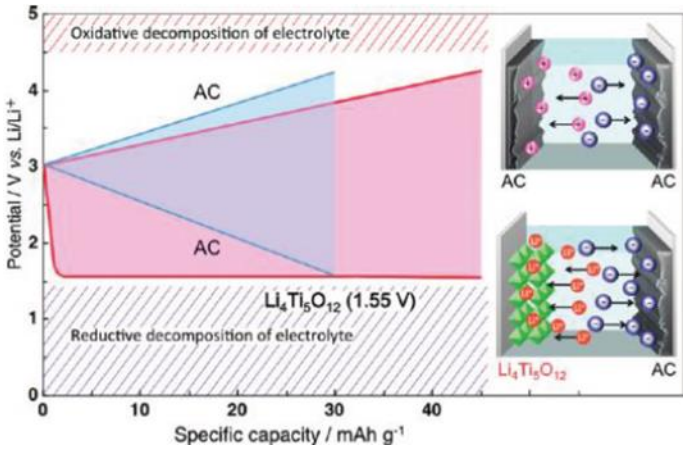


Figure 2.27. Comparison of voltage profile for a hybrid lithium-ion capacitor consists of activated carbon cathode and $Li_4Ti_5O_{12}$ and a AC/AC conventional EDLC [183].

Another novel Li-ion capacitor was successfully fabricated using AC as cathode and $LiCrTiO_4$ as anode in 1 M $LiPF_6$, delivering specific capacitance, maximum energy and power densities of 83 F/g, 23 Wh/kg and 4 kW/kg, respectively [185]. Bockenfeld et al.(2011) have developed composite electrodes consisting of 65 wt% $LiFePO_4$ and 20 wt% AC in 1 M $LiPF_6$ [186], displaying very high specific capacitance of 140 mAh/g or 504 F/g. By adding 10 wt % conductive carbon, the electronic conductivity of this composite electrode is increased significantly. However, the 100-cycle test analysis obtained from the study could not convince a good cycling performance for this composite electrode. A novel hybrid capacitor fabricated with $LiFeSiO_2$ and AC in 1 M $LiPF_6$ delivers the specific capacitance of 49 F/g, the specific energy of 43 Wh/kg and the specific power of 200 W/kg [187]. Another study on the novel hybrid capacitor made of Li_2MnSiO_4 anode and AC cathode has reported the specific capacitance of 43.2 F/g (two-electrode cell) in 1 M $LiPF_6$ with high specific energy of 54 Wh/kg and specific power of 150 W/kg [188]. This hybrid capacitor exhibits good cyclability, retaining about 85 % of its initial capacitance after 1000 cycles.

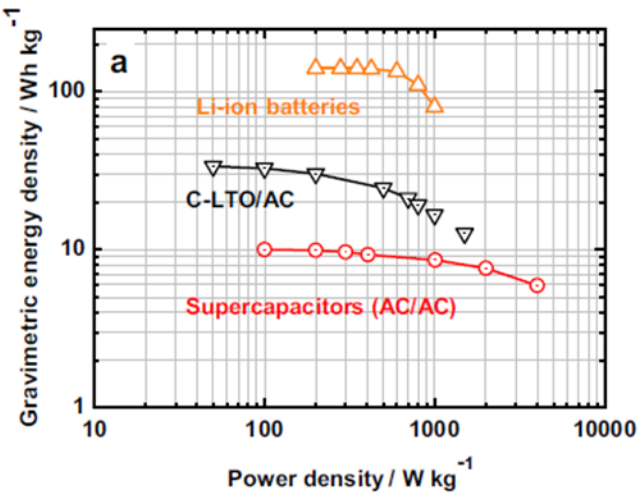


Figure 2.28. Ragone plot comparing lithium-ion batteries, carbon-coated $Li_4Ti_5O_{12}$/AC lithium-ion capacitors and AC/AC conventional EDLCs [184].

To the best of our knowledge, very few studies aimed at designing lithium metal oxide-based electrode materials using aqueous electrolyte. Wang and Xia (2005) have developed the hybrid capacitor consists of AC negative electrode and $LiMn_2O_4$ positive electrode in Li_2SO_4 [189]. This new concept aqueous-based hybrid capacitor is different from any other hybrid capacitors or Li-ion batteries which mostly employ non-aqueous electrolytes. In general, the Li_2SO_4 aqueous electrolyte behaves the same profile as that in EDLCs. It is apparent from Figure 2.29 that the AC/$LiMn_2O_4$ hybrid capacitor exhibits higher specific energy and power densities compared to those of AC/AC conventional EDLC. The practical specific energy of the AC/$LiMn_2O_4$ can be as high as 14 W h/kg. In other study, the hybrid capacitor consisting of $LiMn_2O_4$ working as a positive electrode and AC as negative electrode in 1 M Li_2SO_4 has proven to be able to deliver a capacity of 60 F/g with high specific energy of 36 Wh/kg in two-electrode cell [189].

Very recently, Naoi's group has identified that the conventional lithium metal oxides have the greatest drawback of low power characteristics as a result of poor Li^+ diffusion coefficient and poor electronic conductivity [178]. To overcome these problems, further development on composite electrode materials which couple lithium metal oxide powder with other electroconductive material may become a versatile solution. With regards to this, the research group has developed lithium-ion capacitors comprise AC cathode and

conductive graphite/AC anode pre-doped with lithium ions. It is suggested that the adsorption-desorption of anions from electrolytes occurs on the AC electrode while lithium intercalation-deintercalation occurs in the graphite electrode [178]. Similarly, Sivakkumar and Pandolfo (2012) have fabricated a lithium-ion capacitor assembled with pre-lithiated graphite anode and AC cathode, exhibiting energy density of 100 Wh/kg [190]. However, the study reveals that the instability of pre-doped graphite during the cycling is the main root cause of the capacity deterioration. The work is still in its preliminary stage and much research is needed before this novel lithium-ion capacitor can be realized as potential charge storage device which is complementary to lithium-ion batteries.

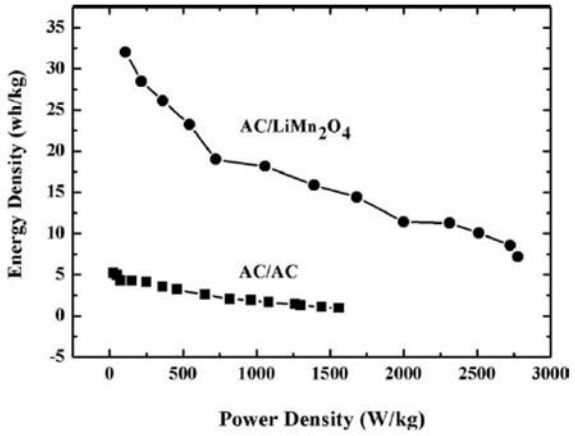


Figure 2.29. Ragone plot showing AC/$LiMn_2O_4$ hybrid capacitor with higher specific energy and power densities compared to those of AC/AC conventional EDLC in Li_2SO_4 [189].

2.5 Electrolyte

The choice of an electrolyte is particularly important because the amount of energy stored in the cell and how quickly this energy can be released are determined by the thermodynamic stability of the electrolyte employed [194]. As discussed earlier, energy density of electrochemical capacitor is proportional to the squared voltage, numerous research efforts have been aimed at exploring highly conducting, stable electrolytes with a wider voltage [195]. Generally, three types of electrolyte are currently employed in electrochemical capacitor applications: (i) aqueous electrolyte, (ii) organic electrolyte, and (iii) ionic liquid.

In aqueous electrolyte, concentrated electrolytes such as H_2SO_4 and KOH are able to minimize internal resistance and maximize power capability due to excellent ionic conductivity (0.5-1 S/cm) or much lower electrolyte resistivity (1-2 Ωcm). The great number of proton (H^+) and hydroxide (OH^-) involved in proton hopping or proton transport explains the higher ionic conductivity in strong acid and alkali, respectively [51]. However, the use of concentrated electrolyte limits the cycle life of electrochemical capacitor and restricts the range of possible electrode materials because most of metal oxides degrade dramatically in concentrated solutions. As a result, neutral and mild aqueous electrolytes including KCl, Na_2SO_4, Na_2SO_3, and Li_2SO_4 have therefore been considered for use with metal oxides [103]. Compared with organic electrolytes, aqueous electrolytes exhibit higher capacitance due to relatively smaller ionic size (5 to 10 Å) and lower internal resistance. The resistance of electrochemical capacitor is strongly dependent on the conductivity of electrolyte and the size of electrolyte ions which penetrate into and out from the pores of electrode particles [51]. With the same reasons, aqueous electrolytes also tend to produce faster rates of charges and discharge. Additionally, preparation of aqueous electrolytes undergoes less stringent purification and drying processes due to the absence of flammable and toxic solvent. Consequently, the fabrication and material cost of aqueous electrolytes are much lower in comparison to organic electrolytes. However, the main drawback of aqueous electrolytes is their relatively smaller voltage window, which is limited by the electrolysis of water to 1.23 V at 25 ^oC [196]. As can be seen from equation (7) and (8), aqueous electrolytes have limitation in term of enhancing both energy and power densities because of their narrow voltage window. This is the reason why organic electrolytes are often recommended.

Moving from aqueous to organic electrolyte, the voltage window is increased from 1.2 V to 3.5 V [51]. By all means, this is a great advantage of organic over aqueous electrolytes. Typically, the operating voltage is set to 2.5 V to prevent decomposition of the electrolyte through over-charging. In order to ensure that organic electrolytes can operate at the higher voltages, an inert atmosphere which is free of water and oxygen is needed to handle these electrolytes. This is because the evolution of H_2 and O_2 gases occurred at the potential difference above 1.23 V [196]. Among organic electrolytes, acetonitrile is the most commonly used solvent [197]. However, its toxicity and

flammability require more stringent and costly preparation processes. Organic electrolytes have low conductivity (0.01-0.05 S/cm) which leads to high internal resistance or ESR (20-60 Ωcm). The increased viscosity in organic electrolytes also further increases the ESR. The organic ions with relatively larger size (15-20 Å) are more difficult to diffuse into or out of the pores of electrode materials. This results in poorer specific capacitance in organic-based electrochemical capacitors.

Ionic liquids (ILs) are room-temperature liquid solvent-free electrolyte. ILs are essentially molten salts with melting temperatures at or below room temperature.[26] Imidazolium, pyrrolidinium and quaternary ammonium slats are among the most widely studied ILs for electrochemical capacitor applications. The main advantages of using ILs include wide electrochemical stability window up to 6 V, high thermal and chemical stability, low flammability and low vapour pressure [197]. Their voltage window stability is thus only driven by the electrochemical stability of the ions. The ionic conductivity of these liquids at room temperature is very low, so they are mainly used at higher temperature [195]. Unfortunately, ILs has relatively high viscosities and much lower ionic conductivities than aqueous electrolytes. In addition, ILs is hygroscopic which require to be handled in stringent and controlled processes. Another major disadvantage of using ILs is their high cost, restricting the larger scale production.

Overall, a variety of electrode materials, such as carbon-based materials, conducting polymers, transition metal oxides and their composites have been studied as electrode materials for supercapacitors. The diversity of electrode materials in chemical and physical properties, preparation methods as well as the evaluation methods renders the reported electrochemical performance highly variable. It is very likely that continual research efforts will be aimed to discover novel electrode materials with high performance and low cost. In this regards, transition-metal-oxide based composites, lithium-ion based materials and graphene-based composite materials**,** will receive increasing research interests in supercapacitor applications.

Reference

[1] A. Simeminski, “International Energy Outlook 2013”, in, U.S. Energy Information, Washington (2013).

[2] X. Li, B. Wei, “Supercapacitors based on nanostructured carbon,” Nano Energy 2 (2013) 159-173.

[3] P.Gogotsi, "Materials for Electrochemical Capacitors," Macmillan Publishers Limited, 2008.

[4] J. Marin, S.Halper, "Supercapacitor: A Brief Overview," MITRE, 2006.

[5] F. Beguin, E.Frackowiak, "Carbon Materials for The Electrochemical Storage of Energy in Capacitors," Carbon 39 (2001) 937-950.

[6] A. Nishino, "Capacitors: Operating Principles, Current Market and technical Trends," Journal of Power Sources 60 (1994) 137-147.

[7] Y. Zhang, H. Feng, X. Wu, L. Wang, A. Zhang, T. Xia, H. Dong, X. Li, and L. Zhang, "Progress of electrochemical capacitor electrode materials: A review," International Journal of Hydrogen Energy 34 (2009) 4889-4899.

[8] A. Davies and A. Yu, "Material advancements in supercapacitors: From activated carbon to carbon nanotube and graphene," The Canadian Journal of Chemical Engineering 89 (2011) 1342-1357.

[9] S. Bose, T.Kuila, A.K.Mishra, R.Rajasekar, N.H.Kim, J.H.Lee, "Carbon-based nanostructured materials and their composites as supercapacitor electrodes," Journal of Materials Chemistry 22 (2012) 767-784.

[10] B.E. Conway, J.Wojtowicz, "The Role and Utilization of Pseudocapacitance for Energy Storage by Supercapacitors " Journal of Power Sources 66 (1997) 1-14.

[11] P. J. Hall, M. Mirzaeian, S. I. Fletcher, F. B. Sillars, A. J. R. Rennie, G. O. Shitta-Bey, G. Wilson, A. Cruden, and R. Carter, "Energy storage in electrochemical capacitors: designing functional materials to improve performance," Energy & Environmental Science 3 (2010) 1238.

[12] A. G. Pandolfo and A. F. Hollenkamp, "Carbon properties and their role in supercapacitors," Journal of Power Sources 157 (2006) 11-27.

[13] M. V. Kiamahalleh, S. H. S. Zein, G. Najafpour, S. A. Sata, and S. Buniran, "Multiwalled Carbon Nanotubes Based Nanocomposites for Supercapacitors: A Review of Electrode Materials," Nano 7 (2012) pp. 1230002.

[14] T. Cottineau, M. Toupin, T. Delahaye, T. Brousse, and D. Bélanger, "Nanostructured transition metal oxides for aqueous hybrid electrochemical supercapacitors," Applied Physics A 82 (2005) 599-606.

[15] B.E.Conway, W.G.Pell, N.Marincic, "Analysis of Non-uniform Charge-Discharge and rate Effects in Porous Carbon Capacitors Containing Sub-Optimal Electrolyte Concentrations," Journal of Electroanalytical Chemistry 491 (2000) 9-21.

[16] M.Carlen, R.Kotz, "Principles and Applications of Electrochemical Capacitors," Electrochimica Acta 45 (2000) 2483-2498.

[17] J. H. Kim, K.W. Nam, S. B. Ma, and K. B. Kim, "Fabrication and electrochemical properties of carbon nanotube film electrodes," Carbon 44 (2006) 1963-1968.

[18] Y. Wang, Z. Shi, Y. Huang, Y. Ma, C. Wang, M. Chen, and Y. Chen, "Supercapacitor Devices Based on Graphene Materials," The Journal of Physical Chemistry C 113 (2009) 13103-13107.

[19] A. Davies and A. Yu, "Material advancements in supercapacitors: From activated carbon to carbon nanotube and graphene," The Canadian Journal of Chemical Engineering 89 (2011) 1342-1357.

[20] D. Qu, H. Shi, "Studies of Activated Carbons Used in Double-Layer Capacitors," Journal of Power Sources 74 (1998) 99-107.

[21] J. Chmiola, G. Yushin, Y. Gogotsi, C. Portet, P. Simon, P. L. Taberna, "Anomalous Increase in Carbon Capacitance at Pore Sizes Less Than 1 Nanometer, Science Magazine 313 (2006) 1760-1763.

[22] E.R.Pinero, K. Kierzek, J. Machnikowski and F. Beguin, "Relationship between the nanoporous texture of activated carbons and their capacitance properties in different electrolytes, "Carbon 44 (2006) 2498-2507.

[23] E. Frackowiak, "Carbon materials for supercapacitor application," Phys Chem Chem Phys 9 (2007) 1774-1785.

[24] G.Feng, R.Qiao, J.S.Huang, B.G.Sumpter and V.Meunier, "Ion Distribution in Electrified Micropores and Its Role in the Anomalous Enhancement of Capacitance, " ACS Nano 4 (2010) 2382-2390.

[25] L.L.Zhang and X.S.Zhao, "Carbon-based materials as supercapacitor electrodes," The Royal Society of Chemistry 38 (2009) 2520-2531.

[26] E.R.Pinero, F.Leroux, F.Beguin, "A High-Performance Carbon for Supercapacitors Obtained by Carbonization of a Seaweed Biopolymer," Advanced Materials 18 (2006) 1877-1882.

[27] S. Akbulut, "Optimization of Carbon Nanotube Supercapacitor Electrode," Master Thesis, 2011.

[28] C.Niu, E.Sichel, R.Hoch, D.Moy, H.Tennent, "High power electrochemical capacitors based on carbon nanotube electrodes", Applied Physics Letter, vol.70 (1997) 1480-1484.

[29] E.Frackowiak, K.Metenenier, V.Bertangna, F.Beguin, "Supercapacitor electrodes from multiwalled carbon nanotubes", Applied Physics Letter 77 (2000) 2421–2423.

[30] B.Zhang, J.Liang, C.Xu, B.Wei, D.Ruan, D.Wu, "Electric double-layer capacitors using carbon nanotube electrodes and organic electrolyte", Material Letter 51 (2001) 539–542.

[31] H.Zhang, G.P.Cao, Z.Y.Wang, Y.S.Yang, Z.J.Shi, Z.N.Gu, "Growth of Manganese Oxide Nanoflowers on Vertically-Aligned carbon Nanotube Arrays for High-rate Electrochemical Capacitive Energy Storage," ACS Nano 8 (2008) 2664-2668.

[32] D. N. Futaba, K. Hata, T. Yamada, T. Hiraoka, Y. Hayamizu,Y. Kakudate, O. Tanaike, H. Hatori, M. Yumura and S. Iijima, "Shape-engineerable and highly densely packed single-walled carbon nanotubes and their application as supercapacitor electrodes," Natural Materials 5 (2006) 987.

[33] S. D. K.Jurewics, V.Bertagna, F.Beguin, E.Frackowiak, "Supercapacitor From Nanotubes/Polypyrrole Composites," Chemical Physics Letters 347 (2001) 36-40.

[34] X. Wang, X. Han, M. Lim, N. Singh, C. L. Gan, M. Jan, and P. S. Lee, "Nickel Cobalt Oxide-Single Wall Carbon Nanotube Composite Material for Superior Cycling Stability and High-Performance Supercapacitor Application," The Journal of Physical Chemistry C 116 (2012) 12448-12454.

[35] T. Lu, Y. Zhang, H. Li, L. Pan, Y. Li, and Z. Sun, "Electrochemical behaviors of graphene–ZnO and graphene–SnO_2 composite films for supercapacitors," Electrochimica Acta 55 (2010) 4170-4173.

[36] Y. Chen, X. Zhang, D. Zhang, P. Yu, and Y. Ma, "High performance supercapacitors based on reduced graphene oxide in aqueous and ionic liquid electrolytes," Carbon 49 (2011) 573-580.

[37] S.R.C.Vivekchand, C.S.Rout, K.S.Subrahmanyam, A.Govindaraj and C.N.R.Rao,"Graphene-based electrochemical supercapacitors", Journal of Chemical Science 120 (2008) 9-13.

[38] M.D.Stroller, S.J.Park, J.H.An, R.S.Ruoff, "Graphene-based Ultracapacitors", Nano Letters 8 (2008) 3498-3502.

[39] Q. Cheng, J. Tang, J. Ma, H. Zhang, N. Shinya, and L.-C. Qin, "Graphene and nanostructured MnO_2 composite electrodes for supercapacitors," Carbon 49 (2011) 2917-2925.

[40] Y.Sato, K.Yomogida, T.Nanaumi, K.Kobayakawa, Y.Ohsawa, M.Kawai, Electrochemical Behavior of Activated-Carbon Capacitor Materials Loaded with Ruthenium Oxide, Electrochem. Solid-State Lett.2000 volume 3, issue 3, 113-116.

[41] Y. Wang, Z. Shi, Y. Huang, Y. Ma, C. Wang, M. Chen, Y. Chen, Supercapacitor Devices Based on Graphene Materials, The Journal of Physical Chemistry C 113 (30) (2009) 13103-13107.

[42] C. Liu, Z. Yu, D. Neff, A. Zhamu and B. Z. Jang, "Graphene-based supercapacitor with an ultrahigh energy density", Nano Letters 10 (2010) 4863–4868.

[43] S.Bose, T.Kuila, A.K.Mishra, R.Rajasekar, N.H.Kim, J.H.Lee, "Carbon-based nanostructured materials and their composites as supercapacitor electrodes," Journal of Materials Chemistry 22 (2012) 767-784.

[44] T.Nathan, A. Aziz, A. F. Noor, and S. R. S. Prabaharan, "Nanostructured NiO for electrochemical capacitors: synthesis and electrochemical properties," Journal of Solid State Electrochemistry 12 (2007) 1003-1009.

[45] J. J. Yoo, K. Balakrishnan, J. Huang, V. Meunier, B. G. Sumpter, A. Srivastava, M. Conway, A. L. Mohana Reddy, J. Yu, and R. Vajtai, "Ultrathin Planar Graphene Supercapacitors", Nano Letters 11 (2011) 1423.

[46] C.C. Hu, M.J. Liu, and K.H. Chang, "Anodic deposition of hydrous ruthenium oxide for supercapacitors," Journal of Power Sources, 163 (2007) 1126-1131.

[47] C.C. Hu, M.J. Liu, and K.H. Chang, "Anodic deposition of hydrous ruthenium oxide for supercapaciors: Effects of the AcO− concentration, plating temperature, and oxide loading," Electrochimica Acta 53 (2008) 2679-2687.

[48] V. D. Patake and C. D. Lokhande, "Chemical synthesis of nano-porous ruthenium oxide (RuO_2) thin films for supercapacitor application," Applied Surface Science 254 (2008)2820-2824.

[49] J. B. Goodenough, H.Y.Lee, "Supercapacitor Behaviour with KCl Electrolyte," Journal of Solid State Chemistry 144 (1999) 220-223.

[50] A. Kucernak, J.H.Jiang, "Electrochemical Supercapacitor Material Based on Manganese oxide: Preparation and Characterisation," Electrochimica Acta 47 (2002) 2381-2386.

[51] A. Burke, "Ultracapacitors;why, how and where is the technology," Journal of Power Sources 91 (2000) 37-50.

[52] T. Brouse, D.Belanger, Jeffrey W.Long, "Manganse Oxides: Battery Materials Make the Leap to Electrochemical Capacitors," The Electrochemical Society Interface (2008).

[53] S.C.Pang, M.A. Anderson, T.W.Chapman, "Novel Electrode Materials for Thin Film Ultracapacitors: Comparison of Electrochemical Properties of Sol-Gel Derived and Electrodeposited Manganese Dioxide," Journal of The Electrochemical Society 147 (2000) 444-450.

[54] N. Nagarajan, H. Humadi, and I. Zhitomirsky, "Cathodic electrodeposition of MnOx films for electrochemical supercapacitors," Electrochimica Acta 51 (2006) 3039-3045.

[55] J. N. Broughton and M. J. Brett, "Investigation of thin sputtered Mn films for electrochemical capacitors," Electrochimica Acta 49 (2004) 4439-4446.

[56] N.L.Wu, S.Y.Wang, C.Y.Han, D.S.Wu, L.R.Shiue, "Electrochemical Capacitor of Magnetite in Aqueous Electrolytes," Journal of Power Sources 113 (2003) 173-178.

[57] D. P. Dubal, W. B. Kim, and C. D. Lokhande, "Galvanostatically deposited Fe: MnO_2 electrodes for supercapacitor application," Journal of Physics and Chemistry of Solids 73 (2012) 18-24.

[58] C. W. Xuan Du, Mingming Chen, Yang Jiao, Jin Wang, "Electrochemical Performances of Nanoparticle Fe_3O_4-Activated Carbon Supercapacitor Using KOH Electrolyte Solution," Journal of Physics and Chemistry of Solids 113 (2009) 2643-2646.

[59] S.Y. Wang, K.C. Ho, S.L. Kuo, and N.L. Wu, "Investigation on Capacitance Mechanisms of Fe_3O_4 Electrochemical Capacitors," Journal of The Electrochemical Society 153 (2006) A75.

[60] C.Z.Yuan, J.Y.Li, L.R.Hou, L.Yang, L.F.Shen, X.G.Zhang, "Facile growth of hexagonal NiO nanoplatelet arrays assembled by mesoporous nanosheets on Ni foam towards high-performance electrochemical capacitors," Electrochimica Acta 78 (2012) 535-538.

[61] Y.Q.Zhang, X.H.Xia, J.P.Tu, S.J.Shi, X.L.Wang, C.D.Gu, "Self-assembled synthesis of hierarchically porous NiO film and its application for electrochemical capacitors", Journal of Power Sources 199 (2012)413-417.

[62] W.Xing, F.Li, Z.F.Yan, G.Q.Lu, "Synthesis and electrochemical properties of mesoporous nickel oxide", Journal of power Sources 134 (2004) 324-330

[63] M.S.Wu, D.S.Chan, K.H.Lin, J.J.Jow, "A simple route to electrophoretic deposition of transition metal-coated nickel oxide films for electrochemical capacitors", Materials Chemistry and Physics 130 (2011) 1239-1245.

[64] Y.G.Wang, Y.Y.Xia, "Electrochemical capacitance characterization of NiO with ordered mesoporous structure synthesized by template SBA-15", Electrochimica Acta 51 (2006) 3223-3227.

[65] M.S.Wu, M.J.Wang, J.J.Jow, "Fabrication of porous nickel oxide film with open macropores by electrophoresis and electrodeposition for electrochemical capacitors", Journal of Power Sources 195 (2010) 3950-3955.

[66] C.J.Zhao, Z.M.Zhang, Q.Wang, S.D.Min and X.Z.Qian, "Vertically oriented Ni_3S_2/RGO/Ni_3S_2 nanosheets on Ni foam for superior supercapacitors," RSC Adv. 5 (2015) 63528–63536.

[67] M.S.Wu, Y.A.Huang, C.H.Yang, J.J.Jow, "Elecrodeposition of nanoporous nickel oxide film for electrochemical capacitors", International Journal of Hydrogen Energy 32 (2007) 4153-4159.

[68] S. D. Lioudmila M.Doubova, Achille De Battisti, "Examination of RuO_2 Single-Crystal Surfaces: Charge Storage Mechanism in H2SO4 aqueous Solution," Journal of Electroanalytical Chemistry 532 (2002) 25-33.

[69] C. D. Lokhande, D. P. Dubal, and O.S. Joo, "Metal oxide thin film based supercapacitors," Current Applied Physics 11 (2011) 255-270.

[70] T. P. Gujar, V. R. Shinde, C. D. Lokhande, W.Y. Kim, K.-D. Jung, and O.S. Joo, "Spray deposited amorphous RuO_2 for an effective use in electrochemical supercapacitor," Electrochemistry Communications 9 (2007) 504-510.

[71] I.H.Kim and K.B.Kim, Ruthenium Oxide Thin Film Electrodes for Supercapacitors, Electrochem. Solid-State Lett.4 (2001) A62-A64.

[72] C.C. Hu and W.C. Chen, "Effects of substrates on the capacitive performance of RuOx·nH_2O and activated carbon–RuOx electrodes for supercapacitors," Electrochimica Acta 49 (2004) 3469-3477.

[73] J. W. Long, K. E. Swider, C. I. Merzbacher and D. R. Rolison, " Voltammetric Characterization of Ruthenium Oxide-Based Aerogels and Other RuO_2 Solids: The Nature of Capacitance in Nanostructured Materials", Langmuir 15 (1999) 780-785.

[74] W. Sugimoto, H. Iwata, K. Yokoshima, Y. Murakami , Y. Takasu, " Proton and Electron Conductivity in Hydrous Ruthenium Oxides Evaluated by Electrochemical Impedance Spectroscopy: The Origin of Large Capacitance", Journal of Physical Chemistry B 109 (2005) 7330-7338.

[75] J.P. Zheng, P.J. Cygan, T.R. Jow, "Hydrous Ruthenium Oxide as an Electrode Material for Electrochemical Capacitors", Journal of the Electrochemical Society 142 (1995) 2699.

[76] V. D. Patake, S. M. Pawar, V. R. Shinde, T. P. Gujar, and C. D. Lokhande, " The growth mechanism and supercapacitor study of anodically deposited amorphous ruthenium oxide films," Current Applied Physics 10 (2010) 99-103.

[77] Y. Wang, A. Yuan, and X. Wang, "Pseudocapacitive behaviors of nanostructured manganese dioxide/carbon nanotubes composite electrodes in mild aqueous electrolytes: effects of electrolytes and current collectors," Journal of Solid State Electrochemistry 12 (2008) 1101-1107.

[78] M. Selvakumar, D. Krishna Bhat, A. Manish Aggarwal, S. Prahladh Iyer, and G. Sravani, "Nano ZnO-activated carbon composite electrodes for supercapacitors," Physica B: Condensed Matter 405 (2010) 2286-2289.

[79] S. W. Zhang and G. Z. Chen, "Manganese oxide based materials for supercapacitors," Energy Materials: Materials Science and Engineering for Energy Systems 3 (2008) 186-200.

[80] Y. Zhang, H. Feng, X. Wu, L. Wang,, "Manganese oxide–carbon composite as supercapacitor electrode materials," Microporous and Mesoporous Materials 123 (2009) 260-267.

[81] M.S.Wu, C.Y.Huang, K.H.Lin, "Electrophoretic deposition of nickel oxide electrode for high-rate electrochemical capacitor", Journal of Power Sources 186 (2009) 557-564.

[82] C.H.Liang, C.S.Hwang, "Effects of temperatures and cations of electrolyte on the capacitive characteristics of the manganese oxide deposited by hydrothermal electrochemical method", Journal of Alloys and Compounds 500 (2010)102–107.

[83] J.H.Jang, S.J.han, T.H.Hyeon, S.M.Oh, "Electrochemical capacitor performance of hydrous ruthenium oxide/mesoporous carbon composite electrodes", Journal of Power Sources 123 (2003) 79-85.

[84] A.I.Inamdar, Y.S.Kim, S.M.Pawar, J.H.Kim, H.Im, H.Kim, "Chemically grown, porous, nickel oxide thin film for electrochemical supercapacitors", Journal of Power Sources 196 (2011) 2393-2397.

[85] T. Brousse, M. Toupin, R. Dugas, L. Athouel, O. Crosnier and D. Belanger, "Crystalline MnO_2 as Possible Alternatives to Amorphous Compounds in Electrochemical Supercapacitors", Journal of the Electrochemical Society 153 (2006)2171–2180.

[86] W.F.Wei, X.W.Cui, W.X.Chen and D.G.Ivey, "Manganese oxide-based materials as electrochemical supercapacitor electrodes", Chem. Soc. Rev 40 (2011) 1697–1721.

[87] O. Ghodbane, J. L. Pascal and F. Favier, "Microstructural Effects on Charge-Storage Properties in MnO_2-Based Electrochemical Supercapacitors", Applied Materials & Interfaces 1 (2009)1130–1139.

[88] X.Wu, W.Xing, L.Zhang, S.Zhuo, J.Zhou, G.Wang, S.Qiao, "Nickel nanoparticles prepared by hydrazine reduction and their application in supercapacitor", Powder Technology 224 (2012) 162-167.

[89] Z.A. Hu, Y.L. Xie, Y.X. Wang, L.P. Mo, Y.Y. Yang, and Z.Y. Zhang, "Polyaniline/SnO_2 nanocomposite for supercapacitor applications," Materials Chemistry and Physics 114 (2009) 990-995.

[90] R.Liu, S.Choo and S.B.Lee, "Poly (3, 4-ethylenedioxythiophene) nanotubes as electrode materials for a high-powered supercapacitor," Nanotechnology 19 (2008).

[91] J. Huang, H. Wu, D. Cao, and G. Wang, "Influence of Ag doped CuO Nanosheet Arrays on Electrochemical Behaviours for Supercapacitors," Electrochimica Acta 75 (2012) 208-212.

[92] B.A. Bolto, R. McNeill, D.E. Weiss, "Electronic Conduction in Polymers", Austrian Journal of Chemistry 16 (1963)1090-1103.

[93] L. L. Zhang, T. Wei, W. Wang, and X. S. Zhao, "Manganese oxide–carbon composite as supercapacitor electrode materials," Microporous and Mesoporous Materials 123 (2009) 260-267.

[94] G.A.Snook, P.Kao, A.S.Best, "Review: Conducting-polymer-based supercapacitor devices and electrodes", Journal of Power Source 196 (2011) 1-12.

[95] Y.X.Huang, S.L.Candelaria, Y.W.Li, Z.Mi.Li, J.J.Tian, L.L.Zhang, G.Z.Cao, "Sulfurized activtaed carbon for high energy density supercapacitors," Journal of Power Sources 252 (2014) 90-97.

[96] E.E.Kalu, T.T.Nwoga, V.Srinvasan, J.W.Weidner, "Cyclic voltammetric studies of the effects of time and temperature on the capacitance of electrochemically deposited nickel hydroxide", Journal of Power Sources 92 (2001) 163-167.

[97] J. Zhang, D. Shu, T. Zhang, H. Chen, H. Zhao, Y. Wang, Z. Sun, S. Tang, X. Fang, and X. Cao, "Capacitive properties of PANI/MnO_2 synthesized via simultaneous-oxidation route," Journal of Alloys and Compounds 532 (2012) 1-9.

[98] M.Lee, S.K.Balasingam, H.Y.Jeong , W.G. Hong , H.B.R.Lee , B.H.Kim and Y.S.Jun, “One-step hydrothermal synthesis of graphene decorated V_2O_5 nanobelts for enhanced electrochemical energy storage,” Scientific Report 5 (2015) 8151.

[99] Y.H.Jin, M.Q.Jia, “Design and synthesis of nanostructured graphene-SnO_2-polyanilineternary composite and their excellent supercapacitor performance,” Colloids and Surfaces A: Physicochem. Eng. Aspects 464 (2015) 17–25.

[100] S.Giri , D.Ghosh and C.K.Das , “Growth of Vertically Aligned Tunable Polyaniline on Graphene/ZrO_2 Nanocomposites for Supercapacitor Energy-Storage Application,” Adv. Funct. Mater.24 (2014)1312–1324.

[101] J. Chen, K. Huang, and S. Liu, "Hydrothermal preparation of octadecahedron Fe_3O_4 thin film for use in an electrochemical supercapacitor," Electrochimica Acta 55 (2009) 1-5.

[102] A.Mansour, M.Sassin, K.Pettigrew, D.Rolison, J.Long, "Electroless Deposition of Conformal Nanoscale Iron Oxide on Carbon Nanoarchitectures for Electrochemical Charge Storage," ACS Nano 4 (2010) 4505-4514.

[103] T. Brousse and D. Bélanger, "A Hybrid Fe_3O_4-MnO_2 Capacitor in Mild Aqueous Electrolyte," Electrochemical and Solid-State Letters 6 (2003) A244.

[104] X.Zhao, C.Johnston, P.S.Grant, "A novel hybrid supercapacitor with a carbon nanotube cathode and an iron oxide/carbon nanotube composite anode", Journal of Materials Chemistry 19 (2009)8755-8760.

[105] K.W.Chung, K.B.Kim, S.H.Han, H.Lee, "Novel synthesis and electrochemical characterization of nano-sized cellular Fe_3O_4 thin film", Electrochemical and Solid State Letters 8 (2005) 259-262.

[106] N.Nagarajan and I.Zhitomirsky, "Cathodic electrosynthesis of iron oxide films for electrochemical supercapacitors", Journal of Applied Electrochemistry 36 (2006)1399–1405.

[107] H.Talbi, P.E. Just, L.H. Dao, "Electropolymerization of aniline on carbonized polyacrylonitrile aerogel electrodes: applications for supercapacitors", Journal of Applied Electrochemistry 33 (2003) 465-473.

[108] S.R. Sivakkumar, D.W. Kim, "Polyaniline/Carbon Nanotube Composite Cathode for Rechargeable Lithium Polymer Batteries Assembled with Gel Polymer Electrolyte", Journal of the Electrochemical Society 154 (2007) A134.

[109] K.S. Ryu, K.M.Kim, Y.J.Park, N.G.Park, M.G.Kang, S.H.Chang, "Redox supercapacitor using polyaniline doped with Li salt as electrode", Solid State Ionics 152–153 (2002) 861–866.

[110] K.S. Ryu, K.M.Kim, Y.J.Park, N.G.Park, M.G.Kang, S.H.Chang, "Symmetric redox supercapacitor with conducting polyaniline electrodes ", Journal of Power Source 103 (2001)305-309.

[111] K.Lota, V.Khomenko, E.Frackowiak, "Capacitance properties of poly(3,4 ethylenedioxythiophene)/carbon nanotubes composites", Journal of Physics and Chemistry of Solids 65 (2004)295–301.

[112] W.K.Li, J.Chen, J.Zhao, R.Zhang and J.Zhu, Materials Letters 59 (2005) 800-803.

[113] Y. Hou, Y. Cheng, T. Hobson, and J. Liu, "Design and synthesis of hierarchical MnO_2 nanospheres/carbon nanotubes/conducting polymer ternary composite for high performance electrochemical electrodes," Nano Letters 10 (2010) 2727-2733.

[114] Y. Wang, H. Liu, X. Sun, and I. Zhitomirsky, "Manganese dioxide–carbon nanotube nanocomposites for electrodes of electrochemical supercapacitors," Scripta Materialia 61 (2009) 1079-1082.

[115] M.T.Lee, J.K.Chang, W.T.Tsai, "Effects of iron addition on material characteristics and pseudo-capacitive behaviour of Mn-oxide electrodes", Journal of The Electrochemical Society 154 (2007) A875-A881.

[116] J. Y. Lee, K. Liang, K. H. An, and Y. H. Lee, "Nickel oxide/carbon nanotubes nanocomposite for electrochemical capacitance," Synthetic Metals 150 (2005) 153-157.

[117] H. Kim and B. N. Popov, "Synthesis and Characterization of MnO_2-Based Mixed Oxides as Supercapacitors," Journal of The Electrochemical Society 150 (2003) D56 .

[118] X. M. Liu and X. G. Zhang, "NiO-based composite electrode with RuO_2 for electrochemical capacitors," Electrochimica Acta 49 (2004) 229-232.

[119] J.Chen, C.Y.Jia, Z.Q.Wan, “Novel hybrid nanocomposite based on poly(3,4-ethylenedioxythiophene)/multiwalled carbon nanotubes/graphene as electrode material for supercapacitor,” Synthetic Metals 189 (2014) 69–76.

[120] N.L.Wu, "Nanocrystalline oxide Supercapacitors," Materials Chemistry and Physics 75 (2002) 6-11.

[121] S.J.Park, Y.H.Kim, "Roles of Nanosized Fe_3O_4 on Supercacitive Properties of Carbon Nanotubes," Current Applied Physics 11 (2011) 462-466.

[122] S.C. Pang, W.H.Khoh, S.F.Chin, "Synthesis and Characterization of Magnetite/Carbon Nanocomposite Thin Films for Electrochemical Applications", Journal. Material Science Technology 27 (2011) 873-878.

[123] D. Kalpana, K. S. Omkumar, S. S. Kumar, and N. G. Renganathan, "A novel high power symmetric ZnO/carbon aerogel composite electrode for electrochemical supercapacitor," Electrochimica Acta 52 (2006) 1309-1315.

[124] M. P. M.Jayalakshmi, K.Balasubramanian, "Single Step Solution Combustion Synthesis of ZnO/Carbon Composite and its Electrochemical Characterisation for Supercapacitor Application," International Journal of Electrochemical Science 3 (2008) 96-103.

[125] Y. Zhang, X. Sun, L. Pan, H. Li, Z. Sun, C. Sun, and B. K. Tay, "Carbon nanotube–zinc oxide electrodes for electrochemical supercapacitors," Solid State Ionics 180 (2009) 1525-1528.

[126] Z.A. Hu, Y.L. Xie, Y.X. Wang, L.P. Mo, Y.Y. Yang, Z.Y. Zhang, "Polyaniline/SnO_2 nanocomposite for supercapacitor applications," Materials Chemistry and Physics 114 (2-3) (2009) 990-995.

[127] C.J.Lin, Y.H.Yu, Y.H.Liou, "Free-standing TiO_2 nanotube array films sensitized with Cds as highly active solar light-driven photocatalysts", Applied Catalysis B: Environmental 93 (2009)119-125.

[128] H.Wang, Z.Y.Tang, L.Sun, Y.B.He, Y.X.Wu, Z.Y.Li, "Capacitance performance enhancement of TiO_2 doped with Ni and graphite", Rare Metals 28 (2009) 231-236.

[129] F.Yao, Y.Z.Shen, Y.Y.Liang, H.L.Li, "Synthesis and characterization of $Co(OH)_2/TiO_2$ nanotube composites as supercapacitor materials." Journal of Solid State Electrochem 11 (2007)853-858.

[130] J.Shibata, K.Fujii, N.Murayama and H.Yamamoto, "Dispersion and Flocculation Behavior of Fine Metal Oxide Particles in Various Solvents", KONA 20 (2002)263-269.

[131] Y.R.Ahn, C.R.Park, S.M.Jo, D.Y.Kim, "Enhanced charge-discharge characteristics of RuO_2 supercapacitors on heat-treated TiO_2 nanorods." Applied Physics Letter 90 (2007)122106.

[132] Y.B.Xie, D.G.Fu, "Supercapacitance of ruthenium oxide deposited on titania and titanium substrates." Materials Chemistry and Physics 122 (2010)23-29.

[133] C.D.Lokhande, B.O.Park, H.S.Park, K.D.Jung, O.S.Joo, "Electrodeposition of TiO_2 and RuO_2 thin films for morphology-dependent applications." Ultrmicroscopy 105 (2005).

[134] Y.G.Wang et al, "An asymmetric supercapacitor using RuO_2/TiO_2 nanotube composite and activated carbon electrodes." Electrochimica Acta, vol.50, pp.5641-5646, 2005.

[135] M.K.Seo, S.J.Park, "Effect of nanosized titanium oxide on electrochemical characteristics of activated carbon electrodes." Current Applied Physics 10 (2009)391-394.

[136] M.Selvakumar, D.Krishna Bhat, "Microwave synthesized nanostructured TiO_2-activated carbon composite electrodes for supercapacitor, Applier Surface Science 263 (2012) 236-241.

[137] G. He, J. Li, H. Chen, J. Shi, X. Sun, S. Chen, X. Wang, "Hydrothermal preparation of Co_3O_4/graphene nanocomposite for supercapacitor with enhanced capacitive performance," Materials Letters 82 (2012) 61-63.

[138] L.Yang, S.Cheng, Y.Ding, X.B.Zhu, Z.LWang, M.L.Liu, "Hierarchical Network Architectures of Carbon Fiber Paper Supported Cobalt Oxide Nanonet for High-Capacity Pseudocapacitors," Nano Letter 12(2012) 321-325.

[139] C.Zhou, Y.W.Zhang, Y.Y.Li, J.P.Liu, "Construction of High-Capatance 3D CoO@ Polypyrrole Nanowire Array Electrode for Aqueous Asymmetric Supercapacitor," Nano Letters 13 (2013) 2078-2085.

[140] D.W. Kim, K.Y. Rhee, S.J. Park, "Synthesis of activated carbon nanotube/copper oxide composites and their electrochemical performance," Journal of Alloys and Compounds 530 (2012) 6-10.

[141] J.L.Kang, A.Hirata, H.J.Qiu, L.Y.Chen, X.B.Ge, T.Fujita, M.W.Chen, "Self-Grown Oxy-Hydroxide @ Nanoporous Metal Electrode for High-Performance Supercapacitors," Nano Letters 26 (2014) 269-272.

[142] W.Sugimoto, T. Ohunma, Y. Murakami, Y. Takasu, "Molybdenum Oxide/Carbon Composite Electrodes as Electrochemical Supercapacitors," Electrochemical and Solid-State Letters 4 (2001) A145-A147.

[143] L.S. Aravinda, K.K. Nagaraja, K.U. Bhat, B.R. Bhat, "Magnetron sputtered MoO_3/carbon nanotube composite electrodes for electrochemical supercapacitor," Journal of Electroanalytical Chemistry 699 (2013) 28-32.

[144] G. Lota, E. Frackowiak, J. Mittal, M. Monthioux, "High performance supercapacitor from chromium oxide-nanotubes based electrodes," Chemical Physics Letters 434 (1-3) (2007) 73-77.

[145] M.D. Stoller, R.S. Ruoff, "Best practice methods for determining an electrode material's performance for ultracapacitors," Energy & Environmental Science 3 (9) (2010) 1294.

[146] W. Zhang, Y.H. Qu, L.J. Gao, "Performance of PbO_2/activated carbon hybrid supercapacitor with carbon foam substrate," Chinese Chemical Letters 23 (5) (2012) 623-626.

[147] Y.Y.Tian, S.Cong, W.M.Su, H.Y.Chen, Q.W.Li, F.X.Geng, Z.G.Zhao, "Synergy of $W_{18}O_{49}$ and Polyaniline for Smart Supercapacitor Electrode Integrated with Energy Level Indicating Functionality," Nano Letters (2014) Article ASAP.

[148] M. Jayalakshmi, M.M. Rao, N. Venugopal, K.-B. Kim, "Hydrothermal synthesis of SnO_2–V_2O_5 mixed oxide and electrochemical screening of carbon nano-tubes (CNT), V_2O_5, V_2O_5–CNT, and SnO_2–V_2O_5–CNT electrodes for supercapacitor applications," Journal of Power Sources 166 (2) (2007) 578-583.

[149] C.C. Hu, C.C. Wang, K.H. Chang, "A comparison study of the capacitive behavior for sol–gel-derived and co-annealed ruthenium–tin oxide composites," Electrochimica Acta 52 (7) (2007) 2691-2700.

[150] Y. Yan, Q. Cheng, V. Pavlinek, P. Saha, C. Li, "Fabrication of polyaniline/mesoporous carbon/MnO_2 ternary nanocomposites and their enhanced

electrochemical performance for supercapacitors," Electrochimica Acta 71 (2012) 27-32.

[151] Y. Hou, Y. Cheng, T. Hobson, J. Liu, "Design and synthesis of hierarchical MnO_2 nanospheres/carbon nanotubes/conducting polymer ternary composite for high performance electrochemical electrodes," Nano letters 10 (7) (2010) 2727-2733.

[152] Y.W.Cheng, S.T.Lu, H.B.Zhang, C.V.Varanasi, J.Liu, "Synergisitc Effects from Graphene and Carbon Nanotube Enable Flexible and Robust Electrodes for High-Performance Supercapacitors," Nano Letters 12 (2012) 4206-4211.

[153] H. Su, T. Wang, S. Zhang, J. Song, C. Mao, H. Niu, B. Jin, J. Wu, Y. Tian, "Facile synthesis of polyaniline/TiO_2/graphene oxide composite for high performance supercapacitors," Solid State Sciences 14 (6) (2012) 677-681.

[154] D. Antiohos, G. Folkes, P. Sherrell, S. Ashraf, G.G. Wallace, P. Aitchison, A.T. Harris, J. Chen, A.I. Minett, "Compositional effects of PEDOT-PSS/single walled carbon nanotube films on supercapacitor device performance," Journal of Materials Chemistry 21 (40) (2011) 15987.

[155] L.M. Huang, T.C. Wen, A. Gopalan, "Electrochemical and spectroelectrochemical monitoring of supercapacitance and electrochromic properties of hydrous ruthenium oxide embedded poly(3,4-ethylenedioxythiophene)–poly(styrene sulfonic acid) composite," Electrochimica Acta 51 (17) (2006) 3469-3476.

[156] G.Q.Zhang, X.W.Lau, "General Solution Growth of MEsoporous $NiCo_2O_4$ Nanosheets on Various Conductive Substrates as High-Performance Electrodes for Supercapacitors," Advanced Materials 25 (2013) 976-979.

[157] L.H.Bao, J.F.Zang, X.D.Li, "Flexible Zn_2SnO_4/MnO_2 Core/Sheel Nanocable-Carbon Microfiber Hybrid Composites for High-Performance Supercapacitor Electrodes," Nano Letters 11 (2011) 1215-1220.

[158] X.Z.Yu, B.G.Lu and Z.Xu, "Super Long-Life Supercapacitors Based on the Construction of Nanohoneycomb-Like Strongly Coupled $CoMoO_4$ –3D Graphene Hybrid Electrodes," Adv. Mater. 26 (2014) 1044–1051.

[159] Y.Y.Wei, S.Q.Chen, D.W.Su, B.Sun, J.G.Zhu and G.X.Wang, "3D mesoporous hybrid $NiCo_2O_4$/graphene nanoarchitectures as electrode materials for supercapacitors with enhanced performances," J. Mater. Chem. A 2 (2014), 8103–8109.

[160] Z.S.Wu, D.W.Wang, W.Ren, J.Zhao, G.Zhou, F.Li, H.M.Cheng, "Anchoring Hydrous RuO_2 on Graphene Sheets for High-Performance Electrochemical Capacitors," Adv. Funct. Mater 20 (2010) 3595-3602.

[161] X.M. Liu, X.G. Zhang, "NiO-based composite electrode with RuO_2 for electrochemical capacitors," Electrochimica Acta 49 (2) (2004) 229-232.

[162] C.C. Hu, W.C. Chen, "Effects of substrates on the capacitive performance of $RuO_x \cdot nH_2O$ and activated carbon–RuO_x electrodes for supercapacitors," Electrochimica Acta 49 (21) (2004) 3469-3477.

[163] H. Kim, B.N. Popov, "Characterization of hydrous ruthenium oxide/carbon nanocomposite supercapacitors prepared by a colloidal method," Journal of Power Sources 104 (2002) 52-61.

[164] O.O. Park, J.H. Park, "Morphology and Electrochemical Behaviour of Ruthenium Oxide Thin Film Deposited on Carbon Paper," Journal of Power Sources 109 (2002) 121-126.

[165] S.L.Kuo, N.L.Wu, "Composite Supercapacitor Containing Tin Oxide and Electroplated Ruthenium Oxide," Electrochemical and Solid-State Letters 6 (5) (2003) A85.

[166] M. Jayalakshmi, N. Venugopal, K.P. Raja, M.M. Rao, "Nano SnO_2–Al_2O_3 mixed oxide and SnO_2–Al_2O_3–carbon composite oxides as new and novel electrodes for supercapacitor applications," Journal of Power Sources 158 (2) (2006) 1538-1543.

[167] G.H.Yuan, Z.H.Jiang, A. Aramata, Y.Z.Gao, "Electrochemical behavior of activated-carbon capacitor material loaded with nickel oxide," Carbon 43 (14) (2005) 2913-2917.

[168] J.Y. Lee, K. Liang, K.H. An, Y.H. Lee, "Nickel oxide/carbon nanotubes nanocomposite for electrochemical capacitance," Synthetic Metals 150 (2) (2005) 153-157.

[169] Y.Haldorai, W.Voit, J.J.Shim, "Nano ZnO/reduced graphene oxide composite for high performancesupercapacitor: Green synthesis in supercritical fluid," Electrochimica Acta 120 (2014) 65–72.

[170] L.L. Zhang, T. Wei, W. Wang, X.S. Zhao, "Manganese oxide–carbon composite as supercapacitor electrode materials," Microporous and Mesoporous Materials 123 (1-3) (2009) 260-267.

[171] S.J. Park, Y.H. Kim, "Roles of Nanosized Fe_3O_4 on Supercacitive Properties of Carbon Nanotubes," Current Applied Physics 11 (2011) 462-466.

[172] J.G.Wang, Y.Yang, Z.H.Huang, F.Kang, "Interfacial synthesis of mesoporous MnO_2/polyaniline hollow spheres and their application in electrochemical capacitors," Journal of Power Sources 204 (2012) 236-243.

[173] Q.Li, Z.L.Wang, G.R.Li, R.Guo, L.X.Ding, Y.X.Tong, "Design and Synthesis of MnO_2/Mn/MnO_2 Sandwich-Structured Nanotube Arrays with High Supercapacitive Performance for Electrochemical Energy Storage," Nano Letters 12 (2012) 3803-3807.

[174] X.F.Xia, Q.L.Hao, W.Lei, W.J.Wang, H.L.Wang and X.Wang, "Reduced-graphene oxide/molybdenum oxide/polyaniline ternary composite for high energy density supercapacitors: Synthesis and properties," J. Mater. Chem.22 (2012) 8314–8320.

[175] A.Ramadoss, S.J.Kim, "Facile preparation and electrochemical characterization of graphene/ZnO nanocomposite for supercapacitor applications," Materials Chemistry and Physics 140 (2013) 405-411.

[176] H. D. Liu, J. L. Zhang, D. D. Xu, L. H. Huang, S. Z. Tan, W. J. Mai, "Easy one-step hydrothermal synthesis of nitrogen-doped reduced graphene oxide/iron oxide hybrid as efficient supercapacitor material," J Solid State Electrochem 19 (2015) 135–144.

[177] F.Yu, Y.Liu, Y.J.Zhu, F.Dai, L.Zhang, Z.B.Wen, "Polypyrrole@MoO_3/reductive graphite oxide nanocomposites as anode material for aqueous supercapacitors with high performance," Materials Letters 171 (2016), 104-107.

[178] K. Naoi, Y. Nagano, "Li-ion Hybrid Supercapacitors in Organic Medium," Wiley-VCH, Germany, 2013.

[179] A.S.Arico, P.Bruce, B. Scrosati, J.M.Tarascon, W.V. Schalkwij, "Nanostructure materials for advanced energy conversion and storage devices," Nature Materials 4 (2005) 366-377.

[180] G.G.Amatucci, F. Badway, A.D. Pasquier, T. Zheng, "An Asymmetric Hybrid Nonaqueous Energy Storage Cell," Journal of Eletrochemical Society 148 (2001) A930-A939.

[181] K. Naoi, P. Simon, "New Materials and New Configurations for Advanced Electrochemical Capacitors," Journal of The Electrochemical Society 17 (2008) 34-37.

[182] A.D. Pasquier, I. Plitz, J. Gural, S. Menocal, G.G. Amatucci, "Characteristic and performance of 500 F asymmetric hybrid advanced supercapacitor prototypes," Journal of Power Sources 113 (2003) 62-71.

[183] K. Naoi, W. Naoi, S. Aoyagi, J.I.Miyamoto, T. Kamino, "New Generation Nanohybrid Supercaapcitor," Accounts of Chemical Research 46 (2011) 1075-1083.

[184] H.G.Jung, N.Venugopal, B. Scrosati, Y.K.Sun, "A high energy and power density hybrid supercapacitor based on an advanced carbon-coated $Li_4Ti_5O_{12}$ electrode," Journal of Power Sources 221 (2013) 266-271.

[185] V. Aravindan, W. Chuiling, S. Madhavi, "High power lithium-ion hybrid electrochemical capacitors using spinel $LiCrTiO_4$ as insertion electrode," Journal of Materials Chemistry 22 (2012) 16026.

[186] N. Böckenfeld, R.S. Kühnel, S. Passerini, M. Winter, A. Balducci, "Composite $LiFePO_4$/AC high rate performance electrodes for Li-ion capacitors," Journal of Power Sources 196 (2011) 4136-4142.

[187] K. Karthikeyan, V. Aravindan, S.B. Lee, I.C. Jang, H.H. Lim, G.J. Park, M. Yoshio, Y.S. Lee, "A novel asymmetric hybrid supercapacitor based on Li_2FeSiO_4 and activated carbon electrodes," Journal of Alloys and Compounds 504 (2010) 224-227.

[188] K. Karthikeyan, V. Aravindan, S.B. Lee, I.C. Jang, H.H. Lim, G.J. Park, M. Yoshio, Y.S. Lee, "Electrochemical performance of carbon-coated lithium manganese silicate for asymmetric hybrid supercapacitors," Journal of Power Sources 195 (2010) 3761-3764.

[189] Y.G.Wang, Y.Y.Xia, "A new concept hybrid electrochemical surpercapacitor: Carbon/$LiMn_2O_4$ aqueous system," Electrochemistry Communications 7 (11) (2005) 1138-1142.

[190] K.X.Tang, Y.P.Li, H.B.Cao, F.Duan, J.Zhang, Y.Zhang and Y.Wang, "Integrated electrospun carbon nanofibers with vanadium and single-walled carbon nanotubes through covalent bonds for high-performance supercapacitors," RSC Adv. 5 (2015) 40163–40172.

[191] S.R. Sivakkumar, A.G. Pandolfo, "Evaluation of lithium-ion capacitors assembled with pre-lithiated graphite anode and activated carbon cathode," Electrochimica Acta 65 (2012) 280-287.

[192] H.L.Li, Y.He, V.Pavlinek, Q.L.Cheng, P.Sahab and C.Z.Li, "MnO_2 nanoflake/polyaniline nanorod hybrid nanostructures on graphene paper for high performance flexible supercapacitor electrodes," J. Mater. Chem. A. 3 (2015) 17165-17171.

[193] W.K. Chee , H.N. Lim, I. Harrison, K.F. Chong , Z. Zainal, C.H. Ng, N.M. Huang, "Performance of Flexible and Binderless Polypyrrole/Graphene Oxide/ Zinc Oxide Supercapacitor Electrode in a Symmetrical Two-Electrode Configuration," Electrochimica Acta 157 (2015) 88–94.

[194] A. Davies, A. Yu, "Material advancements in supercapacitors: From activated carbon to carbon nanotube and graphene," The Canadian Journal of Chemical Engineering 89 (6) (2011) 1342-1357.

[195] P. Simon, Y. Gogotsi, "Materials for electrochemical capacitors," Nature Materials 7 (2008) 845-854.

[196] P.J. Hall, M. Mirzaeian, S.I. Fletcher, F.B. Sillars, A.J.R. Rennie, G.O. Shitta-Bey, G. Wilson, A. Cruden, R. Carter, "Energy storage in electrochemical capacitors: designing functional materials to improve performance," Energy & Environmental Science 3 (2010) 1238.

[197] G. Wang, L. Zhang, J. Zhang, "A review of electrode materials for electrochemical supercapacitors," Chemical Society reviews 41(2012) 797-828.

CHAPTER 3
Experimental Techniques

3.1 Reagents and apparatus

The chemicals and reagents used in this thesis are listed in Table 3.1. They were used as it is and without any further purification.

Table 3.1. Chemical/reagents used for the preparation of various electrode materials.

Chemical/ Material	Characteristic/Grade	Supplier
Iron oxide	Particle size < 50 nm	Sigma Aldrich
Titanium oxide	Particle size < 100 nm	Sigma Aldrich
Zinc oxide	Particle size < 100 nm	Sigma Aldrich
Lithium iron phosphate	Particle size < 5 µm	RHE RESOURCES
Activated carbon	BET surface ~ 900 m^2/g	Sigma Aldrich
Activated carbon	BET surface ~ 1800 m^2/g	RHE RESOURCES
Graphite	99% carbon purity	Bay Carbon
Tin chloride	98%	Sigma Aldrich
Ammonium molybdate tetrahydrate	99%	R & M Chemicals
Ketjenblack	Surface area ~ 1400 m^2/g	Akzo Nobel
Isopropanol	>99.8%	Merck
Ethanol	>99.5%	Merck
Poly(tetrafluoroethylene)	60% dispersion in water	Sigma Aldrich
Poly(vinylidene fluride)	Aqueous-based	Kynar
N-methyl-2-pyrrolidone	>99.7 %	Merck
Na_2SO_3	>99 %	Merck
Na_2SO_4	>99%	Merck
D-(+)-Glucose	ACS reagent	R & M Chemicals
Ethylene glycol	>99.8 %	Sigma Aldrich

The general equipment used for materials preparation and electrochemical measurement is given in Table 3.2.

Table 3.2: General apparatus used for the preparation of electrode materials.

Apparatus	Model / Specification	Manufacturer
Hot Plate & Magnetic stirrer	KMC-130SH	Vision Scientific
Overhead stirrer	Digital model	JEIO TECH
Autoclave	Stainless steel lined with Teflon	Self-made
Oven	OV-11/12	JEIO TECH
Analytical Balance	GR200 (10 mg-210 g)	A&D Company
Furnace	Type-300	Carbolite
Ultrasonicator	WUC-A03H	Wiseclean
Centrifuge	2420	KUBOTA

3.2 Preparation of metal oxide-based materials

3.2.1 Preparation of metal-oxide/activated carbon composite electrodes

A series of transition metal oxides (Fe_3O_4, TiO_2 and ZnO), phosphate-based materials ($LiFePO_4$) and activated carbon (AC) composites were synthesized by doping different amount of metal oxide or phosphate onto AC via simple and facile mechanical mixing (Table 3.3). The electrochemical properties of two different AC materials were evaluated, namely AC_LSA (Sigma Aldrich, BET surface ~ 900 m^2/g) and AC_HSA (RHE Resources, BET surface ~ 1800 m^2/g). In a typical preparation procedure, the composite materials were mixed with carbon black powder and organic binder polytetrafluoroethylene (PTFE) in the weight ratio of 80:15:5 using overhead stirrer. The mixture was dissolved into a 1:1 mixed solution of distilled water and isopropanol. 15 wt% carbon black was added to increase the electrode conductivity of composite electrodes. The mixtures in dough form were then cold rolled into 0.8 mm thick films. Electrodes were punched into coin-shaped electrodes of 1 cm^2 and were dried in a vacuum oven at 80℃ for 45 mins to ensure the isopropanol solvent was evaporated completely. The dried electrodes were

then sandwiched with a porous separator in the middle, forming an electrode separator assembly (ESA). The assembly was then impregnated overnight with 1 M Na_2SO_3, 1 M Na_2SO_4 and 1 M $LiSO_4$ respectively. This electrolyte-impregnated ESA was then assembled into the two-electrode test cell for electrochemical measurements.

Table 3.3. Different mass percentage of materials in the various metal oxide-activated carbon electrodes.

Electrode Material	Fe_3O_4 (wt %)	ZnO (wt %)	TiO_2 (wt %)	$LiFePO_4$ (wt %)	Activated carbon (wt %)	Carbon black (wt %)	PTFE (wt %)
AC	0	-	-	-	80	15	5
4Fe-AC	4	-	-	-	76	15	5
20Fe-AC	20	-	-	-	60	15	5
40Fe-AC	40	-	-	-	40	15	5
60Fe-AC	60	-	-	-	20	15	5
Fe_3O_4	80	-	-	-	0	15	5
4ZnO-AC	-	4	-	-	76	15	5
20ZnO-AC	-	20	-	-	60	15	5
40ZnO-AC	-	40	-	-	40	15	5
60ZnO-AC	-	60	-	-	20	15	5
ZnO	-	80	-	-	0	15	5
4TiO-AC	-	-	4	-	76	15	5
20TiO-AC	-	-	20	-	0	15	5
40TiO-AC	-	-	40	-	80	15	5
60TiO-AC	-	-	60	-	76	15	5
TiO_2	-	-	80	-	60	15	5
4LFP-AC	-	-	-	4	76	15	5
20LFP-AC	-	-	-	20	60	15	5
40LFP-AC	-	-	-	40	40	15	5
60LFP-AC	-	-	-	60	20	15	5
LFP	-	-	-	80	0	15	5

3.2.2 Synthesis of graphene

Graphene was synthesized via liquid phase exfoliation method as reported in [1]. Typically, 100 mg graphite flakes was dispersed in 200 ml solution of ethanol and deionized water (2:3 ratio). Sonication treatment was carried out in a conventional ultrasonic bath with working frequency of 50/60 Hz at room temperature for 3 hours to form a darkish black suspension. The sonicated dispersions were then centrifuged at 1000 rpm for 30 min to remove unexfoliated graphite flakes. The supernatant was then filtered and dried at 80^oC overnight and graphene was collected.

3.2.3 Preparation of SnO_2-graphene composites

The SnO_2-graphene composite was prepared by a solvothermal method. First, 0.2 g of as-prepared graphene was dispersed in the mixture of ethanol and distilled water (2:3) under sonication for 15 min. Then 2.40 g of tin chloride ($SnCl_2$) and 0.18 g glucose were added to graphene dispersion and were mixed together under sonication treatment for 15 min. The resulting mixture was transferred to a 50 ml Teflon stainless steel autoclave. A total of four samples were prepared at 140 ^oC with different reaction times, namely SnO_2, GS6, GS12 and GS24 (Table 3.2). Finally, the solid precipitation was isolated from the solution by centrifugation, washed repeatedly with excess water and ethanol, respectively and dried overnight at 80 ^oC in an oven. The resulted solid powder was heated in the air at a rate of 10 ^oC/min to 500 ^oC for 4 hours.

3.2.4 Preparation of MoO_3-graphene composites

The MoO_3-graphene composite was prepared by a solvothermal method. First, 0.2 g of as-prepared graphene was dispersed in 20 ml of ethylene glycol under sonication for 15 min while 2.40 g of ammonium molybdate tetrahydrate ($(NH_4)_6Mo_7O_{24}\cdot 4H_2O$) was separately dissolved in 30 ml of ethylene glycol under vigorous stirring. Then, the two solutions were mixed together under sonication treatment for 15 min. The resultant mixture was transferred to a 50 ml Teflon stainless steel autoclave. A total of four samples were prepared at 140 ^oC with different reaction times, namely MoO_3, GM6, GM12 and GM24 (Table 3.2). The solid precipitations were then isolated from the solution by centrifugation, washed repeatedly with excess water and ethanol, and dried overnight at 70 ^oC in an oven. Finally, the products were thermally heated at 500 ^oC with a ramping rate of 10 ^oC/min for 4 hours in the air.

3.2.5 Preparation of electrodes for electrochemical characterization

To evaluate the electrochemical properties of the metal oxide / graphene composites, the electrodes were prepared by mixing the active materials, carbon black and polyvinylidene fluoride (PVDF) with mass ratio of 80:15:5 and dispersed homogeneously in N-methyl-2-

pyrrolidinone (NMP). The resultant mixture was coated on an aluminium foil and dried overnight at 80^{o}C in an oven. The electrochemical cell was assembled by sandwiching two symmetric electrodes separated by a thin porous separator, forming an electrode separator assembly (ESA). The assembly was then impregnated with 1 M Na_2SO_3 for at least one hour. This electrolyte-impregnated ESA was then assembled into the two-electrode test cell. Table 3.4 summarise the series of electrode materials synthesized via solvothermal processes.

Table 3.4. Different solvothermal reaction times for electrode materials.

Name of sample	Electrode materials	Reaction time
SnO_2	Pure SnO_2	12 hours
GS6	SnO_2-graphene composite	6 hours
GS12	SnO_2-graphene composite	12 hours
GS24	SnO_2-graphene composite	24 hours
MoO_3	Pure MoO_3	12 hours
GM6	MoO_3-graphene composite	6 hours
GM12	MoO_3-graphene composite	12 hours
GM24	MoO_3-graphene composite	24 hours

3.3 Characterization techniques

3.3.1 Field Emission Scanning Electronic Microscopy (FESEM)

Field Emission Scanning Electron Microscopy (FESEM) is the most widely used microscopy technique because of its versatility, its various modes of imaging, ease of sample preparation as well as easy interpretation of the images [2]. In order to overcome the limitations of the diffraction limit and wavelength of visible light employed in optical microscopy, FESEM has been developed to improve higher resolution and magnification. FESEM uses a focused beam of accelerated electrons instead of light to magnify images of objects beyond the capability of optical microscopes. Imaging lenses are constructed by using the principles of refraction in optical microscopy, while in electron microscopy, electromagnetic lenses generating a magnetic field by applying current through a coil that changes the trajectory of the electrons. The use of electrons with shorter wavelength in place of light allows much higher resolution because energetic electrons are subjected to lesser deflection [3]. FESEM has a large depth of field due to

the very narrow electron beam, yielding a characteristic three-dimensional appearance that useful for understanding the surface topography, morphology and composition of a sample compared to optical microscopy [2].

Optical microscopy is limited by the wavelength of visible light and can only magnify objects by approximately 2000 times. A magnification of the order of 500,000 is possible in FESEM, which is about 250 times the magnification limit of the best optical microscopes. Unlike optical microscopy, the image magnification in a FESEM is not a function of the power of the objective lens. The condenser and objective lenses available in a FESEM are not to image the sample but to spot the beam to about 0.4 nm to 5 nm in diameter. In FESEM, magnification results from the ratio of the area scanned sample to the viewing size on display device which is controlled by the current and voltage supplied to the electromagnetic lenses [2].

The environment within the column is an extremely important part of in a FESEM. Without sufficient vacuum in the FESEM, the electron beam cannot be generated nor controlled as because electrons will quickly disperse or scatter due to collisions with other molecules. In addition, the presence of oxygen or other molecules will shorten the life of the filament dramatically. Most microscopes operate at 10^{-6} Torr or greater vacuum. The higher the vacuum, the lower the pressure, the fewer are the molecules present and thus the better the microscope will function. Generally, in order to pump from atmospheric pressure down to 10^{-6} Torr, two classes of pumps including a low vacuum pump (atmosphere down to 10^{-3}) and a high vacuum pump (10^{-3} down to 10^{-6} or greater depending on type of pump) are used [4].

In FESEM, a confined electron beam is scanned across the sample. These energetic electrons interact with the atoms that make up the sample, generating signals which contain the information about surface topography, morphology and composition. Two different types of interactions occur inside the irradiated sample. In elastic interactions, no energy is transferred from the electron to the sample. The electron either passes without any interaction or is scattered by the positive potential inside the electron cloud. Backscattered electrons are the beam of electrons that are reflected from the sample by elastic scattering. There are also inelastic interactions in which energy is transferred from the incident electrons to the sample where secondary electrons or phonons, are produced, shooting out inner shell electrons which leads to the emission of X-rays or Auger electrons [5].

Figure 3.1 shows the schematic diagram of a FESEM [7]. A stream of electrons is thermally emitted from an electron gun fitted with a tungsten filament cathode in a FESEM and accelerated towards the specimen using a positive electrical potential. The electron beam which typically has an energy ranging from 0.5 keV to 40 keV then travels through a series of condenser lenses, confining the beam onto the sample. The beam passes through pairs of deflector coils in the electron column, which deflect the beam in the X and Y axes resulting in raster scanning [2].

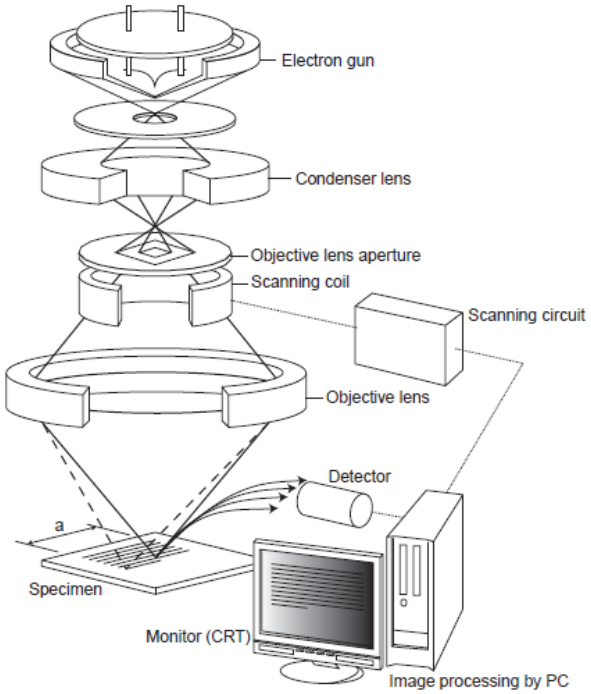


Figure 3.1. Schematic diagram of a FESEM [7].

Once the beam strikes the sample, electrons and photons are ejected as Auger electrons (AE), secondary electrons (SE) and backscattered electrons (BSE) and X-rays. Figure 3.2 shows the regions from which the electrons are scattered within a teardrop-shaped volume of the sample known as the interaction volume, when the incident beam strikes the surface. The interaction volume extends from less than 100 nm to around 5µm into the surface, depending on the energy of incident electron beam as well as the atomic number and density of the sample. Typically, images are formed either from low-energy secondary electrons (SE) by inelastic scattering or

high- energy backscattered electrons (BSE) by elastic scattering. SE allows insight into the morphology of the specimens. The intensity of the BSE signal is strongly related to the atomic number (Z) of the specimen, providing useful information about the distribution of different elements in multiphase samples. Characteristic X-rays are emitted when the electron beam removes an inner shell electron from the sample, causing a higher energy electron to fill the shell and release energy. These characteristic X-rays are used to identify the composition and measure the abundance of elements in the sample [6].

The interaction volume depends on the material as well as the beam energy. At large energies, the beam interacts to a greater extent, while the depth of interaction decreases with a decrease in electron energy till about 100 eV. On the other hands, the depth of interaction increase again at very low energies. The reduced interaction volume at low voltage FESEM makes it possible to measure images without conductive coatings avoid beam-induced damage at surfaces [2].

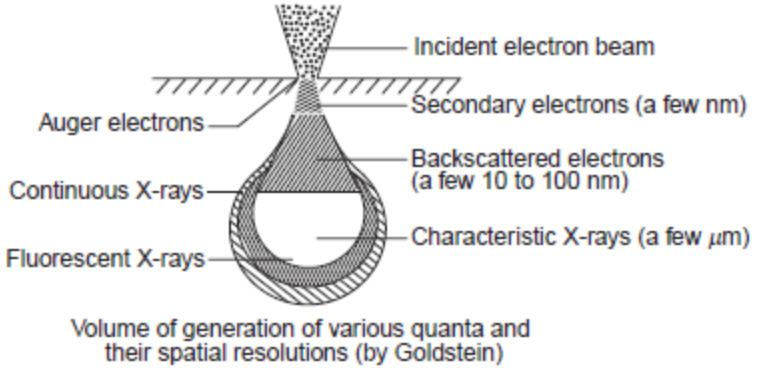


Figure 3.2. The regions from which SE, BSE and X-rays can be detected in FESEM interaction volume [7].

In the present work, an FEI-Quanta 400 FESEM system has been used throughout the study. The powder samples as well as the electrode specimens were placed on black magnetic double sided tape which was cut into small pieces. The pieces with samples on them were then plastered on the microscope sample holder and entered into the vacuum chamber of the FESEM for viewing. The samples were viewed under various magnifications at 20 kV. Low vacuum mode and secondary electron images were used for microstructural observation.

3.3.2 Energy Dispersive X-Ray (EDX)

In conjunction with FESEM analysis, the Energy Dispersive X-Ray Spectroscopy (EDX) also can be used to detect the element present in a selected area of the SEM image and thus provides qualitative and semi-quantitative information on the element. EDX is a chemical microanalysis technique used to characterise the elemental composition of the samples. It is conducted concurrently with the SEM, utilizing an electron gun and imaging equipment to locate the desired sample position. EDX applications include qualitative X-ray mapping, line scan and spot analysis. To perform EDX analysis on a sample, the electron imaging detector is replaced by an x-ray detector system. As previously noted, the electron beam that hits a sample produces a variety of signals including characteristic x-rays. The x-rays are created when the incident electrons cause ejection of an electron in the inner shell. An outer shell electron fills the hole and releases the energy difference as an x-ray [8]. The x-ray energy which is unique for all elements is characteristic of the atomic structure and the difference between the electron shells. The detector collects the x-rays, converting them to voltage before they are sent for processing and analysis to generate an intensity spectrum.

Features or phases as small as 1 μm or less can be analysed. Both qualitative and quantitative analysis can be conducted with the EDX. For the qualitative analysis, the X-ray energy values from the EDX spectrum are compared with known characteristic X-ray energy values to determine the presence of an element in the sample. Elements with atomic numbers ranging from that of beryllium to uranium can be detected. The minimum detection limits vary from approximately 0.1 to a few atomic percent, depending on the element and the sample matrix. Quantitative results can be obtained from the relative X-ray counts at the characteristic energy levels for the sample constituents [9].

3.3.3 Transmission electron microscopy (TEM)

Transmission electron microscopy (TEM) is a microscopy technique whereby a beam of electrons is transmitted through an ultra-thin specimen, interacting with the specimen as it passes through. Similar to SEM, TEM imaging utilizes a highly focused electron beam which requires a very thin specimen to achieve good image quality. This means that sample preparation is extremely important. A sample layer must be thin enough to allow electrons to pass through [10]. An electron gun emits high energy beams that can penetrate several microns into a thin specimen.

An image is formed from the interaction of the electrons transmitted through the specimen, and the image is magnified and focused onto an imaging device.

Before measurement, the sample was dispersed in ethanol and then dripped and dried on a copper grid. In the operation of TEM, an electron beam is focused on a specimen and part of the electron beam is transmitted. This transmitted portion is focused by objective lens into an image and the image is passed down through enlarged lenses and a projection lens, being enlarged all the way. A three- or four-stage condenser system will control the variation of the illuminating aperture and the area of the specimen illuminated [11-12]. TEM is essential for material tomography or examining crystalline defects. However, the combination of ultrahigh voltage beam and high power electron sources makes the technique destructive for many sample types [10].

In electrochemical supercapacitors, TEM is used to collect and examine the microstructures of electrode materials, providing information about pore arrangements [15]. If a specimen is crystalline, the electrons will diffract or scatter off atomic planes inside the material, enabling the resolution of the crystal lattice structure down to atomic scale [20]. In this study, the TEM was used to characterize the internal structure of particles and the TEM images were obtained using a JEOL JEM-2100F transmission electron microscope operated at an acceleration voltage of 200 kV.

3.3.4 X-Ray Diffraction (XRD)

X-ray Diffraction (XRD) is a powerful and non-destructive technique for identifying the crystalline phase present in materials by comparing the diffraction pattern with the standard patterns of the International Powder Diffraction File (PDF) or the International Centre of Diffraction Data (ICDD) database. In addition, it is used to characterise the structural properties including grain size, crystal symmetry, preferred crystal orientation and defect structure. Crystalline materials irradiated by any of these beams give diffraction patterns that can be transformed into the atomic arrangement [13].

X-rays are electromagnetic waves in the wavelength range of 1 Å which is below that of ultraviolet light but above the gamma rays. It can interact with electrons, causing them vibrate. Electrons can be ejected from various energy levels accompanied by the emission of characteristic X-rays. The electron transition from the 2p to the vacant 1s orbital leads to the

emission of K_α radiation. Commonly, the copper K_α radiation at 0.154 nm is used for X-ray analysis. A similar transition is possible from the 3p level resulting in K_β radiation with wavelength of 0.139 nm. $K_{\alpha 1}$ and $K_{\alpha 2}$ correspond to electronic transition from the two possible spin states of the 2p electron [2]. These energetic electrons decelerated by metals will emit electromagnetic radiation which is in phase or coherent with the incident X-rays.

Electron diffraction occurred in XRD can be described as a reflection of X-ray at planes of atoms (Figure 3.3). Crystals consist of many atomic planes, each with different d-spacings. The d-spacing between (hkl) planes intercept the crystallographic a-,b- and c- axes is denoted as

$$d_{hkl} = \frac{a_0}{\sqrt{h^2 + k^2 + l^2}} \qquad \text{Eq. (3.1)}$$

where a_0 is the lattice constant of the crystal. A diffraction peak is observed when there is a constructive interference from X-ray scattered by the atomic planes in a crystal, given by Bragg's law:

$$n\lambda = 2d_{hkl} sin\theta_{hkl} \qquad \text{Eq. (3.2)}$$

where n is the order of reflection, λ_{hkl} and θ_{hkl} are the wavelength and the angle between the atomic planes and the incident X-ray beam respectively [14]. In other words, constructive interference only occurs for certain θ correlating to a (hkl) plane, specifically when the path difference is equal to n wavelengths.

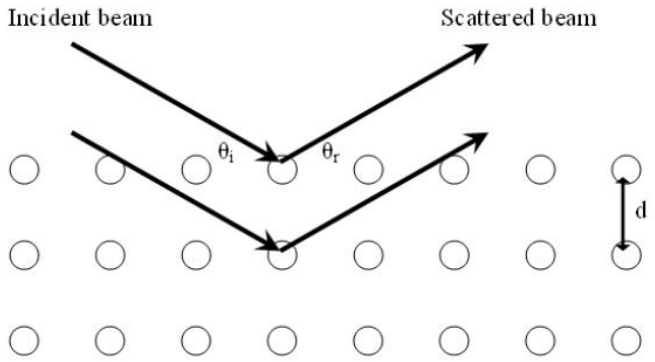


Figure 3.3. Reflection of X-ray at planes of atoms occurred in XRD [13].

Figure 3.4 shows the basic features of XRD experiment where the diffraction angle 2θ is the angle between the incident and diffracted X-rays. In the typical experiment, the diffracted intensity is measured as a function of 2θ and the orientation of the specimen. For diffraction to be observed, the detector must be positioned so the diffraction plane is coplanar with the incident and diffracted X-ray so that the angle between the diffracting plane and the incident X-ray is equal to the Bragg angle [2].

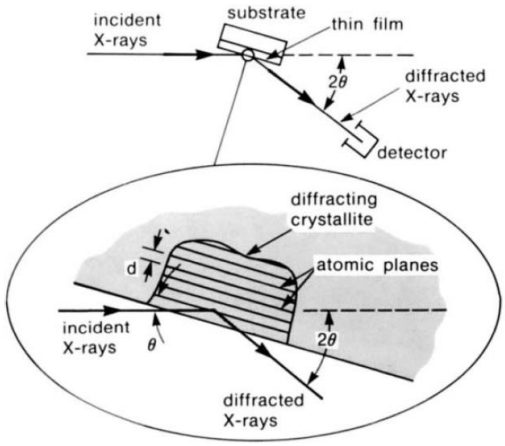


Figure 3.4. Basic features of XRD experiment setup [2].

The intensities are important in determining unknown crystal structures and quantitative phase analysis which are generally taken as peak heights. Preferred orientations can be identified when these peaks are manifested. Defects in the materials will show up as a broadening of diffraction peaks [14].

In this study, a PANanalytical X'Pert Pro system has been employed for the XRD study. The phase analysis was done in the range of 20˚ to 70˚ using Cu-k_α electrode. The particle size effects seen as broadening of the diffracted lines is given by the Scherrer formula,

$$t = 0.9\,\lambda / (B \cos\theta), \qquad \text{Eq. (3.3)}$$

where t is the thickness of the crystallite and θ is the Bragg angle. B is the line broadening, indicating the extra peak width of the sample in comparison to the standard [15].

3.3.5 Brunauer-Emmett-Teller (BET)

The determination of surface area and porosity of composite electrodes are generally considered to be important requirements in solid material characterisation since these characteristics may control the interfacial charge transfer and solid-state diffusion in intercalation processes [5]. In general, the smaller the particle, the higher is the surface area and the smaller is the diffusion length which in turn enhances the kinetics of the electrochemical reaction. Additionally, high porosity of composite electrodes also assures good interparticle contact. However, it is important to be noted that too small particles can lead the problems with interparticle electric contact. The contact between the active materials and electrolyte is critical. Thereby, the properties of both electrodes and electrolytes have to be optimised in order to obtain the sufficient wetting of the active materials [5].

The standard method for the determination the surface area and pore size distribution of solids is based on the physical adsorption of nitrogen on a solid surface, using the BET method, developed by Brunauer, Emmet and Teller in 1938 with the BET equation [16]:

$$\frac{1}{V[(P_0/P)-1]} = \frac{1}{V_m C} + \frac{C-1}{V_m C}\left(\frac{P}{P_0}\right) \qquad \text{Eq. (3.4)}$$

where V = volume of gas adsorbed at a relative pressure

P/P_0 = relative pressure

V_m = volume of the monolayer adsorbed gas

C = BET constant

A plot of 1/[V(Po/P)-1] versus P/Po, called BET plot (Figure 3.5) can yield a straight line in the range of 0.05 < P/Po <0.35. The value of the gradient, G and the intercept, I of the line are used to calculate the monolayer adsorbed gas quantity, V_m and the BET constant, C as follows:

$$V_m = \frac{1}{G+I} \qquad \text{Eq. (3.5)}$$

$$C = 1 + \frac{G}{I} \qquad \text{Eq. (3.6)}$$

BET constant (C) is an indication of the magnitude of the adsorbent/adsorbate interactions which is related to the energy of adsorption in the first adsorbed layer. Low values represent weak gas adsorption typical of low surface area solids [16].

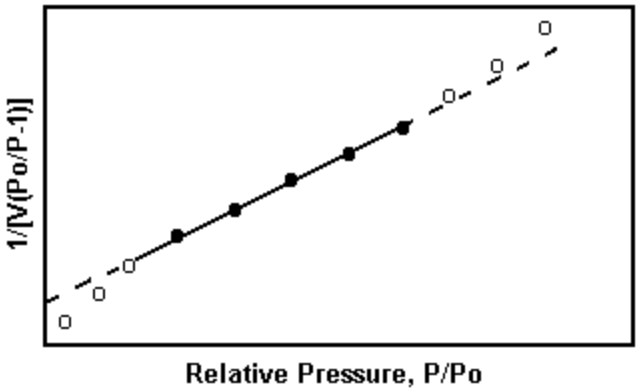


Figure 3.5. Typical BET plot [16].

It is possible to estimate the total surface area (S_T) and the BET specific surface area (S_{BET}) of a solid material by the following equations:

$$S_T = \frac{V_m N A_m}{M_V} \qquad \text{Eq. (3.7)}$$

$$S_{BET} = \frac{S_T}{a} \qquad \text{Eq. (3.8)}$$

where N = Avogadro's number

A_m = adsorption cross section of the adsorbing species

M_V = molar volume of adsorbate gas

a = mass of adsorbent (in g)

An Adsorption Isotherm is obtained by measuring the amount of gas adsorbed across a wide range of relative pressures at a constant temperature (typically liquid N_2, 77K). Conversely desorption isotherms are achieved by measuring gas removed as pressure is reduced. There are 6 types of isotherms as described by Brunauer, Deming and Teller and are shown in Figure 3.6 [17-18].

- *Type I* -This is characteristic of either a chemisorption isotherm (in which case the final upswing at high pressures may not be present) or physisorption on a material that has extremely fine pores (micropores).
- *Type II* - This is characteristic of a material, which is not porous, or possibly macroporous, and has a high energy of adsorption.
- *Type III* - This is characteristic of a material, which is not porous, or possibly macroporous, and has a low energy of adsorption.
- *Type IV* -This is characteristic of a material, which contains mesoporosity and has a high energy of adsorption. These often contain hysteresis attributed to the mesoporosity.
- *Type V* - This is characteristic of a material, which contains mesoporosity and has a low energy of adsorption. These often contain hysteresis attributed to the mesoporosity.
- *Type VI*- This type of isotherm is attributed to several possibilities the most likely being, if the temperature is below the adsorptive triple point, that the adsorbate is more like a solid forming a structured layer, i.e. epitaxial growth. Other possible explanations include specific pore size distribution. If the steps are at the low pressure portion of the isotherm, then the steps may be due to two or more distinct energies of adsorption. If the steps are at the high pressure part of the isotherm, then the steps might be due to sharp steps on the adsorbate surface.

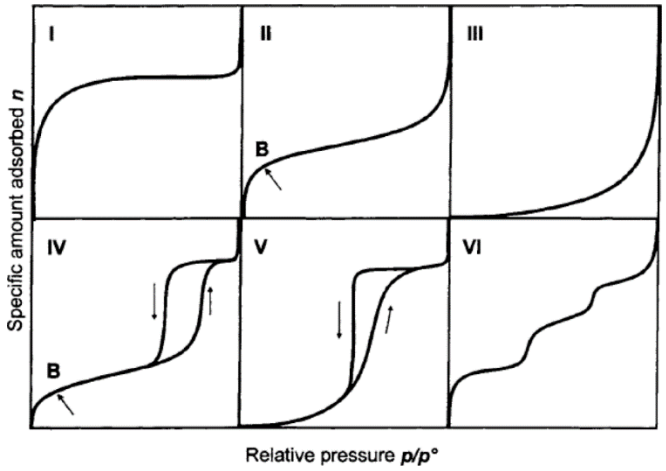


Figure 3.6. Different types of isotherm [18].

In the present study, the composite electrodes were heated at 300℃ for 120 minutes. The solid was then connected to a gaseous nitrogen source that was added or removed in finite volumes at controlled pressures. The temperature was held constant at the critical temperature of the gas (about 77 K) by a bath of liquid nitrogen. Prior to nitrogen adsorption experiment, solid surfaces must be free of contaminants such as water and other adsorbed species. This is because contaminants can block pores and negatively affect the measurement process. Typically, physisorbed species can be removed by outgasing the sample under vacuum at elevated temperatures. After surface cleaning or degassing, nitrogen adsorption and desorption experiments were carried out at 77.3 K using Micromeritic ASAP 2020 analyzer.

3.3.6 Raman spectroscopy

Raman spectroscopy is a spectroscopic technique used to study vibrational, rotational, and other low-frequency modes in a system. It relies on inelastic scattering, or Raman scattering, of monochromatic light, usually from a laser in the visible, near infrared, or near ultraviolet range. A typical Raman spectroscopy instrument should have an excitation source (laser generation), sample illumination and light collection optic system, spectrophotometer (for filtering and selecting wavelength) and a detector [19]. The technique measures weak inelastic scattering that occurs when photos interact with the electron cloud (Raman effect). The molecules absorb the photons, becoming excited and then re-emit photons of different wavelengths, returning the molecule to a different rotational or vibrational state than its original ground state [20]. A filter removes all the elastically scattered light that retains the same wavelength as the incident photons. Energy shifting information collected over the spectrum of wavelengths is used to study vibrational, rotational and other low-frequency transitions in molecules.

Raman spectroscopy can identify mixtures through characteristic peaks that fingerprint certain functional groups in a molecule. It is used as a complementary tool with TEM to examine structures and chemical composition changes of electrode materials that have undergone chemical or physical alterations [20]. The Raman spectra were collected using a scanning confocal Raman microscope (Reni Shaw In-Via Raman 2000) at room temperature, with a 514 nm diode laser excitation source. The system is equipped with a CCD detector and a holographic notch filter, for capturing the required signals.

3.3.7 Thermogravimetric analysis (TGA)

Thermogravimetric analysis (TGA) TGA is a thermal analysis in which the mass changes are measured as a function of change in temperature or time. Typically it is carried out at constant heating rate under desired atmosphere (inert/air/oxidising/reducing). Typically it is carried out at constant heating rate under desired atmosphere (inert/air/oxidising/reducing). The choice of heating rate and atmosphere used in TGA experiments plays a crucial role on the measurement. Diverse effects can cause a sample to lose or gain weight, which produces steps in the TGA curve. These curves are known as thermograms. The results of a TGA are usually portrayed as weight present versus temperature, alternatively first derivative of the TGA curve with respect to temperature also presented known as differential thermogravimetric or DTG curve. This curve can be used to notify the precise point at which weight loss occurs.

TGA is an effective materials characterization technique for quantitative analysis of thermal reactions that are accompanied by mass changes, such as dehydration, evaporation, decomposition, and desorption. It is commonly employed in research and testing to determine characteristics of materials such as polymers in terms of the degradation temperatures, moisture content in a sample, the contents of inorganic and organic components in a sample , the decomposition point of explosives, and solvent residues. It is also often used to estimate the corrosion kinetics in high-temperature oxidation. In the present work, the TA Instruments (SDT-2960 Simultaneous DTA-TGA) was used and the experiments were performed at a heating rate of 10 ^{o}C/min in N_2 or air flow of 100 mL/min.

3.4 Electrochemical Characterisation

The conventional three-electrode electrochemical cell is commonly used in electrochemical research to determine electrochemical-specific material characteristics while two-electrode cells are recommended for the evaluation of cell performance approaching to the actual supercapacitors [25]. Figure 3.7 is a schematic showing the components of a modern operational amplifier potentiostat for carrying out electrochemical measurements. The cell consists of three electrodes immersed in an electrolyte, namely working electrode, reference electrode and counter or Auxiliary electrode [21]. The electrometer circuit measures the voltage difference between the reference and working electrodes and adjusts the current carried from the counter electrode to the working electrode in order to make the potential difference between the

working electrode and the reference electrode identical to the output voltage from the signal generator. The resulting current which is directly proportional to the potential difference between the working electrode and the reference electrode is then converted to a voltage by current-to-voltage (I/E) converter and recorded as a function of time by the data-acquisition system [21]. It should be noted that the electrical resistance of an ideal electrometer should be large enough so that it has zero input current. This is because current flow through the reference electrode can change its potential which in turn affects the data accuracy [21].

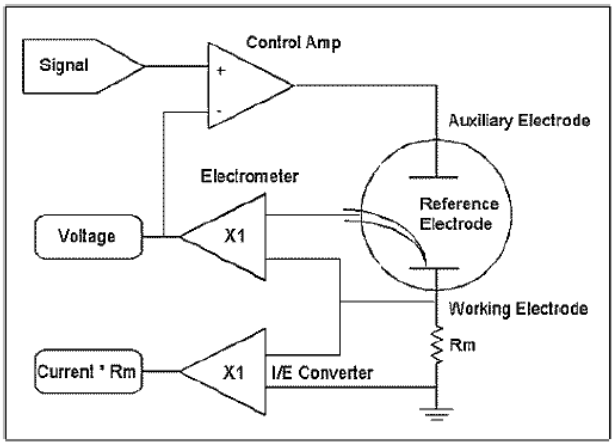


Figure 3.7. A simplified schematic of a potentiostat [22].

For a two-electrode supercapacitor cell, two working electrodes sandwiched with a separator are in contact with an electrolyte solution. Figure 3.8 shows a two-electrode test fixture configuration that is similar to that of a packaged supercapacitor cell that provide better representative of the electrochemical performance of electrode materials [25]. It should be noted that at a given potential range on the electrochemical system, the working electrode of a three-electrode cell has twice the potential range applied as is applied to the electrodes in a two electrode cell, which results in a doubling of the calculated capacitance. This can be explained by the fact that the potential differences applied to a symmetrical two-electrode cell distribute equally to each electrode.

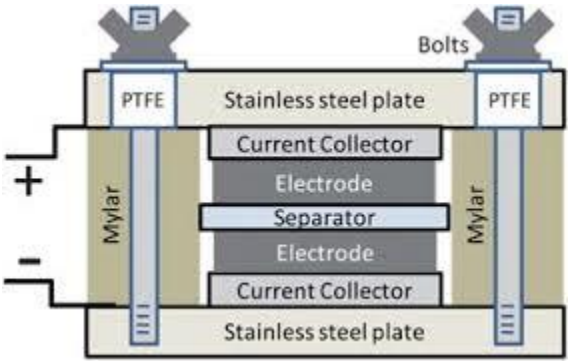


Figure 3.8. Two-electrode cell configuration [25].

To evaluate the electrochemical performance of supercapacitors, cyclic voltammetry (CV), galvanostatic charge/discharge (GCD) curve, and electrochemical impedance spectroscopy (EIS) are the most commonly used techniques.

3.4.1 Cyclic Voltammetry (CV)

Voltammetry is widely used for fundamental studies of oxidation and reduction processes in various media, adsorption processes on surfaces and electron-transfer mechanisms at chemically modified electrode surfaces [21]. Among the different types of voltammetric excitation signal used in voltammetry, cyclic voltammetry (CV) is commonly employed in electrochemical characterisation of a supercapacitor. CV analysis evaluates the current that flows through an electrochemical cell as the voltage is swept repetitively over a voltage range, yielding the basic information about a capacitive electrochemical cell including voltage window, capacitance and cycle life [22]. Additionally, it also reveals the presence of intermediates in redox reactions. Reactions that result in charge transfer are mainly of the redox type where changes in the oxidation state of the materials occur, analogous to energy transfer in battery systems during the charging and discharging process [23].

Materials exhibiting pure double-layer capacitance produce parallelogram-shaped CV curve whereas irregular peaks are generated by pseudocapacitive materials [24]. Figure 3.9 shows the cyclic voltammogram of the symmetric peaks of a reversible surface redox couple. The range of potentials that can be used in voltammetry in an electrolyte varies and depends not only on electrode material but also on the composition of the electrolyte. In general, the positive potential limitations are caused by the large negative current arises from the oxidation of water to

produce oxygen. In contrast, the negative limits result from the reduction of water to give hydrogen.

The respective capacitances (C) were calculated from the CV curves using a two-electrode cell by dividing the current (I) by the voltage scan rate ($\Delta V/\Delta t$) using Eq. (3.9).

$$C = I / (\Delta V/\Delta t) \qquad \text{Eq. (3.9)}$$

In a two-electrode system, the capacitance values of the two electrodes connected in series yield the total capacitance according to Eq. (3.10):

$$1/C_{2E} = 1/C_1 + 1/C_2 \qquad \text{Eq. (3.10)}$$

Assuming that $C_1=C_2$ for symmetrical electrodes, the specific capacitance (C_{sp}) of the electrode can be obtained by dividing the capacitance (C_{2E}) in Eq. (6) by the mass of a single composite electrode (m), as shown in Eq. (3.11) [20]. The factor of 2 converts the capacitance and combined mass of the two-electrode cell to the capacitance and mass of a single electrode:

$$C_{sp}\ (F/g) = 2 \times C_{2E}/m \qquad \text{Eq. (3.11)}$$

In this work, the linear sweep cyclic voltammetry technique was applied using Autolab Potentiostat by connecting the positive probe to the positive electrode and the negative probe to the negative electrode of the fabricated Teflon cell. To investigate the single electrode behaviour, the parameters below were used:

Potential window: 0.0 to 1.0 V
Scan rate: 5, 10, 20, 50 and 100 mV/s

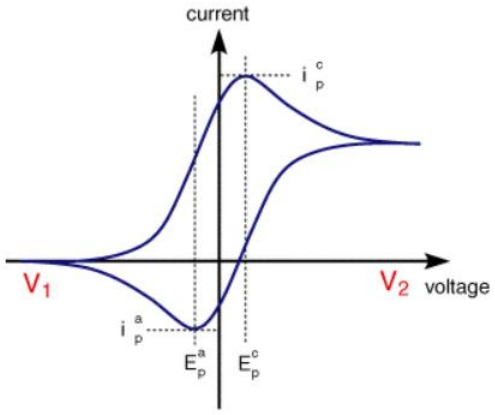


Figure 3.9. A typical cyclic voltammogram showing the characteristic symmetrical peaks of a reversible single electrode transfer reaction [24].

3.4.2 Galvanostatic Charging- Discharging (GCD)

Characterization via galvanostatic charging-discharging (GCD) is one of the most reliable approaches to determine capacitance energy density, power density, equivalent series resistance and cycle life of a supercapacitor. Generally, GCD is performed by applying a constant cell current during which the cell voltage is recorded as a function of charging or discharging time. In recording charging-discharging curves, the conventional three-electrode or two-electrode test cells can be employed, depending on availability, similar to the procedure described above for CV characterization. However, for characterizing cycle life of a supercapacitor, two-electrode test cells are favourable because they more closely resemble practical operating conditions.

The specific capacitance values (C_{sp}) can be calculated from the applied current density (I), the mass of a single electrode (m) and the slope of the discharge curve ($\Delta V/\Delta t$) [22]:

$$C_{sp}\ (F/g) = 2 \times I / (-\Delta V/\Delta t) \times m \qquad \text{Eq. (3.12)}$$

The upper half of the discharge curve after the IR drop was employed to calculate the slope of the curve ($\Delta V/\Delta t$) using Eq. (3.13). t_2-t_1 is the time interval of the voltage decrease between 0.5 V_{max} and V_{max}. Excluding the lower half of the discharge curve in the calculation can minimise the overestimation of the specific capacitance values for practical applications [22].

$$\Delta V/\Delta t = (V_{max} - 0.5\ V_{max}) / (t_2 - t_1) \qquad \text{Eq. (3.13)}$$

The average internal resistance (ESR) of a supercapacitor cell can be calculated according to [22]:

$$ESR = (E_{+I} - E_{-I}) / (2I) \quad \text{Eq. (3.14)}$$

where E_{+I} is the cell voltage at the end of the charge or the last voltage point recorded before the charge current is reversed, E_{-I} is the beginning of the discharge or the first voltage point after the discharge current is applied and I is the current for which the absolute value was the same during the charge and discharge [23].

Specific energy and specific power are two key parameters to characterize the performance of a supercapacitor cell. The specific energy (Wh/kg) is the capacity to perform work, whereas the specific power (W/kg) exhibits how fast the energy is delivered. The maximum energy stored (E_{max}) and power delivered (P_{max}) for a supercapacitor cell are based on the specific capacitance (C_T) and the ESR (R_{esr}) of a two-electrode system as well as the cell voltage (V) determined by the thermodynamic stability of the electrolyte solution [26]:

$$E_{max} = \frac{1}{2} C_T (V^2) \quad \text{Eq. (3.15)}$$

$$P_{max} = \frac{1}{4} \frac{(V^2)}{R_{esr}} \quad \text{Eq. (3.16)}$$

In some fundamental research, Eq. (3.17) and Eq. (3.18) are also used to calculate the average energy density (E) in Wh/kg and average power density (P) in W/kg [32], where E is the average energy density (J), C_T is the specific capacitance (F/g), V is the cell voltage (V) and t is the time for a sweep segment (s). The origin of "3.6" in Eq. (3.17) is based on the unit conversion from "Joule" to "Wh/kg" while "3600" is originated from the conversion of hour to second in Eq. 3.18.

$$E = \frac{0.5 C_T V^2}{3.6} \quad \text{Eq. (3.17)}$$

$$P = \frac{E_{max} \times 3600}{t} \qquad \text{Eq. (3.18)}$$

3.4.3 Electrochemical Impedance Spectroscopy (EIS)

Electrochemical Impedance spectroscopy (EIS) measures the impedance of a system or the dielectric properties of a material over a range of frequencies. It is a powerful tool to investigate the penetration of current into the surface of the electrode and determine the degree to which ions access through the surface at specific frequencies using a variety of output format such as Nyquist and Bode plots [27]. EIS technique has an advantage over direct circuit (dc) techniques in measuring uncompensated resistance of an electrochemical cell especially in low conductivity solution where dc techniques are subjected to serious potential-control errors. This electrochemical technique is also able to reveal information about the reaction mechanism and the rate limiting step of an electrochemical process [28]. When the cell is electrically stimulated, several microscopic processes take place throughout the entire cell: (i) the diffusion of electrons through the electronic conductors; (ii) the transfer of electrons at the electrode-electrolyte interfaces via redox reactions; (iii) the transport of ions or atom agglomerates via defects in the electrolyte [29]. The diffusion rate of charged species can vary substantially depending on the species of charge present, the microstructure of the electrodes and the nature of the electrolytes which in turn determine the ohmic resistance of electrodes and electrolyte as well as the reaction rates at the electrode–electrolyte interfaces. If there are second phases, agglomerations or point defects present at the electrode-electrolyte interface, the diffusion may be impeded further. A host of adsorbed and included foreign chemical species at the interfaces can also influence the local electric field [29].

Each electrode-electrolyte interface represents a capacitor and a resistance. In order to determine the equivalent circuit that best describes the behaviour of an electrochemical system, an alternative current (ac) voltage or current is applied over a wide range of frequencies to measure the impedance. Typically, a supercapacitor behaves as a pure resistor at high frequencies while it shows characteristic of a capacitor at low frequencies. In the mid-frequency range, the electrode porosity and thickness of electroactive materials play a vital role in determining capacitance values, behaving as a combination of resistor and capacitor [30].

A perfect capacitor can be described using the expression:

$$Z = 1/ j\omega C \qquad \text{Eq. (3.19)}$$

where Z is the total impedance and $\omega=2\pi f$ is the angular frequency. Nevertheless, the double-layer capacitor measured in the EIS experiment often does not behave ideally. To describe the non-ideality in a real cell, Q or the constant-phase element (CPE) is typically used in place of the capacitive element (C) due to imperfections in the real electrochemical cell, including the surface roughness, a leaky capacitor and a non-uniform current distribution [31]. The impedance of the constant-phase element (Q) can be expressed as a power of n as

$$Z = 1/ (j\omega Q)^{n} \qquad \text{Eq. (3.20)}$$

The material resembles a resistor when n = 0 and an ideal capacitor when n=1. Generally, real capacitors exhibit values of $0<n<1$ [31]. The degree of deviation from the vertical line along the imaginary axis (-Z") is dependent on the value of n.

For the work reported in this thesis, the EIS test was carried using an Autolab Potentiostat electrochemical system, according to the following condition: (i) open circuit condition on the frequency regime: 10 kHz – 10 mHz; (ii) AC-perturbation amplitude of 10 mV sinusoidal signal. Frequency Analysis Response mode was used where a frequency signal is applied to observed the impedance behaviour. An impedance plot was displayed in real time mode as the AC signal passed through the Teflon cell. The data collected was later used to calculate specific capacitance of the electrodes. The fitting of the impedance expressions from the equivalent circuit in accordance to the experimental Nyquist spectra was performed using the NOVA equivalent circuit editor in order to determine the most representative physical processes that taking place in the systems under investigation.

Reference

[1] J.S.Y.Chia, M.T.T. Tan, P.S.Khiew, J.K.Chin, H.W.Lee , D.C.S Bien, C.W.Siong, "A novel one step synthesis of graphene via sonochemical-assisted solvent exfoliation approach for electrochemical sensing application," Chemical Engineering Journal 249 (2014) 270–278.

[2] T.Pradeep, Nano: The Essentials, Understanding Nanoscience and Nanotechnology. US: McGraw-Hill Education (2007).

[3] A.P.Yu, V.Chabot and J.J.Zhang, “Characterization and Diagnosis Techniques for Electrochemical Supercapacitor, in: Electrochemical Supercapacitors for Energy Storage and Delivery,” Boca Raton: CRC Press (2013) 304.

[4] M.Dunlap and J.E.Adaskaveg, " Introduction to the Scanning Electron Microscope," Facility For Advanced Instrumentation, U.C.Davis (1997).

[5] M.Broussely and G. Pistoia, “Industrial Applications of Batteries: From Cars to Aerospace and Energy Storage,” (2007).

[6] S.Zhang, L.Li, A.Kumar, “Scanning Electron Microscopes, in: Materials Characterization Techniques,” Baca Raton: CRC Press (2009) 177-205.

[7] Jeol Ltd.SEM Q & A [Online]. Available: www.stcloudstate.edu/cmia/documents/SEMQAe.pdf. [access in March 2014].

[8] D.C.Bell and A.J.Garratt-Reed, “Energy Dispersive X-ray Analysis in the Electron Microscope. Microscope Handbooks Series.” New York: BIOS Scientific (2003).

[9] J.Goldstein et al. “Scanning Electron Microscopy and X-ray Microanalysis”, 3rd ed., New York: Kluwer (2002).

[10] D.B.Williams and C.B.Carter, “Transmission Electron Microscopy: A Textbook for Materials Science,” New York: Springer 141 (2004).

[11] L.Reimer and H.Kohl, “Transmission Electron Microscopy Physics of Image Formation,” New York: Springer 141 (2004).

[12] The Transmitted Electron Microscope [Online]. Available: www.nobelprize.org/educational/physics/microscope/tem/index.html. [access in March 2014].

[13] S.Marco, "Introduction to Diffraction, HighScore Plus Workshop," PANanalytical (2016).

[14] M.Birkholz, “Principles of X-ray Diffraction, in Thin Film Analysis by X-ray Scattering,” Wiley-VCH Verlag GmbH & Co. KGaA (2006) 1-40.

[15] J.Santos-Peña, O. Crosnier, and T. Brousse, " Nanosized α-$LiFeO_2$ as electrochemical supercapacitor electrode in neutral sulfate electrolytes," Electrochimica Acta 55 (2010) 7511-7515.

[16] S.J.Gregg and K. S. W. Sing, “Adsorption, Surface Area and Porosity,” Academic Press (1982).

[17] S.Brunauer et al., “On a Theory of the van der Waals Adsorption of Gases,” Journal of the American Chemical Society 62 (1940) 1723-1732.

[18] J.B.Condon, “Chapter 1 - An Overview of Physisorption, in Surface Area and Porosity Determinations by Physisorption,” Elsevier Science: Amsterdam (2006) 1-27.

[19] Princeton Instruments. Raman Spectroscopy Basic [Online]. Available: content.piacton.com/Uploads/Princeton/Documents/Library/UpdatedLibrary/Raman_Spectroscopy_basics.pdf. [access in March 2014].

[20] D.J.Gardiner, “Practical Raman Spectroscopy,” Heidelberg: Springer (1989).

[21] D.A.Skoog, "22. Voltammetry," in Principles of Instrumental Analysis, ed Fort Worth, Texas Saunders College Pub. (1992).

[22] Gamry. Instruments. Application Note: Testing Super-Capacitors Part 1 – CV, EIS and Leakage Current [Online]. Available: www.gamry.com [access in March 2014].

[23] P. J. Hall, M. Mirzaeian, S. I. Fletcher, F. B. Sillars, A. J. R. Rennie, G. O. Shitta-Bey, G. Wilson, A. Cruden, and R. Carter, " Energy storage in electrochemical capacitors: designing functional materials to improve performance," Energy & Environmental Science 3 (2010) 1238.

[24] Univeristy of Cambridge. Linear Sweep and Cyclic Voltametry: The Principles [Online]. Available:http://www.ceb.cam.ac.uk/pages/linear-sweep-and-cyclic-voltametry-the-principles.html [access in March 2014].

[25] M.D. Stoller, R.S. Ruoff, "Best practice methods for determining an electrode material's performance for ultracapacitors," Energy & Environmental Science 3 (9) (2010) 1294.

[26] D. Hulicova-Jurcakova, A.M.Puziy, O.I.Poddubnaya, F. Suárez-Garccia, J.M.D. Tascón, G.Q.Lu, "Highly Stable Performance of Supercapacitors from Phosphorus-Enriched Carbons," J. Am. Chem. Soc. 131 (2009) 5026-5027.

[27] A.Chu and P. Braatz, " Comparison of Commercial Supercapacitors and High-Power Lithium-ion batteries for Power-Assist Applications in Hybrid Electric Vehicles: Initial Characterisation," Journal of Power Sources 112 (2002) 236-246.

[28] Princeton Applied Research. Application Note AC 1: Basics of Electrochemical Impedance Spectroscopy [Online]. Available: www. princeton applied research.com [access in March 2014].

[29] E.Barsoukov and J. R. Macdonald, "Impedance Spectroscopy, Theory Experiment and Applications," Canada: John Wiley & Sons, Inc (2005).

[30] V.Ganesh, S.Piychumani, and V.Lakshminarayanan, "New Symmetric and Asymmetric Supercapacitors based on High Surface Area Porous Nickel and Activated Carbon." Journal of Power Sources 158 (2006) 1523-1532.

[31] V. D. Jovic, Determination of the correct value of C_{dl} from the impedance results fitted by the commercially available software, [Online]. Available: http://www.gamry.com [access in March 2014].

[32] Z.J.Li, Z.H.Zhou, G.Q.Yun, K.Shi, X.W.Lv, B.C.Yang, "High-performance solid-state supercapacitors based on graphene-ZnO hybrid nanocomposites", Nanoscale research Letters (2013) 473.

CHAPTER 4

Electrochemical Performance of Nano Fe_3O_4 - Activated Carbon Composites in Symmetric Supercapacitors

4.1 Introduction

Limited reserves of fossil fuels and severe impacts of burning fossil fuels on both human beings and environment have been increasingly driving the world towards the environmentally friendly energy resources [1]. Supercapacitors are one of the most competitive energy storage systems for clean renewable energy resource and electric automobile. It differs from conventional capacitor by storing charge using the double layer concept in which charge accumulation occurs at the interface between electrode and electrolyte via the double-layer charging effects [2]. Additional contribution of pseudocapacitance may also be part of the observed capacitance due to some participation of functional groups present on the electrode surface in redox reactions or chemisorption processes involving partial charge transfer [3].

On the basis of electrode materials used and the charge storage mechanisms, the core electrode material of supercapacitor generally can be classified into three main categories: (i) carbon materials with high surface area, such as activated carbon and carbon aerogel; (ii) transition metal oxides such as RuO_2, NiO_2, MnO_2, Fe_3O_4 and (iii) conducting polymers such as polypyrrole [4–6]. The carbon systems employ the double layer storage mechanism involving the charge separation at the interface between the carbon electrode and electrolyte. No charge transfer takes place across the interface of the electrode material. For this reason, this process is non-Faradaic in nature and therefore we classify the carbonaceous materials as electrochemical double layer capacitor or EDLC [7]. In contrast, the charge storage mechanism achieved by the transition metal oxides and conducting polymers is Faradaic in nature. The redox reaction between electrode materials and electrolyte ions in the appropriate voltage window gives rise to

the pseudo-capacitance through the electron transfer that is produced from the oxidation state changes, according to Faraday's laws [8].

Over the past few years, significant effort has been devoted to the fabrication of advanced nanostructured metal oxides as the core electrode material, especially on hydrous $RuO_2.xH_2O$ [9–11]. RuO_2 is widely studied because it is conductive and has three accessible distinct oxidation states. The pseudo-capacitive behaviour of RuO_2 in acidic solutions has been the focus of research in the past 30 years [12]. Although $RuO_2.nH_2O$ gives high specific capacitance, its application has been hindered by its high cost [13]. Therefore, there is a need to search for cost-effective metal oxides to support the growing demand on supercapacitor in manufacturing industry, as a result of rapid advancement of consumer electronic products and technology. A number of research studies have showed increased interests in other transition metal oxides with various oxidation states, such as NiO [14–17], MnO_2[18–20], SnO_2[21–23], Fe_2O_3[24–26] and Fe_3O_4 [27–29].

Iron oxides have been identified as potential electrode materials in view of the low-cost and environmentally friendly nature. Recently, large capacitance exhibited by iron powder electrodes has been reported in alkali sulphites and sulphate solutions [24, 25, 28–33]. Wu (2002) firstly reported that Fe_3O_4-SnO_2 composite electrode can achieve a specific capacitance of 33 F/g in 1.0 M Na_2SO_4 aqueous solution [2]. It is suggested that the low conductivity of Fe_3O_4 combined with other conductive materials such as SnO_2 is essential to obtain large capacitance. In order to identify the effect of different electrolytes on Fe_3O_4 electrodes, Wu and his co-researchers also have prepared an electrode that is consisted of a mixture of Fe_3O_4 (90 wt %), CB (10 wt %), PTFE (4 wt %) via co-precipitation method [27]. The specific capacitances of the composite electrode are found to be 38, 5.3, 4.9, 5.8 F/g in 1 M Na_2SO_3, 1 M Na_2SO_4, 1 M NaCl and 1 M KOH respectively.

Both results are consistent with the investigation on capacitive mechanism of Fe_3O_4 in Na_2SO_3, Na_2SO_4, and KOH aqueous electrolyte [30] and suggested that the capacitance of the oxide was found to be sensitive to the anion species. Experimental results indicate that Fe_3O_4 electrodes in Na_2SO_3 exhibit the highest specific capacitance value (170 F/g), followed by Na_2SO_4 (25 F/g) and KOH (3 F/g). In the work of Du et al.

(2009), they reported the capacitive characteristic of nanostructured Fe_3O_4-AC based asymmetric supercapacitor in 6 M KOH solution [13]. This hybrid system (a positive Fe_3O_4 electrode and a negative AC electrode) is found to deliver a specific capacitance of 37.9 F/g within potential range of 0 – 1.2 V. A composite supercapacitor containing Fe_3O_4 nanoparticles dispersed in multiwalled carbon nanotubes (MWNTs) was reported by Kim and Park (2011) [34]. The Fe_3O_4/MWNTs composite electrode exhibits specific capacitance of 165 F/g in 1 M Na_2SO_3, which this value is almost 3-fold enhancement if compared to the pure MWNT electrode (58 F/g).

To our best knowledge, there have been few investigations on Fe_3O_4-AC nanocomposite supercapacitor to date. In this study, we reported the capacitive performance of Fe_3O_4-AC symmetric supercapacitor in mild aqueous electrolyte solutions. The nanostructured Fe_3O_4-AC composite as the core electrode materials via simple facile mechanical mixing method is explored for the first time. Although the poor electric conductivity of Fe_3O_4 limits its application in high power storage devices, the incorporation of carbon black can improve the electrochemical performance of the composite electrodes. In this study, two AC materials with different surface areas were employed to evaluate the effect of composition, the effect of scan rate, the effect of anions and the effect of heat treatment. AC_LSA refers to the AC materials with lower surface area (Sigma Aldrich, BET surface ~ 900 m^2/g) while AC_HSA was denoted as the AC materials with higher surface area (RHE Resources, BET surface ~ 1800 m^2/g).

4.2 Characterisation of Fe_3O_4-AC composites

Figure 4.1 compares the XRD patterns of carbon black, AC_LSA, Fe_3O_4 and their composites. Six diffraction peaks at 2θ value f 30˚, 36˚ 43˚, 54˚, 57˚ and 53˚, corresponding to (2 2 0), (3 1 1), (4 0 0), (4 2 2), (5 1 1) and (4 0 0) diffractions of Fe_3O_4, can be seen on the high Fe_3O_4 loaded composite. It can be observed that the intensities of these peaks increased with the amount of Fe_3O_4 nanoparticles incorporated into the composites. XRD shows that the mixed composites contain Fe_3O_4 as the predominant iron-containing species.

AC_LSA, carbon black and 4Fe-AC_LSA composites demonstrate very broad diffraction peaks thus reflecting an amorphous structure. However, composites with more

than 20 % of iron oxide loading exhibit sharp peaks that were ascribed to Fe_3O_4, revealing that these iron-based nanocomposites are more crystalline than the pure AC and carbon black. In fact, the capability of supercapacitor is strongly dependent on the microstructure of electrode material. In order to achieve high capacitance, amorphous behaviour exhibited in pure AC_LSA and 4Fe-AC_LSA composite electrode is desirable because of shorter ionic diffusion and electronic hopping pathway, which will be further discussed in section 4.3 [35].

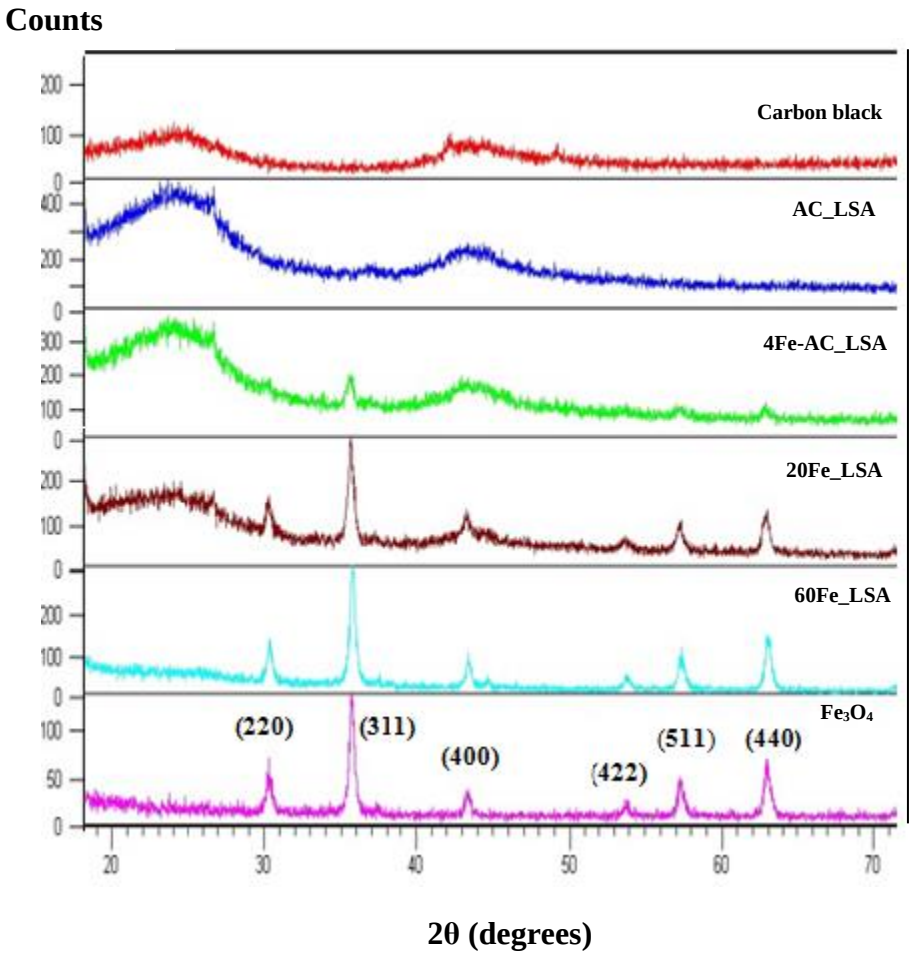


Figure 4.1. XRD patterns of carbon black, AC_LSA, Fe_3O_4 and their nanocomposites.

In order to elucidate the porosity property of the electrode, BET analysis has been conducted. Figure 4.2 (a) and (b**)** show the nitrogen adsorption/desorption isotherms of 4Fe-AC_LSA and 60Fe-AC_LSA composites. Both samples display a type-IV isotherm

indicating that they are mesoporous or macroporous materials. Hysteresis shown in the BET plots confirms the capillary condensation in mesopores and macropores [36].

The BET surface areas of the samples are summarized in Table 4.1. The incorporation of 4 wt% Fe_3O_4 onto AC_LSA increases the specific surface area of AC_LSA electrode from 916 to 949 m^2/g and thus improves the capacitive performance improvement of the composite electrode effectively. This observation is in good accordance to research finding by Zhang and Chen (2008), which clearly indicate that the enhanced capacitance is mainly attributed to the high surface area of the core electrode material [37]. On the other hand, further increase of Fe_3O_4 compound to 60 wt% causes the specific surface area of the composite electrode decreased to 800 m^2/g. It should be noted that the specific surface area of Fe_3O_4 (38 m^2/g) is lower than that of the AC_LSA; when the Fe_3O_4's content is increased, the specific surface area of the composite decreases. Additionally, Fe_3O_4 nanopowder can coalesce to form agglomerates within AC_LSA electrodes as evidenced by the SEM micrographs shown in Figure 4.3.These findings are consistent with other studies and suggest that the crystal growth of Fe_3O_4 reduces the ionic migration and thus causes the increase in diffusion path length [38-39].

Table 4.1. BET surface area of carbon black, AC_LSA, Fe_3O_4 and their nanocomposites.

Electrode Material	BET Surface Area (m^2/g)
CB	1338.44
AC_LSA	916.00
4Fe-AC_LSA	949.03
20Fe-AC_LSA	831.76
60Fe-AC_LSA	800.73
Fe_3O_4	38.41

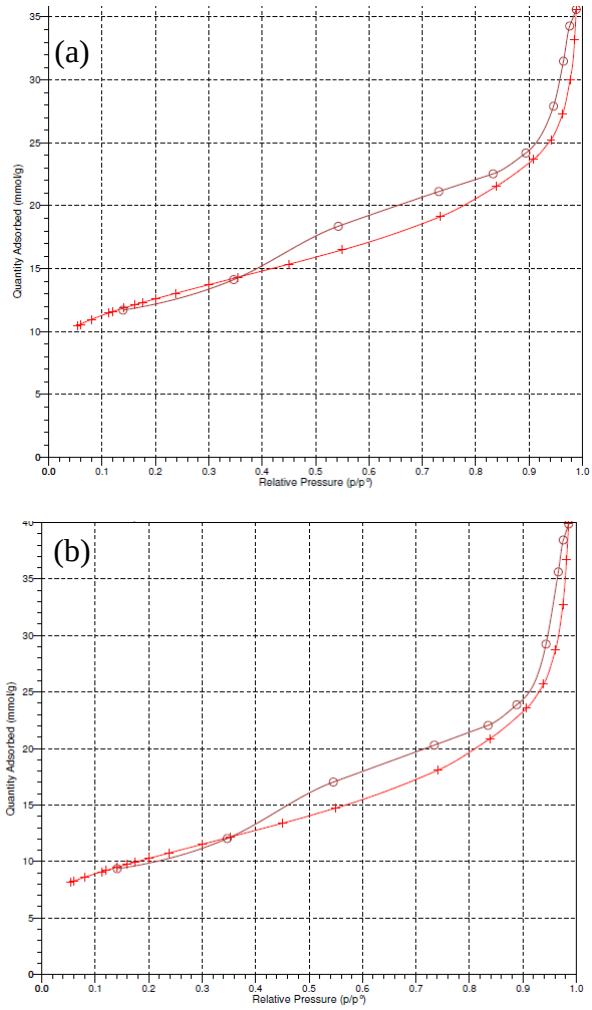


Figure 4.2. BET plots for (a) 4Fe-AC_LSA and (b) 60Fe-AC_LSA.

However, previous research on the study of Mn_2O_3-AC nanocomposite electrodes which reported the similar findings proposed different explanation. They explained that the reduction in specific surface area with increasing loading of Mn_2O_3 is mainly due to the increased density of the composite materials rather than due to pore blocking by Mn_2O_3nanomaterials [40]. Kim and co-workers also suggested that by loading RuO_2 on carbon, the total weight of the composite increases for a given volume of the material due to the higher density of RuO_2, resulting in reducing the BET surface area since this is normalized to the weight of the active material [38].

Scanning electron micrographs in Figure 4.3 (a) – (d) indicate the morphology behaviour of the samples with different amount of iron oxide loaded onto the composite

electrodes. SEM photograph (a) and (b) show that the pitted and fragmented surfaces are more prominent for the pure AC_LSA and 4Fe-AC_LSA composite electrodes while the formation of compact and rigid surface structures are observed for samples with increasing Fe_3O_4 loading, as depicted in SEM photograph (e) and (f). The compact surface contour will retard the ion diffusion to the porous AC electrode, resulting in the loss of overall capacitance of the composite electrodes. The present findings are consistent with other research study, which found that increasing the amount of ruthenium oxide [4] would decrease the surface roughness of the composite electrodes and subsequently distort the specific capacitance.

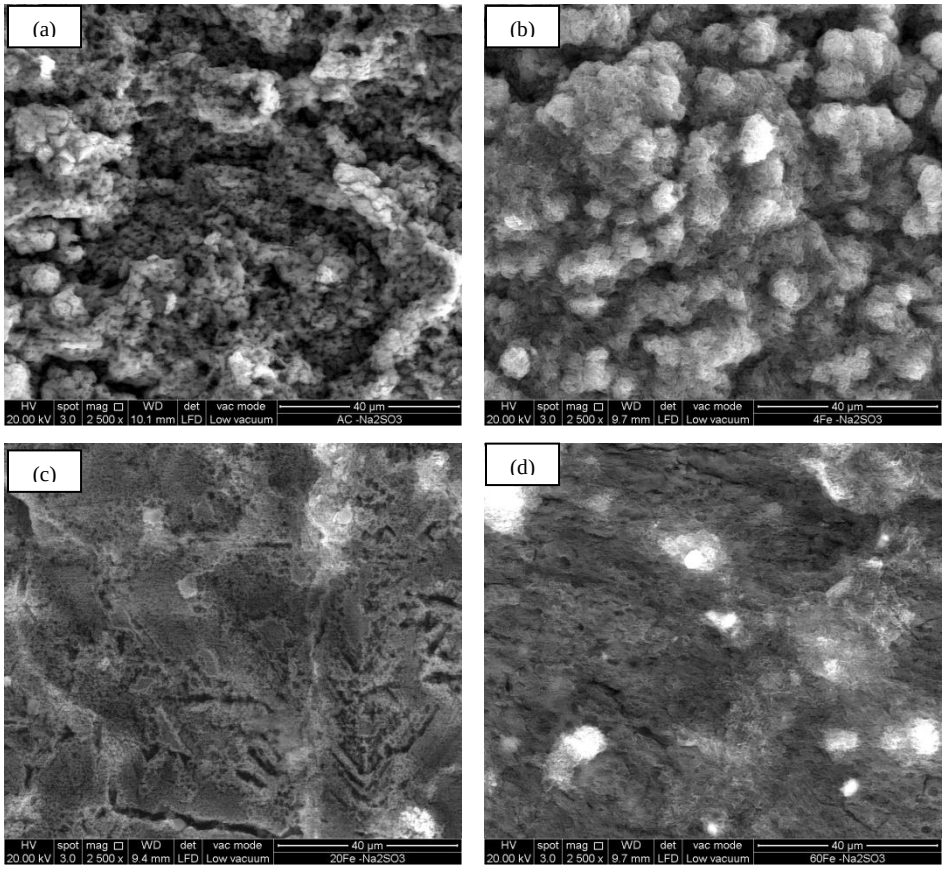


Figure 4.3.Scanning electron micrographs of different Fe_3O_4 loading in AC_LSA electrodes: (a) AC_LSA, (b) 4Fe-AC_LSA, (d) 20Fe-AC_LSA, (e) 60Fe-AC_LSA, at magnification of 2500x.

4.3 The electrochemical performance of the composite electrodes

4.3.1 Cyclic Voltammetry (CV)

4.3.1.1 Effect of Fe_3O_4 loading

The investigation of the capacitive behaviour of the pure AC_LSA electrodes and different Fe_3O_4-AC_LSA composite electrodes were carried out through CV test. The CV plots for the Fe_3O_4-AC_LSA nanocomposite electrodes with different Fe_3O_4 loading in 1 M Na_2SO_3 at a constant scan rate of 10 mV s^{-1} are shown in Figure 4.4. It can be seen that the voltammograms for the samples are not symmetrical along the current axes, especially at the high end of positive potentials. The fact that the voltammograms do not show perfect rectangular features with a mirror image characteristic implies that there is a substantial pseudocapacitance contribution to the overall measured capacitance.

In this study, it can be seen that the current response of the 4Fe-AC_LSA electrodes in 1 M Na_2SO_3 electrolyte is found to be greater than those of AC_LSA electrode and other composite electrodes, suggesting that highest specific capacitance is achieved for such composition. It is believed that the presence of Fe_3O_4 nanoparticles in AC_LSA electrodes can provide favourable surface adsorption sites for sulphite anions which act as catalysts for subsequent redox and intercalation reactions. Additionally, it is noteworthy that the more manifest non-rectangular CV behaviour can be observed with increasing amount of Fe_3O_4 added to AC_LSA electrodes. This may be attributed to the charge storage behaviour transition from double-layer capacitance to pseudocapacitance for composite electrodes that with high loading of Fe_3O_4.

An implication of these results also suggests that the difference in electrode polarisation behaviours is related to the physical morphology of the electrode materials in sulphite electrolytes. It strongly indicates that excess Fe_3O_4 addition has affected the pore size of the nanocomposites, causing more Fe_3O_4 agglomerates in the bulk electrode materials. Similar implication is also proposed in the recent study on the effect of CNT addition to $NiCo_2O_4$/CNT ternary composite electrodes [41]. The low energy of agglomerated CNTs at high concentration favours a faster nucleation of nanocrystals which can deteriorate the capacitive performance.

Similarly, in the present study, a further increase in Fe_3O_4 content within the range 20 – 60 wt % starts deteriorating the capacitive behaviour of the composite

electrodes. The specific capacitances of pure Fe_3O_4 electrodes were found to be less than 17.0 F/g in Na_2SO_3 which clearly dictates its poor capacitive performance. Our observations are well complement with the similar effort by Wu et al. (2002) [42]. They reported that Fe_3O_4 has a very poor conductivity and preliminary tests showed that it was necessary to combine the iron oxide with some conductive additives in order to significantly enhance its capacitive performance. The low conductivity of Fe_3O_4 nanoparticles in large amount, which in turn increase the equivalent series resistance (ESR) of the electrode, is the main factor causing the decreased of capacitive performance at high Fe_3O_4 loading.

On top of low conductivity of Fe_3O_4, a fade in capacitance with increasing Fe_3O_4 could be also due to the particle agglomeration, as shown in Figure 4.2 (c) and (d). This phenomenon is similar to another investigation on the hydrous RuO_2-AC composite electrode in which a significant distortion on the capacitive behaviour is observed for the electrode with more than 40 wt % RuO_2 loading [38]. Since ion diffusion through the active materials controls the redox reactions of the electrode, the diffusive capability of these materials will decrease with increasing of the particle size. Under such circumstances, the ions thus require longer time to reach the entire electrodes. In addition, the agglomeration of the metal oxide nanoparticles will reduce the porosity of the electrode material, which in turn distorts the effective surface area that is available for the redox process. Similar trend has been observed by Dubal et al. [43] for galvanostatically deposited Fe doped MnO_2 thin films. The low porosity of composite electrodes contributes to the poor diffusive capability since the large Fe_3O_4 precipitates agglomerated on the AC surface and block most of the pores, preventing the ions to diffuse into the inner pores of the electrodes.

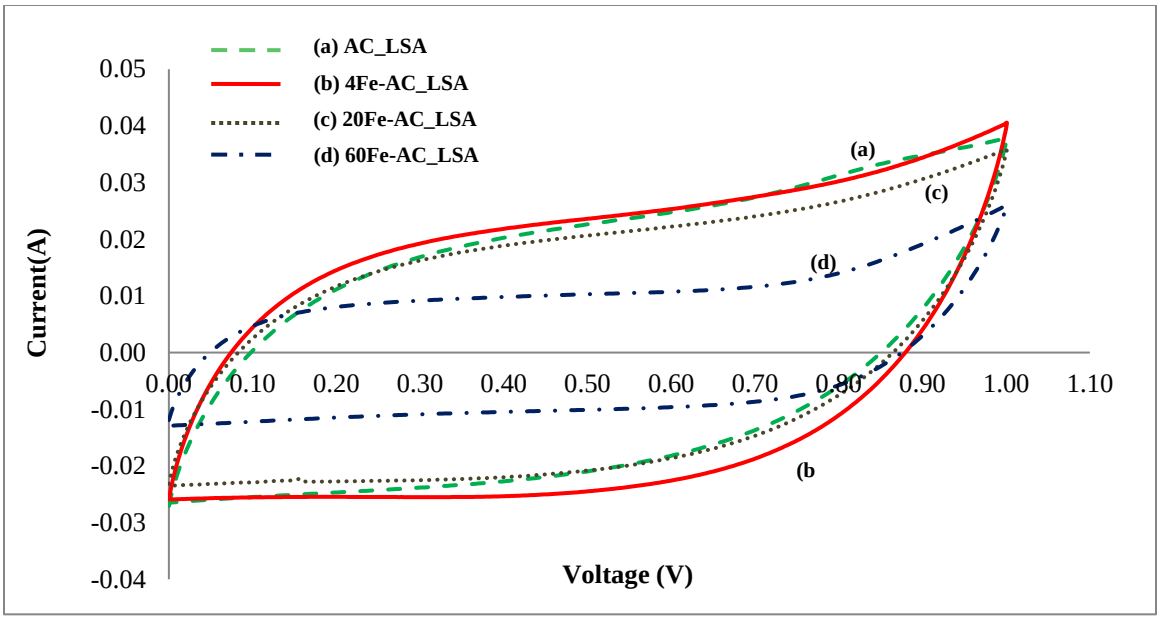


Figure 4.4. Cyclic voltammograms for different compositions of Fe_3O_4 loaded in AC_LSA electrodes, scanned at 10 mV/s, in 1 M Na_2SO_3.

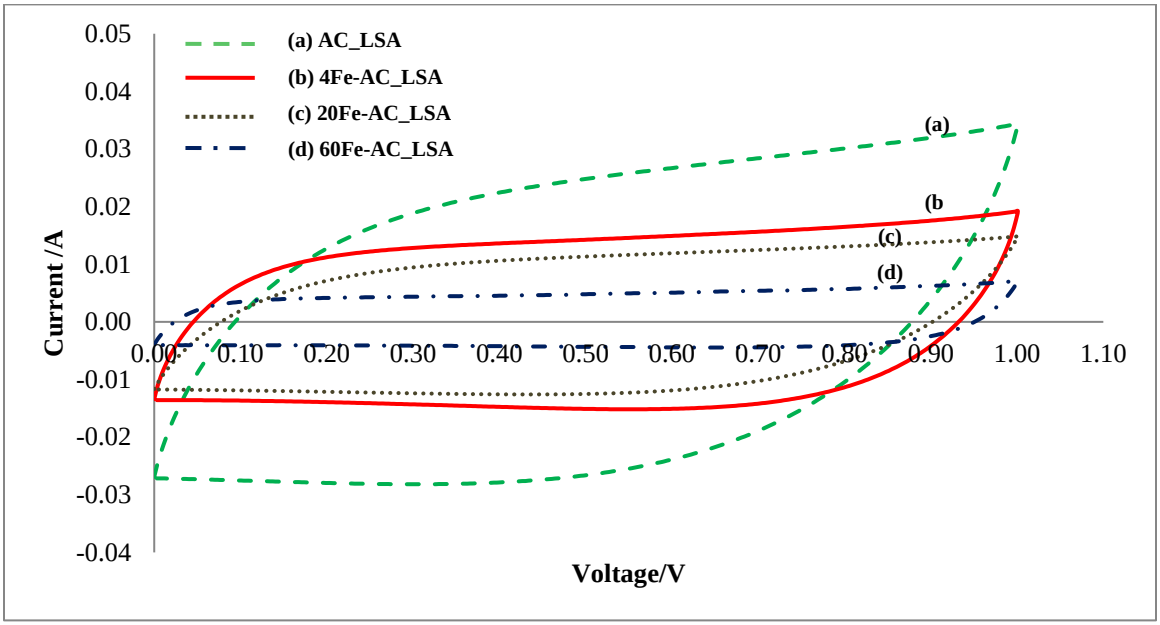


Figure 4.5. Cyclic voltammograms for different compositions of Fe_3O_4 loaded in AC_LSA electrodes, scanned at 10 mV/s, in 1 M Na_2SO_4.

4.3.1.2 Effect of anion

The type of electrolyte actually is playing a vital role in this context since the CV performance of the electrode material in Na_2SO_4 solution is found to be distinctly different if compared to Na_2SO_3 electrolyte. In fact, the AC electrode is found to exhibit the highest specific capacitance when 1 M Na_2SO_4 solution is adopted as the electrolyte. Table 4.2 summarises the effects of electrolyte and different Fe_3O_4 loading on the specific capacitance of the electrodes.

Table 4.2. Effects of electrolyte and Fe_3O_4 loading on specific capacitance of Fe_3O_4-AC composite electrodes, at the scan rate of 10 mV/s.

Electrode Material	Specific Capacitance (F/g)	
	1 M Na_2SO_3	1 M Na_2SO_4
AC_LSA	67.76	72.06
2Fe-AC_LSA	71.33	63.92
4Fe-AC_LSA	85.92	60.86
6Fe-AC_LSA	72.08	55.10
8Fe-AC__LSA	60.57	51.00
20Fe-AC_LSA	59.95	46.60
40Fe-AC_LSA	48.41	40.40
60Fe-AC_LSA	34.46	31.20
80Fe-AC_LSA	16.75	7.44

The enhancement of electrochemical storage properties of the AC_LSA electrode with a small amount of Fe_3O_4 nanoparticles in Na_2SO_3 is clearly observed, mainly attributed to the synergistic effect of the pseudocapacitance from metal oxide compound with the double layer capacitance AC_LSA material. Addition of relatively small amount of Fe_3O_4 nanoparticle is able to increase the surface area of AC_LSA material electrode. These results are also in good agreement with our observations in SEM (Figure 4.3) and BET analysis (Table 4.1). The large porosity of the structure with a higher specific surface area facilitates a better accessibility of the electrolyte inside the bulk of the electrodes during the electrochemical process. In addition to the increase of the effective

surface area, a small amount of Fe_3O_4 is also able to supply more electroactive sites for the adsorption/de-adsorption of sulphite (SO_3^{2-}) anions and promotes subsequent redox reactions to occur effectively across the interface of electrode-electrolyte.

The results obtained clearly indicate that overall a higher specific capacitance can be achieved in the SO_3^{2-} solutions than that in SO_4^{2-} electrolyte. The maximum specific capacitance of 85.92 F/g is obtained for the 4 wt % Fe_3O_4 added onto AC_LSA electrodes in Na_2SO_3 solution while this value is found to decrease to 60.86 F/g when Na_2SO_4 solution is adopted as the electrolyte. In an earlier work [44], the capacitance of the oxide was found to be sensitive to the anion species but not to either alkaline cations or electrolyte pH (<=11). Wu and his co-workers (2002) have characterized the capacitive behaviour of Fe_3O_4- carbon black electrodes in several aqueous electrolytes including Na_2SO_3 and Na_2SO_4 [2]. The authors suggested that the significant capacitive performance in Na_2SO_3 is attributed from the synergistic effect of both EDLC and the pseudocapacitance which involves successive reduction of the adsorbed sulphite anions. The capacitive current when Na_2SO_4 is used as electrolyte on the other hand is due to the contribution from EDLC mechanism only.

Qu et al. (1998) have suggested that the double layer capacitance contributed from the AC electrode could be associated with the separation of ions with opposite charges at electrode-electrolyte interface with no faradic reactions occurred [45]. However, some insignificant side reactions that involve Faradic charge transfer could happen over the potential range of operation, including the redox reaction of impurities in solution and functional group on the carbon surface. These kinds of faradaic reactions should be avoided as total amount of charges in the double layer will be consumed and thus self-discharge could happen and reduce the charge storage capability of the device.

Thus, it is strongly suggested that the enhanced capacitive performance in Na_2SO_3 electrolyte solution is believed originates from the combination of double layer capacitance and the pseudocapacitance that involves the successive reduction of the adsorbed sulphite anions. On the other hand, for the Na_2SO_4 solution, the capacitive characteristic is mainly due to the double layer capacitance contribution. Nevertheless, redox peaks were still observed on all the Fe_3O_4-AC_LSA composite electrodes in Na_2SO_4, revealing some extent of pseudocapacitive character though not as significant as

those in Na_2SO_3. The redox reactions can be viewed as adsorption/de-adsorption of sulphate or sulphite anions accompanied by the charge transfer process at the electrode/electrolyte interface with variation of iron valence state. Figure 4.6 shows the specific capacitances of Fe_3O_4-AC as a function of Fe_3O_4 loading in 1 M Na_2SO_3 and 1 M Na_2SO_4, respectively at the scan rate of 10 mV/s.

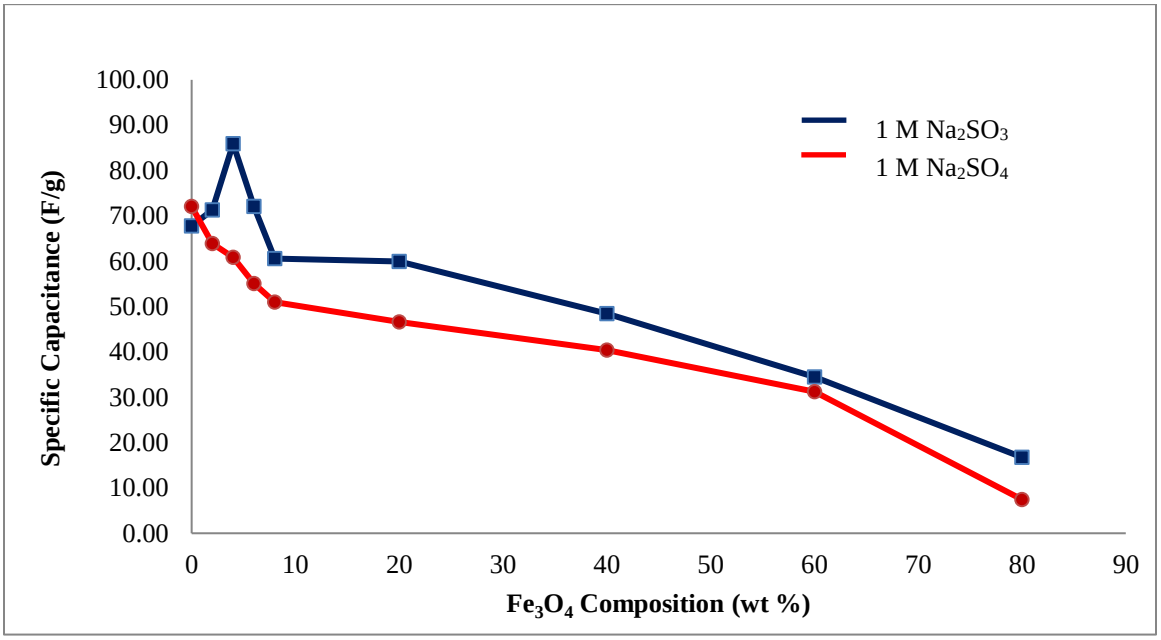


Figure 4.6. Specific capacitance of Fe_3O_4-AC_LSA composite electrodes as a function of Fe_3O_4 loading, in 1 M Na_2SO_3 and 1 M Na_2SO_4 respectively, at the scan rate of 10 mV/s between 0 to 1 V.

4.3.1.3 Effect of scan rate

The CV curves for 4Fe-AC_LSA composite and AC_LSA electrode at different scan rates within the voltage range of 0 to +1 V are shown in Figure 4.7 and 4.8, respectively. It can be seen that the total current increases with increasing scan rate. In a slow voltage scan, the diffusion layer will grow much further from the electrode compared to a fast scan. Consequently the flux reaching to the electrode surface is considerably smaller at slow scan rates than it is at faster rates. This reveals that the voltammetric current is directly proportional to the scan rate of CV, indicating an ideally capacitive behaviour of both AC electrodes and 4Fe-AC_LSA composite electrodes [47].

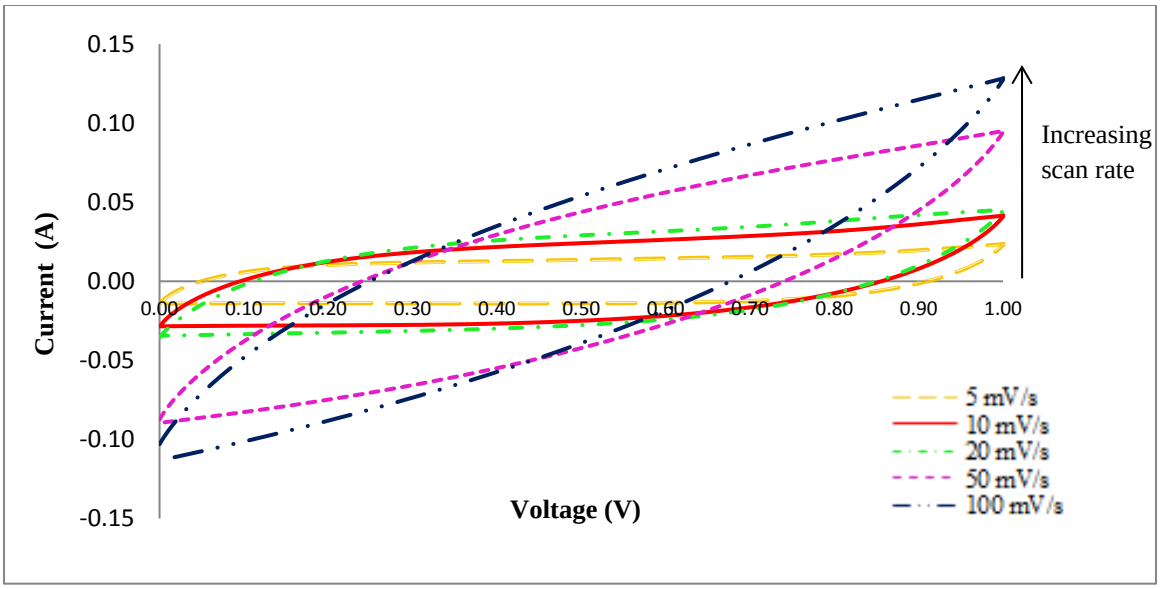


Figure 4.7. Cyclic voltammogram of (a) 4Fe-AC_LSA in 1 M Na_2SO_3 under different scan rates.

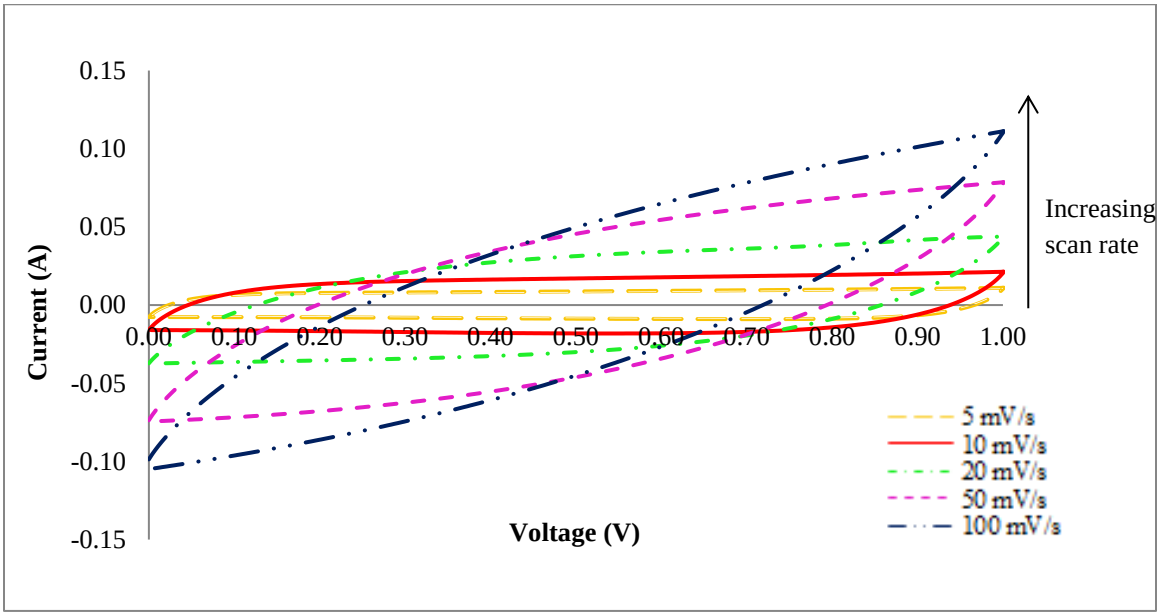


Figure 4.8. Cyclic voltammograms of AC_LSA electrodes in 1 M Na_2SO_3 under different scan rates.

Figure 4.9 presents the variation of specific capacitance of 4Fe-AC composite electrode and pure AC electrode at different scan rates in 1 M Na_2SO_3. It is apparent that the maximum specific capacitance values were obtained at 5 mV/s for 4Fe-AC_LSA (98.96 F/g) and pure AC_LSA electrodes (69.72 F/g), respectively. However, as the

voltage scan rate is increased, the CV diagrams become more inclined (45˚to the voltage axis). The capacitance of the electrode that is scanned at 100 mV/s is found to be 76 % less if compared to the sample that is analysed at a 5 mV/s scan rate.

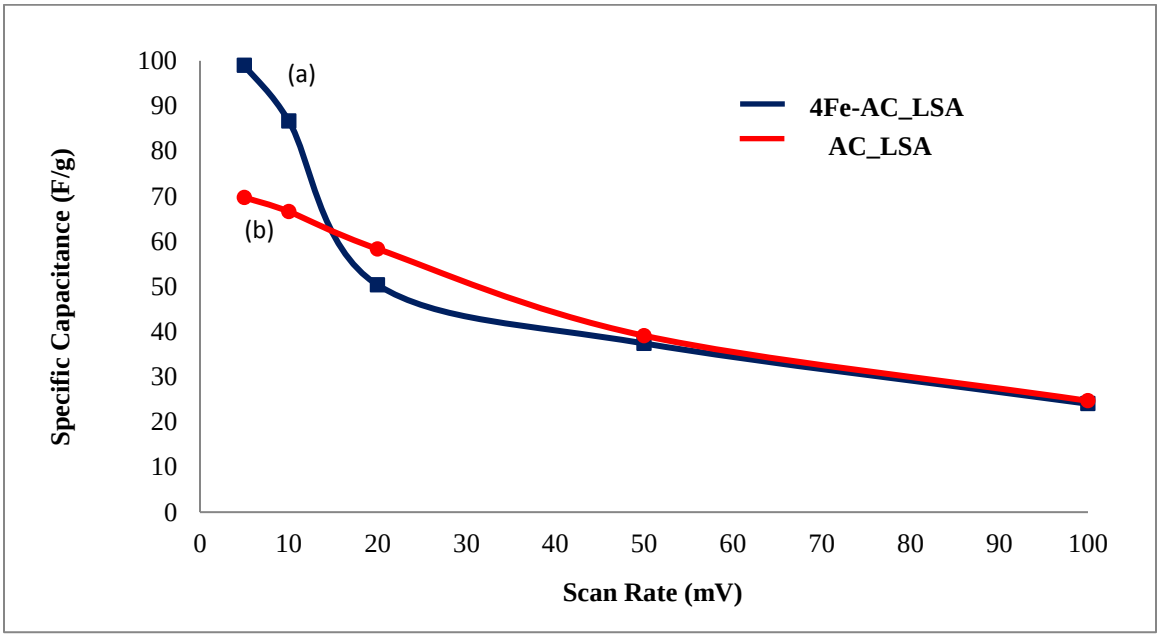


Figure 4.9. Variation of specific capacitance of (a) 4Fe-AC_LSA composite electrode and (b) AC_LSA electrode at different scan rates in 1 M Na_2SO_3.

4.3.2 Galvanostatic Charge-Discharge (GCD)

Figure 4.10 shows the galvanostatic charge and discharge profiles of AC_LSA, 4Fe-AC_LSA, 20Fe-AC_LSA and 60Fe-AC_LSA nanocomposite electrodes respectively, in 1 M Na_2SO_3 electrolytes at a current density of 10 mA/cm^2. An almost linear variation of the potential and the symmetrical charge- discharge profiles of AC electrode can be observed in Figure 4.10 (a), revealing the characteristics of a pure double layer supercapacitor. For the composite electrode with addition of 4 wt% Fe_3O_4 nanoparticles (Figure 4.10 (b)), the charge profiles are curved slightly at the later stage of charging process while the discharge curves are not perfectly linear, suggesting the pseudocapacitive behaviour of the oxide-based materials. The additional

pseudocapacitance behaviour could be attributed to the electrochemical adsorption and de-adsorption as well as the redox reactions occurred at the interface between electrode and electrolyte. This finding is in agreement with the little oxidation peak occurring in CV plot (Figure 4.4 (a))at the upper limit potential of 1 V. Similar deviation of the shape of the discharge curves from straight line are observed for 20Fe-AC_LSA and 60Fe-AC_LSA composite electrodes (Figure 4.10 (c) and (d)) as well.

Table 4.3 shows the comparison of specific capacitances and ESR values of AC_LSA, Fe_3O_4 and their composites obtained from charge-discharge measurement. The capacitance of 4Fe-AC_LSA composite electrodes demonstrate the highest in comparison to the other electrodes. This order of specific capacitance is consistent with the CV results. The average internal resistance (ESR) of the capacitor can be calculated according to Eq. (3.14) (refer to chapter 3). At the moment of current reversing from charging to discharging, the potential drop caused by electrode polarization at 10 mA/cm^2 in different Fe_3O_4 loading follows the order: 60Fe-AC_LSA > 20Fe-AC_LSA > AC_LSA > 4Fe-AC_LSA. This result is consistent with the AC impedance result in Table 4.5. The higher ESR value in the case of symmetric porous 60Fe-AC_LSA composite electrodes could be resulted from to the diffusional resistance of the electrolyte with the presence of low conductivity of Fe_3O_4 nanoparticles.

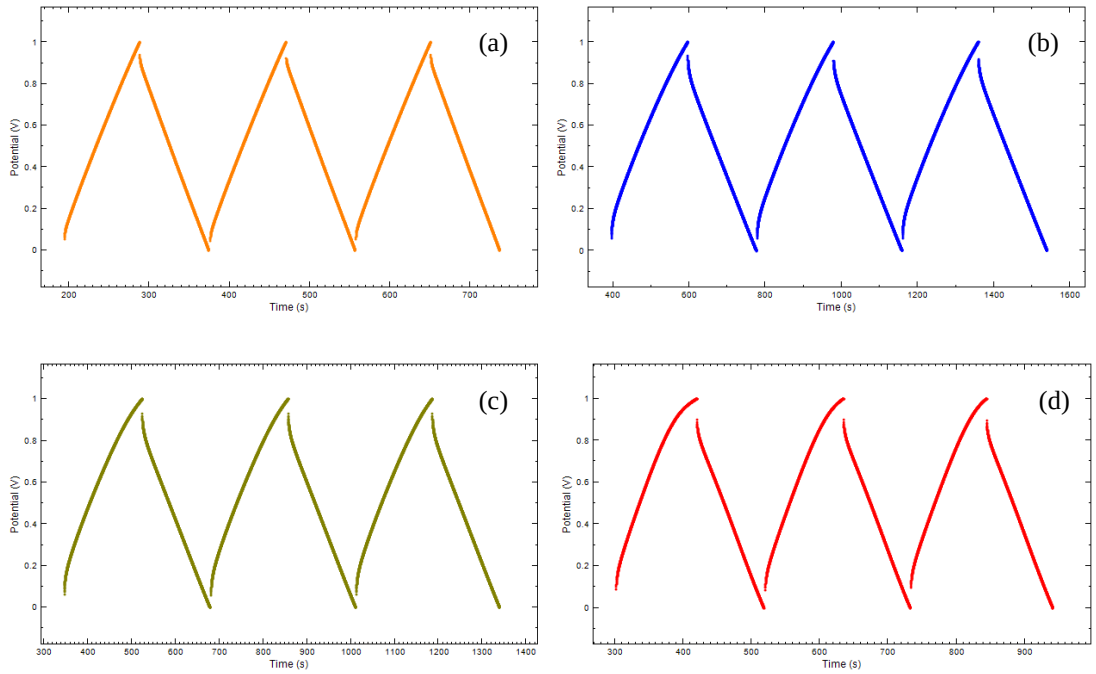


Figure 4.10. Charge-discharge curves of (a) AC_LSA electrode, (b) 4Fe-AC_LSA, (c) 20Fe-AC_LSA, (d) 60Fe-AC_LSA composite electrodes obtained at the constant density of 10 mA/cm^2.

Table 4.3.Comparison of specific capacitances and ESR values between AC, 4Fe-AC_LSA, 20Fe-AC_LSA, 60Fe-AC_LSA composite electrodes.

Electrode material	Charge-discharge measurement at 10 mA/cm^2	
	Specific capacitance (F/g)	ESR (Ω)
AC_LSA	69.26	1.67
4Fe-AC_LSA	93.54	1.79
20Fe-AC_LSA	72.24	1.96
60Fe-AC_LSA	43.26	2.59

The specific capacitance values of AC_LSA and 4Fe-AC_LSA composite electrodes corresponding to the current densities of 10, 15, 20 and 25 mA/cm^2 are demonstrated in Figure 4.11. It can be seen that the specific capacitance values of the electrodes decreased as the current

density increased. In general, the specific capacitance decreases gradually with increasing current density due to large IR drop at a large discharge current density that leads to the small specific capacitance [46]. This is because the mobile ions do not have enough time to diffuse into the core of the material due to the strong polarisation at higher current density [55]. At lower current densities, complete intercalation /extraction take place at the inner and outer of electrodes as a result of easy accessibility of ions to almost all available pores of the electrode. However, at higher current densities, an effective utilization of pseudocapacitive material for the ion insertion is limited only to the outer surface of electrodes. It results in the reduction of specific capacitance values. The same phenomenon has been observed for increasing the voltage scan rate [56].

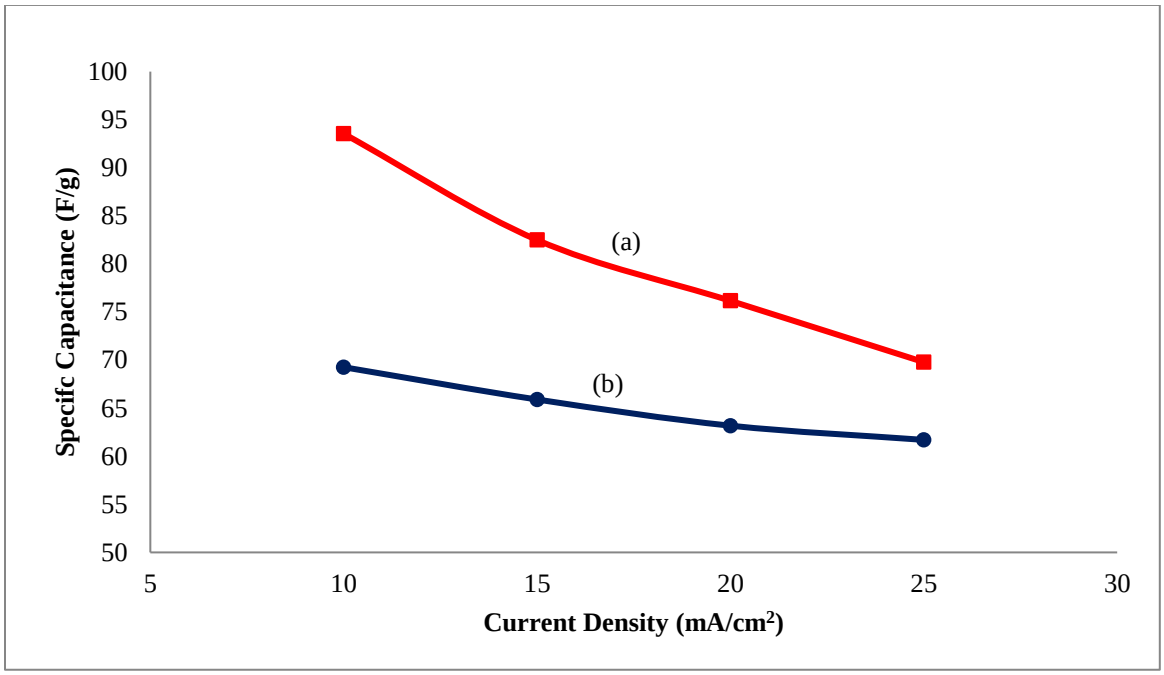


Figure 4.11. Variation of specific capacitance of (a) 4Fe-AC__LSA composite electrode and (b) AC electrode at different current densities in 1 M Na_2SO_3.

4.3.3 Electrochemical Impedance Spectroscopy (EIS)

The EIS measurement was carried out on AC_LSA and Fe_3O_4-AC_LSA composite electrodes in the frequency range of 10^4 to 10^{-2} Hz. Figure 4.12 displays the Nyquist plots of the nano-Fe_3O_4-AC_LSA composite electrodes with different compositions in 1 M Na_2SO_3. It can be seen that all the impedances consist of an arc and a slanted line at low frequency. In the high

frequency region, the intercept of the semicircle on the real axis of the Nyquist spectrum represents the solution resistance (R_S) which provides the resistance at the electrode-electrolyte interface. The R_S arise mainly due to the difference in the conductivity between solid electrode (electronic conductivity) and the aqueous electrolyte (ionic conductivity) [57]. Additionally, the impedance behaviour in this region is the characterisitc of the resistance from Faradaic reaction associated with the interfacial processes of the porous composite electrode.

The semicircles in the high- and mid-frequency regions are attributed to an interfacial charge transfer resistance (R_{CT}) or polarisation resistance (R_p) and the double layer capacitance (C_{DL}) connected parallel to each other [58]. The observed charge transfer resistance represents the sum of the resistance due to the ion migration through the bulk of the composite electrode, the resistance of the charges in the pores of the composite electrode, the electrode-electrolyte resistance and the electrode resistance.After the semicircle, the Nyquist spectrum shows a straight line in the low-frequency region corresponding to the Warburg element, W [58]. Typically, the Warburg element represents the diffusion of SO_3^{2-} ions from electrolyte into the pores on the surface of the electrode, which happened during the transition from the high-frequency semicircle to the mid-frequency spike. With the improved diffusion process, electrochemical performance could be increased accordingly. Reduced ohmic and charge transfer resistances can lead to larger current reaching on the electrode which in turn enhance the diffusion rate of ions towards the electrodes [59].

From the Nyquist plot showed in Figure 4.12, it is apparent that the major difference in term of the diameter of semicircle can be clearly observed between the AC_LSA with different compositions of Fe_3O_4 loading. The 4Fe-AC_LSA composite electrode exhibits the smallest diameter at high frequency and reveals its minimum R_{CT}. A reduction in the value of R_{CT} implies that the surface modification by addition of small amount of Fe_3O_4 is able to provide more accessible sites which are ready for the mobile charges near the electrode surface, leading to an increase in the value of double layer capacitance.

However, the diameter of the semicircles is found to increase with further addition of Fe_3O_4 in the range of 20 – 60 wt %, indicating the higher charge transfer resistance for such compound. The observed increase in charge transfer resistance seems to be consistent with the observation in another study [46], which suggested that the irreversible oxidation or reduction process involving the formation of insulating oxide layer on the electrode surface could occur

during the oxidative scan near the high-potential end. All the Nyquist spectra show the straight line inclined at an angle of around 45° to the real axis at low frequency, indicating the diffusion controlled process in these electrodes.

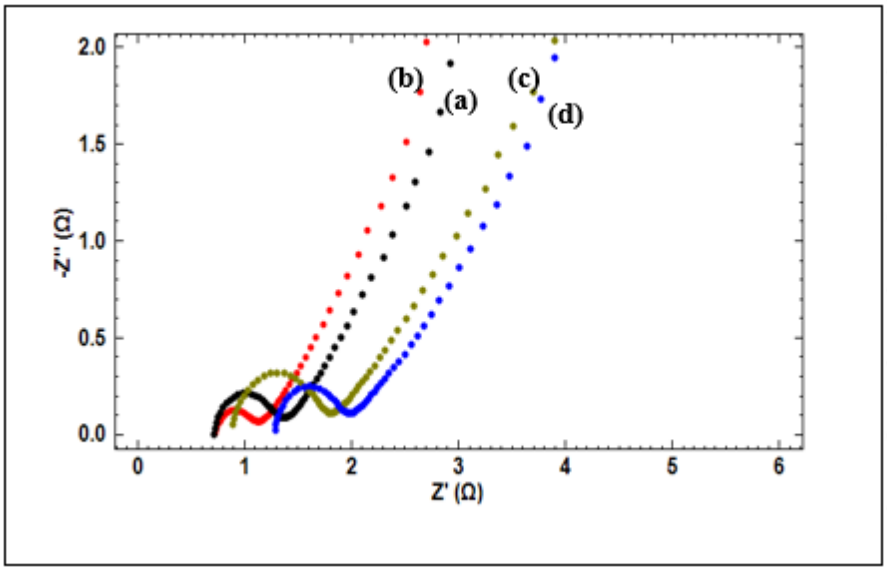


Figure 4.12: Nyquist plots obtained for composite electrodes with different Fe_3O_4 loading: (a) AC_LSA, (b) 4Fe-AC_LSA, (c) 20Fe-AC_LSA, (d) 60Fe-AC_LSA, at 0 V over the frequency range of 100 kHz – 0.01 Hz in 1 M Na_2SO_3.

The fitting of the impedance expressions obtained from the equivalent circuit to the experimental Nyquist spectra was performed using the NOVA equivalent circuit editor in order to determine the most representative physical processes that taking place in the systems under investigation (Figure 4.13).Table 4.4 summarises the equivalent circuit parameters obtained from the fitting results in 1 M Na_2SO_3.

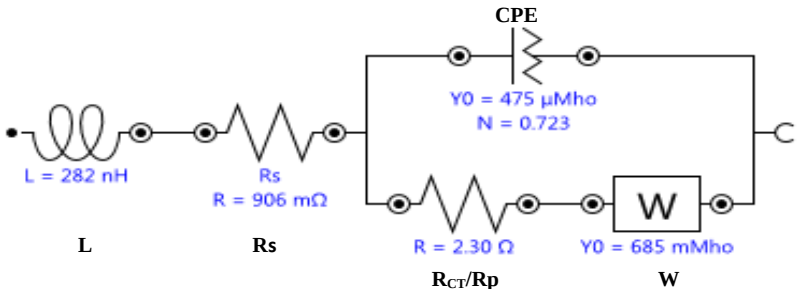


Figure 4.13. The equivalent circuit used to fit the Nyquist spectra using NOVA equivalent circuit editor.

In the present study, the double layer capacitor in EIS experiments often behaves like constant-phase element (CPE) as a result of imperfection on the real electrochemical cell including surface roughness, leaky capacitor and non-uniform current distribution [60]. The negative phase at high frequencies reveals the effect of inductance error (L) on the impedance spectra of an electrochemical cell attributed to the improper length of lead and wiring configuration [61].

Table 4.4. Simulated Values of L. R_S, R_{CT}, CPE, W, n from the Equivalent Circuit in Figure 4.13.

Electrode Composition	Inductance, L (nH)	Solution Resistance , R_S (Ω)	Charge Transfer Resistance, R_{CT} (Ω)	Constant-Phase Element, CPE (µMho)	Warburg Element, W (mMho)	Exponent (n)
AC_LSA	282	0.90	2.30	475	685	0.723
4Fe-AC_LSA	230	0.83	1.37	772	487	0.695
20Fe-AC_LSA	235	1.55	1.87	583	622	0.710
60Fe-AC_LSA	274	1.48	4.28	452	519	0.727

From Table 4.4, it is found that 4 wt % Fe_3O_4 in the composite electrode shows relatively lower R_S (0.83 Ω) and Rct (1.37 Ω) in comparison to R_S (0.90 Ω) and R_{CT} (2.30 Ω) of pure AC_LSA electrode. A reduced value of R_{CT} implies that the surface modification with very small amount of Fe_3O_4 enhances the conductivity of the composite electrodes. Additionally, Warburg impedance (W) of 4Fe-AC_LSA composite materials shows a much lower value compared to pure AC electrode, which corresponds to more vertical line leaning to the imaginary axis at a low frequency region. Similar EIS investigations were reported in other studies as well ([41], [58]) showing that enhanced capacitive performance is related to lower Warburg impedance values.

These findings reveal that 4Fe-AC_LSA composite materials demonstrate better capacitive behaviour due to more facile electrolyte diffusion to the composite surface.

In general, porous electrodes generate an exponent value of n = 0.5 while rough electrode possesses n value between 0.5 and 1 [62]. In this case, it can be observed that the values of n increase with increasing Fe_3O_4 loading. The higher values of the exponent in 20Fe-AC_LSA and 60Fe-AC_LSA composite materials reveal that these composite electrodes are behaving as typical non-porous electrodes in which the ion diffusion is taking place only on the surface of the composite electrodes. These findings are consistent with SEM micrographs (Figure 4.3) and BET surface area measurement (Table 4.1) on composite electrodes with different Fe_3O_4 loading. The non-porous nature limits the number of ions that diffuse into the bulk of electrodes and thus yields lower specific capacitance compared to the porous electrodes.

4.3.4 Ragone Plot and Cyclability Analysis

In order to further improve the electrochemical performance of the composite electrodes, higher surface area of AC was employed to fabricate the composite electrodes. The capacitive performance of composite electrodes fabricated with 4 wt% Fe_3O_4 loading on low-surface-area AC (4Fe-AC_LSA) and high-surface-area AC (4Fe-AC_HSA), were evaluated by using cyclic voltammetry (CV). Figure 4.14 shows the typical CV curves of the composites and pure AC electrodes at a scan rate of 10 mV/s. As expected, 4Fe-AC_HSA demonstrates the highest specific capacitance (127 F/g) in comparison to 4Fe-AC_LSA (86 F/g) while AC_HSA (104 F/g) is also more superior than that of AC_LSA electrodes (64 F/g). Meanwhile, the specific energy and the specific power of the composite electrodes were calculated using the Eq. (3.17) and (3.18) (Chapter 3). The relationship between the specific energy and the specific power of 4Fe-AC_HSA is shown in the Ragone plot (Figure 4.15). The composite electrodes delivered high specific energy of ~15 Wh/kg at specific power of 206 W/kg, though this value reduced with increasing specific power. To evaluate the electrochemical cycling stability 4Fe-AC_HSA, the capacitive retention was measured by continuous CV at a scan rate of 10 mV/s. As shown in Figure 4.16, the specific capacitance of composite electrodes exhibits good cycling stability with about 96 % of the original capacitance is retained after 1000 cycles. Figure 4.17 shows the comparative CV profiles between 100^{th} cycle (127.2 F/g) and 1000^{th} cycle (124.5 F/g), revealing

no significant capacitance degradation during cycling. The support of AC matrix would enhance the mechanical strength of composite materials, hence resulting in good cycling stability.

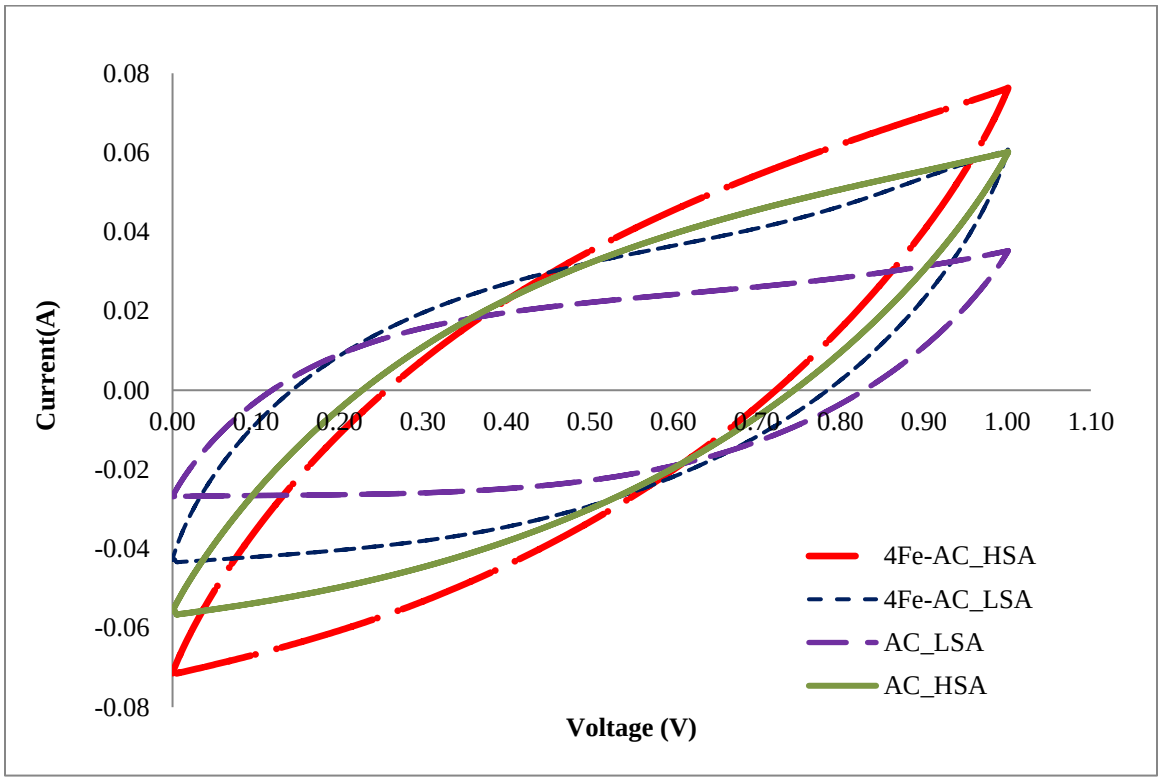


Figure 4.14. CV profile comparison of AC electrodes with lower surface area (AC_LSA), AC electrodes with higher surface area (AC_HSA) and their composite electrodes at 10 mV/s in 1 M Na_2SO_3.

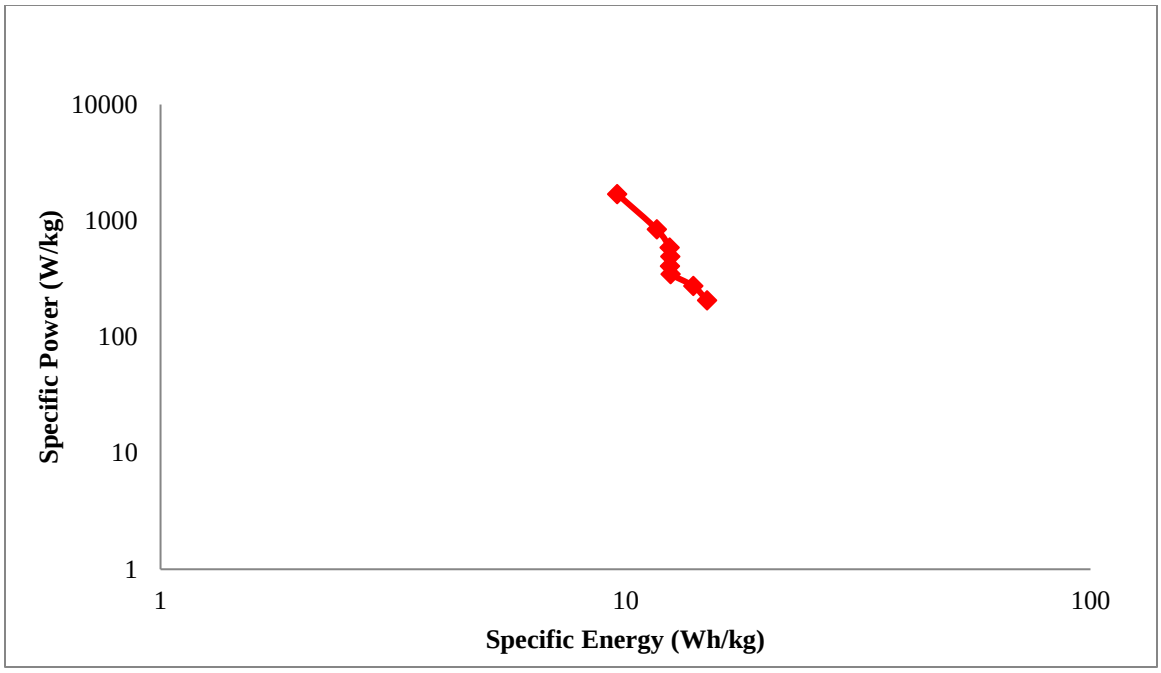


Figure 4.15. Ragone plot of 4Fe-AC_HSA composite electrodes.

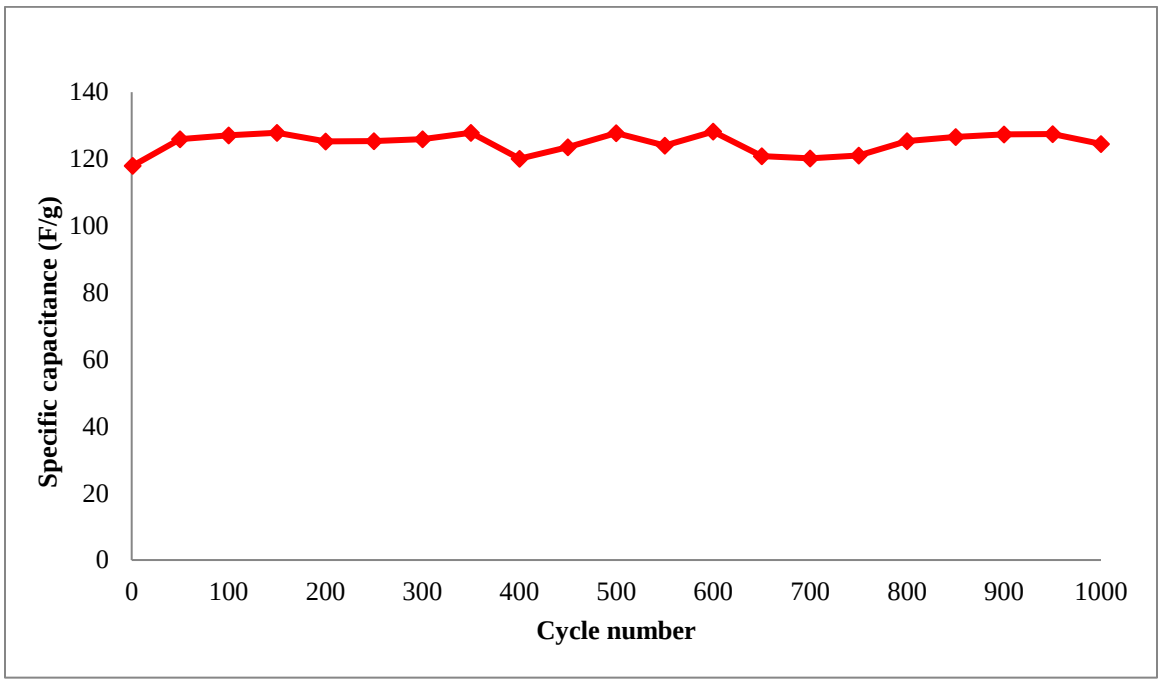


Figure 4.16. Cycle stability of 4Fe-AC_HSA composite electrodes in aqueous Na_2SO_3 electrolyte at scan rate of 10 mV/s between 0 and 1 V.

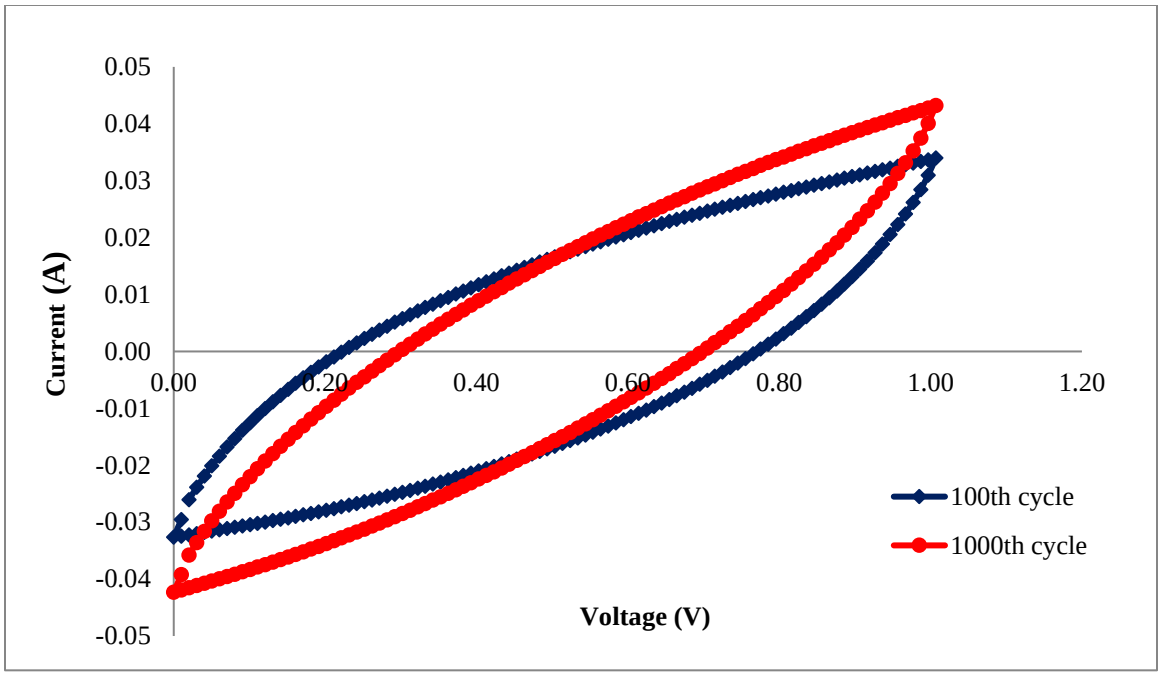


Figure 4.17. CV profile comparison of 4Fe-AC_HSA composite electrodes between 100th cycle and 1000th cycle at 10 mV/s in 1 M Na_2SO_3.

4.5 Summary

The capacitive performance of Fe_3O_4 -AC nanocomposite electrode materials in Na_2SO_3 and Na_2SO_4 has been characterized. The highest specific capacitance of 127 F/g is achieved with a relatively low Fe_3O_4 loading on high-surface-area AC. However, bulk increasing of the Fe_3O_4 content is found to distort the capacitive performance and deteriorate the specific surface area of the electrode, mainly due to the aggregation of the Fe_3O_4 particles within the composite. Additionally, the Fe_3O_4-AC nanocomposite electrode in Na_2SO_3 electrolyte exhibits a better charge storage performance if compared with Na_2SO_4 solution. It is believed that Fe_3O_4 nanoparticles can provide favourable surface adsorption sites for sulphite (SO_3^{2-}) anions during the redox and intercalation reactions. The improvement of the capacitive performance of the Fe_3O_4 –AC composite electrode is believed attributed to the contribution of synergistic effect of EDLC and pseudocapacitance charge storage mechanism, as well as the enhancement on the specific surface areas of the electrode. Additionally, over 96 % of the original capacitance was retained after 1000 cycles, indicating a good cycle stability of composite materials.

Reference

[1] A. D. Pasquier, I. Plitz, J. Gural, S. Menocal, and G. Amatucci, "Characteristics and performance of 500 F asymmetric hybrid advanced supercapacitor prototypes," Journal of Power Sources 113 (2003) 62-71.

[2] N.L. Wu, "Nanocrystalline oxide supercapacitors,"Materials Chemistry and Physics 75 (2002) 6-11.

[3] B. E. Conway, V. Birss, and J. Wojtowicz, "The role and utilization of pseudocapacitance for energy storage by supercapacitors," Journal of Power Sources 66 (1997)1-14.

[4] S. W. Zhang and G. Z. Chen, "Manganese oxide based materials for supercapacitors," Energy Materials: Materials Science and Engineering for Energy Systems 3(2008)186-200.

[5] D. Kalpana, K. S. Omkumar, S. S. Kumar, and N. G. Renganathan, "A novel high power symmetric ZnO / carbon aerogel composite electrode for electrochemical supercapacitor," Electrochimica Acta 52 (2006)1309-1315.

[6] H.Wang, Z.Y.Tang, L.Sun, Y.B.He, Y.X.Wu, Z.Y.Li, "Capacitance performance enhancement of TiO_2 doped with Ni and graphite," Rare Metals 28 (2009) 231-236.

[7] T. Cottineau, M. Toupin, T. Delahaye, T. Brousse, and D. Belanger, "Nanostructured transition metal oxides for aqueous hybrid electrochemical supercapacitors," Applied Physics A 82 (2005) 599-606.

[8] A. K. Shukla, S. Sampath, and K. Vijayamohanan, "Electrochemical supercapacitors : Energy storage beyond batteries,"Current Science 79 (2000)1656-1661.

[9] H. Kim and B. N. Popov, "Characterization of hydrous ruthenium oxide / carbon nanocomposite supercapacitors prepared by a colloidal method," Journal of Power Sources 104 (2002) 52-61.

[10] C.C.Hu and W.C.Chen, "Effects of substrates on the capacitive performance of $RuO_x \cdot nH_2O$ and activated carbon – RuO_x electrodes for supercapacitors," Electrochimica Acta 49 (2004)3469-3477.

[11] C.C.Hu, M.J.Liu, and K.H.Chang, "Anodic deposition of hydrous ruthenium oxide for supercapacitors," Journal of Power Sources 163 (2007) 1126-1131.

[12] P. Simon and Y. Gogotsi, "Materials for electrochemical capacitors," Nature Materials 7(2008) 845-854.

[13] X. Du, C. Wang, M. Chen, Y. Jiao, and J. Wang, "Electrochemical Performances of Nanoparticle Fe_3O_4 / Activated Carbon Supercapacitor Using KOH Electrolyte Solution" Journal of Physical Chemistry C 113 (2009) 2643-2646.

[14] T. Nathan, A. Aziz, A. F. Noor, and S. R. S. Prabaharan, "Nanostructured NiO for electrochemical capacitors : synthesis and electrochemical properties" Journal of Solid State Electrochemistry 12 (2008) 1003-1009.

[15] G.H.Yuan, Z.H.Jiang, A. Aramata, and Y.Z.Gao, "Electrochemical behaviour of activated-carbon capacitor material loaded with nickel oxide," Carbon 43 (2005) 2913-2917.

[16] V. Ganesh, S. Pitchumani, and V. Lakshminarayanan, "New symmetric and asymmetric supercapacitors based on high surface area porous nickel and activated carbon," Journal of Power Sources 158 (2006) 1523-1532.

[17] J. Yeong, K. Liang, K. Hyeok, and Y. Hee, "Nickel oxide / carbon nanotubes nanocomposite for electrochemical capacitance," Synthetic metals 150 (2005) 153-157.

[18] H. Y. Lee and J. B. Goodenough, "Supercapacitor Behaviour with KCl Electrolyte," Journal of Solid State Chemistry 223 (1999) 220-223.

[19] N. Nagarajan, H. Humadi, and I. Zhitomirsky, "Cathodic electrodeposition of MnO_x films for electrochemical supercapacitors," Electrochimica Acta 51 (2006) 3039-3045.

[20] D.Belanger, T. Brousse and J. W. Long, "Manganese Oxides : Battery Materials Make the Leap to Electrochemical Capacitors," Interface (2008) 49-52.

[21] S.L.Kuo and N.L.Wu, "Composite Supercapacitor Containing Tin Oxide and Electroplated Ruthenium Oxide," Electrochemical Solid State Letter 6 (2003) A85-A87.

[22] M. Jayalakshmi, M. M. Rao, N. Venugopal, and K.-bum Kim, "Hydrothermal synthesis of $SnO_2 - V_2 O_5$ mixed oxide and electrochemical screening of carbon nano-tubes (CNT), $V_2 O_5$, $V_2 O_5$ – CNT , and $SnO_2 - V_2 O_5$ – CNT electrodes for supercapacitor applications," Journal of Power Sources 166 (2007) 578-583.

[23] T. Lu, Y. Zhang, H. Li, L. Pan, Y. Li, and Z. Sun, "Electrochemical behaviours of graphene – ZnO and graphene – SnO_2 composite films for supercapacitors," Electrochimica Acta 55 (2010) 4170-4173.

[24] N. Nagarajan and I. Zhitomirsky, "Cathodic electrosynthesis of iron oxide films for electrochemical supercapacitors," Journal of Applied Electrochemistry 36(2006)1399-1405.

[25] K.Y. Xie, J.Li, Y.Q.Lai, W.Lu, Z.A.Zhang, Y.X.Liu, L.M.Zhou, H.T.Huang, "Highly ordered iron oxide nanotube arrays as electrodes for electrochemical energy storage," Electrochemistry Communications 13 (2011) 657-660.

[26] M. Mallouki, F. Tran-Van, C. Sarrazin, P. Simon, B. Daffos, A. De, C. Chevrot, J. Fauvarque, "Polypyrrole-Fe_2O_3 nanohybrid materials for electrochemical storage," Journal of Solid State Electrochemistry 11(2006) 398-406.

[27] N.L.Wu, S.L.Wang, and C.Y.Han, "Electrochemical capacitor of magnetite in aqueous electrolytes," Journal of Power Sources 113(2003)173-178.

[28] J. Chen, K. Huang, and S. Liu, "Hydrothermal preparation of octadecahedron Fe_3O_4 thin film for use in an electrochemical supercapacitor," Electrochimica Acta, vol. 55(2009)1-5.

[29] T. Brousse and D. Belanger, "A Hybrid Fe_3O_4-MnO_2 Capacitor in Mild Aqueous Electrolyte," Electrochemical and Solid-State Letters 6(2003)A244-A248.

[30] S.Y. Wang, K.C. Ho, S.L.Kuo and N. L. Wu, "Investigation on Capacitance Mechanisms of Fe_3O_4 Electrochemical Capacitors," Journal of The Electrochemical Society 153(2006)A75-A80.

[31] M. B. Sassin, A. N. Mansour, K. A. Pettigrew, D. R. Rolison, and J. W. Long, "Electroless Deposition of Conformal Nanoscale Iron Oxide on Carbon Charge Storage," ACS Nano 4 (2010)4505-4514.

[32] D. P. Dubal, W. B. Kim, and C. D. Lokhande, "Galvanostatically deposited Fe: MnO_2 electrodes for supercapacitor application," Journal of Physics and Chemistry of Solids 73 (2012) 18-24.

[33] S.C. Wang, C.Y. Chen, T.C. Chien, P.Y. Lee and C.K. Lin, "Supercapacitive properties of spray pyrolyzed iron-added manganese oxide powders deposited by electrophoretic deposition technique," Thin Solid Films 517 (2008) 1234-1238.

[34] Y.H.Kim and S.J.Park, "Roles of nanosized Fe_3O_4 on supercapacitive properties of carbon nanotubes," Current Applied Physics 11 (2011) 462-466.

[35] C.C. Hu, M.J. Liu, and K.H. Chang, "Anodic deposition of hydrous ruthenium oxide for supercapaciors: Effects of the AcO− concentration, plating temperature, and oxide loading," Electrochimica Acta 53 (2008) 2679-2687.

[36] S. J. Gregg and K. S. W. Sing, Adsorption, Surface Area and Porosity Academic Press 1982.

[37] S. W. Zhang and G. Z. Chen, "Manganese oxide based materials for supercapacitors," Energy Materials: Materials Science and Engineering for Energy Systems 3 (2008)186-200.

[38] H. Kim and B. N.Popov, "Characterisation of Hydrous Ruthehium Oxide/Carbon nanocomposite Supercapacitors Prepared by a Colloidal Method," Journal of Power Sources 104 (2002) 52-61.

[39] C.C. Hu and W.C. Chen, "Effects of substrates on the capacitive performance of $RuO_x \cdot nH_2O$ and activated carbon–RuO_x electrodes for supercapacitors," Electrochimica Acta 49 (2004) 3469-3477.

[40] L. L. Zhang, T. Wei, W. Wang, and X. S. Zhao, "Manganese oxide–carbon composite as supercapacitor electrode materials," Microporous and Mesoporous Materials 123 (2009) 260-267.

[41] X. Wang, X. Han, M. Lim, N. Singh, C. L. Gan, M. Jan, and P. S. Lee, "Nickel Cobalt Oxide-Single Wall Carbon Nanotube Composite Material for Superior Cycling Stability and High-Performance Supercapacitor Application," The Journal of Physical Chemistry C 116 (2012) 12448-12454.

[42] N.L. Wu, S.Y. Wang, C.Y. Han, D.S. Wu, and L.R. Shiue, "Electrochemical Capacitor of Magnetite in Aqueous Electrolytes," Journal of Power Sources 113 (2003) 173-178.

[43] D. P. Dubal, W. B. Kim, and C. D. Lokhande, "Galvanostatically deposited Fe: MnO2 electrodes for supercapacitor application," Journal of Physics and Chemistry of Solids 73 (2012) 18-24.

[44] S.Y. Wang, K.C. Ho, S.L. Kuo, and N.L. Wu, "Investigation on Capacitance Mechanisms of Fe_3O_4 Electrochemical Capacitors," Journal of The Electrochemical Society 153 (2006) A75.

[45] D. Qu, H. Shi, "Studies of Activated Carbons Used in Double-Layer Capacitors," Journal of Power Sources 74 (1998) 99-107.

[46] X. Du, C. Wang, M. Chen, Y. Jiao, and J. Wang, "Electrochemical Performances of Nanoparticle Fe_3O_4-Activated Carbon Supercapacitor Using KOH Electrolyte Solution," Journal of Physics and Chemistry of Solids 113 (2009) 2643-2646.

[47] Electrochemistry Fundamentals [Online]. Available: http://www.cheng.cam.ac.uk/research/groups/electrochem/teaching.html[access in Jan 2012]

[48] P. M. Kulal, D. P. Dubal, C. D. Lokhande, and V. J. Fulari, "Chemical synthesis of Fe_2O_3 thin films for supercapacitor application," Journal of Alloys and Compounds 509 (2011) 2567-2571.

[49] Morales, Julián, L. Sánchez, F. Martín, F. Berry, and X. Ren, "Synthesis and Characterization of Nanometric Iron and Iron-Titanium Oxides by Mechanical Milling," Journal of The Electrochemical Society 152 (2005) A1748.

[50] Y.H. Kim and S.J. Park, "Roles of Nanosized Fe_3O_4 on Supercacitive Properties of Carbon Nanotubes," Current Applied Physics, vol. 11, pp. 462-466, 2011.

[51] J. H. Park and O. O. Park, "Morphology and Electrochemical Behaviour of Ruthenium Oxide Thin Film Deposited on Carbon Paper," Journal of Power Sources, vol 109 (2002) 121-126.

[52] Gamry Instruments. (2012). Application Note: Testing Super-Capacitors Part 1 – CV, EIS and Leakage Current [Online]. Available: www.gamry.com[access in Jan 2012]

[53] J. Chen, K. Huang, and S. Liu, "Hydrothermal preparation of octadecahedron Fe_3O_4 thin film for use in an electrochemical supercapacitor," Electrochimica Acta 55 (2009) 1-5.

[54] T. Brousse and D. Bélanger, "A Hybrid Fe_3O_4-MnO_2 Capacitor in Mild Aqueous Electrolyte," Electrochemical and Solid-State Letters 6 (2003) A244.

[55] K.Kathikeyan, V.Aravindan, S.B.Lee, I.C.Jang, H.H.Lim, G.J.Park, M.Yoshio and Y.S.Lee "A novel asymmetric hybrid supercaapcitor based on Li_2FeSiO_4 and actiavted carbon electrodes," Journal of Alloys and Compounds 504 (2010) 224–227.

[56] A. Malak, K. Fic, G. Lota, C. Vix-Guterl, and E. Frackowiak, "Hybrid materials for supercapacitor application," Journal of Solid State Electrochemistry 14 (2009) 811-816.

[57] S. K. Meher and G. R. Rao, "Ultralayered Co_3O_4 for High-Performance Supercapacitor Applications," The Journal of Physical Chemistry C 115 (2011)15646-15654.

[58] C. Masarapu, H. F. Zeng, K. H. Hung, and B. Wei, "Effect of Temperature on the Capacitance of Carbon Nanotube Supercapacitors," ACS Nano 3 (2009) 2199–2206.

[59] A. Chu and P. Braatz, "Comparison of Commercial Supercapacitors and High-Power Lithium-ion batteries for Power-Assist Applications in Hybrid Electric Vehicles: Initial Characterisation," Journal of Power Sources 112 (2002) 236-246.

[60] V. D. Jovic. (2012).Determination of the correct value of Cdl from the impedance results fitted by the commercially available software [Online]. Available: http://www.gamry.com [access in Jan 2012]

[61] J. R. Macdonald, E.Barsoukov, Impedance Spectroscopy, Theory Experiment and Applications Canada: John Wiley & Sons, Inc, 2005.

[62] C. Masarapu, H. F. Zeng, K. H. Hung, and B. Wei, "Effect of Temperature on the Capacitance of Carbon Nanotube Supercapacitors," ACS Nano 3 (2009) 2199-2206.

[63] W.C.Fang, J.H.Huang, L.C.Chen, Y.L.Su,K.H.Chen, "Effect of temperature annealing on capacitive and structural properties of hydrous ruthenium oxides," Journal of Power Sources 160 (2006) 1506-1510.

CHAPTER 5

Electrochemical Studies on Calcined TiO_2-Activated Carbon and ZnO-Activated Carbon Composite Electrodes for Aqueous Supercapacitors

5.1 Introduction

Electrochemical capacitor, also well-known as supercapacitor, has significant potential to become an alternative or complement to other energy storage systems such as secondary battery and fuel cell [1]. In particular, metal oxide-based composite materials have demonstrated as the most promising electrode materials for various large scale applications in load levelling, hybrid electric vehicle, distributed power generator, cold-start assistance and catalytic converter preheating [2]. Although ruthenium oxide-, nickel oxide- and manganese oxide-based composite materials are well-established as effective core materials for electrochemical capacitor, the demand for novel compound with low processing cost and minimum environmental impact continues to become the subject of research interest during the recent years.

Titanium oxide (TiO_2) and zinc oxide (ZnO) have received a great deal of attention in many applications such as solar cells, sensors, dielectric materials and photocatalysts. The natural abundance and environmental compatibility have made TiO_2 and ZnO potentially advantageous electrode materials [3-4]. Several researchers have used TiO_2 nanotubes as a solid support to improve the dispersibility of some metal oxides including RuO_2 as the pseudocapacitive electrodes [5]. In fact, the polarization of AC can be reduced through the modification with nanosized TiO_2 via the increased ion concentration on the double-layer of AC [6]. A novel approach by coating nanosized TiO_2 on graphene via atomic layer deposition was reported recently [7]. A comparative evaluation of ZnO-graphene and pure graphene electrodes shows that the specific capacitances of ZnO-graphene and graphene electrodes that calculated from the study are 62 and 39 F/g respectively, a distinctively 58% enhancement [8]. The increase of the total capacitance is attributed to the redox reactions through the electrochemical conversion of Zn^{2+} to other valence states.

Heat treatment on the core electrode material is one of the possible optimisation techniques for improved electrochemical capacitor performance as calcining temperature plays a critical role in affecting the electrochemical characteristic of the supercapacitor [9]. Essentially, three significant transformations as a consequence of heat treatment are observed in the oxide electrodes: (i) removal of water molecules, (ii) surface area reduction, and (iii) changes in microstructure [10]. Attempts to investigate the effects of heat treatment on the electrochemical performance of hydrous ruthenium oxides (RuO_2) [11, 12], nickel oxides (NiO) [13,14] and manganese oxide-based (MnO_2) electrodes [15, 16] have been widely reported. Hu et al (2002) reported the effect of annealing temperatures on the electrochemical performance of hydrous RuO_2 electrodes in 0.5 M H_2SO_4 [12]. With increasing the post heat treatment temperature, the vaporization of trapped water molecules and the crystallization of hydrous RuO_2 have caused a significant degradation in pseudocapacitance. The authors explained that the decreased pseudocapacitance is attributed to the loss of nonstoichiometric sites of oxides as a result of the structural reconstruction and crystallisation of oxide. Similarly, another study on the effect of temperature on capacitive and structural properties of hydrous RuO_2 was conducted by Fang and co-workers (2006) [11]. The results indicated that the suitable nanostructure of oxide electrodes which could be controlled by proper post heat treatment can help to facilitate the balanced electron and ionic conduction. The optimal temperature of 200 ^oC for 2 h has enhanced the capacitive properties of oxide electrodes significantly. Recently, Lee et al (2008) presented detailed analytic data about the effects of heat treatment (100 – 400 ^oC) on Mn-Fe oxides for supercapacitor applications [17]. The highest specific capacitance value of 280 F/g was observed for the oxides electrode that was treated at 100 ^oC. The possible explanations for the superior capacitive performance of these oxides could be due to the release of adsorbed water at ~100 ^oC, as confirmed by simultaneous thermogravimetric and differential thermal analyses (TG/DTA). So far, however, little is known how heat treatment affects the capacitive performance of TiO_2-AC and ZnO-AC symmetrical nanocomposite electrodes. In order to understand the mechanism of charge storage, the characteristics of the composite materials as a function of heat treatment temperature (200 – 500 ^oC) were studied. With these insights, both TiO_2-AC and ZnO-AC composite electrodes could be further developed and optimised as commercially viable electrodes in electrochemical capacitor applications.

5.2 Characterisation of TiO_2-AC and ZnO-AC composites

5.2.1 Effect of heat treatment

TGA was carried out on 4TiO-AC and 4ZnO-AC respectively from 25 °C to 800 °C with a heating rate of 10 °C/min respectively. As shown in Figure 5.1 and 5.2, there are two stages of major weight loss occurred in both 4TiO-AC and 4ZnO-AC composite materials. The first weight loss occurred from 25 °C to 50 °C which is attributed to the removal of water molecules from the nanocomposite powder. The second stage of weight loss occurred at temperature around 500 °C, which is mainly caused by burnt off of AC or decomposition of cellulose, hemicellulose and lignin on carbon as well as formation of volatile materials such as CO and CO_2 [18]. These finding suggest that the heat treatment temperature on both 4TiO-AC and 4ZnO-AC composite materials should not exceed 500 °C in order to prevent any decomposition or burnt off of active materials which could subsequently deteriorate the capacitive performance of electrodes.

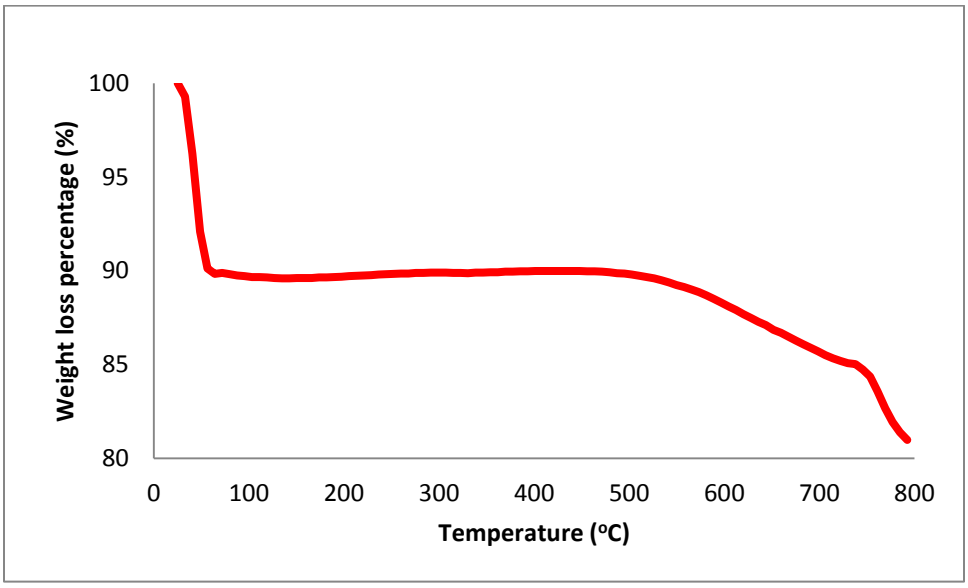


Figure 5.1. TGA plot for 4TiO-AC composite materials.

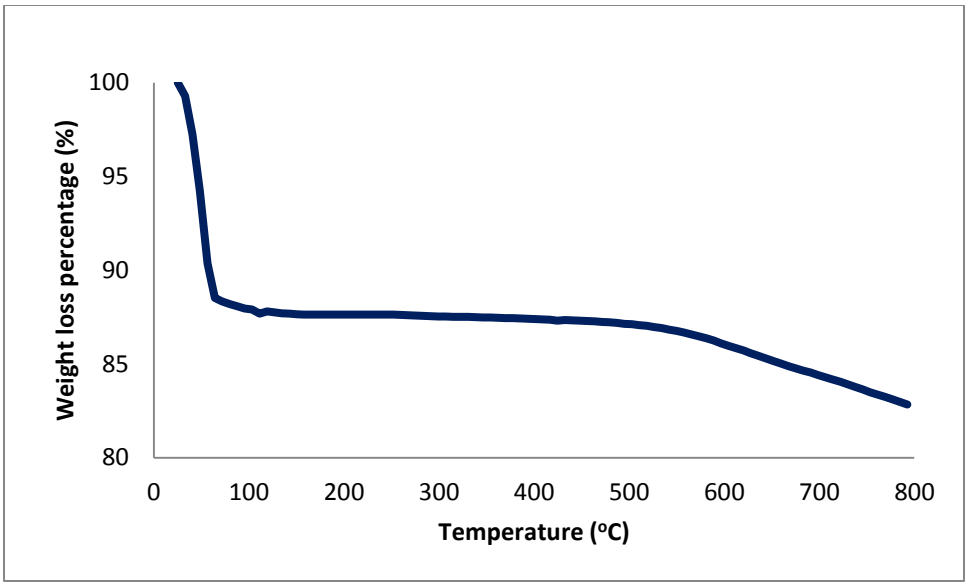


Figure 5.2. TGA plot for 4ZnO-AC composite materials.

The physical appearance of various thermally treated composite materials is presented in Table 5.1. All the composite materials were thermally treated at various temperatures for 6 hours. It can be seen that composite materials that were heat-treated at 200 °C and 300 °C do not show any significant changes in appearance. However, colour change was observed visually when the composite materials were thermally treated at temperatures of 400 and 500 °C respectively, indicating some of the active materials have been decomposed or have undergone phase transformation at these temperatures. Weight loss measurements in various temperatures are summarised in Table 5.2. It is clearly seen that both TiO-AC and ZnO-AC composite materials demonstrate the most significant weight loss (~96 %) after heat treatment at 500 °C. Conversely, weight loss was insignificant when 4TiO-AC (6.36 %) and 4ZnO-AC (4.23 %) when they were heat treated at 200 and 300 °C respectively. (as shown in Table 5.2).

Table 5.1. Physical appearance of TiO-AC and ZnO-AC composite materials thermally treated at various temperatures.

Temperature (ºC)	4TiO-AC	4ZnO-AC
200		
300		
400		
500		

Table 5.2. Weight loss for 4TiO-AC and 4ZnO-AC in various heat treatment temperatures

Composite materials	Temperature (° C)	Initial weight (g)	Remaining weight (g)	Percentage of weight loss (%)
4TiO-AC	200	5.0323	1.9523	3.08
	300	5.0513	4.7300	6.36
	400	5.0270	1.0032	80.04
	500	5.0278	0.1969	96.08
4ZnO-AC	200	5.0416	2.7817	2.26
	300	5.0124	4.8002	4.23
	400	5.0270	1.0029	79.97
	500	5.0313	0.2125	95.78

Table 5.3 summarise the weight loss of individual components of active materials after heat treatment at 400 ºC. The results show that AC recorded the highest weight loss (78.8 %) as compared to carbon black (CB, 16.5 %) and pure metal oxides (TiO_2 – 1.6 %; ZnO – 0.8 %). Thus, it can be concluded that the significant weight loss observed for the composite samples calcined at 500 ºC is mainly due to the decomposition of AC.

Table 5.3. Weight loss for AC, CB, TiO_2 and ZnO after heat treatment at 400ºC.

Materials	Initial weight (g)	Remaining weight (g)	Percentage of weight loss (%)
AC	1.0276	0.2176	78.8
CB	1.0693	0.8929	16.5
TiO_2	1.0020	0.9860	1.6
ZnO	1.0045	0.9963	0.8

Figure 5.3 shows the XRD patterns of pure AC and 4TiO-AC composite materials calcined at different temperatures. As shown in Figure 5.3(a), AC demonstrates very broad diffraction peaks thus reflecting an amorphous structure. On the other hand, all the thermally

treated 4TiO-AC composites show improved crystallinity in which the diffraction peaks ascribed to the mixture of anatase and rutile phases could be observed in Figure 5.3 (b-f). Kim and Branko who studied on the characterization of hydrous ruthenium oxide/carbon nanocomposite prepared by a colloidal method revealed that crystallinity increased drastically as the nanocomposite annealed above 200 °C [19]. The composite material shows the existence of almost fully anatase with a little rutile phase of TiO_2 even before calcination (Figure 5.3 (b). The diffraction peaks remain unchanged when 4TiO-AC composites were heated at calcination temperature of 100 to 300 ^oC.

Figure 5.7 shows the XRD pattern of as prepared ZnO-AC composite materials. All the peaks of the ZnO nanoparticles can be indexed to the zincite single phase ZnO, suggesting no phase transformation was observed when composite materials thermally treated from 100 to 400 ^oC. These findings reveal that the colour change on 4ZnO-AC (as shown in Table 5.1) is not due to the phase change but the decomposition of active materials at 400 and 500 ^oC respectively. As such, we have chosen 200 ^oC as optimal calcination temperature for subsequent study.

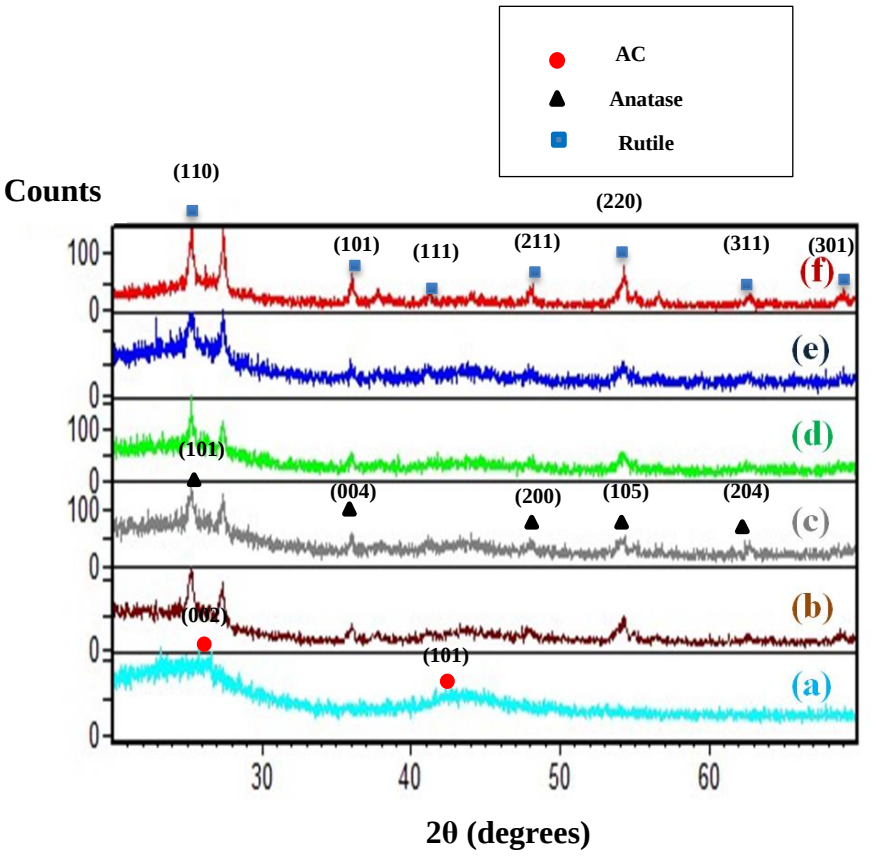


Figure 5.3. XRD patterns of (a) pure AC, 4TiO-AC composites calcined at temperature of (b) 25, (c) 100, (d) 200, (e) 300, (f) 400 °C.

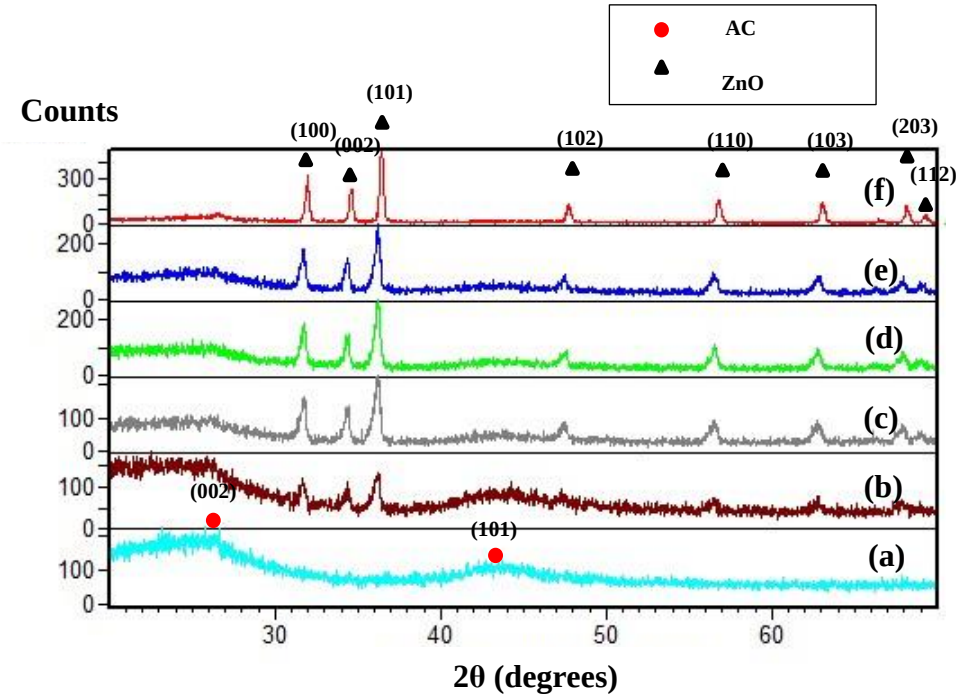


Figure 5.4. XRD patterns of (a) pure AC, 4ZnO-AC composites calcined at temperature of (b) 25, (c) 100, (d) 200, (e) 300, (f) 400 °C.

5.2.2 Effect of metal oxide loading

Figure 5.5 demonstrates the surface morphologies of the calcined TiO_2-AC composite materials with various compositions. As revealed in Figure 5.1(a), high porosity of AC electrode with irregular and rough surfaces is observed, giving rise to a high surface area. It seems like low loading of TiO_2 (4 wt %) does not alter the porous structure of AC electrodes (Figure 5.5 (b)). However, it is clearly seen that the formation of compact and rigid surface structures is observed for samples with increasing TiO_2 loading above 20 wt%, as depicted in SEM photograph Figure 5.5 (c) - (e). Agglomeration of TiO_2 nanoparticles occurs in which the clusters of TiO_2 have filled up the pores of AC electrodes at high TiO_2 loading. The compact surface contour will significantly retard the ion diffusion to the porous AC electrode, resulting in the loss of overall capacitance of the composite electrodes. SEM micrographs in Figure 5.6 (a) – (e) indicate that different amount of ZnO loaded onto the composite materials exhibit different extent of surface roughness. The increasing amount of ZnO nanoparticles infiltrated into the porous structure of AC is observed as the composition of ZnO is increased from 4 wt% to 60 wt%. The ZnO nanoparticles are found to form agglomerates within AC electrodes (as shown in Figure 5.6 (e)). The crystal growth of ZnO reduces the ionic migration, and thus causes the increase in diffusion path length.

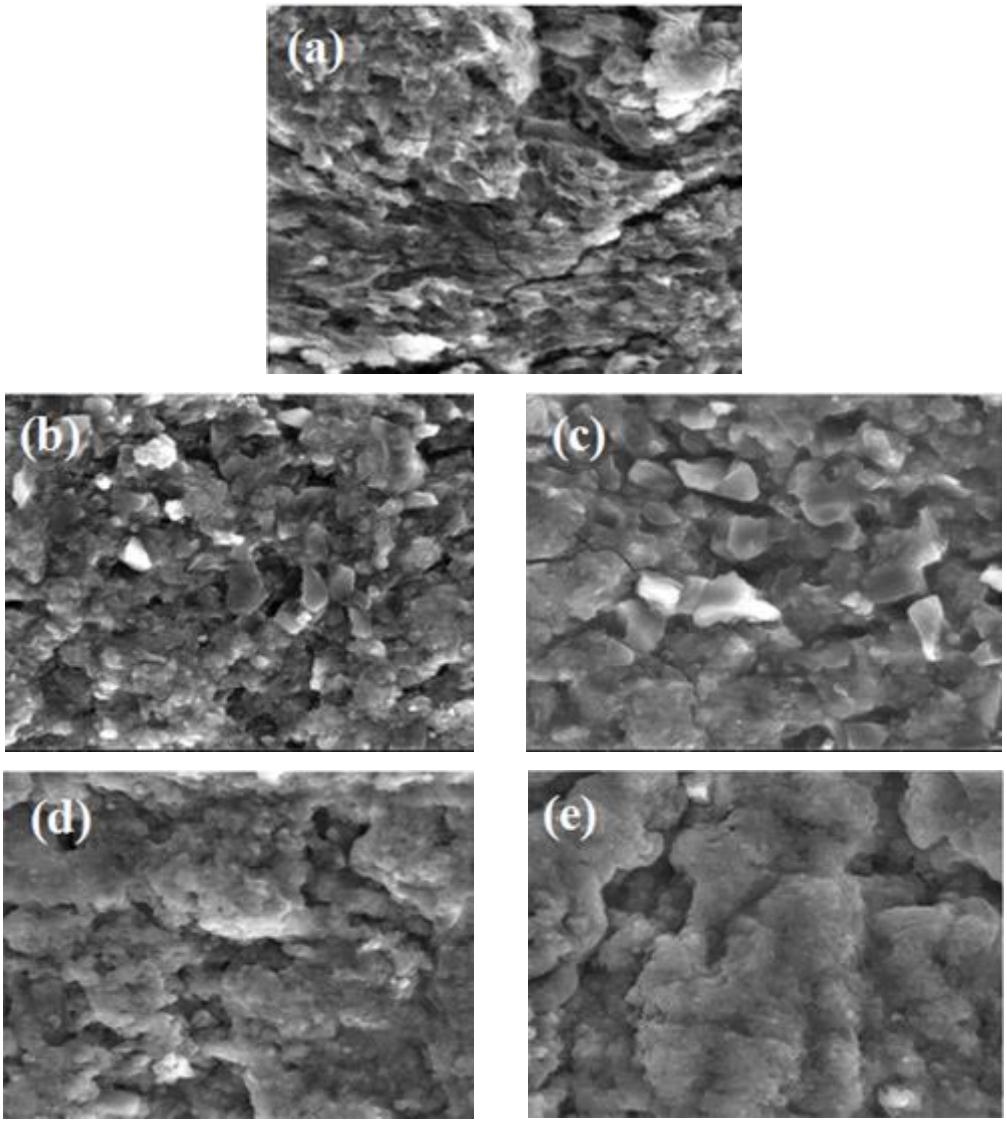


Figure 5.5. SEM images of (a) AC, (b) 4TiO-AC, (c) 20TiO-AC, (d) 60TiO-AC, (e) 80TiO-AC, at magnification of 2500x.

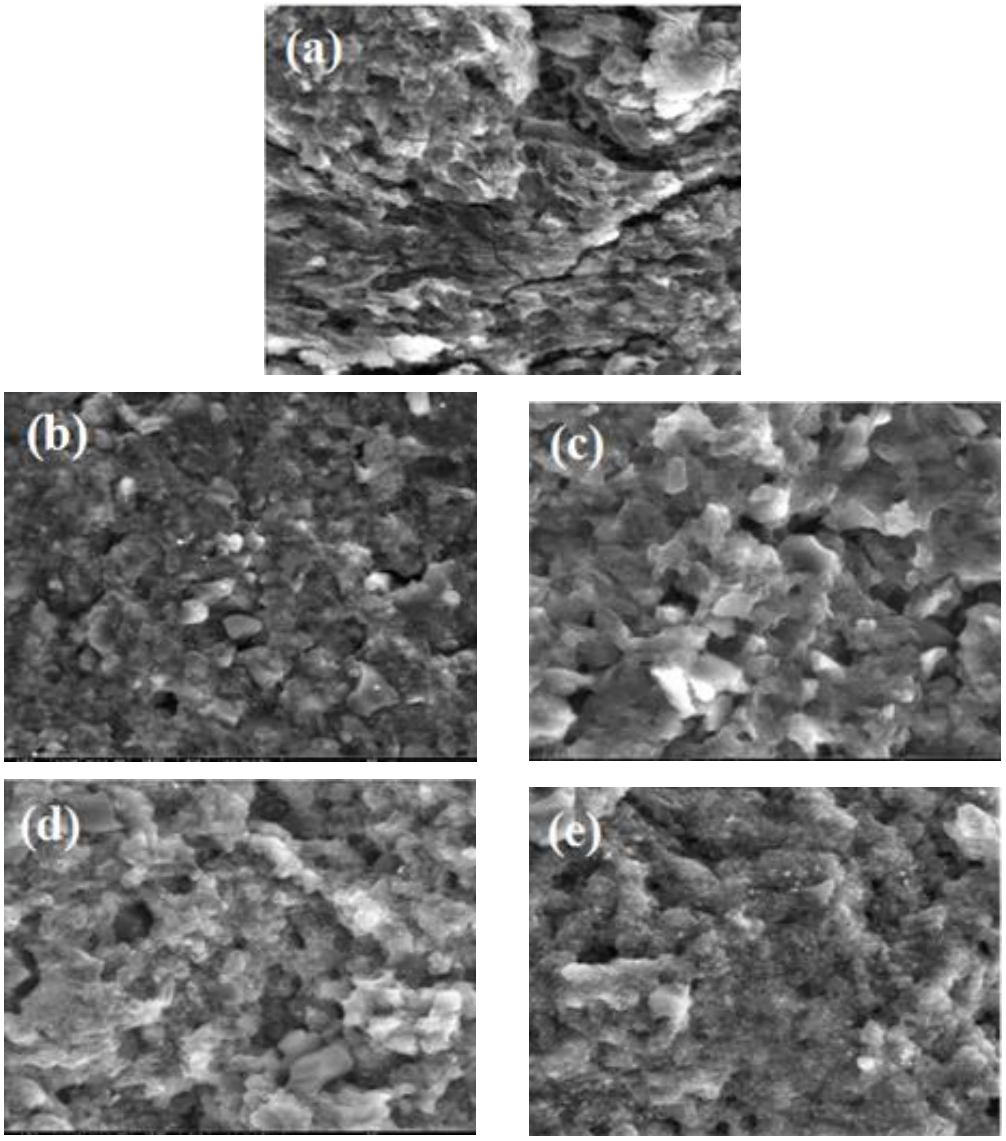


Figure 5.6. SEM images of (a) AC, (b) 4ZnO-AC, (c) 20ZnO-AC, (d) 60ZnO-AC, (e) 80ZnO-AC, magnification of 2500x.

In order to elucidate the porosity property of the electrode, BET analysis has been conducted. The variation of BET specific surface area of TiO_2-AC and ZnO-AC with different compositions of composite materials is summarised in Table 5.4. The BET analysis reveals that the addition of 4 wt % TiO_2 slightly increases the specific surface area of pure AC from 1653 to 1708 m^2/g. The gradual surface area reduction is observed when further increase of TiO_2 compound from 10 wt% to 80 wt %. The specific surface area of pure TiO_2 nanoparticles (100 wt %) is 269 m^2/g. Similar trend of specific surface area versus varying compositions of ZnO is

observed for ZnO-AC composite electrodes. Doping 4 wt % ZnO onto AC achieves the slight increased specific surface area (1685 m^2/g) in comparison to that of pure AC electrode (1653 m^2/g). A drastic drop of specific surface area is observed at loading above 10 wt %. The specific surface area of pure ZnO nanoparticles is 230 m^2/g.

Table 5.4. The variation of BET specific surface area of TiO_2-AC and ZnO-AC with different compositions of the composite materials.

Mass percentage of metal oxide to AC (wt%)	BET surface area of TiO_2-AC (m^2/g)	BET surface area of TiO_2-AC (m^2/g)
0	1653	1653
4	1708	1685
10	1602	1609
20	1412	1366
40	1161	1105
60	863	775
80	555	522
100	269	230

5.3 The electrochemical performance of TiO_2-AC and ZnO-AC composite electrodes

The CV plots for the calcined TiO_2-AC and ZnO-AC composite electrodes with different nanostructured oxides loadings in 1 M Na_2SO_3 are presented in Figure 5.7 and Figure 5.8, respectively. Both systems achieve the highest specific capacitance at fairly low oxide loading in the composite electrodes. 4TiO-AC and 4ZnO-AC composite electrodes demonstrate the superior specific capacitances of approximately 80 F/g and 116 F/g, respectively, in comparison to that of pure AC electrode (approximately 70 F/g). Considerable enhancement of the electrochemical properties of 4TiO-AC and 4ZnO-AC composite electrodes with low concentration of oxides is achieved via the synergistic effects contributed from the

nanostructured metal oxides and the high surface area of the mesoporous AC. Cations and anions from metal oxides and aqueous electrolyte such as $Ti^{4+,}$ Zn^{2+} Na^{+} and SO_3^{2-} can occupy some pores within the high-surface-area AC electrodes, forming the electric double layer which is accompanied by the faradaic reactions at the electrode-electrolyte interface, as expressed by:

$$TiO_2 + xNa^+ + xe^- \rightleftharpoons Na_xTiO_2 \qquad \text{Eq. (5.1)}$$

$$ZnO + xNa^+ + xe^- \rightleftharpoons Na_xZnO \qquad \text{Eq. (5.2)}$$

Additionally, both TiO_2 and ZnO nanoparticles can provide favourable surface adsorption sites for SO_3^{2-} anions which subsequently facilitate the faradaic processes for pseudocapacitive effect, as presented by [20]:

$$2SO_3^{2-} + 3H_2O + 4e^- \rightleftharpoons S_2O_3^{2-} + 6OH^- \qquad \text{Eq. (5.3)}$$

$$S_2O_3^{2-} + 3H_2O + 8e^- \rightleftharpoons 2S^{2-} + 6OH^- \qquad \text{Eq. (5.4)}$$

Nevertheless, it should be noted that the as-prepared TiO_2-AC and ZnO-AC composite electrodes possess an open pseudo-rectangular shaped CV at various compositions without any observable redox peak. Previously published works in [26-29] reported similar results. Several researches also suggest that the presence of nanostructured TiO_2 is likely to increase the ion concentration on the double layer of AC by occupying some pores within the AC and thereby reduce the polarization of the AC electrode [6]. However, a further increase in oxides content starts deteriorating the capacitive behaviour of both TiO_2 and ZnO composite electrodes. There is a study of RuO_2/AC nanocomposites reported that when ruthenium content increases, the specific capacitance of the composites decreases gradually due to the blockage of the mesopores in AC by large RuO_2 particles [21]. It thus causes the decreased in adsorption of charge carriers such as protons and electrons on the surface of the electrodes. In the case of pure TiO_2 and ZnO electrodes, the specific capacitances are only 14 and 19 F/g, respectively, proving that the TiO_2 and ZnO nanoparticles themselves demonstrate poor electronic conductivity and relatively

inferior charge storage capability. Introduction of conductive, porous and high surface area carbon-based materials is a feasible route to enhance the charge-storage capability by shortening electron transport distance and improving electronic conductivity [22].

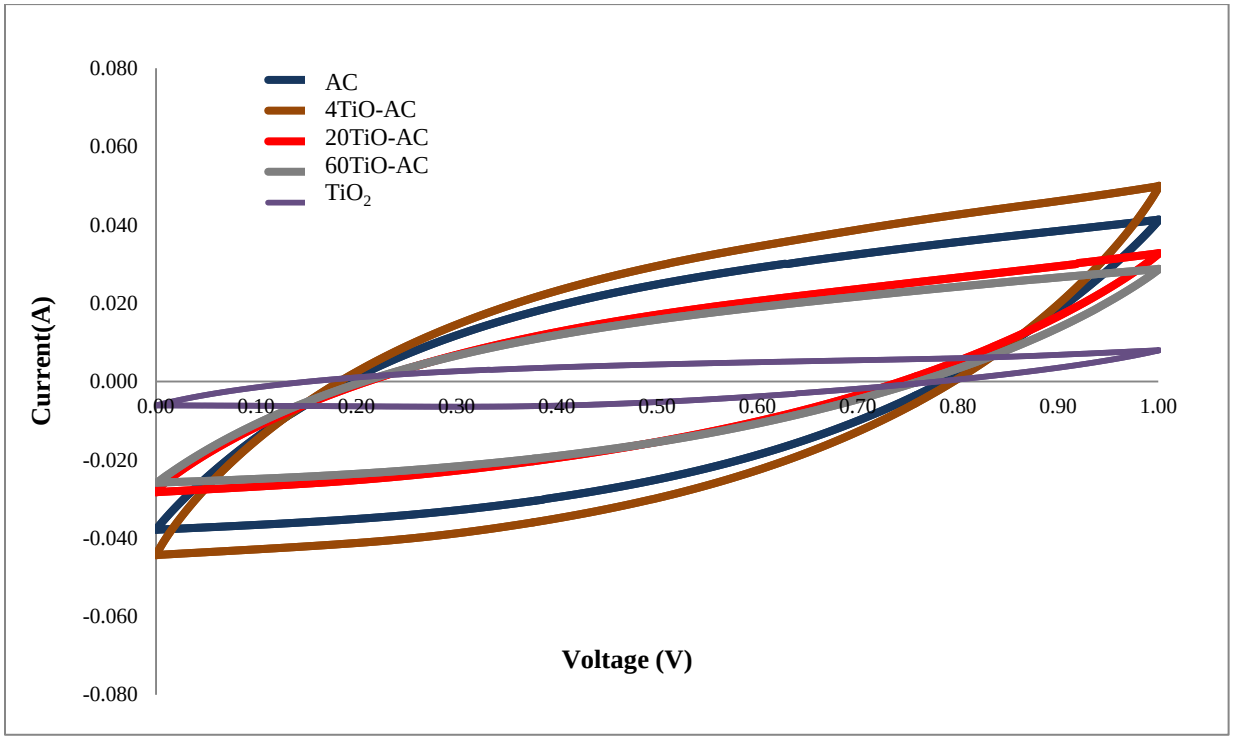


Figure 5.7. Cyclic voltammograms for AC electrodes with different TiO_2 nanomaterials loading in 1 M Na_2SO_3 at a scan rate of 10 mV/s.

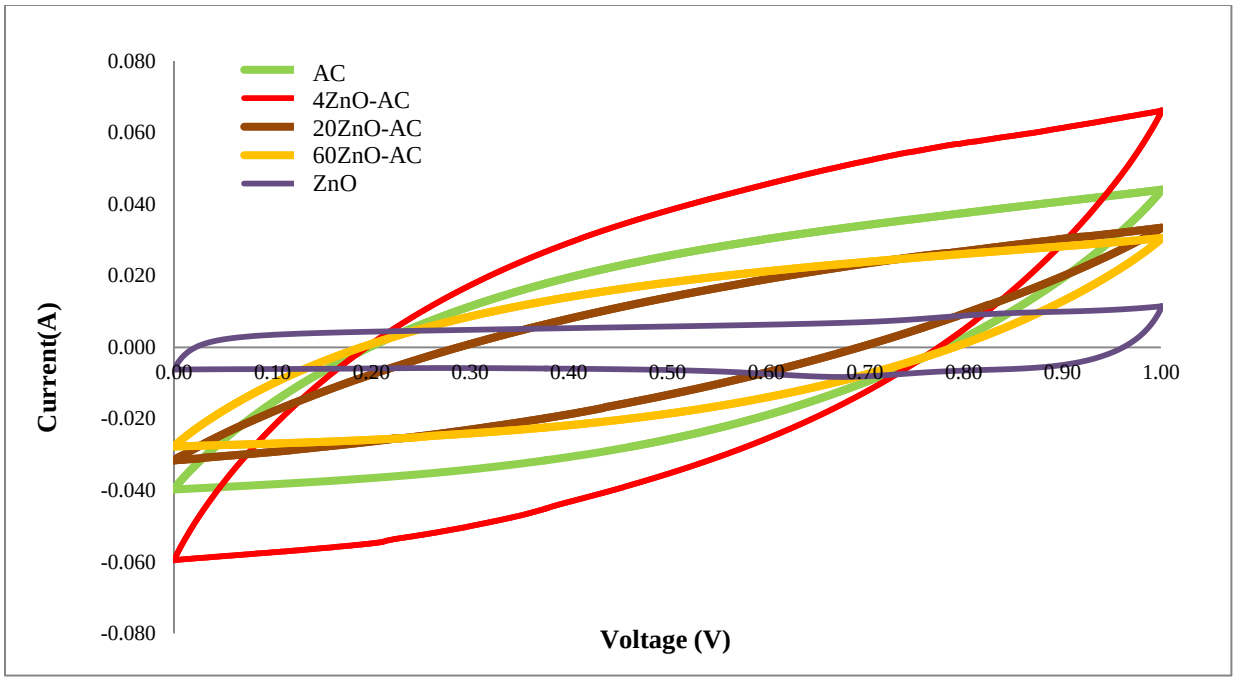


Figure 5.8. Cyclic voltammograms for AC electrodes with different ZnO nanomaterials loading in 1 M Na_2SO_3 at a scan rate of 10 mV/s.

Figure 5.9 and Figure 5.10 demonstrate the relationship between specific capacitance and BET surface area for TiO_2-based and ZnO-based composite electrodes, respectively. Generally, specific capacitance of composite electrodes is improved with increasing BET surface area. Theoretically, it is proposed that an effective surface area of electrode material is directly proportional to the specific capacitance. However, several research studies have reported on the non-linearity of capacitance values to the specific surface area [23]. It is claimed that the main determinant factor for the electrochemical characteristic of composite electrode is not on its effective surface area solely but also depending on surface morphology, core material crystallinity as well as the electronic conductivity. Qu et al. (1998) [24] who studied on the correlation between structural morphology and capacitive performance of high-surface-area ACs revealed that the measured capacitance of ACs did not exhibit a linear relationship with their surface areas. This is because some portions of surface area are not electrochemically accessible when in contact with electrolyte. Nonetheless, the electrochemical capacitive capability of the composite electrodes is well-linked with the specific surface area, which generally substandard charge storage performance is recorded for sample with low surface active area.

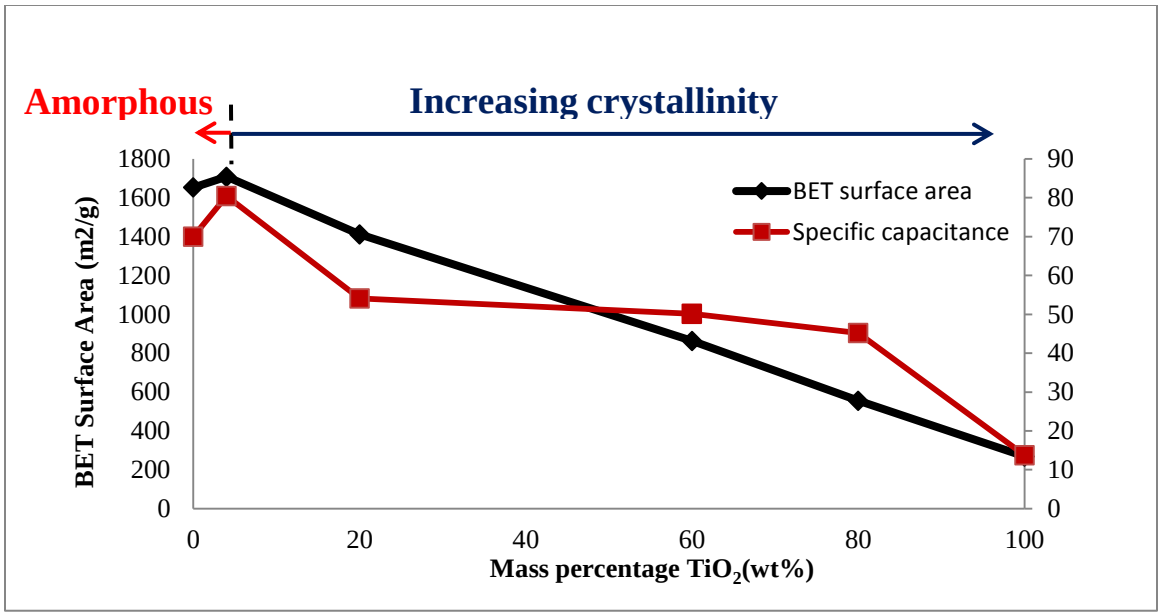


Figure 5.9. Correlation between specific capacitance, crystallinity and BET surface are on TiO_2-AC composite electrodes.

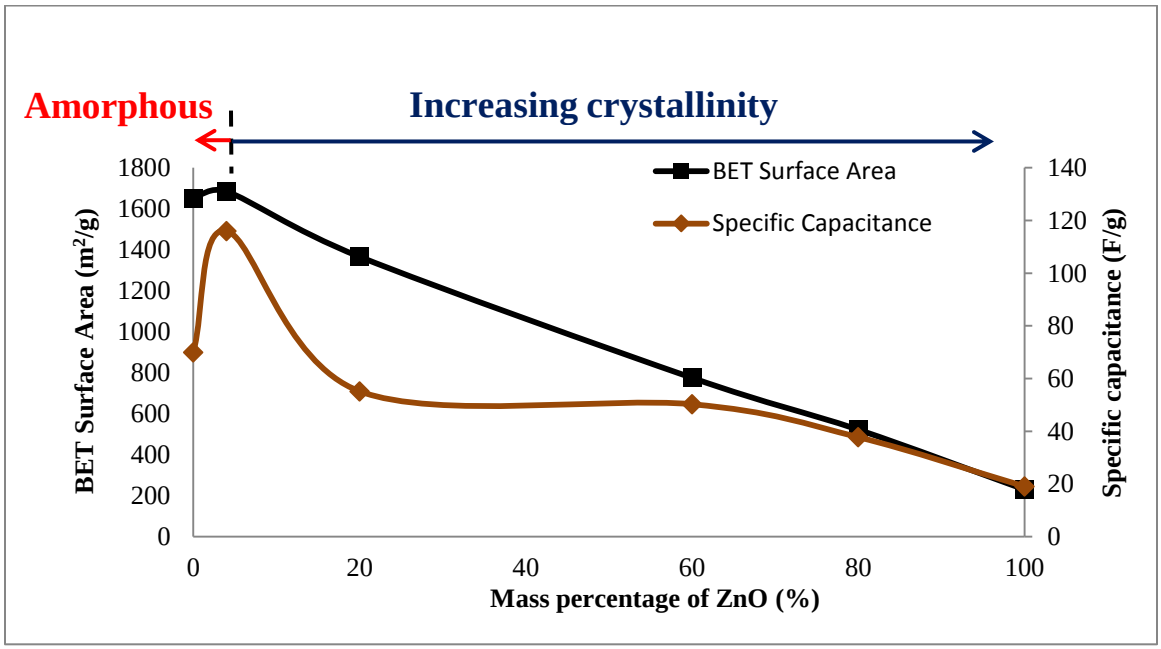


Figure 5.10. Correlation between specific capacitance, crystallinity and BET surface are on ZnO-AC composite electrodes.

Figure 5.11 presents the galvanostatic CD profiles of the AC, 4TiO-AC and 4ZnO-AC composite electrodes in 1 M Na_2SO_3 electrolytes at a current density of 5 mA/cm^2. The IR drop or equivalent series resistance (ESR) which is comprised of the electrode resistance, electrolyte

resistance and ions diffusion resistance in the electrode can be observed on all of the three CD profiles. It can be seen that the pure AC electrode exhibits the highest IR drop (approximately 4.8 Ω), followed by TiO_2-AC nanocomposite electrode (approximately 3.8 Ω) and ZnO-AC nanocomposite electrode (approximately 3.0 Ω). These comparative results generally show that the ZnO-AC composite electrodes exhibit better capacitive performance if compared to the pure AC and TiO_2-AC electrodes.

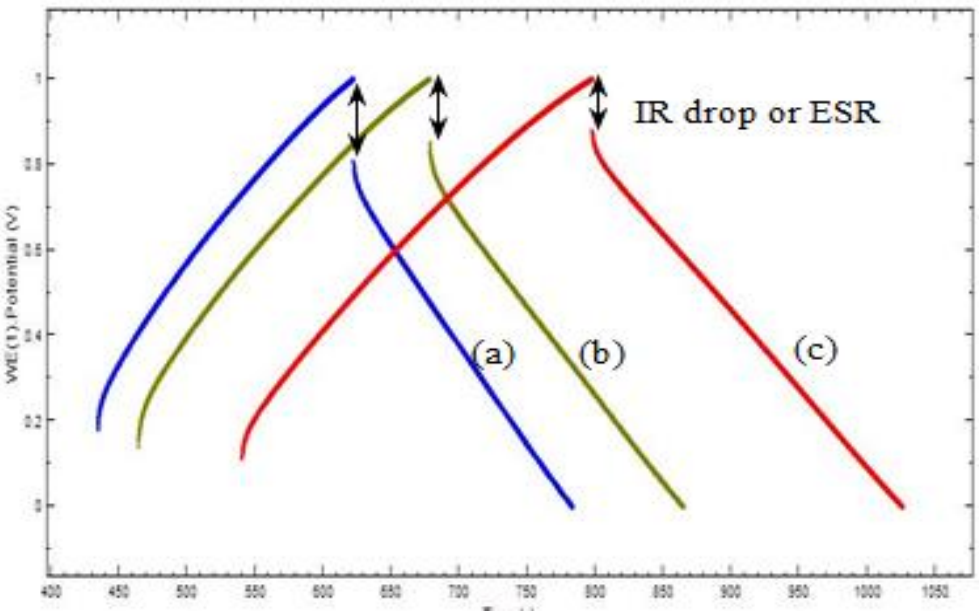


Figure 5.11. Galvanostatic CD profiles of (a) AC, (b) 4TiO-AC and (c) 4ZnO-AC electrodes in 1 M Na_2SO_3 electrolytes at a current density of 5 mA/cm^2.

The EIS measurements were performed on the AC, 4TiO-AC and 4ZnO-AC composite electrodes between 100 kHz and 10 mHz, as presented in Figure 5.12. All of the impedances consist of an arc and slanted line at low frequency. In the high-frequency region, the intercept of the semicircle on the real axis of the Nyquist spectrum represents the solution resistance (R_s), which provides the resistance at the electrode-electrolyte interface while the semicircles are attributed to an interfacial charge transfer resistance (R_{CT}) or polarisation resistance (R_p) and the double-layer capacitance (C_{DL}) connected to each other in parallel. After the semicircle, the Nyquist spectrum exhibits a straight line in the low-frequency region, which corresponds to the

Warburg element, W [25]. The Warburg element represents the diffusion of cations and anions from the metal oxides and the electrolyte into the pores on the surface of the electrode. The ion diffusion occurs during the transition from the high-frequency semicircle to the mid-frequency spike. Another tangent hyperbolic diffusion circuit element (T) is incorporated into the Randles equivalent circuit when the diffusion condition is under restricted diffusion limitation between the electrode and another non-reactive surface (current collector) [25]. Figure 5.12 (i) demonstrates that the diameter of the semicircle varies considerably between the AC, TiO_2-AC and ZnO-AC. The ZnO-AC composite electrode exhibits the smallest diameter and minimum ESR (approximately 2.7 Ω) in comparison to AC and TiO_2-AC. Figure 5.12 (ii) presents the Randle equivalent circuit used to fit the experimental Nyquist spectrum which determines the most representative physical processes for the ZnO-AC electrode in Na_2SO_3.

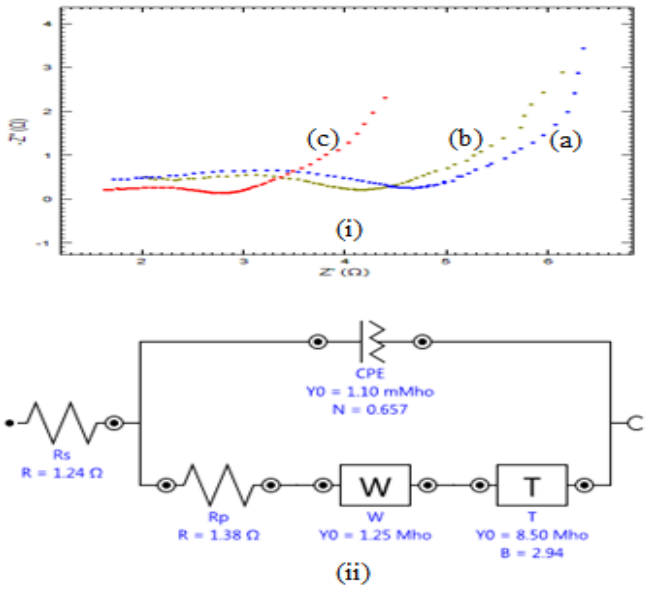


Figure 5.12. (i) Nyquist plots obtained for (a) AC, (b) 4TiO-AC and (c) 4ZnO-AC electrodes at 0 V over the frequency range of 100 kHz – 10 mHz in 1 M Na_2SO_3. (ii) Randles equivalent circuit representing the circuit elements that are used to fit the experimental Nyquist spectrum of 4ZnO-AC electrode using the software Nova.

The long-term cycle stabilities of 4Ti-AC and 4ZnO-AC composite electrodes were tested at a scan rate of 10 mV/s between 0 and 1 V in 1 M Na_2SO_3. 4Ti-AC composite electrodes demonstrate ~7 % capacitance loss at the end of the analysis (Figure 5.13), revealing its outstanding electrochemical stability. Meanwhile, 4ZnO-AC composite electrodes also exhibit

excellent cycling stability, with ~95 % of the original capacitance retained after 1000 cycles (Figure 5.14). The relatively poor electrochemical reversibility of 4ZnO-AC shown at the initial 50-100 cycles was probably due to the rapid consumption of sulphite (SO_3^{2-}) anions in the electrolyte, while the reversibility was improved markedly after approximately 100 cycles when a near steady state was established [20]. The composite electrodes remained integrated without any cracking observed after long term cycling, mainly due to the presence of robust AC backbone, significantly enhances the mechanical strength of the composite materials for prolonged cyclability. The Ragone plots of 4TiO-AC and 4ZnO-AC that correlate the relationship between specific energy and specific power of the systems are shown in Figure 5.15 and 5.16 respectively. It is seen that 4Ti-AC and composite electrodes exhibit a specific energy of 10.9 Wh/kg at 12 mA while another symmetric supercapacitor, 4ZnO-AC, exhibits a maximal specific energy of 17.2 Wh/kg.

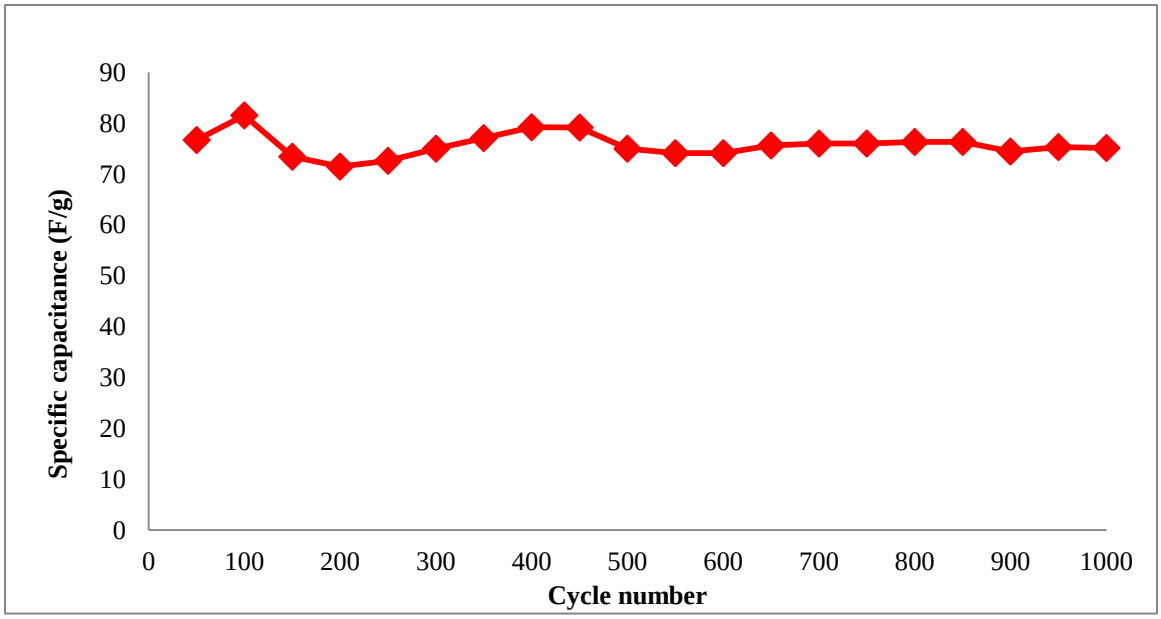


Figure 5.13. Cycling stability of 4TiO-AC composite electrodes in aqueous Na_2SO_3 electrolyte at scan rate of 10 mV/s between 0 and 1 V.

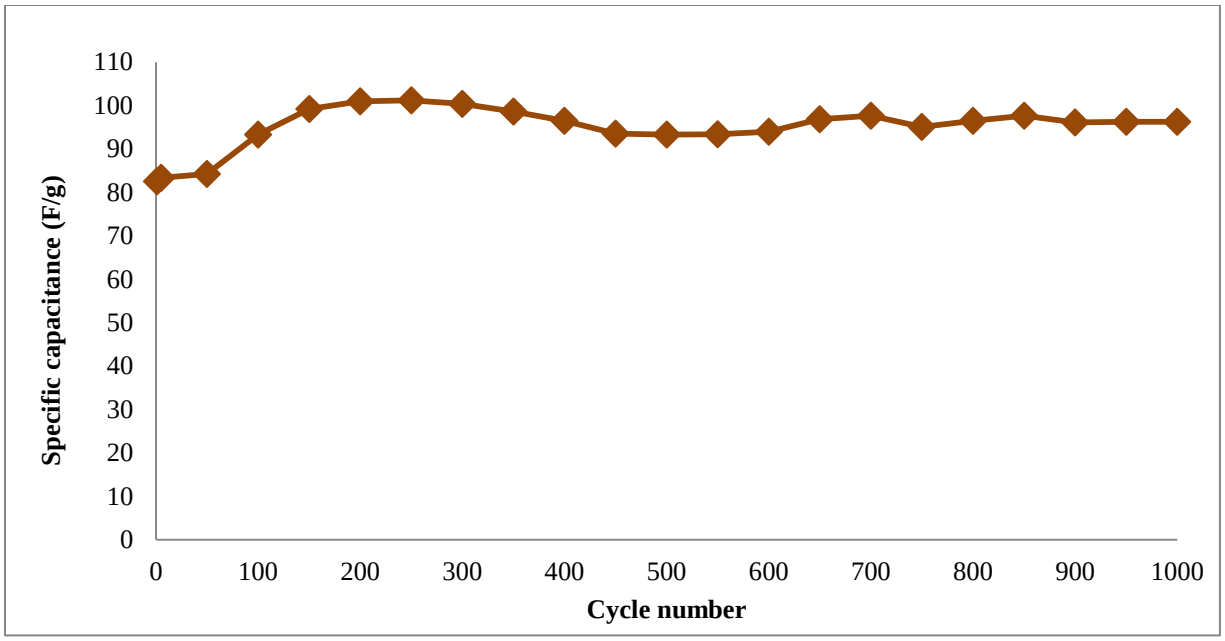


Figure 5.14. Cycling stability of 4ZnO-AC composite electrodes in aqueous Na_2SO_3 electrolyte at scan rate of 10 mV/s between 0 and 1 V.

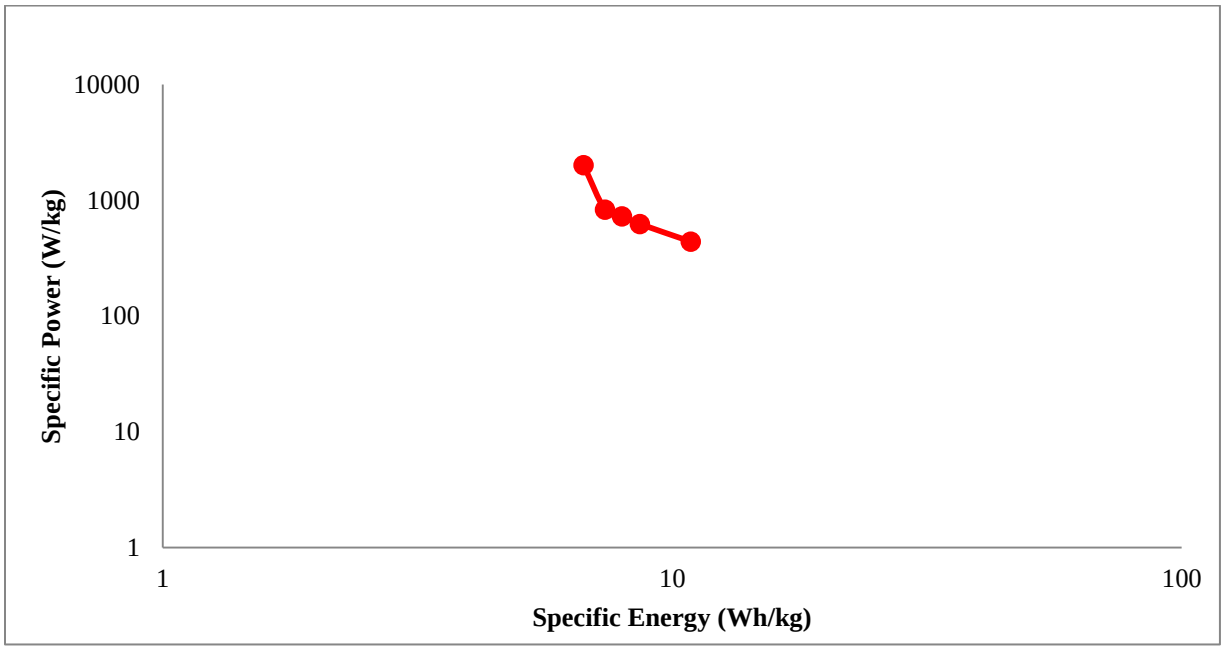


Figure 5.15. Ragone plot of 4TiO-AC composite electrodes.

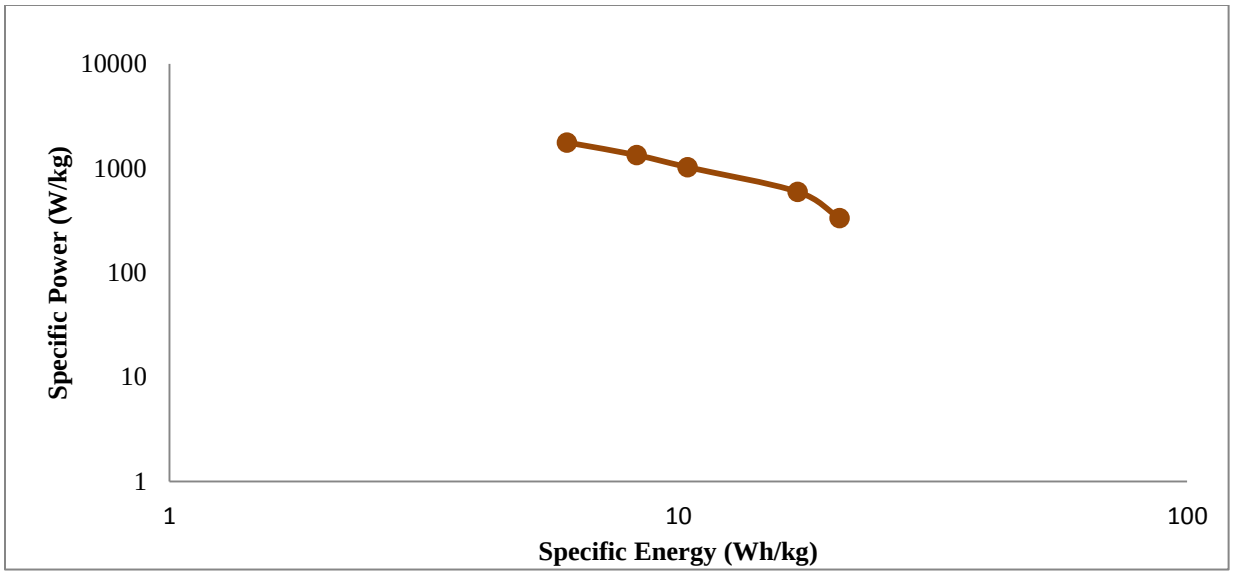


Figure 5.16. Ragone plot of 4ZnO-AC composite electrodes.

5.4 Summary

The electrochemical performance of TiO_2-AC and ZnO-AC nanocomposite electrode materials in mild aqueous Na_2SO_3 electrolyte were studied comprehensively. The highest specific capacitance of both composite electrodes was achieved with fairly low concentration (4 wt %) of oxides loading. The improved capacitive performance of the TiO_2-AC and ZnO-AC composite electrode is attributed to the synergistic effect of the electric double-layer capacitance on the high surface area of AC and the pseudocapacitance via the intercalation/extraction of Ti^{4+}, Zn^{2+}, Na^+ and SO_3^2 ions in oxide lattices. Overall, the results reveal that the low cost TiO_2-AC and ZnO-AC nanocomposite electrodes in a neutral Na_2SO_3 electrolyte display great potential for electrochemical capacitor applications.

Reference

[1] C.Ruiz, C.Blanco, E.Raymundo-Piñero, V.Khomenko, F.Béguin, R.Santamaría, "Effects of thermal treatment of activated carbon on the electrochemical behaviour in supercapacitors," Electrochimica Acta 52 (2007) 4969-4973.

[2] K.H.An, W.S.Kim, Y.S.Park, J.M.Moon, D.J.Bae, S.C.Lim, Y.S.Lee, Y.H.Lee, "Electrochemical Properties of High-Power Supercapacitors Using Single-Walled carbon Nanotube Electrodes," Advanced Functional Materials 11 (2001) 387-392.

[3] F. Tao, Y. Shen, Y. Liang, H. Li, "Synthesis and characterization of $Co(OH)_2/TiO_2$ nanotube composites as supercapacitor materials," Journal of Solid State Electrochemistry 11 (6) (2006) 853-858.

[4] D. Kalpana, K.S. Omkumar, S.S. Kumar, N.G. Renganathan, "A novel high power symmetric ZnO/carbon aerogel composite electrode for electrochemical supercapacitor," Electrochimica Acta 52 (3) (2006) 1309-1315.

[5] C.D. Lokhande, B.-O. Park, H.-S. Park, K.-D. Jung, O.-S. Joo, "Electrodeposition of TiO_2 and RuO_2 thin films for morphology-dependent applications," Ultramicroscopy 105 (2005) 267-274.

[6] M.K. Seo, S.J. Park, "Effect of nanosize titanium oxide on electrochemical characteristics of activated carbon electrodes," Current Applied Physics 10 (2010) 391-394.

[7] X.Sun, M.Xie, G.K.Wang, H.T.Sun, A.S.Cavanagh, J.J.Travis, S.M.George and J.Lian, "Atomic layer deposition of TiO_2 on Graphene for supercapacitor," Journal of The Electrochemical Society 159 (2012) A364-A369.

[8] T. Lu, Y. Zhang, H. Li, L. Pan, Y. Li, Z. Sun, "Electrochemical behaviors of graphene–ZnO and graphene–SnO_2 composite films for supercapacitors," Electrochimica Acta 55 (2010) 4170-4173.

[9] C. Masarapu, H.F. Zeng, K.H. Hung, B. Wei, "Effect of Temperature on the Capacitance of Carbon Nanotube Supercapacitors," ACS Nano 3 (2009) 2199-2206.

[10] S.W. Zhang, G.Z. Chen, "Manganese oxide based materials for supercapacitors, Energy Materials: Materials Science and Engineering for Energy Systems 3 (2008) 186-200.

[11] W.C. Fang, J.H. Huang, L.C. Chen, Y.L.O. Su, K.H. Chen, "Effect of temperature annealing on capacitive and structural properties of hydrous ruthenium oxides," Journal of Power Sources 160 (2006) 1506-1510.

[12] C.C. Hu, Y.H. Huang, K.H. Chang, "Annealing effects on the physicochemical characteristics of hydrous ruthenium and ruthenium-iridium oxides for electrochemical supercapacitors," Journal of Power Sources 108 (2002) 117-127.

[13] E.E. Kalu, T.T. Nwoga, V. Srinivasan, J.W. Weidner, "Cyclic voltammetric studies of the effects of time and tmeperature on the capacitance of electrochmeically deposited nickel hydroxide," Journal of Power Sources 92 (2001) 163-167.

[14] K.W. Nam, W.S. Yoon, K.B. Kim, "X-ray absorption spectroscopy studies of nickel oxide thin film electrodes for supercapacitors," Electrochimica Acta 47 (2002) 3201-3209.

[15] J.K. Chang, Y.L. Chen, W.T. Tsai, "Effect of heat treatment on material characteristics and pseudo-capacitive properties of manganese oxide prepared by anodic deposition," Journal of Power Sources 135 (2004) 344-353.
[16] J.K. Chang, W.T. Tsai, "Microstructure and Pseudocapacitive Performance of Anodically Deposited Manganese Oxide with Various Heat-Treatments," Journal of The Electrochemical Society 152 (2005) A2063.
[17] M.T. Lee, J.K. Chang, Y.T. Hsieh, W.T. Tsai, "Annealed Mn–Fe binary oxides for supercapacitor applications," Journal of Power Sources 185 (2008) 1550-1556.
[18] B. Jurgis, D. Maryte, 2003, "An investigation of the functional groups on the surface of activated carbons," J.Serb.Chem.Soc. 69 (2003) 363 to 375.
[19] H.S. Kim, K. Branko, "Characterization of hydrous ruthenium oxide/carbon nanocomposite supercapacitors prepared by a colloidal methods," Journal of Power Sources 104 (2002) 52-61.
[20] X.Zhao, C. Johnston, A.Crossley, P.S.Grant, "Printable magnetite and pyrrole treated magnetite based electrodes for supercapacitors," Journal of Materials Chemistry 20 (2010) 7637-7644.
[21] H. Kim, B.N. Popov, "Characterization of hydrous ruthenium oxide/carbon nanocomposite supercapacitors prepared by a colloidal method," Journal of Power Sources 104 (2002) 52-61.
[22] W. Wei, X. Cui, W. Chen, D.G. Ivey, "Manganese oxide-based materials as electrochemical supercapacitor electrodes," Chemical Society reviews 40 (2011) 1697-1721.
[23] Y. Wang, Z. Shi, Y. Huang, Y. Ma, C. Wang, M. Chen, and Y. Chen, "Supercapacitor Devices Based on Graphene Materials," The Journal of Physical Chemistry C 113 (2009) 13103-13107.
[24] D. Qu, H. Shi, "Studies of Activated Carbons Used in Double-Layer Capacitors," Journal of Power Sources 74 (1008) 99-107.
[25] C. Masarapu, H. F. Zeng, K. H. Hung, and B. Wei, "Effect of temperature on the capacitance of carbon nanotube supercapacitors," ACS Nano 3 (2009) 2199–2206.
[26] W.K. Chee , H.N. Lim , I. Harrison , K.F. Chong , Z. Zainal , C.H. Ng , N.M. Huang , "Performance of Flexible and Binderless Polypyrrole/Graphene Oxide/ Zinc Oxide Supercapacitor Electrode in a Symmetrical Two-Electrode Configuration," Electrochimica Acta 157 (2015) 88–94.http://dx.doi.org/10.1016/j.electacta.2015.01.080.
[27] Y.S. Lim, Y.P. Tan, H.N. Lim, N.M. Huang, W.T. Tan, "Preparation and characterization of polypyrrole/graphene nanocomposite films and their electrochemical performance," Journal of Polymer Research 20 (2013) 1–10.
[28] Z. Li, Z. Zhou, G. Yun, K. Shi, X. Lv, B. Yang, "High-performance solid-state supercapacitors based on graphene-ZnO hybrid nanocomposites," Nanoscale Research Letters 8 (2013) 473–482.

[29] T. Lu, Y. Zhang, H. Li, L. Pan, Y. Li, Z. Sun, “Electrochemical behaviors of graphene–ZnO and graphene–SnO2 composite films for supercapacitors, “Electrochimica Acta 55 (2010) 4170–4173.

CHAPTER 6

Charge Storage Performance of Lithiated Iron Phosphate - Activated Carbon Composite as Symmetrical Electrode for Electrochemical Capacitor

6.1 Introduction

Recently, electrochemical capacitors have been of great interest in the development of new energy storage systems due to their potential to be applied in power electric vehicles, hybrid electric vehicles and renewable energy systems [1]. Commercial electric double-layer capacitors (EDLCs) are mainly based on a symmetric configuration of two porous activated carbon (AC) electrodes immersed in a non-aqueous electrolyte. The charge is stored in the double layer, building up at the interface of porous electrodes and the electrolyte upon polarisation. Because the charge storage mechanism of EDLCs is based solely on reversible ion adsorption on the surface of porous electrodes, the charging process is fast and allows for high-power applications. However, EDLCs cannot store as much charge as batteries because the charge storage process is limited to the surface of the active material [2]. Due to these properties, EDLCs are characterised by a low specific energy (less than 10 Wh/kg) and a high specific power (above 10 kW/kg) [3]. In contrast, secondary batteries are electrochemical energy storage devices capable of delivering a high specific energy of up to 250 Wh/kg but a rather low specific power compared with electrochemical capacitors, which typically does not exceed 1 kW/kg [3].

Recent studies have demonstrated that the energy density can be increased significantly through the development of a lithium ion capacitor (LIC), which utilises both high-surface-area AC and a lithiated compound in a lithium-based non-aqueous electrolyte [4]. The concept of a non-aqueous LIC was first introduced by Amatucci and co-workers in 2001 [5]. The hybrid system was constructed with a nanosized $Li_4Ti_5O_{12}$ negative electrode and an AC positive electrode in a non-aqueous electrolyte, achieving a specific energy of more than 20 Wh/kg with 85% capacity retention after 5,000 cycles. The high working voltage in a non-aqueous LIC causes an electrolyte depletion problem during the charging process, which may adversely affect the safety and long-term

stability of the LIC [6]. Thus, Wang and co-workers (2005) developed a new concept hybrid electrochemical capacitor technology constructed with a $LiMn_2O_4$ positive electrode and an AC negative electrode in a mild Li_2SO_4 aqueous electrolyte [7]. This new state-of-the-art hybrid aqueous electrochemical capacitor can provide promising solutions for the major problem of electrolyte depletion observed in conventional non-aqueous hybrid capacitors. The results indicate that the use of an aqueous electrolyte can overcome the drawbacks of safety hazards arising from the use of highly toxic and flammable solvents in an organic electrolyte. Similarly, another aqueous-based asymmetric system has been successfully synthesised in which acid-treated $LiMn_2O_4$ was used as the positive electrode in combination with AC operating as the negative electrode in 1 M Li_2SO_4, resulting in a specific capacitance of 60 F/g. The capacitive performance can potentially be improved by acid treatment of the $LiMn_2O_4$ compound, which could lead to the perseverance of the $LiMn_2O_4$ structural framework as well as the oxidation of manganese from Mn^{3+} to Mn^{4+} after lithium-ion removal [8]. Recently, nanosized $LiFeO_2$ has been explored as a potential electrochemical capacitor electrode material in Li_2SO_4. This novel electrode material is able to achieve a stable capacitance of 50 F/g in the neutral electrolyte. The Li^+ ions with the smaller unhydrated radii may reversibly intercalate/de-intercalate in the $LiFeO_2$ lattices, resulting in pseudocapacitance [9].

Lithium iron phosphate ($LiFePO_4$) is a promising phosphate-based material that exhibits high capacity stability during prolonged cycling, good rate performance, environmental friendliness, low cost and safety [10]. Composite electrodes consisting of both this material and AC, which offers low cost and an excellent cycle life and fast charge capability, appears as one of the most viable strategies to develop electrochemical capacitors with high performance without significant safety concerns. Although several papers have focused on $LiFePO_4$ as a potential electrode material for non-aqueous Li-ion capacitors [10-11], few studies have evaluated the electrochemical performance of $LiFePO_4$-based electrode materials in mild aqueous electrolytes. Moreover, to the best of our knowledge, no research has been reported on symmetric composite electrodes assembled using $LiFePO_4$ and AC for Li-ion capacitors. Hence, in this work, we undertake a detailed evaluation of the electrochemical performance of $LiFePO_4$-AC composite electrodes in neutral Na_2SO_3 and Li_2SO_4 aqueous electrolytes. The composite

material is prepared via simple facile mechanical mixing in a dispersive solvent followed by the intercalation of electrolyte ions. The problem associated with the commonly reported poor electric conductivity of $LiFePO_4$ could be overcome by the incorporation of a predetermined amount of carbon black into the system, which can significantly improve the electrochemical performance of oxide-based composite electrodes.

6.2 Results and Discussion

6.2.1 X-Ray Diffraction (XRD)

Figure 6.1 presents the XRD patterns of AC, $LiFePO_4$ and the composite samples. The AC and low $LiFePO_4$-loaded composites (4LFP-AC) generally exhibit a broad diffraction peak, reflecting the amorphous nature of the carbonaceous compound. However, the diffraction profiles of the composites that contain at least 20 wt% $LiFePO_4$ started to exhibit distinct and well-developed diffraction peaks due to the crystallised structures of the $LiFePO_4$ materials. All of the diffraction peaks can be indexed as the orthorhombic structure with the space group Pnmb, which is consistent with a well-crystallised single-phase $LiFePO_4$ according to ICDD #98-005-9133. The lattice parameters of the well-crystallised $LiFePO_4$ are a=10.3240 Å, b=6.0040 Å and c=4.6950 Å, corresponding to the values that have been reported elsewhere [12]. The four main peaks centred at $2\theta \approx 20.8°$, 25.5°, 29.7° and 35.5° are attributed to the (101), (111), (020) and (311) planes of $LiFePO_4$, respectively.

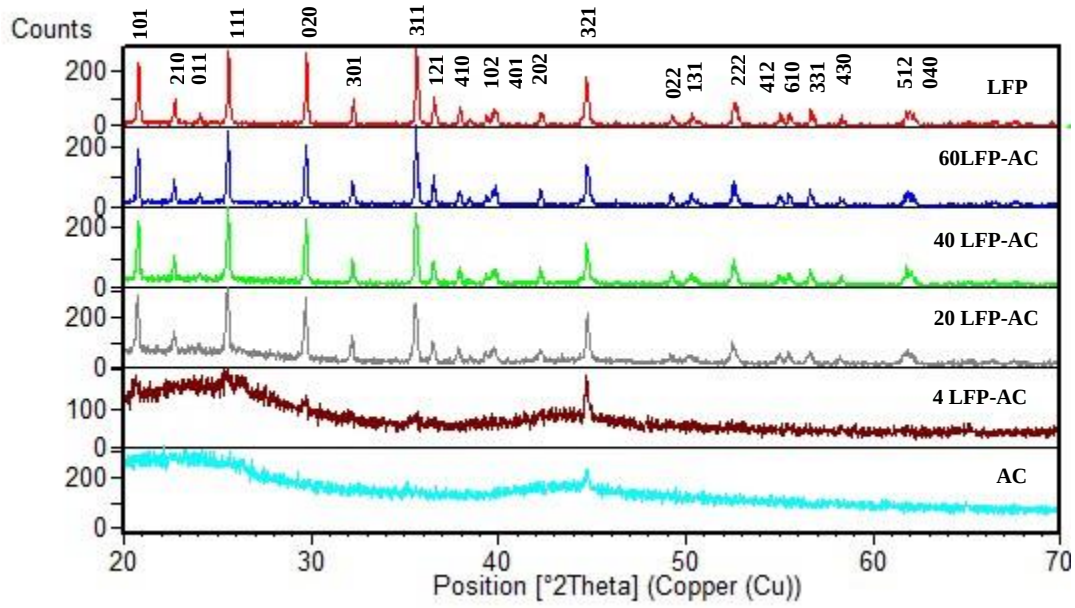


Figure 6.1. XRD patterns of AC electrode and various $LiFePO_4$-AC composite electrodes.

6.2.2 Scanning Electron Microscopy (SEM)

The surface morphologies of the composite electrodes with various $LiFePO_4$ contents were examined by SEM, and the results are presented in Figure 6.2(a-e). As revealed in Figure 6.2(a), the AC electrode possesses non-uniformly distributed aggregates, resulting in a high surface roughness. A similar observation can be made for the 4LFP-AC composite electrode, indicating that no significant morphology change is encountered, as observed in Figure 6.2(b). Figure 6.2(c-d) illustrates that a large number of small dispersed $LiFePO_4$ particles are homogeneously distributed on the surface of the AC particles at approximately 20 wt% loading, providing numerous active sites for electrochemical reaction. The elemental signatures of iron (Fe), phosphorus (P), oxygen (O), carbon (C), sodium (Na) and sulphur (S) in the energy-dispersive X-ray (EDX) spectrum have demonstrated that the $LiFePO_4$ particles are dispersed in the carbon matrix with the intercalation of Na^+ and SO_2^{3-} electrolyte ions, as shown in Figure 6.2(f). No other impurities were detected on the 40LFP-AC composite electrode. Figure 6.2(e) illustrates that high $LiFePO_4$ loading (60 wt%) causes the $LiFePO_4$ particles to start to conglomerate, resulting in a compact and smooth surface. There is a drastic morphological change as the

contents of $LiFePO_4$ increase from 40 % to 60 % loading on AC electrodes. The observed surface characteristic change of 60LFP-AC can be explained by the significant BET surface area reduction (approximately 53 %) due to grain growth and large particle agglomeration. Additionally, the capacitive characteristic of the 60 wt% $LiFePO_4$-loaded electrode can be distorted by such surface characteristics due to the limited diffusion of electrolyte ions into the $LiFePO_4$ particles, leading to a poor charge storage capability [13].

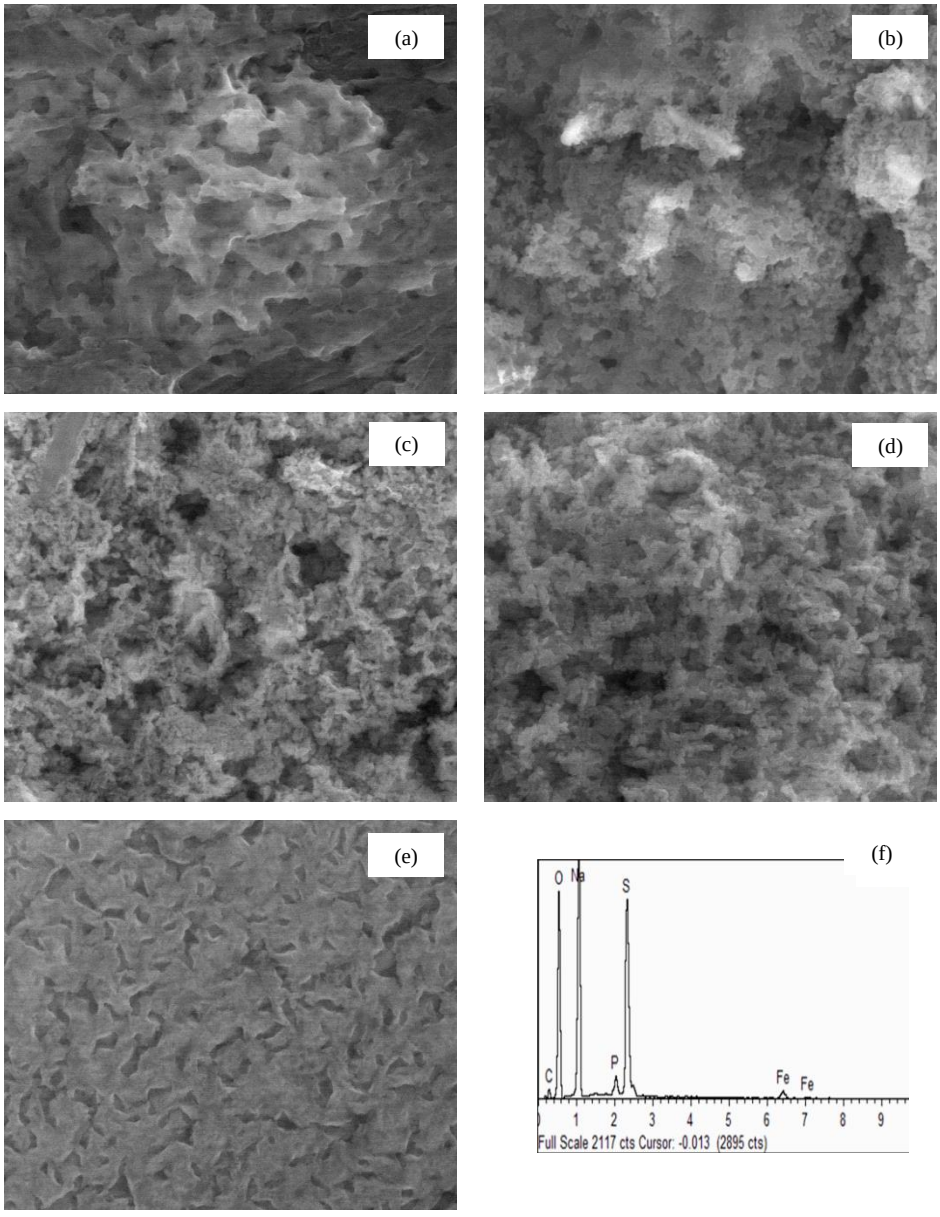


Figure 6.2. Scanning electron micrographs of different $LiFePO_4$ loading in AC: (a) AC, (b) 4LFP-AC, (c) 20LFP-AC, (d) 40LFP-AC, (e) 60LFP-AC, (f) EDX results indicating the elements detected on the 40LFP-AC composite materials, at magnification of 20000x.

6.2.3 Brunauer-Emmett-Teller (BET)

The BET surface areas of the samples with varying compositions are summarised in Table 6.1. The incorporation of 20 wt% of $LiFePO_4$ (20LFP-AC) decreases the specific surface area of the AC electrode from 1,716.61 to 1,351.02 $m^2 g^{-1}$. Further increases in the amount of $LiFePO_4$ from 40 and 60 wt% cause the specific surface area of the composite electrode to decrease to 1,130 and 800 $m^2 g^{-1}$, respectively. The reduced specific surface area of these composite electrodes can be explained by the fact that the specific surface area of the $LiFePO_4$ material (12.87 $m^2 g^{-1}$) is considerably lower than that of the AC. Hence, the specific surface area of the composite material decreases when the $LiFePO_4$ content in the composite is increased. In addition, at high loading content, $LiFePO_4$ particles tend to coalesce to form agglomerates within AC electrodes, as evidenced by the SEM analysis in Figure 6.1. These findings are consistent with other studies suggesting that the particle growth of oxide particles reduces the ionic migration that causes the increase in the diffusion path length and subsequently inhibits the charge storage capability [14-15]. The surface densification of the 60LFP-AC composite electrodes due to particle agglomeration, as evidenced by the SEM micrographs in Figure 6.2(e), provides another explanation for the low BET surface areas.

Table 6.1. BET surface area of $LiFePO_4$-AC composite electrodes.

Electrode Material	$LiFePO_4$ Loading (wt %)	BET Surface Area (m^2/g)
CB	0	1338.44
AC	0	1716.61
4LFP-AC	4	1685.70
20LFP-AC	20	1351.02
40LFP-AC	40	951.74
60LFP-AC	60	684.60
LFP	100	12.88

Figure 6.3 displays a type-IV nitrogen adsorption/desorption isotherm of 40LFP-AC, indicating that the composites consist of mesoporous or macroporous materials. The hysteresis observed in the BET plots confirms the capillary condensation in the mesoporous and macroporous structures [31].

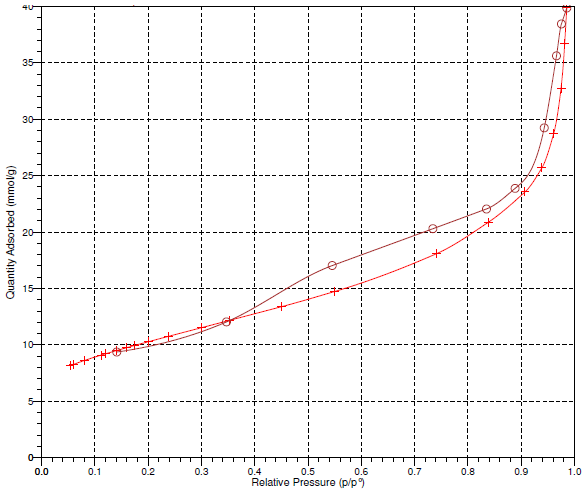


Figure 6.3: BET plot for 40LFP-AC composite materials.

6.2.4 Cyclic Voltammetry (CV)

The CV plots for the $LiFePO_4$-AC composite electrodes with different $LiFePO_4$ loadings in 1 M Na_2SO_3 at a constant scan rate of 10 mV/s are presented in Figure 6.4. All of the curves exhibit mirror-like images with respect to the zero-current line, which is a typical capacitive characteristic. Additionally, the voltammograms of the $LiFePO_4$-based composite electrodes do not exhibit perfect rectangular features, implying that there is a substantial pseudocapacitance contribution to the overall measured capacitance. Two diffusion mechanisms are proposed to be responsible for the charge storage process in the metal oxide-based electrodes. The first mechanism is based on the concept of the adsorption/desorption of a proton (H^+), hydroxide (OH^-), alkali metal cation (Na^+) and sulphide anions (SO_3^{2-}) from an electrolyte on the $LiFeO_4$-AC composite electrodes, thus forming a double layer at the electrode-electrolyte interface. The second mechanism is based on the intercalation/extraction of H^+, OH^-, Na^+ and SO_3^{2-} ions from the electrolyte within the bulk composite electrodes [16]. Both reversible adsorption/desorption and intercalation/extraction processes are accompanied by the faradaic reaction or valence conversion of the electrolyte ions and metal oxides within the bulk electrodes [17].

Recent work on the capacitance mechanisms of metal oxide-based electrode materials in Na_2SO_4, Na_2SO_3 and KOH aqueous solutions has demonstrated that strong

specific adsorption of anions was observed in all solutions [18]. Additionally, the electrolyte cation also plays an important role in the Na_2SO_3 electrolyte system [9]. Hence, the lithiated compounds in Na_2SO_3 likely exploit the intercalated/extracted Na^+ and Li^+ ions in the electrolyte, producing a pseudocapacitance, as described in Eq. (6.1)-(6.3).

$$LiFePO_4 + Na_2SO_3 \rightleftharpoons FePO_4 + Li^+ + 2Na^+ + SO_3^{2-} + e^- \quad \text{Eq. (6.1)}$$

$$2SO_3^{2-} + 3H_2O + 4e^- \rightleftharpoons S_2O_3^{2-} + 6OH^- \quad \text{Eq. (6.2)}$$

$$S_2O_3^{2-} + 3H_2O + 8e^- \rightleftharpoons 2S^{2-} + 6OH \quad \text{Eq. (6.3)}$$

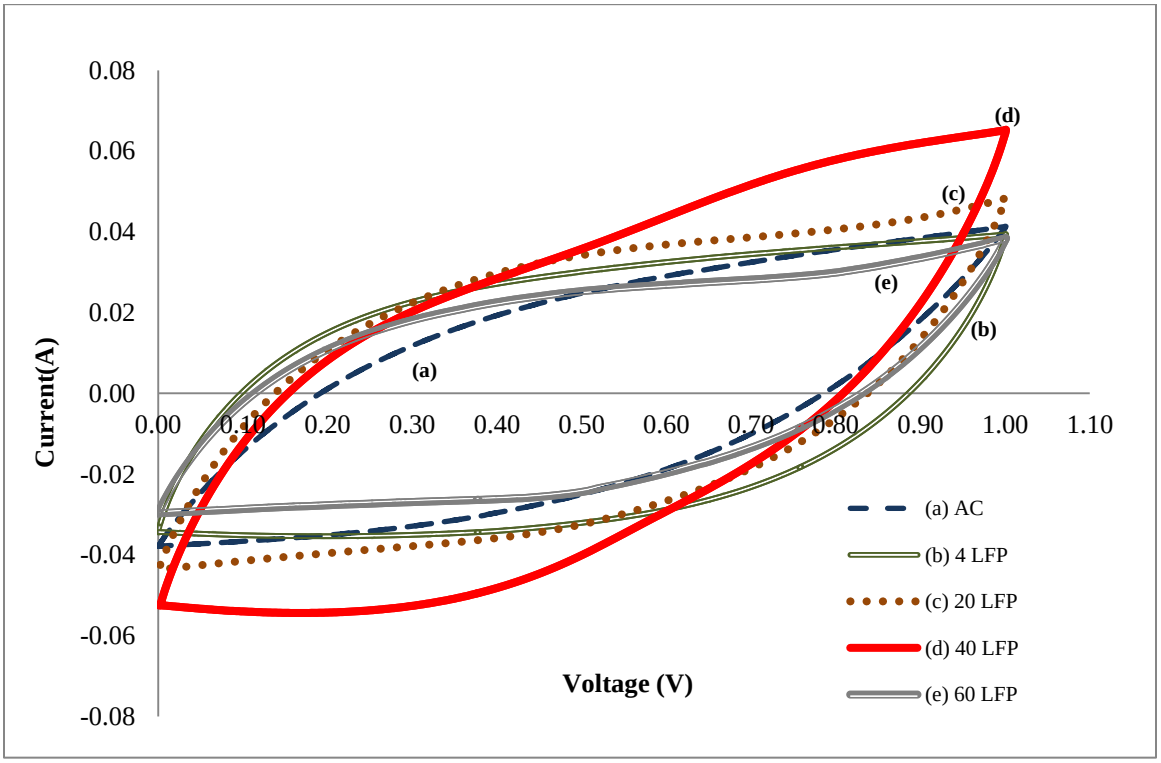


Figure 6.4. Cyclic voltammograms for different compositions of $LiFePO_4$ loaded in AC electrodes, scanned at 10 mV/s, in 1 M Na_2SO_3.

The CV plots for the $LiFePO_4$-AC composite electrodes with different $LiFePO_4$ loadings in 1 M Li_2SO_4 at a constant scan rate of 10 mV s^{-1} are presented in Figure 6.5. Similarly, for the Li_2SO_4 electrolyte, the combination of EDLC and pseudocapacitance is also employed for the energy storage of $LiFePO_4$-based electrodes. The role of sulphate (SO_4^{2-}) anions in contributing to a significant pseudocapacitive effect in Li_2SO_4 is excluded,

as the energy storage mechanism of the electrodes in a Na_2SO_4 electrolyte is based solely on EDLC [18]. Instead, the intercalation and extraction of Li^+ ions in $LiFePO_4$ lattices are responsible for the reversible Faradaic reaction occurring in the Li_2SO_4 electrolyte, balancing the charge transfer upon Fe (III) and Fe (II) in $FePO_4$ [9]. Li^+ ions are extracted from $LiFePO_4$ during the charging state and intercalated into $LiFePO_4$ lattices during the discharging state via the Li_2SO_4 electrolyte [30]. The Faradaic reaction between the $LiFePO_4/FePO_4$ redox couple is described by Eq. (6.4) [19].

$$LiFePO_4 + Li_2SO_4 \rightleftharpoons FePO_4 + 3Li^+ + SO_4^{2-} + e^- \qquad \text{Eq. (6.4)}$$

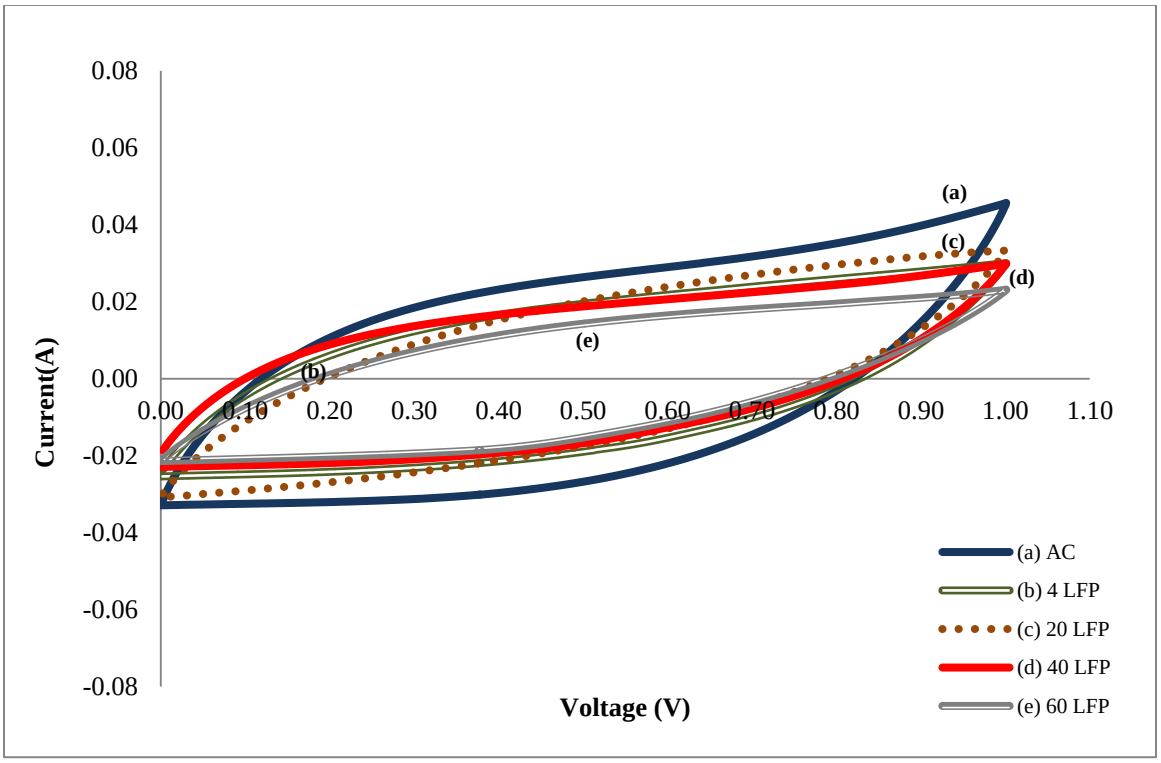


Figure 6.5. Cyclic voltammograms for different compositions of $LiFePO_4$ loaded in AC electrodes, scanned at 10 mV/s, in 1 M Li_2SO_4.

The respective capacitances (C) were calculated from the CV curves using Eq. (3.9) (refer to Chapter 3). As observed in Figure 6.6, the capacitive performance of the AC electrode gradually increases when 4, 20, 40 and 60 wt% $LiFePO_4$ were loaded onto the AC electrodes, respectively. The maximum specific capacitance of 112.41 F/g in 1 M Na_2SO_3 is obtained for 40LFP-AC, which exhibits a capacitance that is 47.44% greater

than that of the pure AC electrode (76.24 F/g). The presence of a substantial amount of $LiFePO_4$ can provide favourable surface adsorption sites for sulphite anions, which act as catalysts for subsequent redox and intercalation reactions in Na_2SO_3. However, the presence of $LiFePO_4$ particles should not block the porous surface of an AC electrode, which could alter the extent of capacitance contribution. The sulphite anions contribute to the pseudocapacitance only minimally when the $LiFePO_4$ content is increased to 60 wt% (60LFP-AC). The large $LiFePO_4$ agglomerates limit the diffusion of sulphite ions into the porous structures of AC electrodes [13]. Thus, the capacitance of 60LFP composite electrodes is relatively poorer than that of electrodes with a lower $LiFePO_4$ content.

$LiFePO_4$-based electrodes in a Li_2SO_4 electrolyte achieve lower specific capacitances than in a Na_2SO_3 electrolyte. Interestingly, the specific capacitance of a pure AC electrode in Li_2SO_4 (72.09 F/g) is higher than those of all of the $LiFePO_4$-AC composite electrodes (43-59 F/g). The incorporation of $LiFePO_4$ into AC electrodes does not increase the charge storage capability but instead adversely affects the capacitive performance. Unlike Na_2SO_3, sulphate anions (SO_4^{2-}) in Li_2SO_4 do not provide pseudocapacitance, as needed in an energy storage system. Thus, the intercalation and extraction of lithium (Li^+) ions become the only predominant phenomenon responsible for the charge storage mechanism in a Li_2SO_4 electrolyte. Hence, the synergistic pseudocapacitance contribution from the $LiFePO_4$ material is greatly affected. In addition, the BET surface area of $LiFePO_4$-AC composite electrodes decreases with increasing $LiFePO_4$ content (as observed in Table 6.1), demonstrating that the porosity of composite electrodes decreases due to the presence of $LiFePO_4$ particles. Therefore, a $LiFePO_4$-AC composite material in Li_2SO_4 exhibits a lower capacitance than the Na_2SO_3 electrolyte system.

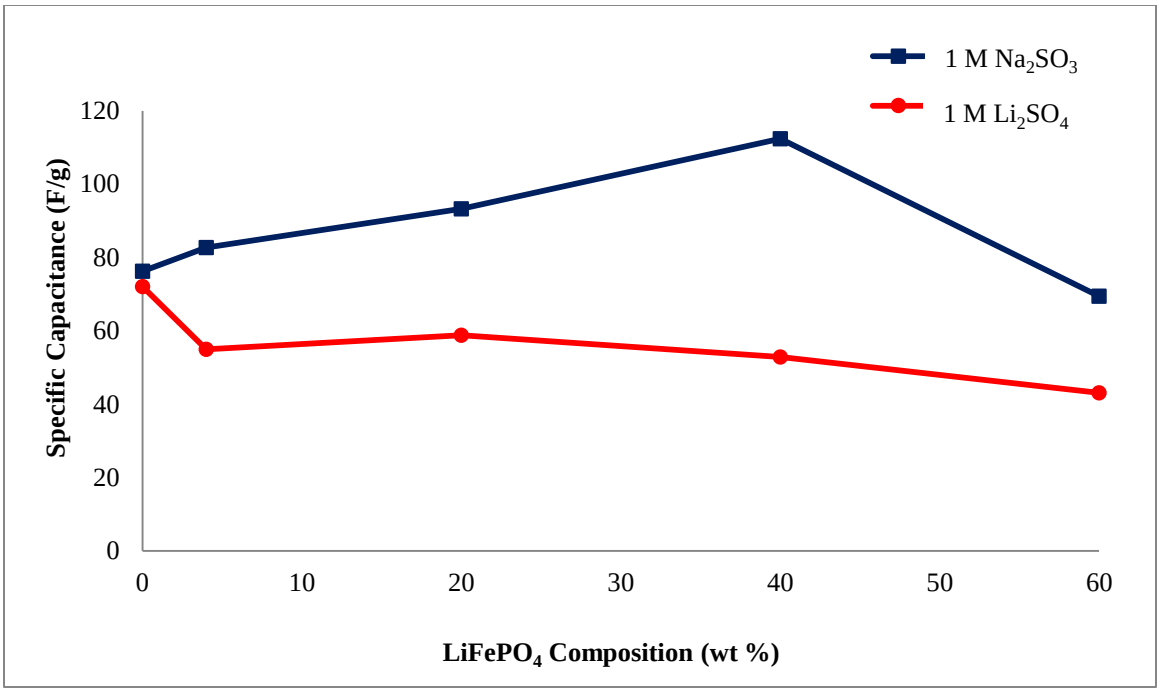


Figure 6.6. Specific capacitance of $LiFePO_4$- AC composite electrodes as a function of $LiFePO_4$ loading, in 1 M Na_2SO_3 and 1 M Li_2SO_4 respectively, at the scan rate of 10 mV/s.

In addition, the cation of the electrolyte has a significant effect on the charge storage capability of the active materials. Reddy and co-workers (2003), who have studied MnO_2-based electrodes in various aqueous electrolytes, including NaCl, KCl, Na_2SO_4 and LiCl, reported that the radius of the hydration sphere decreases in the order: $Li^+ > Na^+ > K^+$ [21]. Li^+ ions have larger hydration spheres than Na^+ ions due to their stronger $Li^{\delta+}$–$H_2O^{\delta-}$ interaction, resulting the inherently slow solid-state diffusion of Li^+ ions in the bulk of the active materials [3]. Additionally, Li^+ ions exhibit low conductivity, which could lead to poor capacitive behaviour. In fact, the conductivity and mobility of cations may be the determining factor for charge storage behaviour in different electrolytes [21].

6.2.5 Galvanostatic Charge-Discharge (GCD)

Figure 6.7 presents the GCD profiles of the AC, 4LFP-AC, 20LFP-AC, 40LFP-AC and 60LFP-AC electrodes in 1 M Na_2SO_3 electrolytes at a current density of 5 mA/cm^2. The voltage increases and decreases linearly over time along the GCD cycle, exhibiting

the typical capacitive characteristic [2]. As observed in Figure 6.7 (d), the GCD slopes of 40LFP-AC diverge from linearity, which is consistent with the non-rectangular CV curve shown in Figure 6.4 (d). During the discharge process, the desorption and extraction of anions and the adsorption and intercalation of cations occur simultaneously on the positive electrode [5]. The Li^+ ions that are supplied from the lithiated compound ($LiFePO_4$) are likely involved in the cation intercalation/extraction of Na_2SO_3, resulting in a loss of Li^+ ions from $LiFePO_4$, according to Eq. (6.1).

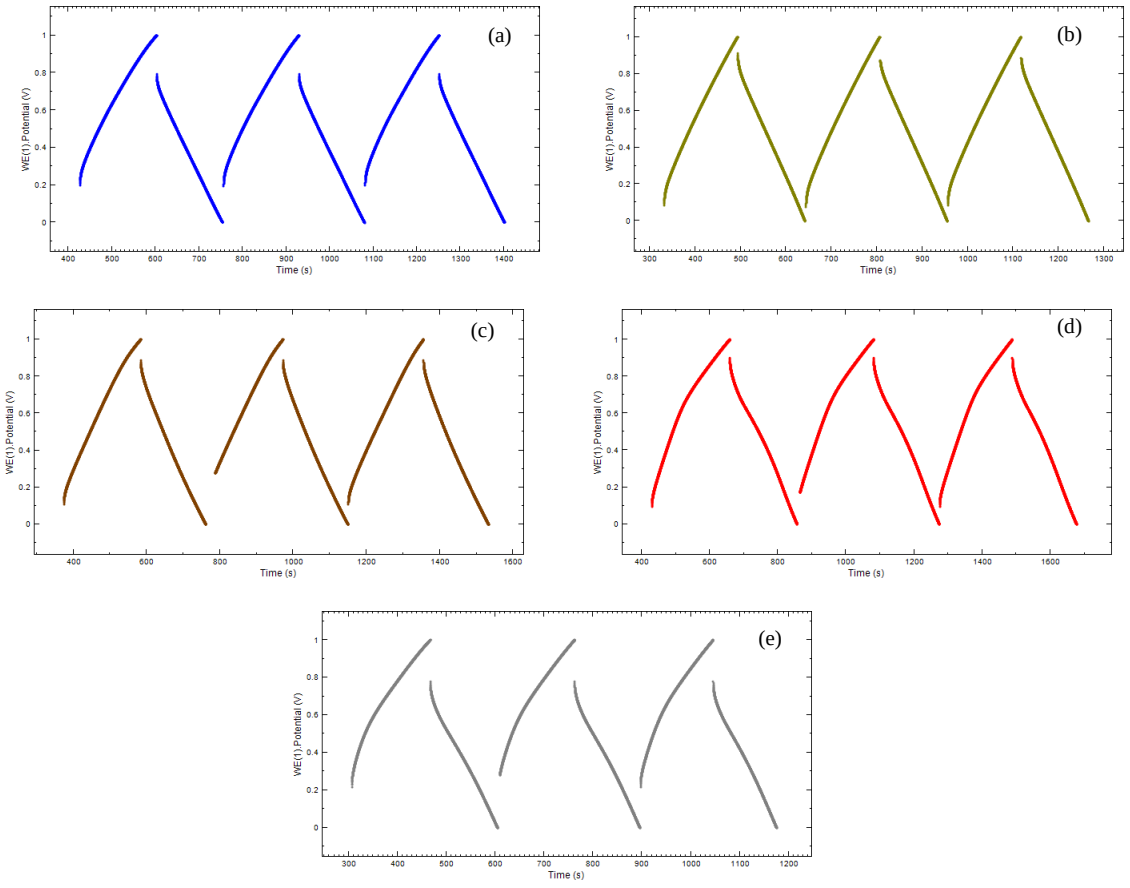


Figure 6.7. Charge-discharge curves of $LiFePO_4$-based composite electrodes with various compositions: (a) AC, (b) 4LFP-AC, (c) 20LFP-AC, (d) 40LFP-AC, (e) 60LFP-AC, obtained at the constant density of 5 mA/cm^2.

Table 6.2 compares the specific capacitances and ESR values of AC, $LiFePO_4$ and their composites obtained from GCD measurements. The maximum specific capacitance (124.88 F/g) is obtained from the discharge curves of the 40LFP-AC composite electrode in Na_2SO_3. The trend of the specific capacitance of the composite electrode is consistent with the observation in the CV measurement (Figure 6.4). However, the specific capacitance values obtained from the GCD measurements are approximately 10 % higher than those determined from the CV testing. Theoretically, both values should be comparable if they were measured at comparable currents. However, in this study, the specific capacitance values obtained from the GCD measurements (5 mA/cm^2) are higher than those determined from the CV testing (10 mV/s) due to the difference in current. A higher current may give a smaller capacitance value due to the insufficient time available for ion diffusion and adsorption inside the pores.

Table 6.2. Comparison of specific capacitances and ESR values between AC, 4 wt %, 20 wt% and 60 wt % $LiFePO_4$-AC composite electrodes.

Electrode material	Charge-discharge measurement at 5 mA/cm^2	
	Specific capacitance (F/g)	ESR (Ω)
AC	84.47	5.17
4LFP-AC	95.75	4.03
20LFP-AC	102.05	2.85
40LFP-AC	124.88	1.87
60LFP-AC	75.81	5.52

The effect of different current density on the discharge time of the 40LFP-AC composite electrodes in 1 M Na_2SO_3 is shown in Figure 6.8. The discharging time decreases with increases in the applied current due to the lower utilisation of active materials. In fact, electrolyte ions do not have sufficient time to diffuse into the core of the active materials because of the high polarisation at higher current densities [30]. As discussed earlier, the predominant energy storage mechanism is contributed by the redox reactions involving intercalation/extraction of cations and anions from both electrode materials and the electrolyte. At lower current densities, complete intercalation/extraction

occurs at the inner structure and outer surface of the electrodes due to the high accessibility of ions to almost all available pores of the electrode. In contrast, ion movement is limited due to their slow diffusion, and only the outer surface can be utilised for charge storage at high current densities [8]. The same phenomenon has been observed when increasing the voltage scan rate. With these explanations, the scan rate of 10 mV/s used in the CV test and the current density of 5 mA/cm^2 may not be able to provide a similar effect for the diffusion of ions in 40LFP.

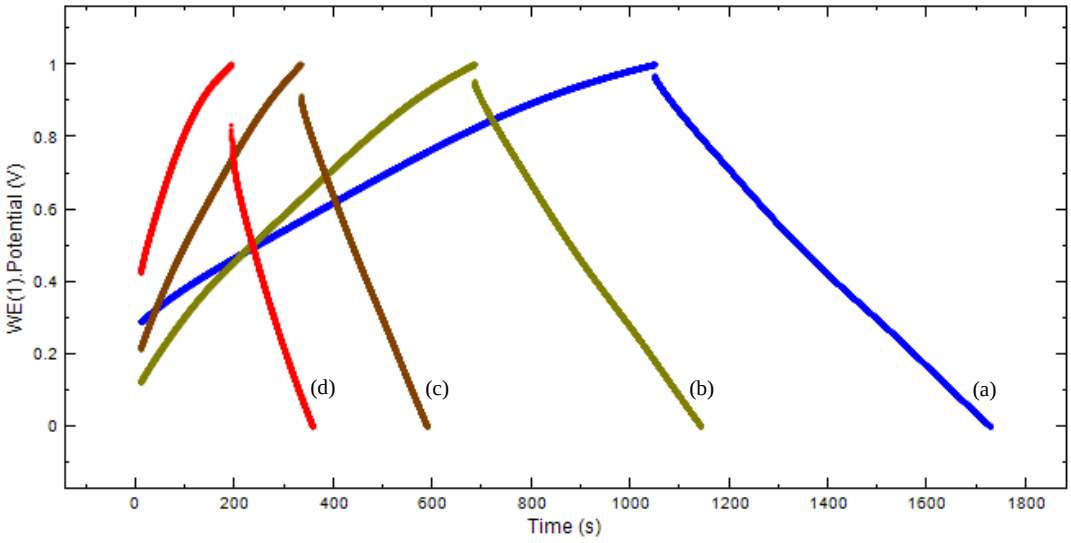


Figure 6.8. Galvanostatic charge-discharge curves of 40LFP-AC composite electrodes at different current densities in 1 M Na_2SO_3: (a) 2, (b) 3, (c) 5, (d) 10 mA/cm^2.

The capacitive performance of the 40LFP-AC composite electrodes examined at various current densities is presented in Figure 6.9. The specific capacitance decreases gradually with increases in the current rate. One possible explanation for this capacitance fading at high current densities is the occurrence of a large IR decrease as well as the high activation and concentration polarisation on the composite electrodes at high current densities [4].

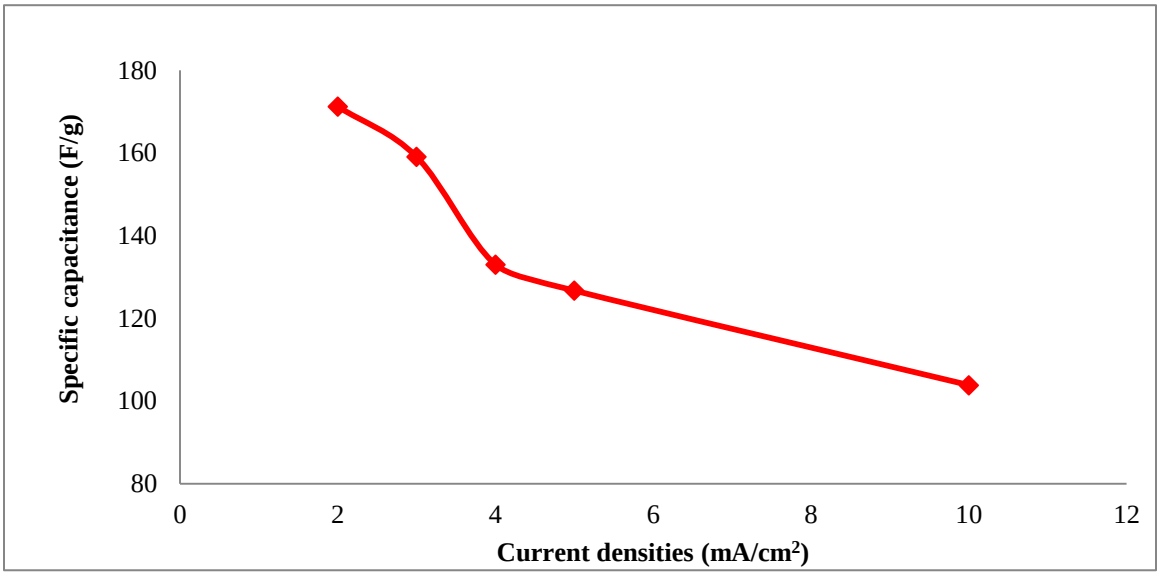


Figure 6.9. Specific capacitance of 40LFP-AC in Na_2SO_3 in the function of current densities.

6.2.6 Electrochemical Impedance Spectroscopy (EIS)

The EIS measurements were performed on AC and $LiFeO_4$-AC composite electrodes between 100 kHz and 10 mHz. Figure 6.10 displays the Nyquist plots of the $LiFePO_4$-AC composite electrodes with different compositions in 1 M Na_2SO_3. All of the impedances consist of an arc and slanted line at low frequency. In the high-frequency region, the intercept of the semicircle on the real axis of the Nyquist spectrum represents the solution resistance (R_s), which provides the resistance at the electrode-electrolyte interface. The R_s arises mainly due to the difference in the conductivity between the solid electrode (electronic conductivity) and aqueous electrolyte (ionic conductivity) [24]. Additionally, the impedance behaviour in this region is characteristic of the resistance from the Faradaic reaction associated with the interfacial processes of the porous composite electrode. The semicircles in the high- and mid-frequency regions are attributed to an interfacial charge transfer resistance (R_{CT}) or polarisation resistance (R_p) and the double-layer capacitance (C_{DL}) connected to each other in parallel [25]. The observed charge transfer resistance represents the sum of the resistance due to the ion migration through the bulk of the composite electrode, the resistance of the charges in the pores of

the composite electrode, the electrode-electrolyte resistance and the electrode resistance. After the semicircle, the Nyquist spectrum exhibits a straight line in the low-frequency region, which corresponds to the Warburg element, W [25]. The Warburg element represents the diffusion of SO_3^{2-} ions from the electrolyte into the pores on the surface of the electrode, which occurs during the transition from the high-frequency semicircle to the mid-frequency spike. The electrochemical performance can be enhanced by increasing the diffusion rate. Reduced ohmic and charge transfer resistances can allow a higher current to reach the electrode, which in turn increases the diffusion rate of ions toward the electrodes [26]. Another tangent hyperbolic diffusion circuit element (T) is incorporated into the Randles equivalent circuit when the diffusion condition is under restricted diffusion limitation between the electrode and another non-reactive surface (current collector). As noted earlier, the diffusion layer is restricted because of the impermeability of ions at current collectors of nanocomposite electrodes [27]. This diffusion parameter, which is also known as the bounded Warburg parameter because of its similarity to the Warburg element at high frequencies, is commonly used to model batteries and electrochemical capacitor electrode materials [27].

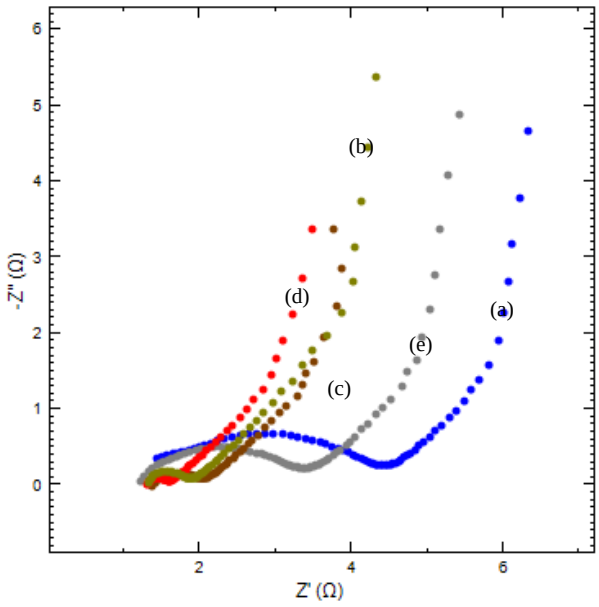


Figure 6.10. (a) Nyquist plots obtained for composite electrodes with different Fe_3O_4 loading at 0 V over the frequency range of 100 kHz – 10 mHz in 1 M Na_2SO_3: (a) AC, (b) 4LFP-AC, (c) 20LFP-AC, (d) 40LFP-AC, (e) 60LFP-AC.

The Nyquist plot in Figure 6.10 demonstrates that the diameter of the semicircle varies considerably between the AC and composite electrodes for different $LiFePO_4$ loadings. The 40LFP composite electrode exhibits the smallest diameter and minimum R_{CT} at high frequencies, as shown in Figure 6.10(d). A reduction in the value of R_{CT} implies that the 1:1 composition ratio of $LiFePO_4$:AC is the optimal composition in the $LiFePO_4$-AC composite electrode system. A high $LiFePO_4$ content ensures that more accessible sites are available for Faradaic reactions, as described in Eqs. (1) - (3), whereas a high AC content improves the electronic conductivity and EDLC of the composite electrodes. At higher contents, $LiFePO_4$ will aggregate and thus hinder the diffusion of ions, as can be clearly observed with the increased R_{ct} in 60LFP-AC in Figure 6.10(e). The composite electrode has R_s (1.07 Ω) and R_{ct} (0.518 Ω) values that contribute a total internal resistance of 1.59 Ω, which is lower than the ESR determined from the decrease in IR in the constant current discharge curve (1.87 Ω).

The impedance expressions obtained from the equivalent circuit were fitted to the experimental Nyquist spectra using the NOVA equivalent circuit editor to determine the most representative physical processes for 40LFP-AC in Na_2SO_3. The fitting result is shown in Figure 6.11 (a), and Figure 6.11 (b) presents the Randle equivalent circuit used to fit the Nyquist spectra. It is worth noting that the double-layer capacitor measured in the EIS experiment often does not behave ideally. To describe the non-ideality in a real cell, Q or the constant-phase element (CPE) is typically used in place of the capacitive element (C) due to imperfections in the real electrochemical cell, including the surface roughness, a leaky capacitor and a non-uniform current distribution [28]. The impedance of the constant-phase element (Q) can be expressed as a power of n as

$$Z = 1/ (j\omega Q)^n \qquad \text{Eq (6.5)}$$

The material resembles a resistor when n = 0 and an ideal capacitor when n=1. Generally, real capacitors exhibit values of $0<n<1$ [28]. In the current study, n=0.662 for 40 LFP-AC. The degree of deviation from the vertical line along the imaginary axis (-Z") is dependent on the value of n. This deviation is likely due to the effect of inductance error (L) under a negative phase at high frequencies on the impedance spectra, which is

attributed to instrumental artefacts, the improper length of the test lead wire and the wiring configuration [29]. In this study, the composite electrodes exhibit R_s (1.07 Ω) and R_{ct} (0.518 Ω) values that contribute a total internal resistance of 1.59 Ω, which is lower than the ESR determined from the decrease in IR in the constant current discharge curve (1.87 Ω).

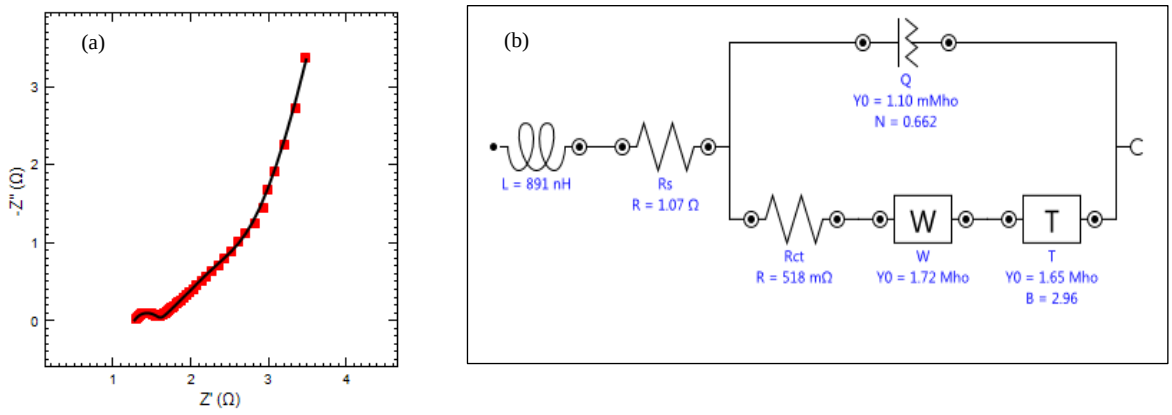


Figure 6.11. (a) The fitting of the impedance expressions (━) obtained from the equivalent circuit to the experimental Nyquist spectra (■); (b) Randles equivalent circuit representing the circuit elements that are used to fit the experimental Nyquist spectra using the software Nova.

6.3.7 Ragone Plot and Cyclability

Figure 6.12 presents the Ragone plot of 40LFP-AC composite electrodes in Na_2SO_3 at various current densities. The specific energy and specific power were determined based on the two composite electrodes using the voltage value without an ohmic drop [8]. Specific energies of 13 and 3.4 Wh/kg were attained at specific powers of 130 and 1,000 W/kg, respectively. The limited rate capability at high current rates is associated with the complex resistance and limited ion diffusion within the bulk electrodes [30]. Only outer regions of the electrode surface accessible by ions are utilised for the charge storage. To demonstrate the long-term stability of the 40LFP-AC composite electrode, a cycling test over 1,000 cycles was conducted at a scan rate of 10 mV/s

between 0 and 1 V in 1 M Na_2SO_3. As observed in Figure 6.13, the CV profiles between the 1st to 1,000th cycles reveal no significant capacitance decay during cycling. The specific capacitance as a function of the cycle number is shown in Figure 6.14. The specific capacitance of the composite electrodes increases to approximately 18% during the first 50 cycles and then decreases slightly. Electrolyte ions penetrate further into the pores of the electrodes during the initial cycling [9]. Such a cyclic behaviour is crucial in industrial applications for electrochemical capacitors. Subsequently, the composite electrodes can sustain a stable capacitive performance of at least 1,000 cycles with an average specific capacitance value of 114±3 F/g. After 1,000 cycles, the specific capacitance loss is only approximately 5% of the maximal specific capacitance. The enhanced capacitive performance of the composite electrodes can be attributed to: (i) the large specific surface area of AC, (ii) the high electroactive property of $LiFePO_4$, (iii) the stable integration of $LiFePO_4$ and the AC matrix and (iv) the high mechanical robustness and stability of AC in the mild aqueous electrolyte.

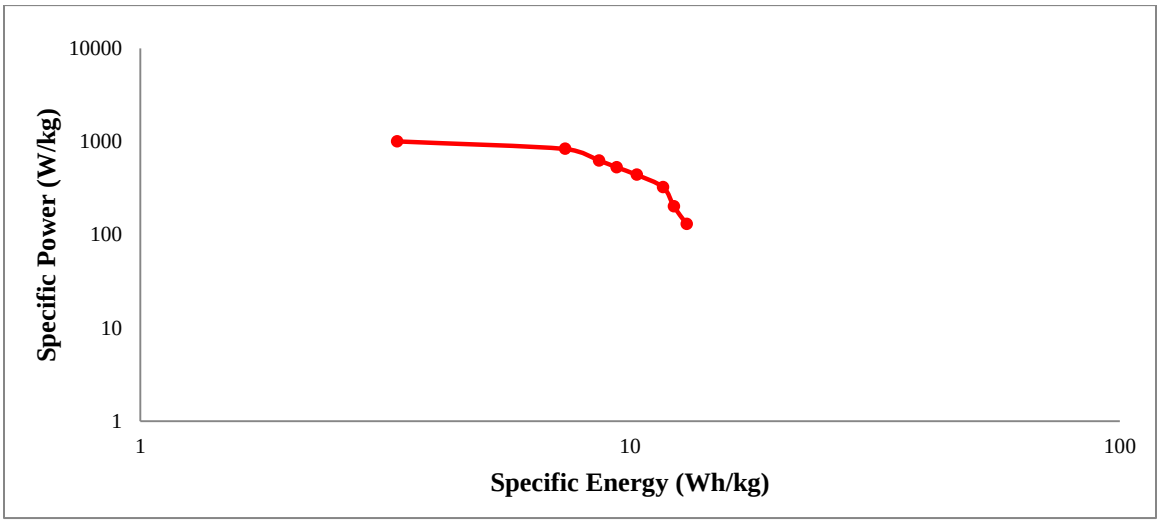


Figure 6.12. Ragone plot of 40LFP-AC composite electrodes.

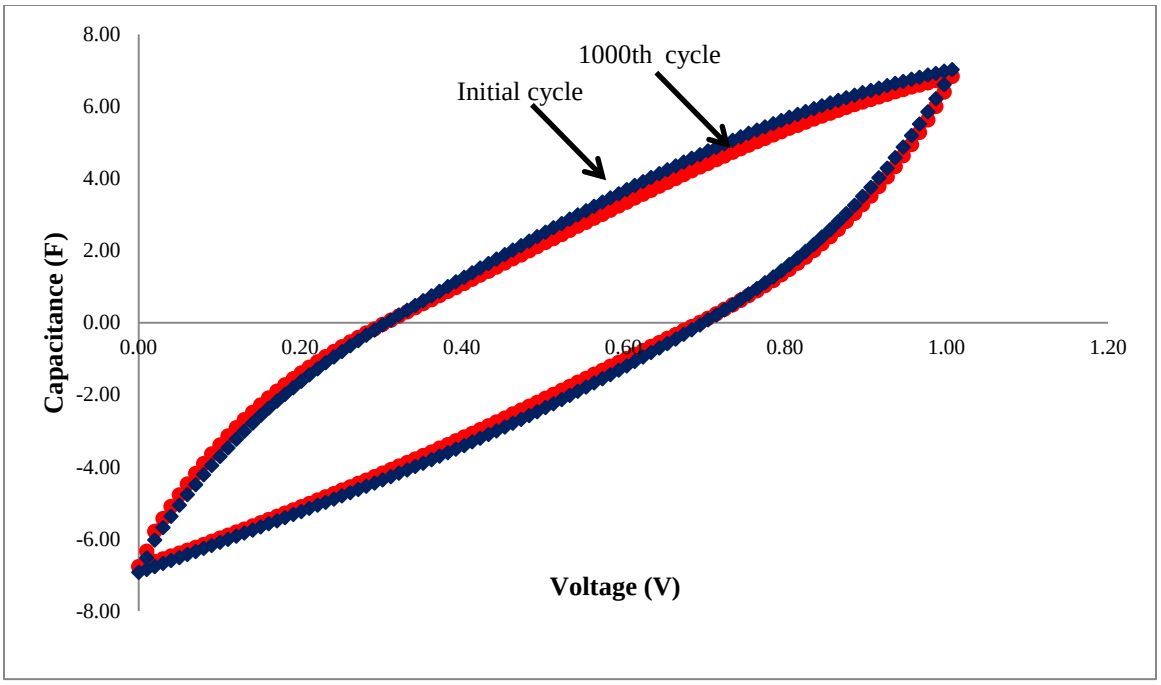


Figure 6.13. CV profile comparison of 40LFP–AC composite electrodes between initial cycle and 1000th cycles at 10 mV/s in 1 M Na_2SO_3.

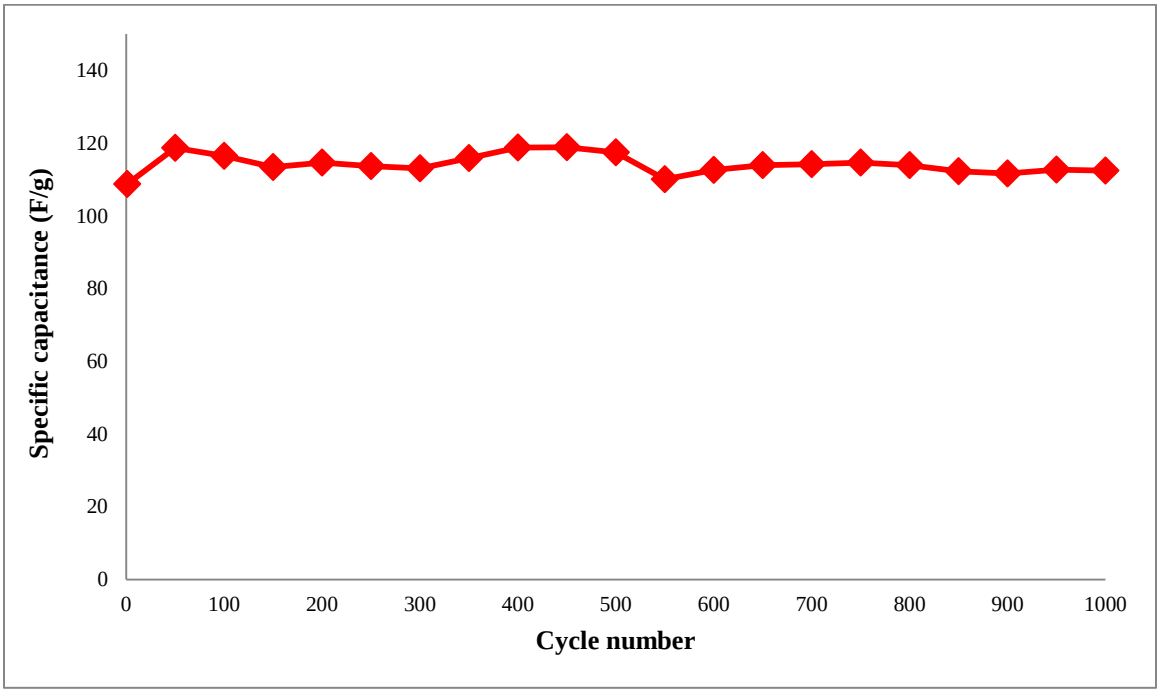


Figure 6.14. Cycling life of 40LFP–AC composite electrodes in aqueous Na_2SO_3 electrolyte at scan rate of 10 mV/s between 0 and 1 V.

6.4 Summary

The structural analysis and capacitive performance of $LiFePO_4$-AC composite electrode materials in mild aqueous Na_2SO_3 and Li_2SO_4 electrolytes were comprehensively evaluated. The highest specific capacitance of 112.41 F/g was achieved with 40 wt% $LiFeO_4$ loaded on AC in 1 M Na_2SO_3 at a current density of 5 mA/cm^2. The improved capacitive performance of the 40LFP composite electrode is attributed to the synergistic effect of the EDLC on the surface of AC and the pseudocapacitance via the intercalation/extraction of H^+, OH^-, Na^+ and SO_3^{2-} and Li^+ ions in $LiFePO_4$ lattices. Overall, the results reveal that the AC composite electrodes with 40 wt% $LiFePO_4$ loading in a Na_2SO_3 neutral electrolyte exhibit high cycling stability and reversibility and thus display great potential for electrochemical capacitor applications.

Reference

[1] V. Aravindan, W. Chuiling, and S. Madhavi, "High power lithium-ion hybrid electrochemical capacitors using spinel $LiCrTiO_4$ as insertion electrode," J. Mater. Chem. 22 (2012)16026.

[2] S. Makino, Y. Shinohara, T. Ban, W. Shimizu, K. Takahashi, N. Imanishi, and W. Sugimoto, "4 V class aqueous hybrid electrochemical capacitor with battery-like capacity," RSC Adv.2 (2012)12144.

[3] D. Cericola, P. Novák, A. Wokaun, and R. Kötz, "Hybridization of electrochemical capacitors and rechargeable batteries: An experimental analysis of the different possible approaches utilizing activated carbon, $Li_4Ti_5O_{12}$ and $LiMn_2O_4$," J. Power Sources 196 (2011) 10305–10313.

[4] K. Karthikeyan, V. Aravindan, S. B. Lee, I. C. Jang, H. H. Lim, G. J. Park, M. Yoshio, and Y. S. Lee, "Electrochemical performance of carbon-coated lithium manganese silicate for asymmetric hybrid supercapacitors," J. Power Sources 195 (2010) 3761–3764.

[5] S. R. Sivakkumar and a. G. Pandolfo, "Evaluation of lithium-ion capacitors assembled with pre-lithiated graphite anode and activated carbon cathode," Electrochim. Acta 65 (2012) 280–287.

[6] K. Naoi, S. Ishimoto, Y. Isobe, and S. Aoyagi, "High-rate nano-crystalline $Li_4Ti_5O_{12}$ attached on carbon nano-fibers for hybrid supercapacitors," J. Power Sources 195 (2010) 6250–6254.

[7] Y. Wang and Y. Xia, "A new concept hybrid electrochemical surpercapacitor: Carbon/$LiMn_2O_4$ aqueous system," Electrochem. commun.7 (2005) 1138–1142.

[8] A. Malak, K. Fic, G. Lota, C. Vix-Guterl, and E. Frackowiak, "Hybrid materials for supercapacitor application, " J. Solid State Electrochem. 14 (2009) 811–816.

[9] J. Santos-Peña, O. Crosnier, and T. Brousse, "Nanosized α-$LiFeO_2$ as electrochemical supercapacitor electrode in neutral sulfate electrolytes," Electrochim. Acta 55 (2010) 7511–7515.

[10] N. Böckenfeld, R.-S. Kühnel, S. Passerini, M. Winter, and a. Balducci, "Composite $LiFePO_4$/AC high rate performance electrodes for Li-ion capacitors," J. Power Sources 196 (2011) 4136–4142.

[11] X.L. Wu, L.Y. Jiang, F.F. Cao, Y.G. Guo, and L.J. Wan, "$LiFePO_4$ Nanoparticles Embedded in a Nanoporous Carbon Matrix: Superior Cathode Material for Electrochemical Energy-Storage Devices," Adv. Mater. 21 (2009) 2710–2714.

[12] Z.R. Chang, H.J. Lv, H.W. Tang, H.J. Li, X.Z. Yuan, and H. Wang, "Synthesis and characterization of high-density $LiFePO_4$/C composites as cathode materials for lithium-ion batteries," Electrochim. Acta 54 (2009) 4595–4599.

[13] M. Takahashi, S. Tobishima, K. Takei, and Y. Sakurai, "Characterization of $LiFePO_4$ as the cathode material for rechargeable lithium batteries," J. Power Sources (2001) 508–511.

[14] C.C.Hu and W.C.Chen, "Effects of substrates on the capacitive performance of $RuO_x \cdot nH_2O$ and activated carbon–RuO_x electrodes for supercapacitors," Electrochim. Acta 49 (2004) 3469–3477.
[15] H. Kim and B. N. Popov, "Characterization of hydrous ruthenium oxide/carbon nanocomposite supercapacitors prepared by a colloidal method," J. Power Sources 104 (2002) 52–61.
[16] M. B. Sassin, A. N. Mansour, K. A. Pettigrew, D. R. Rolison, and J. W. Long, "Electroless Deposition of Conformal Nanoscale Iron Oxide on Carbon Charge Storage," ACS Nano 4 (2010) 4505–4514.
[17] D. P. Dubal, W. B. Kim, and C. D. Lokhande, "Galvanostatically deposited Fe: MnO_2 electrodes for supercapacitor application," J. Phys. Chem. Solids 73 (2012) 18–24.
[18] S.Y.Wang, K.C.Ho, S.L.Kuo, and N.L.Wu, "Investigation on Capacitance Mechanisms of Fe_3O_4 Electrochemical Capacitors," J. Electrochem. Soc.153 (2006) A75.
[19] H. Kang, G. Wang, H. Guo, M. Chen, C. Luo, and K. Yan, "Facile Synthesis and Electrochemical Performance of $LiFePO_4$/C Composites Using Fe−P Waste Slag," ACS Ind.Eng.Che.Res (2012).
[20] N. Nagarajan, H. Humadi, and I. Zhitomirsky, "Cathodic electrodeposition of MnO_x films for electrochemical supercapacitors," Electrochim. Acta 51 (2006) 3039–3045.
[21] R. N. Reddy and R. G. Reddy, "Sol–gel MnO_2 as an electrode material for electrochemical capacitors," J. Power Sources 124 (2003) 330–337.
[22] T. Brousse and J. W. Long, "Manganese Oxides : Battery Materials Make the Leap to Electrochemical Capacitors," Interface (2008).
[23] S. W. Zhang and G. Z. Chen, "Manganese oxide based materials for supercapacitors," Energy Mater.3 (2008) 186–200.
[24] S. K. Meher and G. R. Rao, "Ultralayered Co_3O_4 for High-Performance Supercapacitor Applications," J. Phys. Chem. C 115 (2011) 15646–15654.
[25] C. Masarapu, H. F. Zeng, K. H. Hung, and B. Wei, "Effect of temperature on the capacitance of carbon nanotube supercapacitors," ACS Nano 3 (2009) 2199–206.
[26] A. Chu and P. Braatz, "Comparison of commercial supercapacitors and high-power lithium-ion batteries for power-assist applications in hybrid electric vehicles I . Initial characterization," J. Power Sources 112 (2002) 236–246.
[27] S. P. Taberna, P.Louis, "Electrochemical Techniques, in : Supercapacitors: Materials, Systems and Applications," F. Beguin. and E.Frackowiak, Ed. Germany: Wiley-VCH, 2013, pp. 119–129.
[28] V. D. Jovic, "Determination of the correct value of C_{dl} from the impedance results fitted by the commercially available software," [Online]. Available: http://www.gamry.com (2012)
[29] J. R. Macdonald, E.Barsoukov, "Impedance Spectroscopy, Theory Experiment and Applications," Canada: John Wiley & Sons, Inc (2005).

[30] K. Karthikeyan, V. Aravindan, S. B. Lee, I. C. Jang, H. H. Lim, G. J. Park, M. Yoshio, and Y. S. Lee, "A novel asymmetric hybrid supercapacitor based on Li_2FeSiO_4 and activated carbon electrodes," J. Alloys Compd.504 (2010) 224–227.

[31] S. J. Gregg and K. S. W. Sing, Adsorption, "Surface Area and Porosity," Academic Press(1982).

CHAPTER 7

Glucose-assisted tin oxide-graphene composites via green and facile solvothermal approach for supercapacitor application

7.1. Introduction

Nanostructured tin oxide (SnO_2), as a n-type transparent semiconductor, has a wide range of applications in optoelectronic devices, dye-based solar cells, catalysts , gas sensors, transistors and liquid crystal displays owing to its optical transparency, low cost, high mobility of conduction electrons, superior chemical and thermal stability [1-4]. Despite its widespread use as high-performance electrode materials, SnO_2-based electrode materials are still greatly hampered by the poor capacitance retention upon cycling, mainly attributed to a large volume change which leads to mechanical disintegration and loss of electrical contact between the active material and current collectors [5-6]. To effectively overcome these shortcomings, exploring novel electrode materials is of key importance. Electrochemical evaluations have demonstrated that composite electrodes exhibit significantly enhanced cycle performance via compounding of conducting polymer–SnO_2 [7-9], metal oxide–SnO_2 [10-12] and carbon–SnO_2 [7,13]. Among these, carbon and metal oxide are the two prominent choices of electrode materials in energy storage applications, in which energy is stored via the synergistic effects between electrical double layer and fast faradaic redox reaction.

As a limelight in carbon family, graphene, a two-dimensional nanosheet of graphite arranged in a honeycomb crystal structure, has attracted a great deal of attention in recent years. Owing to its excellent electrical conductivity, large theoretical surface area, good structural flexibility and superior chemical tolerance, graphene has simulated a surge of considerable interest in developing graphene-metal oxide nanocomposites as alternative electrode materials [14-19]. The enhanced electrode performance of such composites can be best observed by comparing the capacitance obtained by pure SnO_2 and pure graphene versus that by SnO_2-graphene composites. Li et al. mixed reduced graphene oxide with $SnCl_2$ in the presence of HCl and urea to gain SnO_2-

graphene nanocomposite which demonstrated a specific capacitance of 34.6 F/g in 1 M H_2SO_4 solution [13]. Lu et al. synthesized SnO_2-graphene composite materials using screen-printing process together with ultrasonic spray pyrolysis (USP) deposition. The capacitance of the electrode obtained is 42.7 F/g in 1 M KCl, which is higher than that of pure graphene (38.9 F/g).

Currently, one obvious challenge is to develop facile and green synthesis routes to synthesis SnO_2-graphene composites that allow scalable production and wide applications. Though various reports are available on the fabrication and performance studies of SnO_2-graphene nanocomposites in energy storage applications, most of the preparation methods were generally complicated, involving a multi-step approach utilizing concentrated acidic/alkaline reagents (HCl, H_2SO_4, H_3PO_4, NaOH) and/or highly toxic and dangerously reactive precursors (N_2H_4, $KMnO_4$, H_2O_2). In this study, we employed a green and facile solvent exfoliation approach to produce graphene in ethanol-water mixture, as reported in our previous study [20]. In the preparation of SnO_2–graphene nanocomposite, solvothermal method was adopted in the presence of ethanol-glucose solution, without the usage of other hazardous reactants. Zhou and co-workers (2014) have successfully developed the glucose-assisted synthesis method via hydrothermal to produce graphene-NiO composites for high-performance supercapacitor [21]. In fact, glucose-assisted solvothermal treatment is considered as a cost-effective, eco-friendly and scalable nanocomposite production as the starting materials (graphite, $SnCl_2$, ethanol, glucose) are non-hazardous, coupling with the low-temperature solvothermal process (140^oC) that does not required high pressure or extreme synthetic condition. Additionally, neutral aqueous electrolyte has been adopted in this study which is much safer in comparison to aggressive acidic or alkaline solutions as well as explosive organic electrolytes.

It is well-known that glucose is a reducing agent due to its ability in forming an aldehyde group (R-CHO) in an open-chain form. This aldehyde group can be oxidised in a reduction-oxidation reaction [22]. In the present study, white precipitation was detected in the Sn-ethanol/water mixed solution with the presence of glucose after solvothermal treatment. It is believed that the formation of hydrated SnO_2 particles could be attributed to the hydrogen bonds and electrostatics effect of glucose, which lead to the rapid aggregation of SnO_2 particles [23]. Similar mechanism has been reported in the synthesis of Fe_3O_4, ZnO and $LiMn_2O_4$ with the assistance of glucose [22, 24-25]. Besides glucose, ethanol and ethylene glycol have been widely utilised as reducing agent in fabrication of nanomaterials, especially silver, gold and platinum

nanoparticles [26-31]. Awasarkar et al. (1988) reported the oxidation mechanism of ethanol to acetic acid, suggesting that ethanol (CH_3CH_2OH) could be oxidised to acetaldehyde (CH_3CHO) and to acetic acid (CH_3COOH) as shown in Eq. (7.1) and (7.2) [33]:

$$CH_3CH_2OH + [O] \rightarrow CH_3CHO + 7H_2O \qquad \text{Eq. (7.1)}$$

$$CH_3CHO + [O] \rightarrow CH_3COOH \qquad \text{Eq. (7.2)}$$

A schematic representation of the formation process of the SnO_2-graphene composite is shown in Figure 7.1. The formation processes of the composite materials are proposed as follows:

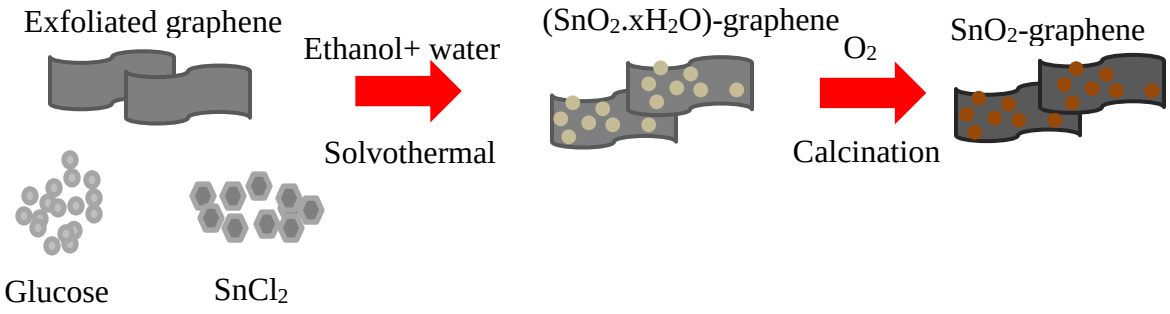


Figure 7.1. A schematic illustration for the synthesis of the SnO_2-graphene composite materials.

7.2 Results and Discussion

7.2.1 X-Ray Diffraction (XRD)

Figure 7.2 shows the X-ray diffraction (XRD) patterns of as-prepared composite samples at different reaction times. The experimental results reveal the XRD peak patterns of pure SnO_2, which are in good agreement with the standard peaks of the tetragonal SnO_2 phase (ICSD 98-006-5289). The three intense diffraction peaks at $2\theta = 26.9^o$, 34.1^o and 52.3^o correspond to the (110), (011) and (121) crystallographic planes of the standard tetragonal SnO_2 respectively [16, 19, 32]. The diffraction peaks of SnO_2 are considered broadened, indicating the formation of small particle size of SnO_2 [14]. From Figure 7.2 (b-d), it can be seen that the characteristic diffraction peaks of SnO_2 are present in all composite samples, suggesting that SnO_2 particles were formed on the graphene sheets in GS6, GS12 and GS24 samples. Additionally, the results

indicate that longer reaction time (24 hours) is favourable for the formation of highly crystalline SnO_2 nanoparticles on graphene sheets. The two diffraction peaks of graphite at 2θ values of 26.8° and 54.9° are attributed to the (002) and (1-20) reflection of graphite (ICSD No: 98-005-2916) and these diffraction maximums are clearly observed for all the composite materials, indicating that the crystalline structure of the graphene is retained, without any lattice disruption after the exfoliation and solvothermal processes.

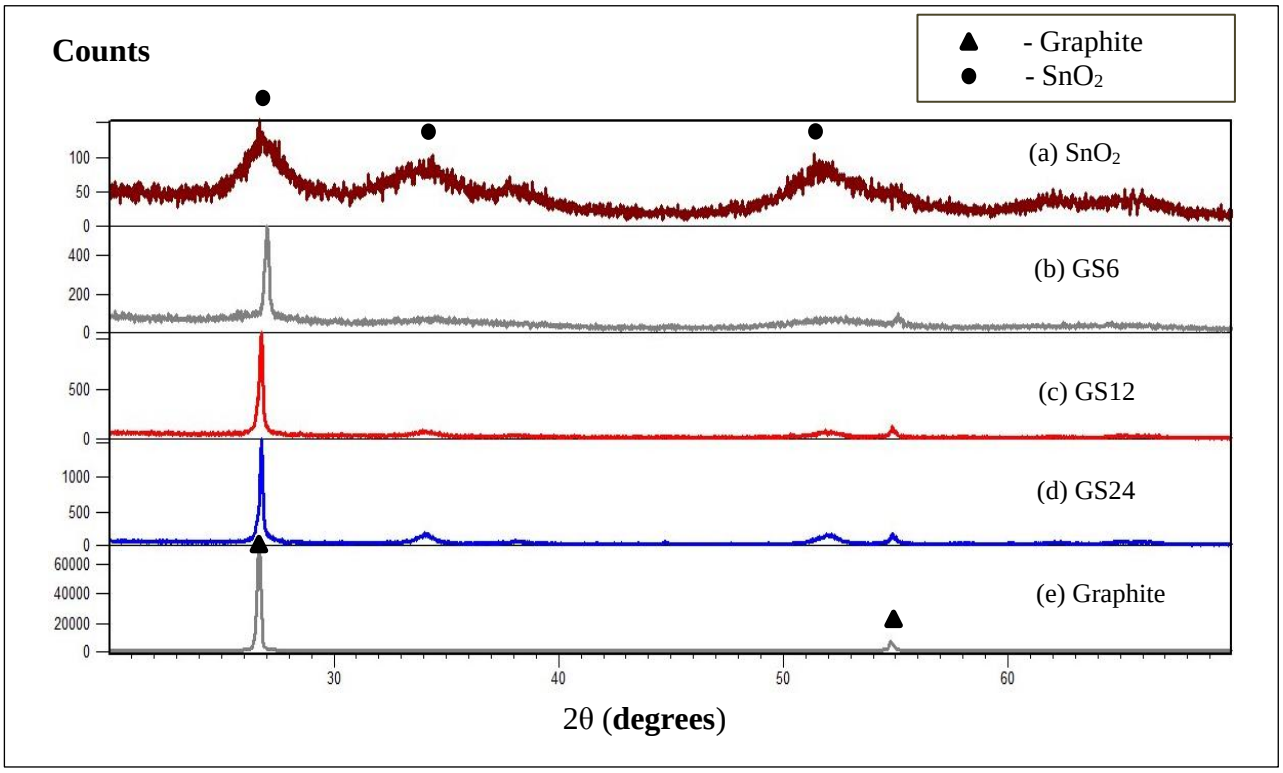


Figure 7.2. XRD patterns of graphite and SnO_2-graphene composites.

7.2.2 Raman Spectroscopy

Raman spectroscopy is an established nanometrology analysis method for further determining the quality of graphene. The peaks at about 1351 cm^{-1} (D band) and 1581 cm^{-1} (G band) are observed in both graphene and SnO_2-graphene composites (as shown in Figure 7.3). The characteristic D-band is associated to the defects or disorders in the hexagonal graphitic layers while G-band is assigned to an E_{2g} mode of graphite, corresponding to the vibration of the sp^2 carbon atoms in 2-dimensional hexagonal lattice [9, 15, 19]. Another major peak at around 2719

cm^{-1} ascribed to 2D-band can be also seen on both samples. Both the D and 2D peaks are of interest as these peaks relate to defects, number of layers and provide a measure of the quality of the produced graphene. Chia et al. (2014) proved that a large increase in the D peak intensity is apparent in the exfoliated graphene in comparison to graphite as a result of the formation of new edges from the exfoliated sheets [20]. Additionally, more effective exfoliation leads to a more prominent edge effect as thinner graphene layers are produced. Chen and co-workers also reported that 2D band at ~2645 is indicative of one layer of graphene while a shift to a higher wavenumber reveals the increased number of graphene layers [36]. Higher wavenumber (~2719) obtained from this study suggests that the composite materials could be few layers of graphene which can be observed from HRTEM image as well (as shown in Figure 7.4 (f)).

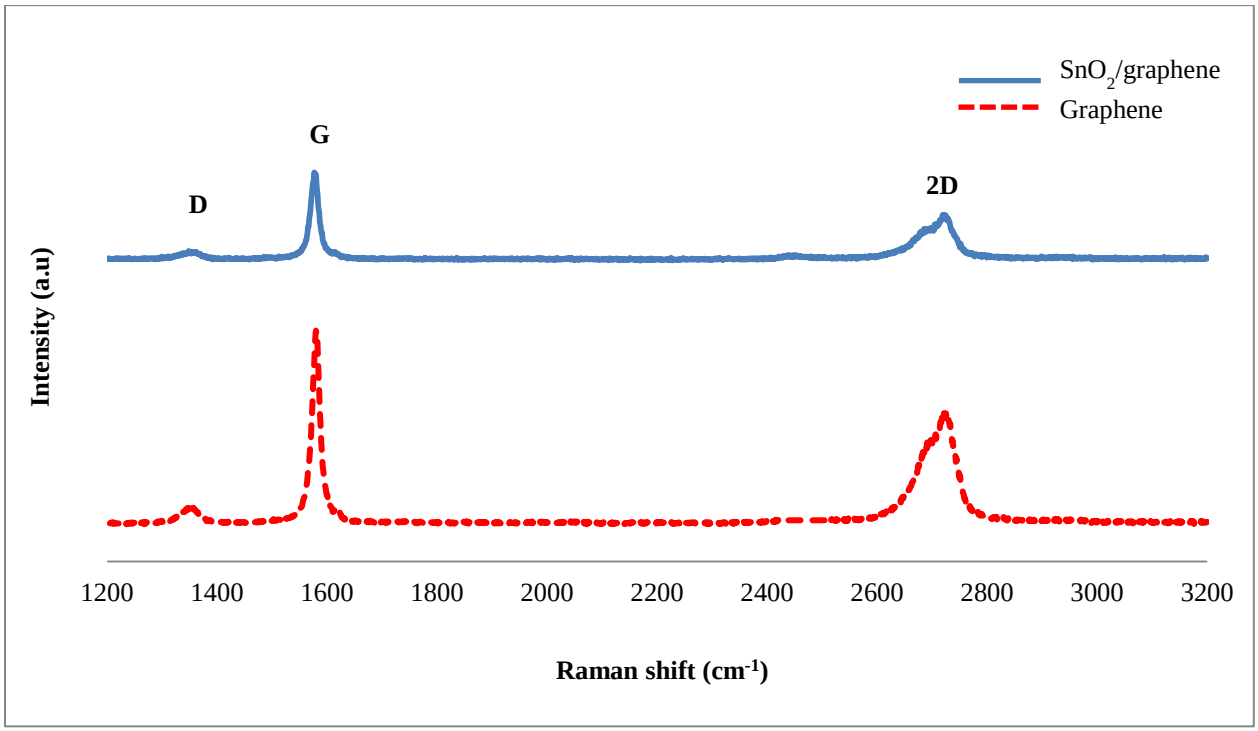
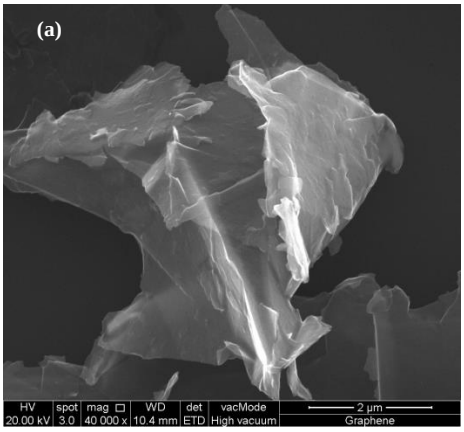


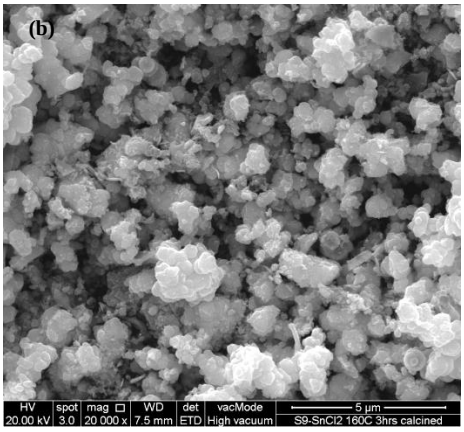
Figure 7.3. Raman spectra of graphene and SnO_2-graphene composites.

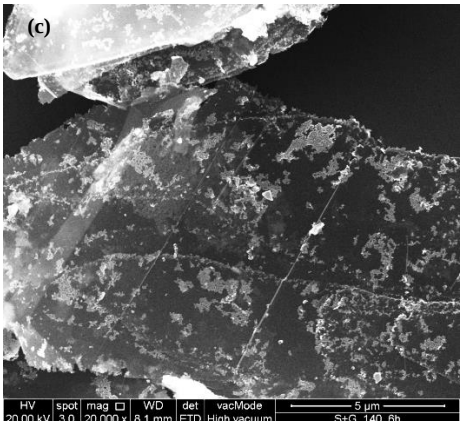
7.2.3 Scanning Electron Microscopy (SEM)

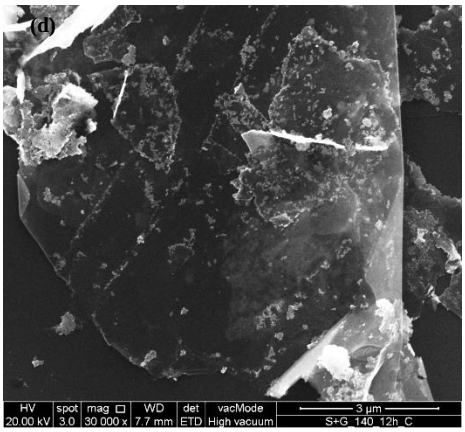
The morphology of the as-prepared products was characterized by field emission scanning electron microscopy (FESEM). Figure 7.4 (a) shows the typical morphology of graphene sheets which is curled and entangled together with a layered structure. The stacking interaction between

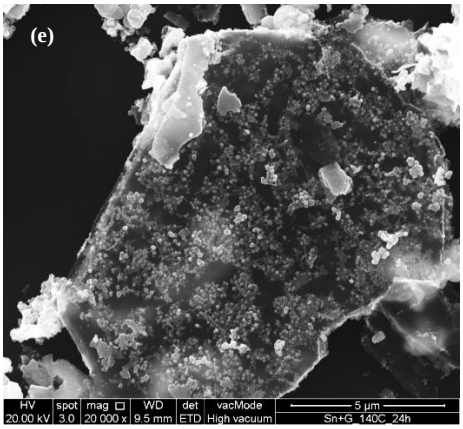
the graphene sheets explains the aggregation of the nanosheets. It can be seen from Figure 7.4 (b), spherical SnO_2 nanoparticles were synthesized successfully using green and simple glucose-assisted solvothermal method. Widiatmoko and coworkers claimed that with the increase of glucose concentration, the particle morphology is dominated by a spherical shape [24]. From Figure 7.4 (c-e), it can be observed that the SnO_2 nanoparticles formed on the layered structures of graphene are found to retain the spherical structures which were homogeneously anchored within the graphene sheets in GS6, GS12 and GS24, respectively. To further investigate the morphology and microstructure information of the samples, TEM studies were conducted and the images are presented in Figure 7.4 (f-g). The corrugated and crumpled thin sheet of graphene with folds at the edges can be observed clearly (Figure 7.4 (f)) whereas small and densely loaded SnO_2 spherical particles are found anchored homogeneously on graphene sheets (Figure 7.4 (g)). The high resolution transmission electron microscopy image (as shown in Figure 7.4 (h)) demonstrates regular lattice fringes with a spacing of around 0.38 nm, which is highly consistent with the d value of the (110) plane of SnO_2 obtained from ICSD 98-006-5289. The chemical composition of the composites were analysed by an energy dispersive spectroscopy (EDX). The peaks of C, O, Sn in the EDX spectrum corresponds to carbon, oxygen and tin compounds respectively, confirming the formation of tin oxide-graphene composites (Figure 7.4 (i)). The peak of Si in the EDX spectrum originated from the silicon substrate used for the characterization.

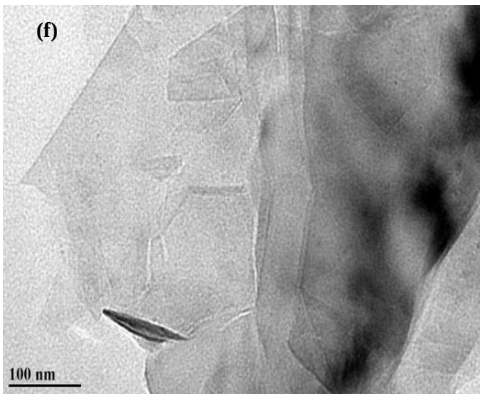

(a)
HV spot mag WD det vacMode 2 µm
20.00 kV 3.0 40 000 x 10.4 mm ETD High vacuum Graphene


(b)
HV spot mag WD det vacMode 5 µm
20.00 kV 3.0 20 000 x 7.5 mm ETD High vacuum S9-SnCl2 160C 3hrs calcined


(c)
HV spot mag WD det vacMode 5 µm
20.00 kV 3.0 20 000 x 8.1 mm ETD High vacuum S+G_140_6h


(d)
HV spot mag WD det vacMode 3 µm
20.00 kV 3.0 30 000 x 7.7 mm ETD High vacuum S+G_140_12h_C


(e)
HV spot mag WD det vacMode 5 µm
20.00 kV 3.0 20 000 x 9.5 mm ETD High vacuum Sn+G_140C_24h


(f)
100 nm

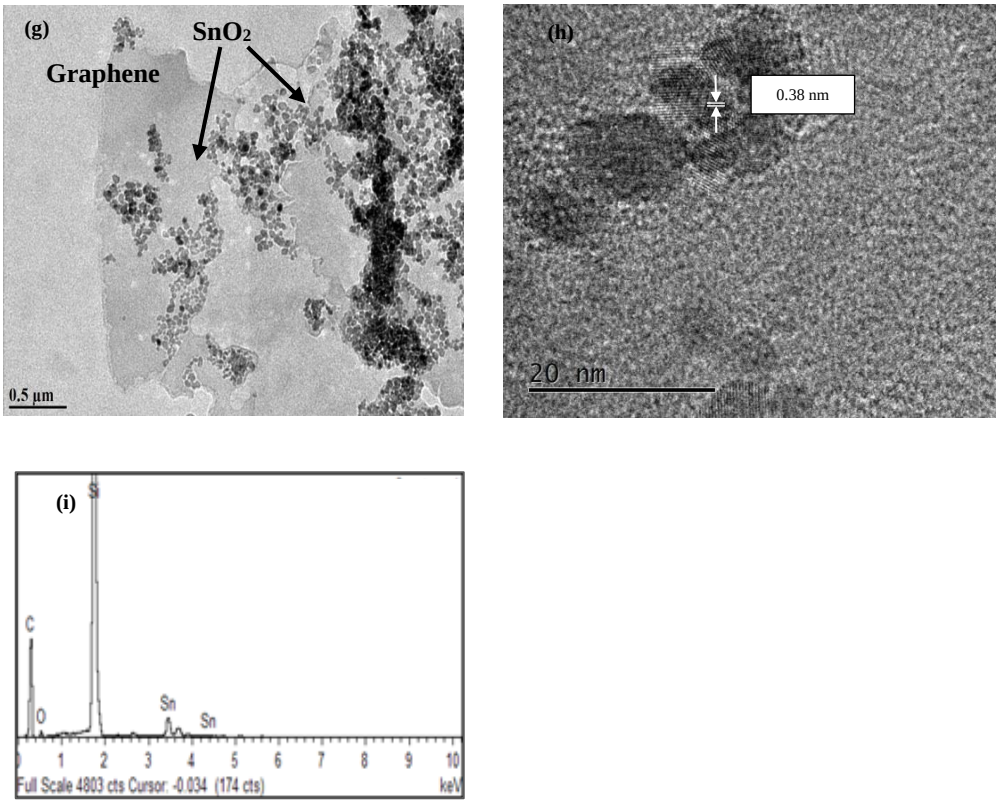


Figure 7.4. FESEM micrographs of (a) graphene, (b) SnO_2, (c)GS6, (d) GS12, (e) GS24, TEM images of (f) graphene , (g) GS24, ,(h) HRTEM of GS24 and (i) EDX spetrum of GS24.

7.2.4 Cyclic Voltammetry (CV)

To understand the macroscopic electrochemical surface reaction at the composite electrodes during charging and discharging process, a cyclic voltammetric measurement was performed. Figure 7.5 shows the CV curves for various electrode materials measured at 5 mV/s using neutral 1 M Na_2SO_3 as electrolyte. The CV of pure SnO_2 electrodes exhibited non-rectangular shape with redox peaks at medium potential range, suggesting a contribution of pseudocapacitance due to the faradaic reactions. Tin oxides have been widely studied as potential anode materials for lithium ion batteries and the plausible electrochemical reaction mechanism of lithium storage in tin oxides was suggested. The cathodic peak at about 0.2 V and anodic peak at about 0.6 V in Na_2SO_3 electrolyte corresponding to the reversible reaction can be described as follows [15]:

$$SnO_2 + 4Na^+ + 4e^- \rightleftharpoons Sn + 2Na_2O \qquad \text{Eq. (7.3)}$$

$$Sn + \chi Na^{+} + \chi e^{-} \rightleftharpoons Na_2Sn\ (0 \leq \chi \leq 4.4) \qquad \text{Eq. (7.4)}$$

By contrast, the shapes of the CV loop for GS12 and GS24 composite electrodes are fairly rectangular shape with small redox peaks at lower and higher potential range, confirming the contribution of both electrical double layer capacitance and pseudocapacitance. The specific capacitance (C_{sp}) was calculated from the CV curve according to Eq. (3.9). On the basis of the CV curves, we can see that all the composite electrodes: GS6 (56 F/g), GS12 (64 F/g) and GS24 (99 F/g) exhibit higher capacitance at a constant scan rate than that of pure SnO_2 (38 F/g), indicating the synergistic effect of SnO_2 and graphene. The enhanced electrochemical performance of composite electrodes could be attributed to the synergistic charge storage effect of electroactive SnO_2 nanoparticles anchored between highly conductive graphene sheets. Previous studies which employed the same electrolyte (Na_2SO_3), also suggested that the metal oxides can provide favourable surface adsorption sites for successive redox reactions of sulphite (SO_3^{2-}) anions [35].

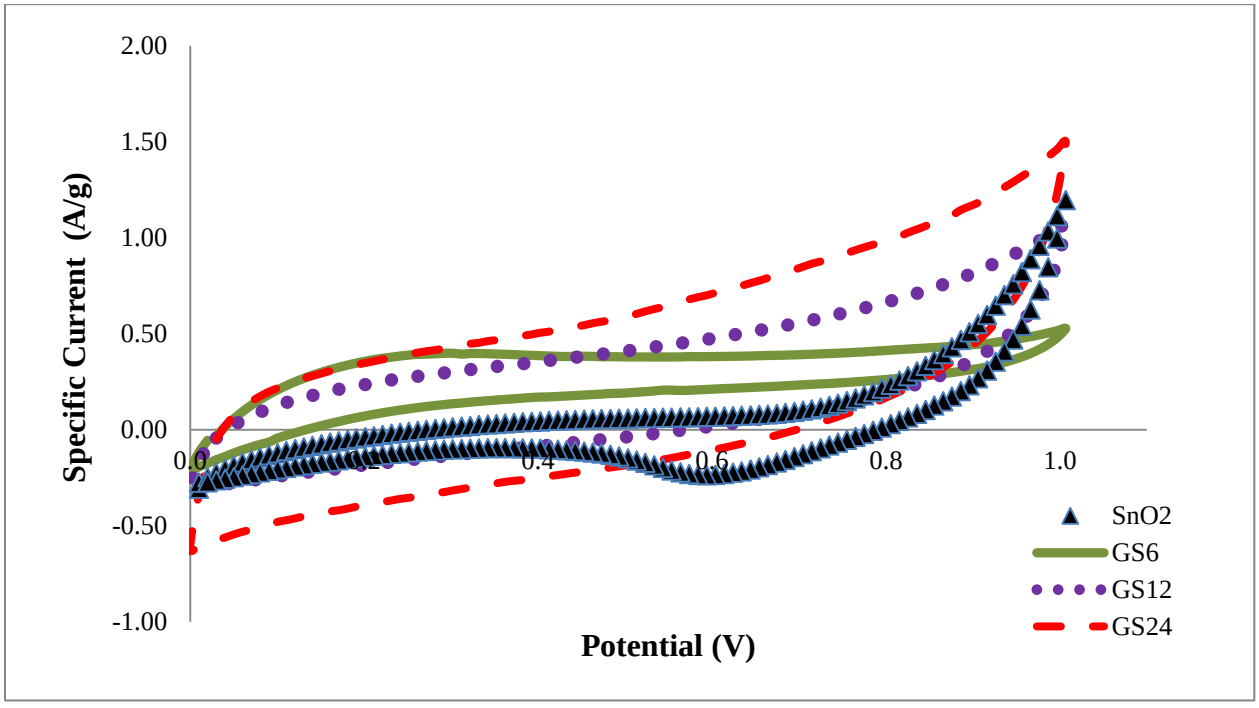


Figure 7.5. CV curves of SnO_2, GS6, GS12 and GS24 electrodes at a scan rate of 5 mV/s.

7.2.5 Galvanostatic Charge-Discharge (GCD)

Figure 7.6 presents the galvanostatic CD profiles of SnO_2, GS6, GS12 and GS24 electrodes at a current density of 2 A/g. Although the curves are not ideally linear, the charge-discharge process retains good symmetry, revealing a good capacitive behaviour [9]. It is observed that the curves deviate from the standard triangle, indicating a combination effect of double-layer capacitance and pseudocapacitance [37]. Comparatively, the voltage drop observed in all the three composite electrodes are smaller than that of pure SnO_2, suggesting that the as-prepared composite electrodes exhibit lower internal resistance. The enhancement of electrochemical performance is mainly due to the improved electronic conductivity with the incorporation of graphene [42]. The specific energy (Wh/kg) and specific power (W/kg) are further determined using Eq (3.17) and Eq (3.18), respectively. GS24 composite electrode deliver the specific energy of 13.8 Wh/kg which is higher that of pure SnO_2 electrodes (5.9 Wh/kg) (Figure 7.7) whereas at low specific energy, the specific power of GS24 and SnO_2 are 1717 and 989 W/kg, respectively. Furthermore, the cycle stability of GS24 composite electrodes was investigated in 1 M neutral Na_2SO_3. Figure 7.8 shows that the specific capacitance retains about 93 % of its original value after 1500 cycles of charging and discharging at a current density of 2 A/g. This clearly shows that the graphene-SnO_2 nanocomposite electrodes are highly stable under cyclic analysis, which is crucial for any potential electrochemical capacitor application. In the present work, the combination of graphene with SnO_2 would contribute to a synergistic effect, leading to the enhanced electrochemical performance. The attachment of SnO_2 nanoparticles on the surface of graphene nanosheets improves the mechanical strength of the composite materials, which is highly favourable for long charge-discharge cycle ability.

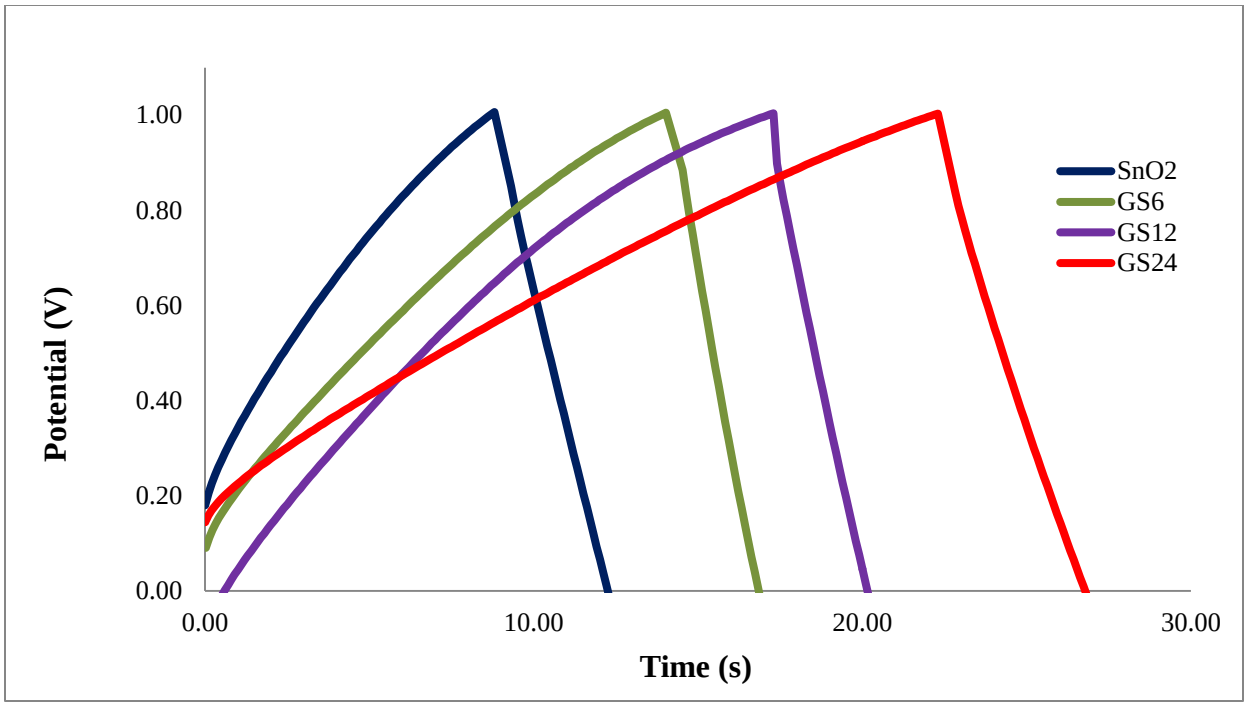


Figure 7.6. Galvanostatic charging/discharging curves of various electrode materials at a current density of 2 A/g in 1 M Na_2SO_3 electrolyte.

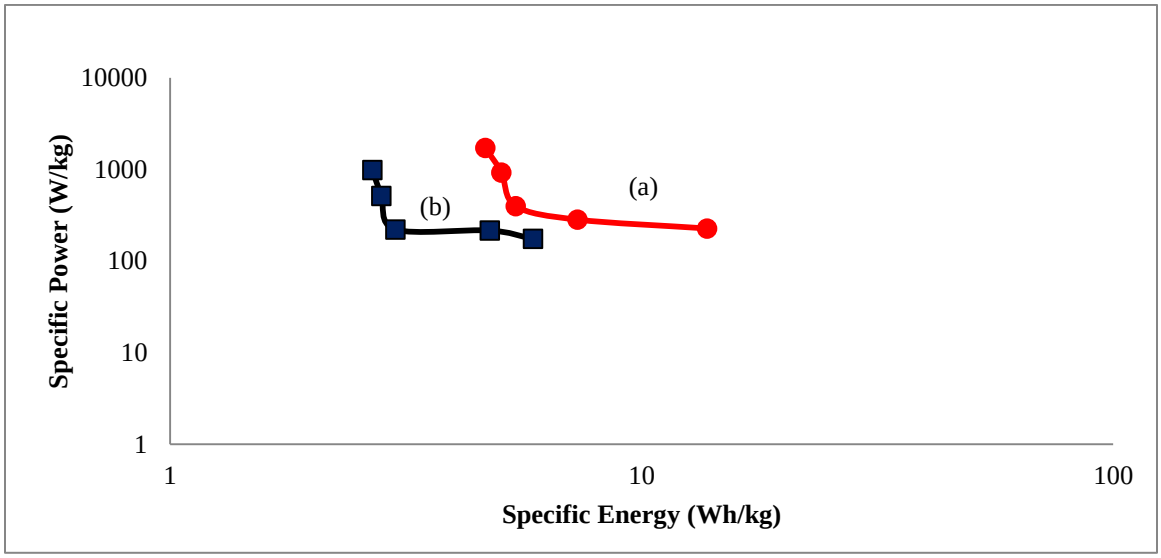


Figure 7.7. Ragone plot of (a) SnO_2-graphene (GS24) and (b) SnO_2 at various scan rates (100, 50, 20, 10, 5 mV/s).

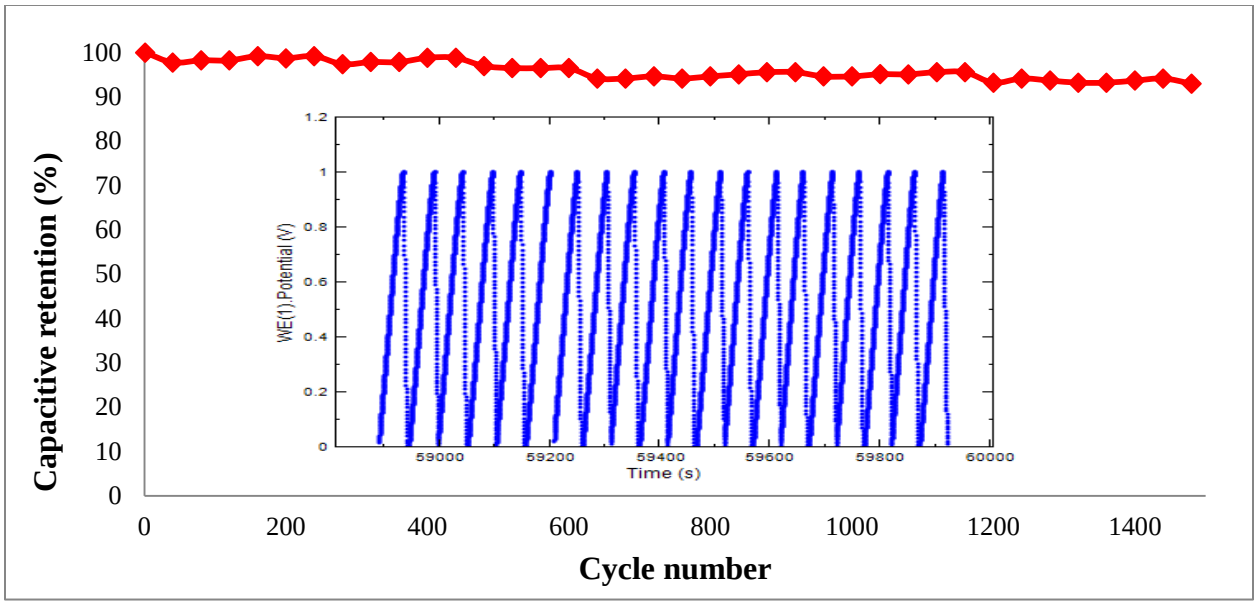


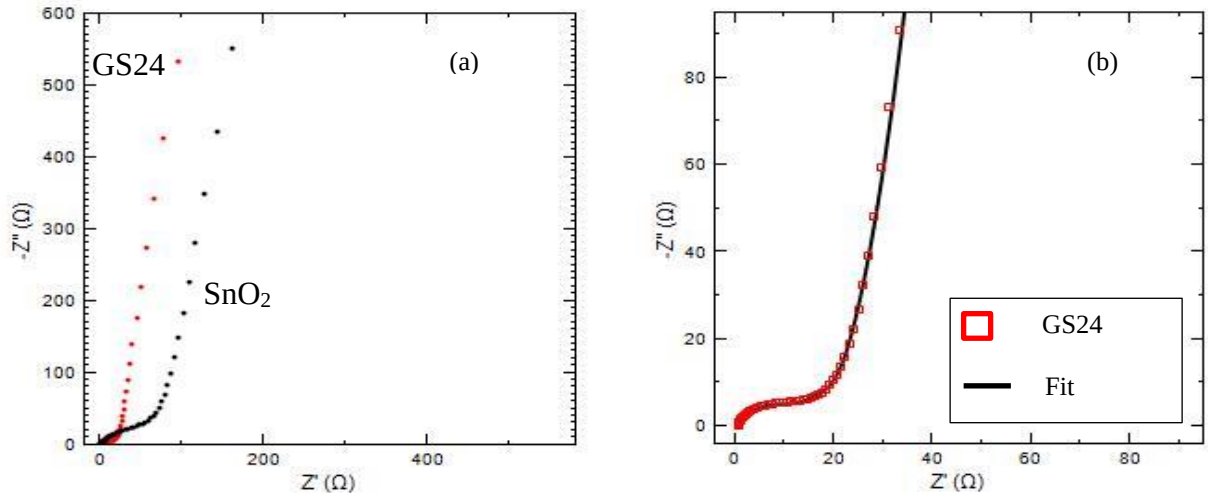
Figure 7.8. Cycle performance of SnO_2-graphene (GS24) composite electrodes.

7.2.6 Electrochemical Impedance Spectroscopy (EIS)

The enhanced electrochemical performance of the SnO_2-graphene composite electrode was further confirmed by the EIS measurements, which was conducted at a frequency range between 100 kHz and 10 mHz. Figure 7.9 (a) demonstrates the Nyquist diagrams of SnO_2-graphene composite electrodes and SnO_2 electrodes. The plot shows a semicircle in the high frequency region and a slanted line at low frequency region. Generally, a semicircle in the high frequency is related to the electronic resistance within the electrode materials while a vertical line parallel to the imaginary axis at low frequency region represents an ideal capacitive behaviour [39]. The slope of the 45^o portion of the curve is called the Warburg impedance (W) which is a result of the frequency dependence of ion diffusion at the electrolyte-electrode interface while the vertical shape at lower frequencies reveals a pure capacitive characteristic, representative of ion diffusion in the structure of the electrode materials [43]. The more vertical the curve to the imaginary axis (-Z"), the more closely the supercapacitor behaves as an ideal capacitor [44]. The EIS results show that SnO_2-graphene composite electrodes demonstrate smallest semicircle, indicating the composite electrodes possesses the lowest charge transfer resistance as compared to the two pure electrodes. Moreover, the near-vertical slope of the composite electrodes at the low-frequency

region suggests a good capacitor behaviour of SnO_2-graphene composite electrodes. A reduced charge transfer resistance and better capacitive behaviour observed for SnO_2-graphene composite electrodes can be rationally explained by the synergistic effects from pseudocapacitive SnO_2 and conductive graphene.

The obtained impedance spectra were fitted and analysed by the software Nova on the basis of the electrical equivalent circuit, which provides a considerable insight of the different capacitive contribution and charge transfer process of SnO_2-graphene composite electrodes. Figure 7.9 (b) shows the fitting of the impedance for GS24 composite electrodes whereas the Randles equivalent circuit representing the circuit elements that are used to fit the experimental Nyquist spectra of GS24 and SnO_2 are illustrated in Figure 7.8(c) and (d) respectively. Q or the constant-phase element (CPE) is typically used in place of the capacitive element (C) to indicate the non-ideal behaviour of electrodes, including the surface roughness, a leaky capacitor and a non-uniform current distribution, electrodes often does not behave ideally. Another tangent hyperbolic diffusion circuit element (T) needs to be incorporated into the Randles equivalent circuit when the diffusion condition is under restricted limitation between the electrode and non-reactive surface (current collector) [40]. It can be observed that the composite electrodes exhibit lower R_{ct} (11.1 Ω) in comparison to that of pure SnO_2 (40.8 Ω). A reduced value of Rct implies that the incorporation of graphene into SnO_2 improved the conductivity of the composite electrodes.



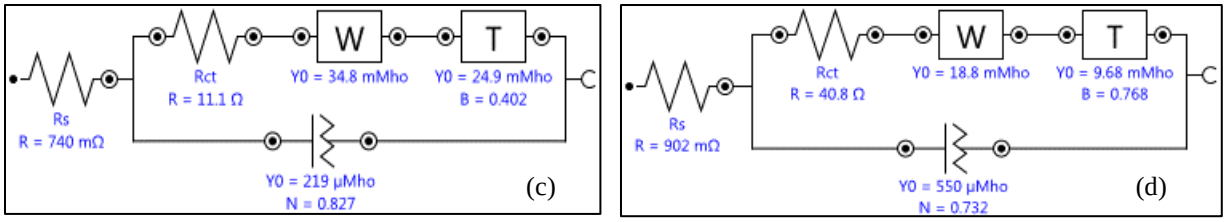


Figure 7.9. (a) Nyquist polts for SnO_2-graphene (GS24) composite electrodes and SnO_2 electrodes; (b) Fitting of the impedance for GS24 composite electrodes; Randles equivalent circuit representing the circuit elements that are used to fit the experimental Nyquist spectra of (c) GS24 and (d) SnO_2.

7.3 Summary

A simple, facile and environment-friendly method to synthesize SnO_2-graphene nanocomposites was established, using graphite, $SnCl_2$ and glucose as precursors. This green synthesis method provides an alternative route to produce nanostructured SnO_2-graphene composite electrodes in a simple, low cost and effective manner, without the needs of extreme synthesis condition. The reversible redox reactions of SnO_2, in combination of high conductivity of graphene, lead to improved electrochemical performance. A maximum specific capacitance of 99 F/g in neutral Na_2SO_3 electrolyte is obtained from the optimized SnO_2-graphene composite electrodes. Though the value is relatively lower compared to those in aggressive acidic or alkaline solutions, the low-cost resources and environmental benign electrolyte system become the key drivers to further extend to other metal oxide-graphene composites as green electrode materials used in neutral aqueous electrochemical storage applications.

References

[1] H.N. Lim, R. Nurzulaikha, I. Harrison, S.S. Lim, W.T. Tan, M.C. Yeo, "Spherical Tin Oxide, SnO_2 Particles Fabricated via Facile Hydrothermal Method for Detection of Mercury (II) Ions," Int. J. Electrochem. Sci. 6 (2011) 4329 – 4340.

[2] H. Taib and C.C. Sorrell, "Preparation of Tin Oxide, J. Aust. Ceram. Soc., 43 (2007) 56-61.

[3] X.W.Lou, Y.Wang, C.L.Yuan, J.Y.Lee, and L.A. Archer, Template-Free Synthesis of SnO_2 Hollow Nanostructures with High Lithium Storage Capacity," Adv. Mater. 18 (2006) 2325–2329.

[4] W.J.Wang, Q.L.Hao, W.Lei, X.F.Xia and X.Wang, "Graphene/SnO_2/polypyrrole ternary nanocomposites as supercapacitor electrode materials," RSC Advances 2 (2012)10268–10274.

[5] X.W.Lou, J.S.Chen, P.Chen and L.A. Archer, "One-Pot Synthesis of Carbon-Coated SnO_2 Nanocolloids with Improved Reversible Lithium Storage Properties," Chem. Mater. 21 (2009) 2868–2874.

[6] Z.S.Wu, G.M.Zhou, L.C.Yin, W.C.Ren, F.Li, H.M.Cheng, "Graphene/metal oxide composite electrode materials for energy storage," Nano Energy, 1 (2012) 107–131.

[7] A. Mirmohseni, M.S. Seyed Dorraji, M.G. Hosseini, "Influence of metal oxide nanoparticles on pseudocapacitive behavior of wet-spun polyaniline-multiwall carbon nanotube fibers," Electrochimica Acta, 70 (2012) 182– 192.

[8] Z.A.Hu, Y.L.Xie, Y.X.Wang, L.P.Mo, Y.Y.Yang, Z.Y.Zhang, "Polyaniline/SnO_2 nanocomposite for supercapacitor applications," Materials Chemistry and Physics, 114 (2009) 990–995.

[9] S.Patil, V.Patil, S.Sathaye and K.Patil, "Facile room temperature methods for growing ultra-thin films of graphene nanosheets, nanoparticulate tin oxide and preliminary assessment of graphene– tin oxide stacked layered composite structure for supercapacitor application," RSC Adv., 4 (2014) 4094.

[10] M. Jayalakshmi, N. Venugopal, K. Phani Raja, M. Mohan Rao, "Nano SnO_2–Al_2O_3 mixed oxide and SnO_2–Al_2O_3–carbon composite oxides as new and novel electrodes for supercapacitor applications," Journal of Power Sources, 158 (2006) 1538–1543.

[11] M. Jayalakshmi, M. Mohan Rao, N. Venugopal, Kwang-Bum Kim, "Hydrothermal synthesis of SnO_2–V_2O_5 mixed oxide and electrochemical screening of carbon nano-tubes (CNT), V_2O_5, V_2O_5–CNT, and SnO_2–V_2O_5–CNT electrodes for supercapacitor applications," Journal of Power Sources, 166 (2007) 578–583.

[12] S.L.Kuo and N.L.Wu, "Composite Supercapacitor Containing Tin Oxide and Electroplated Ruthenium Oxide," Electrochemical and Solid-State Letters, 6 (2003) A85-A87.

[13] F.H.Li, J.F.Song, H.F.Yang, S.Y.Gan, Q.X.Zhang, D.X.Han, A.Ivaska and L.Niu, "One-step synthesis of graphene/SnO_2 nanocomposites and its application in electrochemical supercapacitors," Nanotechnology, 20 (2009) 455602.

[14] Y.M.Li, X.J.Lv, J.Lu, and J.H.Li, "Preparation of SnO_2-Nanocrystal/Graphene-Nanosheets Composites and Their Lithium Storage Ability," J. Phys. Chem. C, 114 (2010) 21770–21774.

[15] M.Zhang, D.N.Lei, Z.F.Du, X.M.Yin, L.B.Chen, Q.H.Li, Y.G.Wang and T.H.Wang, "Fast synthesis of SnO_2/graphene composites by reducing graphene oxide with stannous ions," J. Mater. Chem., 21 (2011)1673–1676.

[16] Q.Guo, Z.Zheng, H.L.Gao, J.Ma, X.Qin, "SnO_2/graphene composite as highly reversible anode materials for lithium ion batteries," Journal of Power Sources, 240 (2013) 149-154.

[17] T.Lu, Y.P.Zhang, H.B.Li, L.K.Pan, Y.L.Li, Z.Sun, "Electrochemical behaviors of graphene–ZnO and graphene–SnO_2 composite films for supercapacitors," Electrochimica Acta, 55 (2010) 4170–4173.

[18] B.Wang, D.H.Guan, Z.Gao, J.Wang, Z.S.Li, W.L.Yang, L.H.Liu, "Preparation of graphene nanosheets/SnO_2 composites by pre-reduction followed by in-situ reduction and their electrochemical performances," Materials Chemistry and Physics, 141 (2013) 1-8.

[19] S.P.Lim, N.M.Huang, H.N.Lim, "Solvothermal synthesis of SnO_2/graphene nanocomposites for supercapacitor application," Ceramics International, 39 (2013) 6647–6655.

[20] J.S.Y.Chia, M.T.T. Tan, P.S.Khiew, J.K.Chin, H.W.Lee , D.C.S Bien, C.W.Siong, "A novel one step synthesis of graphene via sonochemical-assisted solvent exfoliation approach for electrochemical sensing application," Chemical Engineering Journal 249 (2014) 270–278.

[21] M.L.Zhou, H. Chai, D.Z.Jia and W.Y.Zhou, "The glucose-assisted synthesis of a graphene nanosheet–NiO composite for high-performance supercapacitors," New J.Chem. 38 (2014) 2320-2326.

[22] P.Widiatmoko, D.N.Khaemba and I.W.Lenggoro, "Preparation of $LiMn_2O_4$ particles by glucose-assisted combustion method," Journal of the Ceramic Society of Japan, 122 (2014) 976-981.

[23] R.C.Jin, G.Chen, C.S.Yan, D.H.Chen, H.M.Xu and J.Pei, "Glucose assisted synthesis and growth mechanism of hierarchical antimony Chalcogenides," Cryst Eng Comm 14 (2012) 8547–8553.

[24] T.Zhu, J.S.Chen, and X.W.Lou, "Glucose-Assisted One-Pot Synthesis of FeOOH Nanorods and Their Transformation to Fe_3O_4@Carbon Nanorods for Application in Lithium-ion Battery," J. Phys. Chem. C, 115 (2011) 9814–9820.

[25] J. G.Yu and X.X.Yu, "Hydrothermal Synthesis and Photocatalytic Activity of Zinc Oxide Hollow Spheres," Environ. Sci. Technol 42 (2008) 4902–4907.

[26] D.L.Chen, M.Liu, L.Yin, T.Li, Z.Yang, X.J.Li, B.B.Fan, H.L.Wang, R.Zhang, Z.X.Li, H.L.Xu, H.X.Lu, D.Y.Yang, J.Sun and L.Gao, "Single-crystalline MoO_3 nanoplates: topochemical synthesis and enhanced ethanol-sensing performance," J. Mater. Chem.21 (2011) 9332–9342.

[27] L.Obreja, N. Foca, M. I. Popa, V. Melnig, "Alcoholic reduction Platinum Nanoparticles Synthesis by Chemical Method, Biomaterials in Biophysics," Medical Physics and Ecology (2008).

[28] P. Manivel, K. Sivashanmugan, C. Viswanathan, D. Mangalaraj, "Preparation of New Reducing Agent for the Synthesis of Silver Nanoparticles," AIP Conf. Proc.1349 (2011) 415-416.

[29] E.Rodríguez-León, R.Iñiguez-Palomares, R.E.Navarro, R.Herrera-Urbina2, J.Tánori, C.Iñiguez-Palomares5 and A.Maldonado, "Synthesis of silver nanoparticles using reducing

agents obtained from natural sources (Rumex hymenosepalus extracts),” Nanoscale Research Letters 8 (2013) 318.

[30] H.H.Duan, D.S.Wang and Y.D.Li, “Green chemistry for nanoparticle synthesis,” Chem. Soc. Rev.44 (2015) 5778.

[31] C.E. Hoppe, M.Lazzari, I.P.Blanco, and M. A.L.Quintela, “One-Step Synthesis of Gold and Silver Hydrosols Using Poly (*N*-vinyl-2-pyrrolidone) as a Reducing Agent,” Langmuir 22 (2006).

[32] R. B. Rakhi, W.Chen, D.Y.Cha and H. N. Alshareef,“High performance supercapacitors using metal oxide anchored graphene nanosheet electrodes,” J. Mater. Chem.21 (2011) 16197.

[33] P. A. Awasarkar, A. Y. Sonsale, A. K. Chatterjee, “Heterogeneous catalytic oxidation of ethanol: A new process for acetic acid,” Reaction Kinetics and Catalysis Letters, 36 (1988) 301-305.

[34] C. Justin Raj, Byung Chui Kim, Won-Je Cho, Seungil Park, Hyeon Taek Jeong Kicheon Yoo, Kook Hyun Yu, “Rapid hydrothermal synthesis of cobalt oxyhydroxide nanorods for supercapacitor applications,” Journal of Electroanalytical Chemistry 747 (2015) 130–135.

[35] X.Zhao, C. Johnston, A.Crossley, P.S.Grant,“Printable magnetite and pyrrole treated magnetite based electrodes for supercapacitors,” Journal of Materials Chemistry, 20 (2010) 7637-7644.

[36] J. H. Chen, W. G. Cullen, C. Jang, M. S. Fuhrer and E. D. Williams, “Defect Scattering in Graphene,” Phys. Rev. Lett.102 (2009) 236805-236808.

[37] Q.W.Tang, Z.Q.Shan, L.Wang, X.Qin, “MoO_2–graphene nanocomposite as anode material for lithium-ion batteries,” Electrochimica Acta 79 (2012) 148– 153.

[38] Z. Qin, Z.J. Li, M. Zhang, B.C. Yang, R.A. Outlaw, “Sn nanoparticles grown on graphene for enhanced electrochemical properties,” Journal of Power Sources 217 (2012) 303-308.

[39] S. K. Meher and G. R. Rao, “Ultralayered Co_3O_4 for High-Performance Supercapacitor Applications,” J. Phys. Chem. C 115 (2011) 15646–15654.

[40] S. P. Taberna, P.Louis, “Electrochemical Techniques, in : Supercapacitors: Materials, Systems and Applications,” F. Beguin and E.Frackowiak, Ed. Germany: Wiley-VCH (2013) 119–129.

[41] V. Ruiz, C. Blanco, M. Granda, R. Menéndez, R. Santamaría, “Effect of the thermal treatment of carbon-based electrodes on the electrochemical performance of supercapacitors,” Journal of Electroanalytical Chemistry 618 (2008) 17–23.

[42] R. B. Rakhi, W.Chen, D.Y.Cha and H. N. Alshareef,“High performance supercapacitors using metal oxide anchored graphene nanosheet electrodes,” J. Mater. Chem.21 (2011) 16197.

[43] Y.Wang, Z.Q.Shi, T.Huang, Y.F.Ma, C.Y.Wang, M.M.Chen and Y.S.Chen, “Supercapacitor Devices based on Graphene Materials,” J.Phys.Chem.C 113 (2009) 13103-13107.

[44] L.L.Zhang, X.Zhao, M.D.Stoller, Y.W.Zhu, H.X.Ji, S.Murali, Y.P.Wu, S.Perales, B.Clevenger and R.S.Ruoff, “Highly Conductive and Porous Activated Reduced Graphene Oxide Films for High-Power Supercapacitors,” Nano Lett 12 (2012) 1806-1812.

CHAPTER 8

Ethylene glycol assisted molybdenum oxide-graphene composite electrodes via green and facile solvothermal approach for aqueous supercapacitor application

8.1. Introduction

Supercapacitors, also well known as electrochemical capacitors, have become one of the promising electrical energy storage devices in harvesting renewably-generated electrical energy during the optimum production period [1-2]. It is also widely used in electric vehicles, coupling with batteries and fuel cell to deliver high power [3]. In fact, the present commercial supercapacitors are mainly relied on activated carbon-based electrical double layer capacitors (EDLCs) [4-6]. In recent years, a great deal of attention has been shifted from activated carbon and carbon-nanotube to graphene in making nanocomposite electrodes due to its excellent electronic conductivity, broad potential window, extensive surface area and surface-to-volume ratio, ultrathin thickness, high charge carrier mobility, good structural flexibility, superior chemical and thermal stability [7-11].

To date, metal oxide-graphene nanocomposites with different morphologies for specific applications have been reported including ZnO-graphene [12-16], MnO_2-graphene [17-22], Mn_3O_4-graphene [23], Fe_2O_3-graphene [24], $NiCo_2O_4$-graphene [25], Co_3O_4-graphene [26], RuO_2-graphene [22, 27] and $CoMoO_3$-graphene [28]. Most recently, molybdenum oxide-graphene, owing to their unique optical and electronic properties, have been investigated intensively as a promising material candidate for catalysts, solid lubricants, superconductors, field effect transistors, gas sensors, smart window, display devices and Li-ion batteries [29-34]. It is suggested that the metal oxide nanoparticles that were homogeneously anchored or distributed onto graphene sheets not only prevent the aggregation and re-stacking of graphene sheets, but also increase the interlayer spacing, leading to larger surface area available for electrolyte ion accessibility. Moreover, the incorporation of metal oxide nanoparticles can contribute additional pseudocapacitance to the overall capacitive performance of graphene-based electrode materials. [4]. Studies based on graphene- molybdenum oxide composite electrodes for

lithium-ion batteries also reveal similar explanation for their improved electrode performance [29-31].

Despite the importance of molybdenum oxide-graphene nanocomposites and their wide applications, its potential as candidates of electrode materials in supercapacitor is rarely reported. Furthermore, there are a number of preparation methods have been reported successfully in the synthesis of nanostructured molybdenum including combination of thermal evaporation and mechanical exfoliation [38], hydrothermal [39], chemical vapour deposition (CVD) [40] and vacuum thermal deposition [41]. Meanwhile, among the methods employed to synthesize molybdenum oxide-graphene nanocomposites are hydrothermal [29-32], solvothermal [33], chemical reduction [34]. However, the intensive use of concentrated acid/alkaline solutions and strong oxidising/reducing agents during the synthesis processes is harmful to the environment. For this reason, it is highly desirable to devise alternative green methods of nanocomposite preparation, utilizing environmentally benign precursors and less hazardous reducing agents that are important for more sustainable processes in scalable and mass production.

Herein we report a mild and facile solvothermal approach to synthesize molybdenum oxide-graphene nanocomposites. In the first step, the liquid phase exfoliation of graphite was carried out to produce the pristine structure of graphene sheets as reported in our previous works [42-44]. In comparison to the modified Hummers method which requires harsh acid treatments and chemical reduction, this method is a green route to produce graphene as it involves only the mild sonication treatment of graphite flakes in an optimum ratio of ethanol and de-ionized water. In the second step, molybdenum oxide nanoparticles were synthesized and anchored on the as-prepared graphene sheets via low-temperature solvothermal treatment using ammonium molybdate tetrahydrate as starting material and ethylene glycol-distilled water as mixed solvent. Ethylene glycol (EG) and ethanol have been widely utilised as reducing agent in fabrication of nanomaterials, especially silver, gold and platinum nanoparticles [45-49]. Besides noble nanosized metals, VO_2 nanowires and Mn_3O_4 nanorods were also successfully synthesized using ethylene glycol as precursor under mild conditions [50-51]. Recently, Liu and co-workers (2013) reported that the green protic solvent EG that can serve as a sound reducing agent for fabrication of RGO/PPy composite for supercapacitor application [52]. Unlike the commonly employed highly toxic and strongly reductive chemicals such as hydrazine, the moderate EG reductant

could retain the conjugated structure of PPy during the removal of oxygen-containing groups on the graphene oxide (GO), thus facilitating utilization of the electroactive conductive polymer.

Based on previous research, it is speculated that ethylene glycol (CH_2OHCH_2OH) could be oxidised to acetic acid (CH_3COOH). Subsequently, $Mo_7O_{24}^{6-}$ from molybdenum precursor could then react with H^+ from acetic to form hydrated molybdenum trioxide ($MoO_3.H_2O$), which is transformed to MoO_3 after thermal treatment [53-54]. Saha et.al. (2008) successfully synthesized composite electrodes consisting of platinum nanoparticles (Pt), multiwalled carbon nanotubes (MWCNT) and carbon paper using acetic acid as a reducing agent [35]. The results show that acetic acid possesses strong reducing capability and plays a critical role in producing surface functional groups on the CNTs, allowing highly dispersed Pt nanoparticles deposited on MWCNTs. A schematic representation of the MoO_3-graphene composite materials prepared via green and facile EG-assisted solvothermal synthesis is shown in Figure 8.1.

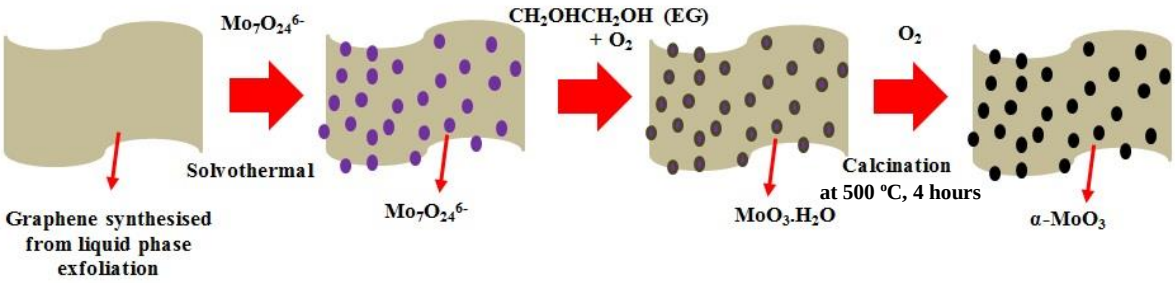


Figure 8.1. Schematic representation of the MoO_3-graphene composite materials prepared via green and facile EG-assisted solvothermal synthesis.

Ammonium molybdate tetrahydrate ($(NH_4)_6Mo_7O_{24}.4H_2O$) is a big complex molecule which is a common precursor used in molybdenum compound synthesis. Parviz et al. studied the size and morphology control of nanostructured MoO_3 via solution combustion method, using $(NH_4)_6Mo_7O_{24}.4H_2O$ as the precursor and with different organic additives including ethylene diamine tetra-acetic acid (EDTA), polyethylene glycol 200 (PEG 200), sorbitol and urea [36]. However, to date, no plausible or comprehensive explanation of mechanisms associated with the reaction of $(NH_4)_6Mo_7O_{24}.4H_2O$ with ethylene glycol to produce α-MoO_3 is available. In 1932, Morris and co-workers reported the potential reactions of ethyl alcohol. It is suggested that ethylene glycol (CH_2OHCH_2OH) could be oxidised to acetaldehyde (CH_3CHO) and to acetic

acid (CH_3COOH) as shown in Eq. (8.1) and (8.2) while acetic acid could decompose to form acetate ions (CH_3COO^-) and hydrogen ions (H^+), as shown in Eq. (8.3) [37, 54].

$$2CH_2OHCH_2OH + O_2 \rightarrow 2CH_3CHO + 2H_2O \quad \text{Eq. (8.1)}$$

$$2CH_3CHO + O_2 \rightarrow CH_3COOH + 2H_2O \quad \text{Eq. (8.2)}$$

$$CH_3COOH \rightarrow CH_3COO^- + H^+ \quad \text{Eq. (8.3)}$$

Zhao and his co-workers have studied the preparation of MoO_3 nanofibers under hydrothermal conditions at 140-200°C [53]. They have explained thoroughly the possible reaction paths from $(NH_4)_6Mo_7O_{24}.4H_2O$ to α-MoO_3 via kinetic investigation, claiming that the hydrated form of ammonium molybdate tetrahydrate in solution consists of hydronium ions (H_3O^+) and heptamolybdate ($Mo_7O_{24}^{-6}$) molecules, as shown in Eq. (8.4). Then $Mo_7O_{24}^{-6}$ could react with H^+ from acetic acid in Eq. (6) to form hydrated molybdenum trioxide ($MoO_3.H_2O$), as indicated in Eq. (8.5) and (8.6) [53].

$$(NH_4)_6Mo_7O_{24}.4H_2O \rightarrow Mo_7O_{24}^{6-} + 6NH_4^+ + 4H_2O \quad \text{Eq. (8.4)}$$

$$Mo_7O_{24}^{6-} + 3H^+ \rightarrow (H\text{-}O)_3Mo_7O_{23}^{3-} \quad \text{Eq. (8.5)}$$

$$(H\text{-}O)_3Mo_7O_{23}^{3-} + 3H^+ \rightarrow (H\text{-}O)_3Mo_7O_{18} \rightarrow 7MoO_3.H_2O \quad \text{Eq. (8.6)}$$

When the hydrated molybdenum trioxide powder was calcined at 300 ^oC and above, it can be converted to α-MoO_3, as shown in Equation (8.7). NH_3 gas could be released at high temperatures from ammonium group in $(NH_4)_6Mo_7O_{24}$ compound, as indicated in Eq. (8.8) [36-37].

$$MoO_3.H_2O + O_2 \rightarrow \alpha\text{-}MoO_3 \quad \text{Eq. (8.7)}$$

$$NH_4^+ \rightarrow H^+ + NH_3 \quad \text{Eq. (8.8)}$$

8.2 Results and Discussion

8.2.1 X-Ray Diffraction (XRD)

X-ray diffraction was performed to identify the diffraction patterns of as-prepared composite samples at different reaction times. As shown in Figure 8.2, all the composite compounds (GM6, GM12 and GM24) show well-defined peaks that match with orthorhombic crystalline structure of α-MoO_3 (a= 13.8250 Å, b= 3.6940 Å and c= 3.9540 Å, ICSD 98-001-7060). It can be observed that the strongest diffraction peaks for MoO_3 in the XRD pattern appear at 2θ = 23.4^o, 25.8^{o,} 27.5^o, 39.2^o, 49.4^o, which correspond to the (101), (400), (210), (111), (600) and (020) crystallographic planes, respectively. The interlayer spacing (d) of MoO_3 particles, which was derived from the (201) plane using Bragg's law, is about 0.33 nm. As compared to GM6 and GM12, a much sharper diffraction pattern is observed for the composite sample GM24. This can be associated with the improved crystallinity in the samples for prolonged reaction time. On contrary, as the reaction time decreases, the diffraction maximum appears to be more broadened and the intensity decreases, as shown in Figure 8.2 (c). This is an indication of a decrease in the crystallite size of MoO_3 [57]. The two diffraction peaks of graphite at 2θ values of 26.8^o and 54.9^o are attributed to the (002) and (1-20) reflection of graphite (ICSD No: 98-005-2916) and these diffraction maximums are clearly observed for all the composite materials, suggesting that the crystalline structure of the graphene is retained, without any lattice disruption after the exfoliation and solvothermal processes.

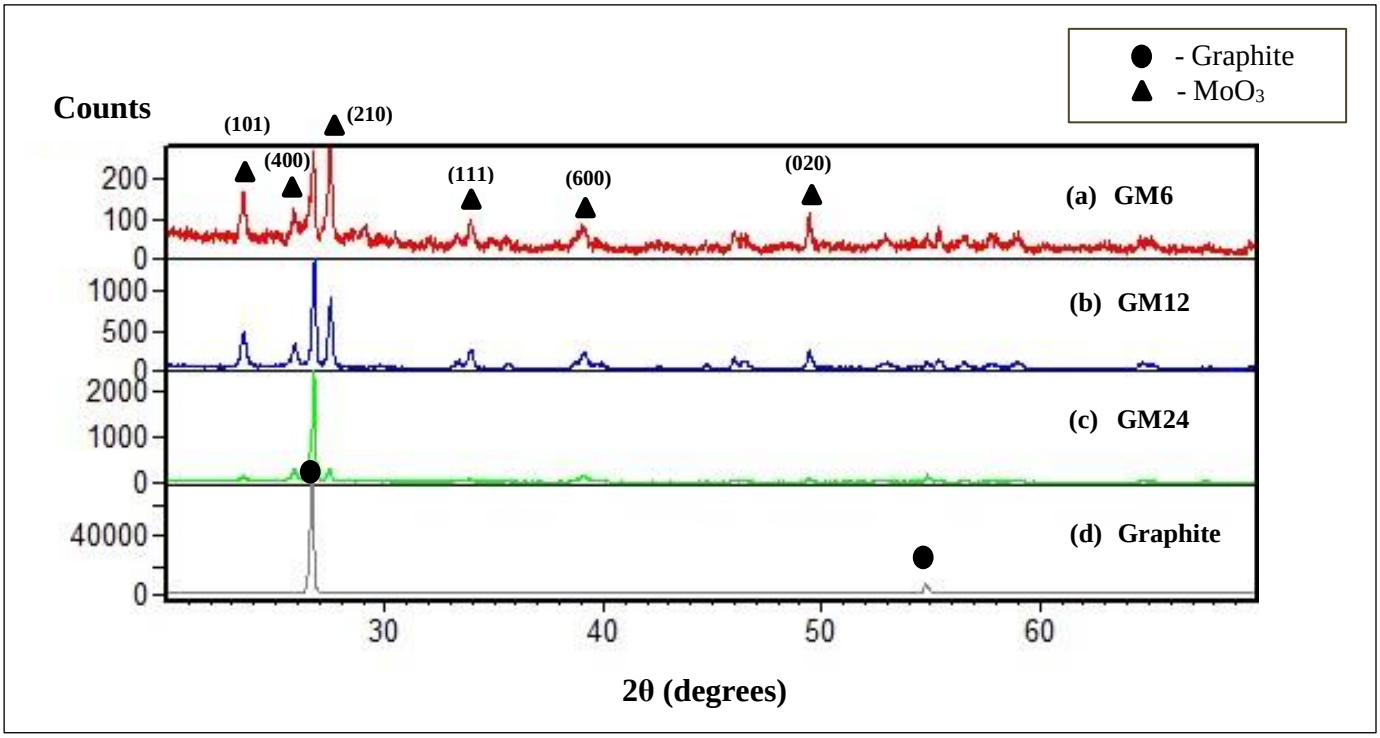


Figure 8.2. XRD patterns of graphite and MoO_3-graphene composites.

8.2.2 Raman Spectroscopy

The Raman spectra of graphene and MoO_3-graphene composite electrode are shown in Figure 8.3. The peaks at ~1351, ~1581 and ~2719 cm^{-1} correspond to D, G and 2D bands of graphene sheets respectively [36]. The G band is ascribed to the in-plane vibration sp2 carbon atoms while the D and 2D bands are associated with the first order zone boundary phonons, which are not observed in defect-free graphene [58]. The defects found in the as-synthesized graphene from this study are due to the formation of new edges from the exfoliation process of graphite [59-60]. The broadening feature of 2D band indicates that the graphene is in multilayers form. The spectrum of the MoO_3-graphene nanocomposite shows six additional peaks labelled as "M" at 994, 819, 668, 381, 338 and 288 cm^{-1}[41]. The peak at 994 cm^{-1} is assigned to the terminal oxygen Mo=O stretching mode (A_g, υ_{as}) which results from an unshared oxygen. The 821 cm^{-1} peak is for the doubly coordinated oxygen (Mo_2-O) stretching mode (A_g, υ_s) which results from corner-sharing oxygen atoms in common to two octahedral. The 671 cm^{-1} peak is

assigned to the triply coordinated oxygen (Mo_3–O) stretching mode which results from edge-shared oxygen atoms in common to three octahedral. The 336 and 378 cm^{-1} peaks represent O–Mo–O bending and scissoring modes (A_g, B_{1g}, δ), respectively. Finally, 288 cm^{-1} peak refers to the wagging mode (B_{2g}, δ) for the double bond O=Mo=O [29, 38]. The characteristic peaks for molybdenum oxide and graphene can be clearly observed in the Raman spectrum, indicating the formation of MoO_3 nanoparticles on graphene sheets after solvothermal treatment.

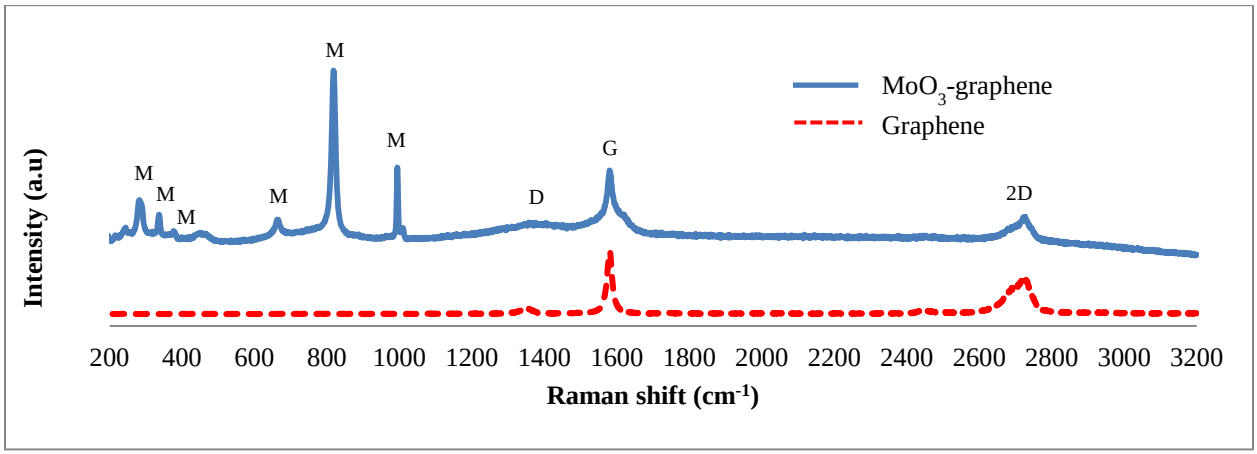


Figure 8.3. Raman spectra of graphene and MoO_3-graphene composites.

8.2.3 Scanning Electron Microscopy (SEM)

The surface morphology of the samples was characterised using SEM and the micrographs are presented in Figure 8.4(a-d). Figure 8.4a shows the typical morphology of graphene sheet and spherical MoO_3 nanoparticles were synthesized successfully using green and simple glucose-assisted solvothermal method (Figure 8.4b). Both samples GM6 and GM12 show a 2-dimensional morphology of graphene sheets with MoO_2 nanoparticles anchored on the surface. On the other hand, sample GM24 shows large agglomerated MoO_3 particles on graphene sheets. Unlike GM6 and GM12, the MoO_3 particles in GM24 are highly aggregated and forms large clusters on graphene layers. The chemical composition of the composites were analysed by an energy dispersive spectroscopy (EDX). The peaks of C, O, Mo in the EDX spectrum corresponds to carbon, oxygen and molybdenum compounds respectively, confirming the formation of molybdenum oxide- graphene composites (Figure 8.4(e)). The peak of Si in the EDS spectrum refers to the silicon substrate used for the characterization. TEM was performed

to further study the morphology of the graphene and composite samples. The TEM images of graphene and GM12 composites are shown in Figure 8.4(f-g) and the images clearly demonstrate that the thin layer of graphene sheets are densely populated with MoO_3 nanoparticles. Previous study [61] has reported that EG solvent is favourable for the formation of spherical MoO_3 nanoparticles, further supporting the evidence of the deposition of MoO_3 nanomaterial on the surface of graphene sheets.

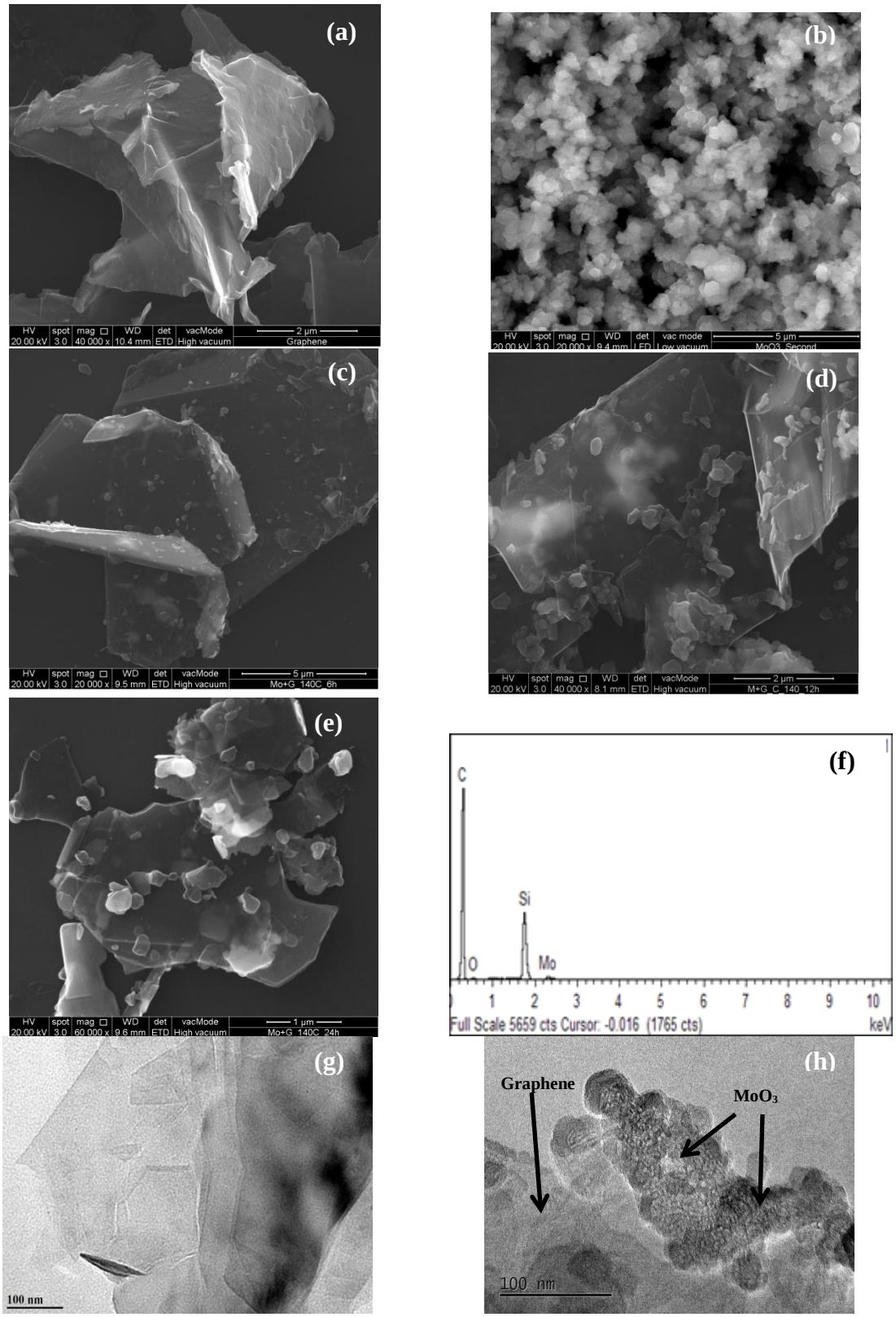


Figure 8.4. SEM micrographs of (a) graphene, (b) MoO_3, (c) GM6, (d) GM12, (e) GM24, (f) EDX spetrum of GM12, TEM images of (g) graphene and (h) GM12.

8.2.4 Cyclic Voltammetry (CV)

CV analysis on the electrode was conducted under the potential from 0 to +1 V in neutral 1 M Na_2SO_3 electrolyte. As shown in Figure 8.5(a), the CV curves of GM6 and GM12 exhibit nearly rectangle shapes, suggesting a good capacitive behaviors. However, an obviously distorted rectangle shape is observed for MoO_3, showing that the current is delayed to reach a horizontal value after reversal of the potential sweep. This deviation from rectangular shape is the indication of an uncompensated resistance in the system due to the poor electrical conductivity of MoO_3 [62]. Obviously, the presence of graphene improves the conductivity of composite materials, leading to the quasi-rectangle shape. On the basis of the curves, the specific capacitance of GM12 (148 F/g) is largest than those of MoO_3 (84 F/g), GM6 (110 F/g) and GM24 (73 F/g) at a scan rate of 5 mV/s. It should be noted that the specific capacitance value of GM24 is lower than that of pure MoO_3. This inferior electrochemical performance could be explained by the fact that the surface area of MoO_3 in GM24 composite material was not utilised effectively due to the heavy MoO_3 cluster on graphene sheets (as shown in Figure 8.3(e)) [64]. The aggregation of metal oxide particles on the surface of graphene sheets would prevent ions from reaching the inner layers of graphene thus preventing electrochemical double layer formation [10], leading to the distortion of charge storage performance. The agglomeration of the MoO_3 nanoparticles could inhibit the mobility of the electrolyte ions and reduce significantly the active contact area for a redox reaction. Figure 8.5(b) shows the CV curves of GM12 at the scan rates of 100, 50, 20, 10 and 5 mV/s. The CV curves show nearly rectangular shape with broad redox peaks appeared, revealing the typical behaviors of the combination of EDLC of graphene and pseudocapacitance from the redox reaction of MoO_3. As expected, the specific capacitance calculated from CV increased as the scan rate decreased (Table 8.1).This can be explained by the fact that at slow scan rates, there was more time for the electrolyte ions to diffuse to the electrode materials [72] .

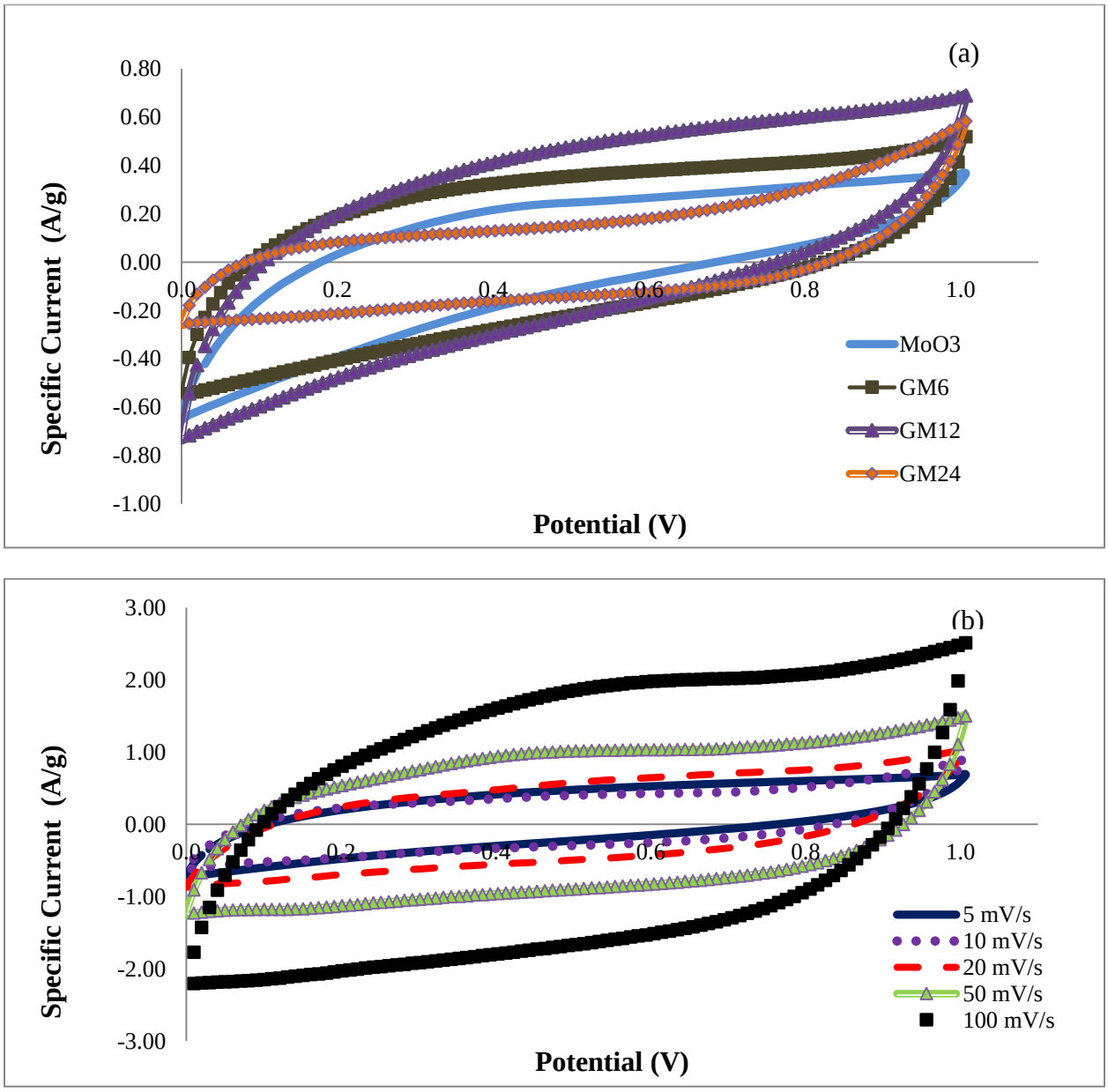


Figure 8.5. (a) CV curves of MoO_3, GM6, GM12 and GM24 electrodes at a scan rate of 5 mV/s in 1 M Na_2SO_3 electrolyte. (b) CV curves of GM12 composite electrodes at different scan rates of 5, 10, 20, 50 and 100 mV/s.

Table 8.1. Specific capacitance of GM12 as a function of scan rate.

Scan rate (mV/s)	Specific capacitance (F/g)
100	31.41
50	34.97
20	52.76
10	73.18
5	148.20

It is speculated that both reversible adsorption/desorption and intercalation/extraction processes accompanied by the enhanced faradaic reactions of the electrolyte ions and metal oxides are found responsible for the excellence electrochemical performance, as a result of the combination of the pseudocapacitance and electrochemical double layer capacitance. Two diffusion mechanisms are proposed to be responsible for the charge storage process in the MoO_3-graphene composite electrodes. The first mechanism is based on the concept of the adsorption/desorption of a proton (H^+), hydroxide (OH^-), alkali metal cation (Na^+) and sulphite anions (SO_3^{2-}) from an electrolyte on the composite electrodes, thus forming a double layer at the electrode-electrolyte interface. The second mechanism is based on the intercalation/extraction of H^+, OH^-, Na^+ and SO_3^{2-} ions from the electrolyte within the bulk composite electrodes, contributing to the successive reduction-oxidation of sulphite anions adsorbed on the surface of composite materials, as presented in the followings: [56, 63]

$$2SO_3^{2-} + 3H_2O + 4e^- \rightleftharpoons S_2O_3^{2-} + 6OH^- \quad \text{Eq. (8.9)}$$

$$S_2O_3^{2-} + 3H_2O + 8e^- \rightleftharpoons 2S^{2-} + 6OH^- \quad \text{Eq. (8.10)}$$

8.2.5 Galvanostatic Charge-Discharge (GCD)

Figure 8.6 presents the galvanostatic CD profiles of MoO_3, GM6, GM12 and GM24 electrodes in 1 M Na_2SO_3 electrolytes at a current density of 2 A/g. The MoO_3 and composite electrodes show nonlinear charge-discharge curves, indicating that the electrodes exhibit pseudocapacitive behaviour [66]. The charging/discharging performance of the MoO_3-graphene composite electrodes is superior to that of pure MoO_3 electrodes. It can be observed that the IR drop observed in both GM12 and GM6 are small if compared to the MoO_3 electrode, which clearly implies that both composite electrodes demonstrate improved charge carrier conductivity with the incorporation of graphene. It shows that the composite electrodes exhibit enhanced capacitive performance in comparison with pure MoO_3 electrodes, attributing to the contributions of the good electrical conductivity of graphene [62] and the pseudocapacitance of the MoO_3 nanoparticles.

The specific energy (Wh/kg) and specific power (W/kg) are further determined using Eq. (3.17) and Eq. (3.18), respectively (Chapter 3). At low specific power, the specific energy of GM12 and MoO_3 electrodes are 16.3 and 11.8 Wh/kg, respectively (Figure 8.7). The specific energy of MoO_3-graphene composites is found higher than those of pure MoO_3 due to the synergetic effect contributed from both electroactive MoO_3 and highly electrical conductive graphene. To evaluate the long-time cycling stability of MoO_3-graphene, the capacitive retention was measured by continuous charge/discharge experiments at a constant current density of 2 A/g. It can be observed that the specific capacitance increased steadily during the initial 100 cycles as a result of the full activation of electrode when the number of available active sites increases which subsequently allows the trapped electrolyte ions to gradually diffuse out [71]. The specific capacitance decreased after this. Importantly, the composite electrodes exhibit superior cycling stability, with the capacitive retention of about 81 % after 1600 cycles at a current density of 2 A/g. The incorporation of graphene into the MoO_3 electrodes would enhance the mechanical strength of composite materials, which is attributed to the more robust graphene backbone, resulting in the good cycling ability [62].

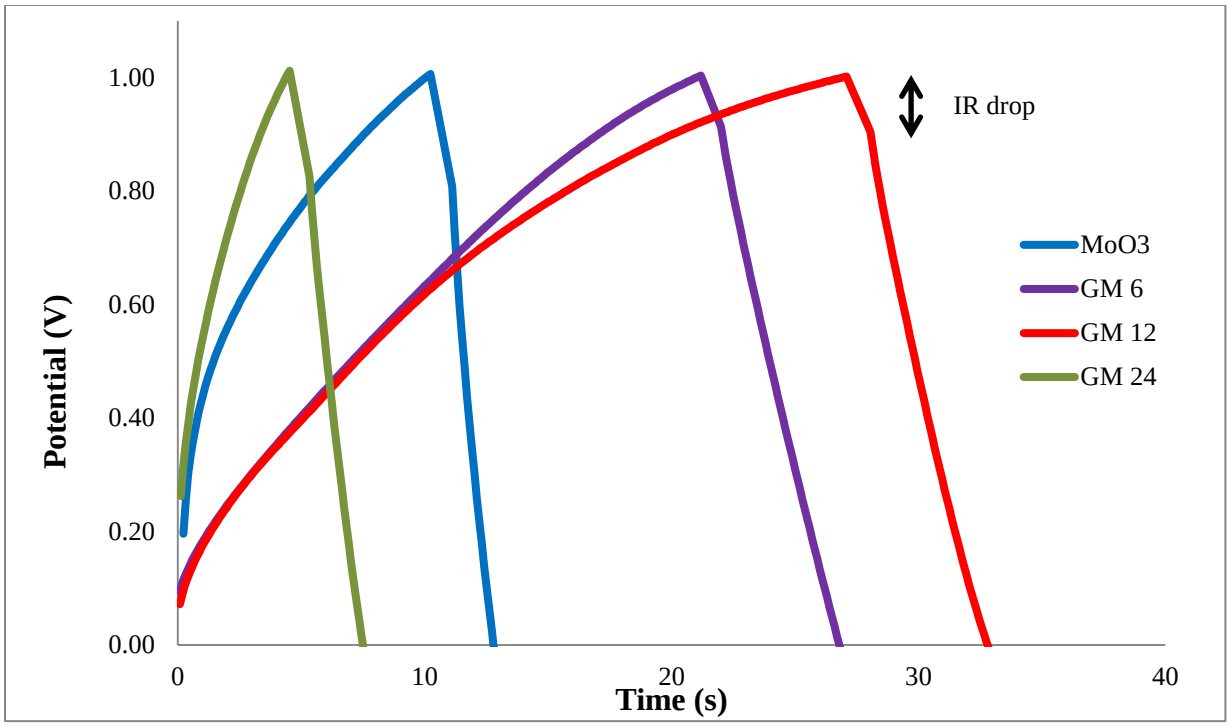


Figure 8.6. Charge-discharge curves of MoO_3, GM6, GM12 and GM24 electrodes at a current density of 2 A/g.

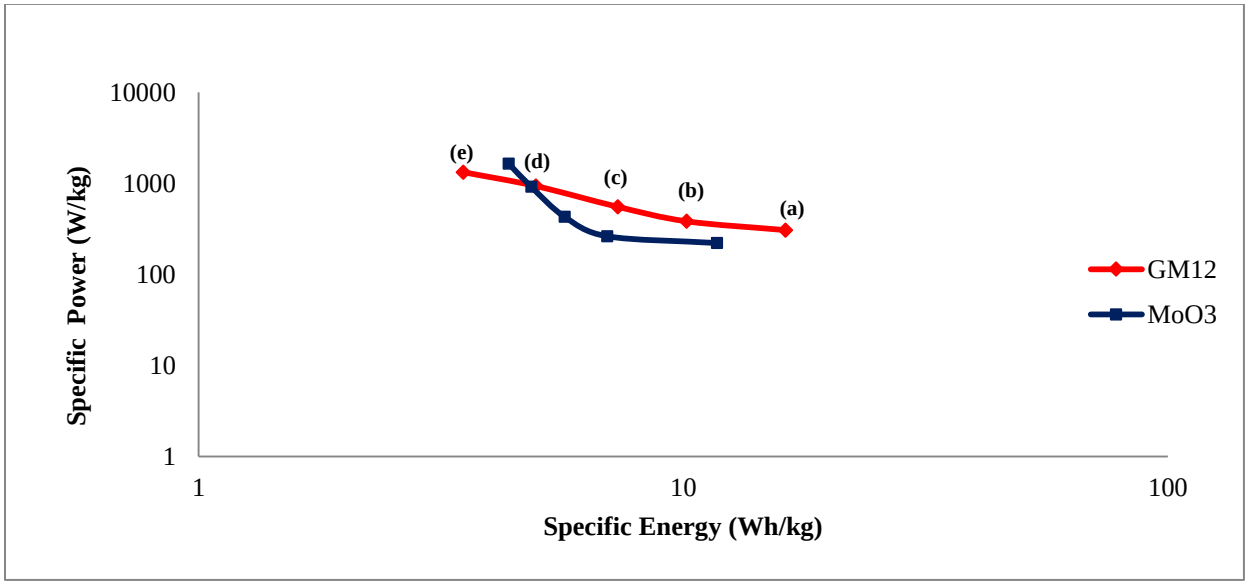


Figure 8.7. Ragone plot of GM12 and MoO_3 at various scan rates (a) 5, (b) 10, (c) 20, (d) 50, (e) 100 mV/s.

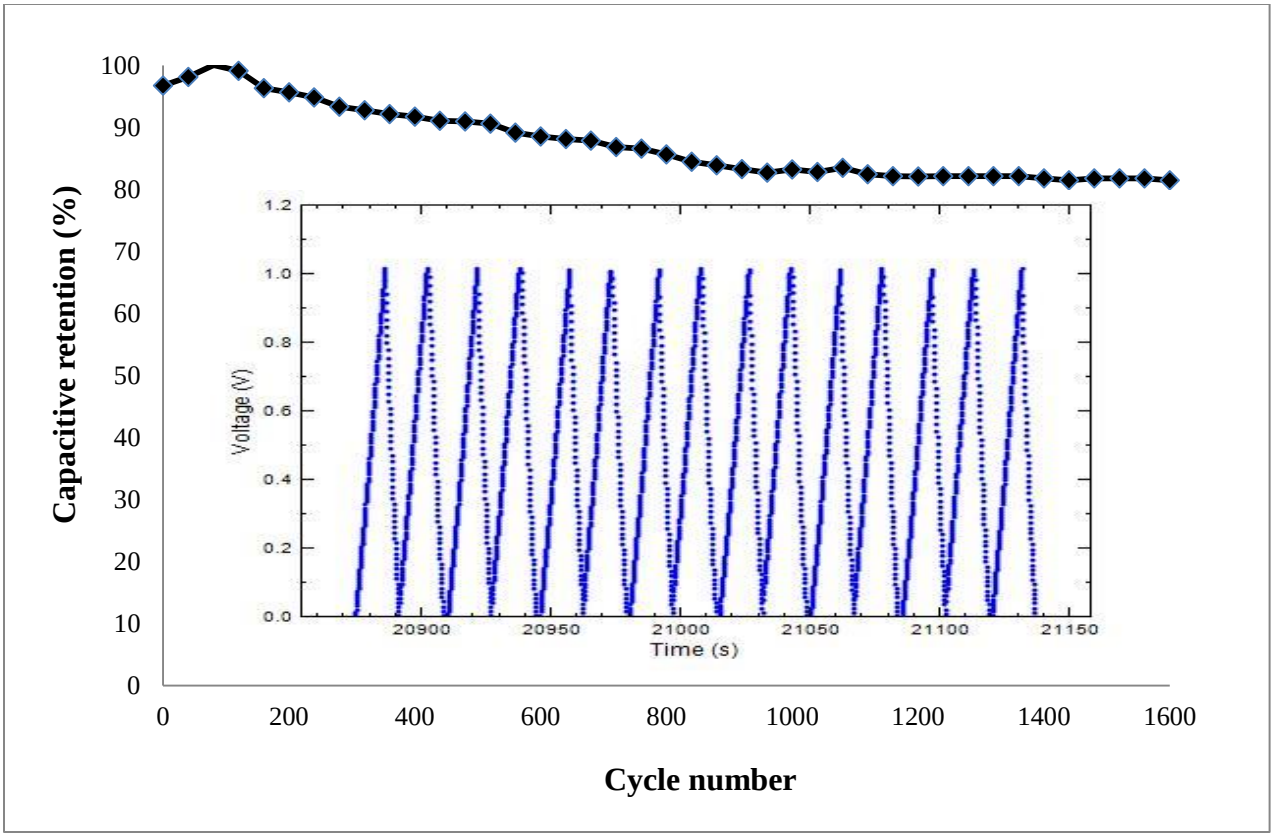


Figure 8.8. Cycling stability of MoO_3-graphene (GM12) composite electrodes at a current density of 2 A/g up to 1600 cycles.

8.2.6 Electrochemical Impedance Spectroscopy (EIS)

The EIS measurements were conducted between 100 kHz and 10 mHz. Figure 8.9 (a-d) demonstrate the Nyquist plots of the pure MoO_3 and MoO_3-graphene composites electrodes. It can be found that all the Nyquist plots are composed of a semicircle and a straight line. The semicircle observed in the Nyquist plot represents the combined response of several resistive effects at the electrode-electrolyte interface with an unimportant capacitive effect. Among the resistive effects include (i) electronic resistance of the electrodes, (ii) interfacial resistance between the electrodes and the current collectors, (iii) the electrolyte solution composition, (iv) ionic diffusion of ions moving within small pores and (v) resistance of charge transfer of faradaic phenomena arisen from the presence of redox species. The linear segment in low frequency region is the resistance arising from the frequency dependence of ion diffusion/transport. For such low frequencies, a greater amount of ionic charge can be accumulated in the available internal surface of the porous materials, contributing to its maximum electrical capacitance. The more vertical the line corresponds to an electrode more closing to an ideal capacitor [68]. The

MoO_3 showed a broad semicircle over the high frequencies, indicating a high ion diffusion resistance. The low conductivity of MoO_3 contributes to the significant charge transfer resistance of the electrodes. In contrast, both GM6 and GM12 exhibited higher phase angles and smaller semicircles, suggesting the reduced charge transfer resistance in the graphene composite electrodes.

Figure 8.9(e) presents the Randle equivalent circuit that is used to fit the Nyquist plot of GM12 composite electrode. The straight line in the low-frequency region makes a 45^o angle with the real axis is attributed to the Warburg impedance (W), which is a result of the frequency dependence of ion diffusion at the electrolyte-electrode interface. A Nyquist plot of a supercapacitor that behaves almost ideally presents a practically vertical line at lower frequencies, which is parallel to the imaginary axis (-Z"). However, due to imperfections in the real electrochemical cell, including the surface roughness, a leaky capacitor and a non-uniform current distribution, electrodes often does not behave ideally. With this reason, Q or the constant-phase element (CPE) is typically used in place of the capacitive element (C) to indicate the non-ideal behaviour of electrodes. Another tangent hyperbolic diffusion circuit element (T) needs to be incorporated into the Randles equivalent circuit when the diffusion condition is under restricted diffusion limitation between the electrode and non-reactive surface (current collector) [70]. These findings have proved that the homogenous deposition of nano-sized MoO_3 particles on the surface of graphene nanosheets is crucial to reduce the impedance of the composite materials during charge transfer.

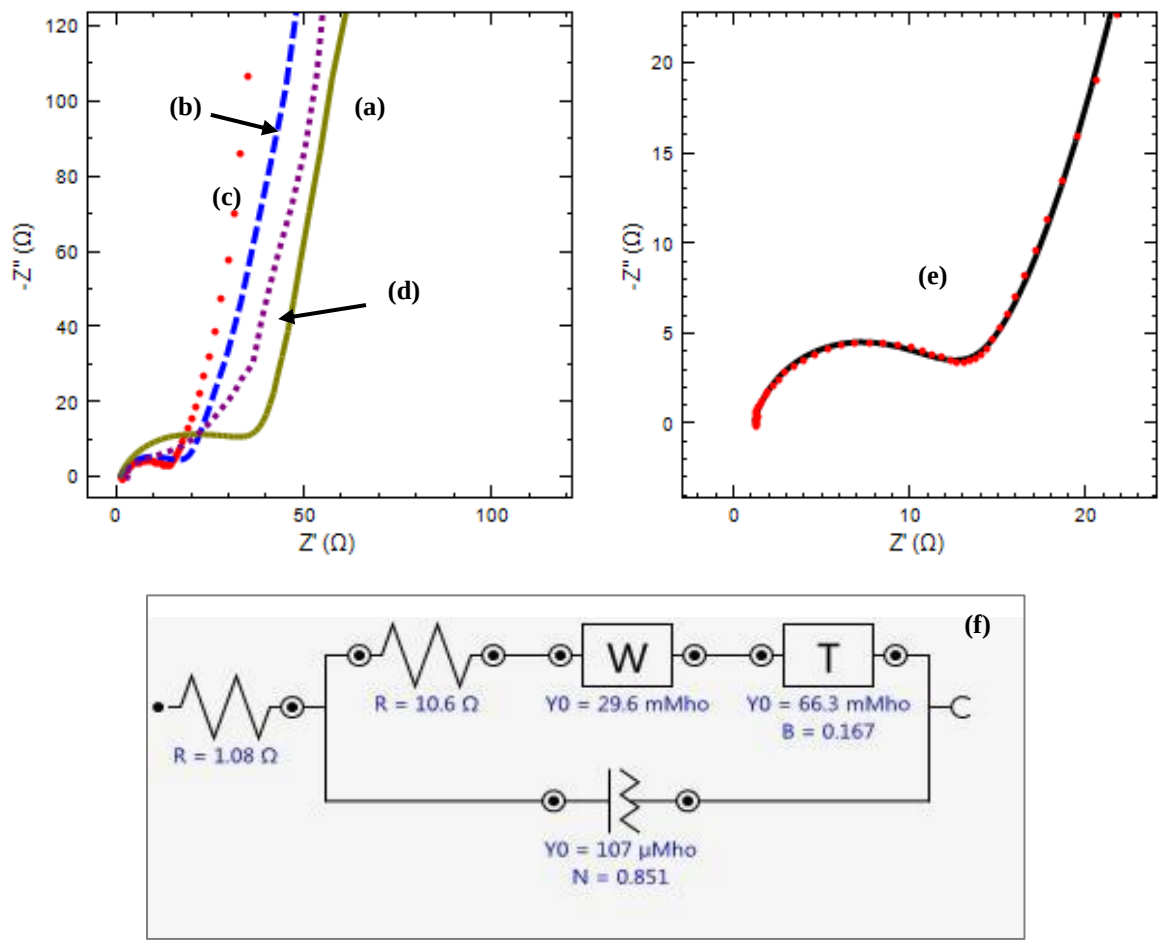


Figure 8.9. Nyquist plots for (a) MoO_3, (b) GM6, (c) GM12, (d) GM24, (e) the fitting of the impedance expressions (▬) obtained from the equivalent circuit to the experimental Nyquist spectra (●) and (f) Randles equivalent circuit representing the circuit elements that are used to fit the experimental Nyquist spectra using the software Nova.

8.3 Summary

In conclusion, a facile and environment-friendly method to synthesize MoO_3-graphene nanocomposites was developed. The synthesis strategy is based on the solvent exfoliation of raw graphite in ethanol-water mixtures followed by ethylene glycol-assisted solvothermal treatment to produce MoO_3-graphene nanocomposites. This green synthesis method provides an alternative route to produce nanostructured MoO_3-graphene composite electrodes in a simple, low cost and effective manner, without the needs of extreme synthesis condition and hazardous precursor chemicals. Additionally, this system employs mild and non-flammable aqueous electrolyte (neutral Na_2SO_3 solution) which is beneficial to the users, the environment and the cycle life of

electrodes. Maximum specific capacitance of 148 F/g is obtained from the MoO_3-graphene composites at a scan rate of 5 mV/s. The specific capacitance of MoO_3-graphene composite electrodes is superior to many reported electrodes that have adopted neutral electrolyte in the systems. Furthermore, in contrast to the previously reported systems that are usually complicated and costly, the present work potentially provides a readily scalable technological platform for economic mass production of energy storage devices.

Reference

[1] T.Y.Kim, H.W.Lee, M.Stoller, D.R.Dreyer, C.W. Bielawski, R.S. Ruoff, and K.S. Suh, "High-Performance Supercapacitors Based on Poly(ionic liquid)-Modified Graphene Electrodes," *ACS Nano 5 (*2011) 436–442.

[2] D.Chen, Q.F.Wang, R.M.Wang and G.Z.Shen, "Ternary oxide nanostructured materials for supercapacitors: a review," J. Mater. Chem. A.3 (2015) 10158–10173.

[3] X.F.Xia, Q.L.Hao, W.Lei, W.J.Wang, H.L.Wang and X.Wang, Reduced-graphene oxide/molybdenum oxide/polyaniline ternary composite for high energy density supercapacitors: Synthesis and properties, J. Mater. Chem.22 (2012), 8314–8320.

[4] B.Xu, S.F.Yue, Z.Y.Sui, X.T. Zhang, S.S.Hou, G.P.Cao and Y.S.Yang, What is the choice for supercapacitors: graphene or graphene oxide?, Energy Environ. Sci.4 (2011), 2826–2830.

[5] Z.S.Wu, G.M.Zhou, L.C.Yin, W.C.Ren, F. Li, H.M.Cheng, Graphene/metal oxide composite electrode materials for energy storage, Nano Energy 1 (2012) , 107–131.

[6] C.L.Liu, Kuo-Hsing Chang, Chi-Chang Hu*, Wei-Chung Wen, Microwave-assisted hydrothermal synthesis of Mn_3O_4/reduced graphene oxide composites for high power supercapacitors, Journal of Power Sources 217 (2012) 184-192.

[7] M. Pumera, Graphene-based nanomaterials and their electrochemistry, Chemical Society Reviews 39 (2010) 4146–4157.

[8] L.L. Zhang, R. Zhou, X.S. Zhao, Graphene-based materials as supercapacitor electrodes, Journal of Materials Chemistry 20 (2010) 5983–5992.

[9] R. B. Rakhi, W.Chen, D.Y.Cha and H. N. Alshareef, High performance supercapacitors using metal oxide anchored graphene nanosheet electrodes, J. Mater. Chem.21 (2011) 16197.

[10] Y.B.Tan and J.M. Lee, Graphene for supercapacitor applications, J. Mater. Chem. A 1 (2013) 14814–14843.

[11] Y. Chen, X. Zhang, D. Zhang, P. Yu and Y. Ma, High performance supercapacitors based on reduced graphene oxide in aqueous and ionic liquid electrolytes, Carbon 49 (2011) 573-580.

[12] Y.Haldorai, W.Voit, J.J.Shim, Nano ZnO @ reduced graphene oxide composite for high performance supercapacitor: Green synthesis in supercritical fluid, Electrochimica Acta 120 (2014) 65–72.

[13] T.Lu, L.K.Pan, H.Bo.Li, G.Zhu, T. Lv, X.J. Liu, Z.Sun, T.Chen, D.H.C. Chua, Microwave-assisted synthesis of graphene–ZnO nanocomposite for electrochemical supercapacitors, Journal of Alloys and Compounds 509 (2011) 5488–5492.

[14] Ananthakumar Ramadoss a, Sang Jae Kim, Facile preparation and electrochemical characterization of graphene/ZnO nanocomposite for supercapacitor applications, Materials Chemistry and Physics 140 (2013) 405- 411.

[15] E.R.Ezeigwe, M.T.T.Tan, P.S.Khiew, C.W.Siong, One-step green synthesis of graphene/ZnO nanocomposites for electrochemical capacitors, Ceramics International 41(2015)715–724.

[16] J.Wang, Z.Gao, Z.S.Li, B.Wang, Y.X.Yan, Q.Liu, T.Mann, M.L.Zhang, Z.H.Jiang, Green synthesis of graphene nanosheets/ZnO composites and electrochemical properties, Journal of Solid State Chemistry 184 (2011) 1421–1427.

[17] X. Dai, W.Shi, H.Cai, R.Li, G.Yang, Facile preparation of the novel structured α-MnO_2/graphene nanocomposites and their electrochemical properties, Solid State Sci.27 (2014)17–23.

[18] Y. Liu, D.Yan, Y.Li, Z.Wu, R.Zhuo, S.Li, J.Feng, J.Wang, P.Yan, Z. Geng, Manganese dioxide nanosheet arrays grown on graphene oxide as an advanced electrode material for supercapacitors, Electrochim. Acta 117 (2014)528–533.

[19] X. Feng, Z.Yan ,N.Chen, Y.Zhang, Y.Ma, X.Liu, Q.Fan, L.Wang, W. Huang, The synthesis of shape-controlled MnO_2/graphene composites via a facile one-step hydrothermal method and their application in supercapacitors, J.Mater.Chem.A 1 (2013) 12818.

[20] J. Cao, Y.Wang, Y.Zhou, J.H.Ouyang, D.Jia, L.Guo, High voltage asymmetric supercapacitor based on MnO_2 and graphene electrodes, J. Electroanal. Chem. 689 (2013)201–206.

[21] W.L .Yang, Z.Gao, J.Wang, B.Wang, Q. Liu, Z.S.Li, T.Mann, P.P.Yang, M.L.Zhang, L.H.Liu, Synthesis of reduced graphene nanosheet/urchin-like manganese dioxide composite and high performance as supercapacitor electrode, Electrochimica Acta 69 (2012) 112– 119.

[22] R. B. Rakhi, W.Chen, D.Y.Cha and H. N. Alshareef, High performance supercapacitors using metal oxide anchored graphene nanosheet electrodes, J. Mater. Chem. 21 (2011) 16197.

[23] J.W.Lee, A.S. Hall, J.D.Kim and T.E. Mallouk, A Facile and Template-Free Hydrothermal Synthesis of Mn_3O_4 Nanorods on Graphene Sheets for Supercapacitor Electrodes with Long Cycle Stability, Chem. Mater.24 (2012) 1158−1164.

[24] H. D. Liu, J. L. Zhang, D. D. Xu, L. H. Huang , S. Z. Tan. W. J. Mai, Easy one-step hydrothermal synthesis of nitrogen-doped reduced graphene oxide/iron oxide hybrid as efficient supercapacitor material, J Solid State Electrochem 19 (2015) 135–144.

[25] Y.Y.Wei, S.Q.Chen, D.W.Su, B.Sun, J.G.Zhu and G.X.Wang, 3D mesoporous hybrid $NiCo_2O_4$@graphene nanoarchitectures as electrode materials for supercapacitors with enhanced performances, J. Mater. Chem. A 2 (2014) 8103–8109.

[26] Z.X.Song, Y.J.Zhang, W.Liu, S.Zhang, G.C.Liu, H.Y.Chen, J.S.Qiu, Hydrothermal synthesis and electrochemical performance of Co_3O_4/reduced graphene oxide nanosheet composites for supercapacitors, Electrochimica Acta 112 (2013) 120–126.

[27] X.Leng J.P.Zou, X.Xiong and H.W.He, Hydrothermal synthesis and pseudo capacitance behavior of a highly homogeneous dispersed graphene sheets/ruthenium oxide nanocomposite, RSC Adv. 4 (2014) 61596-61603.

[28] X.Z.Yu, B.G.Lu, Z.Xu, Super Long-Life Supercapacitors Based on the Construction of Nanohoneycomb-Like Strongly Coupled $CoMoO_4$ –3D Graphene Hybrid Electrodes, Adv. Mater. 26 (2014) 1044–1051.

[29] Q.W.Tang, Z.Q.Shan, L.Wang, X.Qin, MoO_2–graphene nanocomposite as anode material for lithium-ion batteries, Electrochimica Acta 79 (2012) 148– 153.

[30] A.Bhaskar, Me.Deepa, T.N. Rao, U.V. Varadaraju, Enhanced nanoscale conduction capability of a MoO_2/Graphene composite for high performance anodes in lithium ion batteries, Journal of Power Sources 216 (2012) 169-178.

[31] L.Noerochim, J.Wang, D.Wexler, Z.Chao & H.Liu, Rapid synthesis of free-standing MoO_3/ Graphene films by the microwave hydrothermal method as cathode for bendable lithium batteries, Journal of Power Sources 228 (2013) 198-205.

[32] X.F.Yang, H.Y.Ding, D.Zhang, X.H.Yan, C.Y.Lu, J.L.Qin, R.X.Zhang, H.Tang, and H.J.Song, Hydrothermal synthesis of MoO_3 nanobelt-graphene composites, Cryst. Res. Technol. 46 (2011) 1195 – 1201.

[33] Y.Xu, R.Yi, B.Yuan, X.F.Wu, M.Dunwell, Q.L.Lin, L.Fei, S.G.Deng, P.Andersen, D.H.Wang and H.M.Luo, High Capacity MoO_2/Graphite Oxide Composite Anode for Lithium-Ion Batteries, J. Phys. Chem.Lett. 2012, 3, 309−314.

[34] K.H.Seng, G.D. Du, L. Li, Z.X.Chen, H.K.Liu and Z.P.Guo, Facile synthesis of graphene–molybdenum dioxide and its lithium storage properties, J. Mater. Chem., 2012, 22, 16072.

[35] M.S.Saha, R.Y.Li, X.L.Sun, "High loading and monodispersed Pt nanoparticles on multiwalled carbon nanotubes for high performance proton exchange membrane fuel cells," Journal of Power Sources 177 (2008) 314–322.

[36] D. Parviz, M. Kazemeini, A. M. Rashidi, Kh. Jafari Jozani, Synthesis and characterization of MoO_3 nanostructures by solution combustion method employing morphology and size control, J Nanopart Res 12 (2010) 1509–1521.

[37] T.H.Chiang and H.C.Yeh, The Synthesis of α-MoO_3 by Ethylene Glycol, Materials 6 (2013) 4609-4625.

[38] K.Kalantar-zadeh, J.S.Tang, M.S.Wang, K. L.Wang, A.Shailos, K.Galatsis, R.Kojima, V.Strong, A.Lech, W.Wlodarski and R.B. Kaner, Synthesis of nanometre-thick MoO_3 sheets, Nanoscale 2 (2010) 429–433.

[39] X.W.Lou and H.C. Zeng, Hydrothermal Synthesis of α-MoO_3 Nanorods via Acidification of Ammonium Heptamolybdate Tetrahydrate, Chem. Mater.14 (2002) 4781-4789.

[40] T. Ivanova, M. Surtchev, K. Gesheva,Investigation of CVD molybdenum, oxide films, Materials Letters 53 (2002) 250–257.

[41] Z.Q.Yuan, L.L.Si, D.H.Wei, L.Hu, Y.C.Zhu,, X.N.Li, and Y.T.Qian, "Vacuum Topotactic Conversion Route to Mesoporous Orthorhombic MoO_3 Nanowire Bundles with Enhanced Electrochemical Performance," J. Phys. Chem. C 118 (2014) 5091−5101.

[42] E.R.Ezeigwe, M.T.T.Tan, P.S.Khiew, C.W.Siong, Solvothermal synthesis of graphene–MnO_2 nanocomposites and their electrochemical behavior, Ceramics International 41(2015)11418–11427.

[43] E.R.Ezeigwe, M.T.T.Tan, P.S.Khiew, C.W.Siong, One-step green synthesis of graphene/ZnO nanocomposites for electrochemical capacitors, Ceramics International 41 (2015) 715–724.

[44] J.SY.Chia, M.T.T. Tan, P.S.Khiew, J.K.Chin, H.W.Lee , D.C.S Bien, C.W.Siong, A novel one step synthesis of graphene via sonochemical-assisted solvent exfoliation approach for electrochemical sensing application, Chemical Engineering Journal 249 (2014) 270–278.

[45] L.Obreja, N. Foca, M. I. Popa, V. Melnig, Alcoholic reduction Platinum Nanoparticles Synthesis by Chemical Method, Biomaterials in Biophysics, Medical Physics and Ecology (2008).

[46] P. Manivel, K. Sivashanmugan, C. Viswanathan, D. Mangalaraj, Preparation of New Reducing Agent for the Synthesis of Silver Nanoparticles, AIP Conf. Proc.1349 (2011) 415-416.

[47] E.Rodríguez-León, R.Iñiguez-Palomares, R.E.Navarro, R.Herrera-Urbina2, J.Tánori, C.Iñiguez-Palomares5 and A.Maldonado, Synthesis of silver nanoparticles using reducing agents obtained from natural sources (Rumex hymenosepalus extracts), Nanoscale Research Letters 8 (2013) 318.

[48] H.H.Duan, D.S.Wang and Y.D.Li, Green chemistry for nanoparticle synthesis, Chem. Soc. Rev.44 (2015) 5778.

[49] C.E. Hoppe, M.Lazzari, I.P.Blanco, and M. A.L.Quintela, One-Step Synthesis of Gold and Silver Hydrosols Using Poly(*N*-vinyl-2-pyrrolidone) as a Reducing Agent, Langmuir 22 (2006).

[50] X.Y.Chen, X.Wang, Z.H. Wang, J.X. Wan, J.W.Liu and Y.T.Qian, "An ethylene glycol reduction approach to metastable VO_2nanowire arrays," *Nanotechnology* 15 (2004) 7027-7034.

[51] J.W.Lee, A.S.Hall, J.D.Kim, T.E. Mallouk, A Facile and Template-Free Hydrothermal Synthesis of Mn_3O_4 Nanorods on Graphene Sheets for Supercapacitor Electrodes with Long Cycle Stability, Chem. Mater 24 (2012), 1158−1164.

[52] Y.Liu, Y.Zhang, G.H.Ma, Z.Wang, K.Y.Liu, H.T.Liu, "Ethylene glycol reduced graphene oxide/polypyrrole composite for Supercapacitor," Electrochimica Acta 88 (2013) 519– 525.

[53] P.Zhao, Preparation and Characterization and Reducing Properties of MoO_3 Nano-Fibers, in: T.Lin (Eds), Nanofibers – Production, Properties and Functional Applications, InTech, Croatia. 2011,135-152.

[54] H.E.Morris, Reactions of ethyl alcohol. Chem. Rev. 10 (1932) 465–506.

[55] N. Nagarajan, H. Humadi, and I. Zhitomirsky, Cathodic electrodeposition of MnO_x films for electrochemical supercapacitors, Electrochim. Acta 51 (2006) 3039–3045.

[56] M.Y. Ho, P.S. Khiew, D. Isa, T.K. Tan, W.S. Chiu, C.H. Chia, Charge storage performance of lithiated iron phosphate/activated carbon composite as symmetrical electrode for electrochemical capacitor, Current Applied Physics 14 (2014) 1564-1575.

[57] B. S. Murty et al., Tools to Characterize Nanomaterials, in: Textbook of Nanoscience and Nanotechnology, Ch.5, Universities Press, India, 2013, p.149-175.

[58] W. Han, L.Ren, X.Qi, Y.Liu, X.Wei, Z.Huang, J.Zhong, Synthesis of CdS/ZnO/graphene composite with high-efficiency photo electrochemical activities under solar radiation, Appl.Surf.Sci.299 (2014)12–18.

[59] A.C. Ferrari, Raman spectroscopy of graphene and graphite: disorder, electron–phonon coupling, doping and non-adiabatic effects, Solid State Commun.143 (2007)47–57.

[60] A.C. Ferrari, D.M.Basko, Raman spectroscopy as a versatile tool for studying the properties of graphene, Nat.Nanotechnol.8 (2013)235–246.

[61] S.T.Wang, C.H.An, Y.G.Zhang, Z.D.Zhang, Y,T,Qian, Ethanothermal reduction to MoO_2 microspheres via modified Pechini method, Journal of Crystal Growth 293 (2006) 209–215.

[62] Jintao Zhang, Jianwen Jiang, and X. S. Zhao. Synthesis and Capacitive Properties of Manganese Oxide Nanosheets Dispersed on Functionalized Graphene Sheets. J. Phys. Chem. C 115 (2011) 6448–6454.

[63] X.Zhao, C.Johnston, A.Crossley and P.S. Grant, Printable magnetite and pyrrole treated magnetite based electrodes for supercapacitors, J. Mater. Chem.20 (2010) 7637–7644.

[64] L.Mao, K.Zhang, H.S.O.Chan and J.S.Wu, Nanostructured MnO_2/graphene composites for supercapacitor electrodes: the effect of morphology, crystallinity and composition, J. Mater. Chem.22 (2012) 1845–1851.

[65] Jintao Zhang, Wei Chu, Jianwen Jiang and X. S. Zhao. Synthesis, characterization and capacitive performance of hydrous manganese dioxide nanostructures. Nanotechnology 22 (2011) 125703.

[66] I.Shakir, M.Shahid, H.W.Yang, D.J.Kang, Structural and electrochemical characterization of α-MoO_3 nanorod-based electrochemical energy storage devices, Electrochimica Acta 56 (2010) 376–380.

[67] C. Yuan, L. Chen, B. Gao, L. Su and X. Zhang. Synthesis and utilization of $RuO_2 \cdot xH_2O$ nanodots well dispersed on poly(sodium 4-styrene sulfonate) functionalized multi-walled carbon nanotubes for supercapacitors. J. Mater. Chem. 19(2009)246-252.

[68] L.Mao, K.Zhang, H.S.O.Chan and J.S.Wu, Surfactant-stabilized graphene/polyaniline nanofiber composites for high performance supercapacitor electrode, J. Mater. Chem.22 (2012) 80–85.

[69] V. D. Jovic, Determination of the correct value of C_{dl} from the impedance results fitted by the commercially available software, [Online]. Available: http://www.gamry.com (2012)

[70] Pierre-Loius Taberna, Patrice-Louis Simon, Electrochemical Techniques, in : Supercapacitors: Materials, Systems and Applications, F. Beguin and E.Frackowiak, Ed. Germany: Wiley-VCH (2013) 119–129.

[71] C.J.Zhao, Z.M.Zhang, Q.Wang, S.D.Min and X.Z.Qian, "Vertically oriented Ni_3S_2/RGO/Ni_3S_2 nanosheets on Ni foam for superior supercapacitors," RSC Adv. 5 (2015) 63528–63536.

[72] W.K. Chee , H.N. Lim , I. Harrison , K.F. Chong , Z. Zainal , C.H. Ng , N.M. Huang , "Performance of Flexible and Binderless Polypyrrole/Graphene Oxide/ Zinc Oxide Supercapacitor Electrode in a Symmetrical Two-Electrode Configuration," Electrochimica Acta 157 (2015) 88–94.

CHAPTER 9
Conclusions and Recommendations

9.1. Conclusions

This thesis has described the preparation, characterization and electrochemical applications of a series of cost effective transition-metal-oxide based materials, a hybrid lithium-ion/EDLC based symmetrical electrodes and two graphene-based composite materials. Several key conclusions drawn out from the results of this work are summarise and reviewed as follows:

1) A comprehensive study of the electrochemical performance of Fe_3O_4-AC, TiO_2-AC and ZnO-AC nanocomposite electrodes was carried out. Different loading ratios of metal oxide and AC were used to investigate the synergetic effects. It is found that the morphology, crystallinity and composition all play important roles in the capacitor performance. The three composite electrodes exhibit the similar trend, that is, with a relatively low loading of metal oxide (4 wt %), the enhancement of electrochemical storage properties of the AC electrodes is clearly observed. In this case, the synergetic effect of the pseudocapacitive metal oxides with the double layer capacitance AC material is excellently demonstrated. However, bulk increasing of the metal oxide content is found to distort the capacitive performance and deteriorate the specific surface area of the electrode, mainly due to the aggregation of the metal oxide particles within the composite.

2) The type of electrolyte anions actually is playing a vital role in the capacitive performance in view of the fact that the as-prepared composites exhibit different electrochemical behaviors in 1 M Na_2SO_3 and 1 M Na_2SO_4 electrolytes. The electrochemical results reveal that the Fe_3O_4-AC systems employing Na_2SO_3 electrolyte exhibit the improved electrochemical performance in terms of a specific capacitance of 127 F/g at the scan rate of 10 mV/s. Higher specific capacitances and more obvious pseudocapacitive behaviors could be found in the

electrolyte containing sulphite (SO_3^{2-}) anions, while more dominant EDL capacitive behavior were observed in the 1 M Na_2SO_4 electrolyte.The significant capacitive performance in Na_2SO_3 is attributed from the synergistic effect of both EDLC and the pseudocapacitance which involves adsorption/de-adsorption of SO_3^{2-} anions and successive redox reactions of the adsorbed sulphite anions across the interface of electrode-electrolyte.The high surface area and amorphous nature are essential to achieve the good capacitive performance.

3) The structural analysis and capacitive performance of $LiFePO_4$-AC composite electrode materials in mild aqueous Na_2SO_3 and Li_2SO_4 electrolytes were comprehensively evaluated. High specific capacitance of 125 F/g at a current density of 5 mA/cm^2 was achieved for 40 wt% $LiFeO_4$ loaded on AC in 1 M Na_2SO_3. The improved capacitive performance of the composite electrode is attributed to the synergistic effect of the EDLC on the surface of AC and the pseudocapacitance via the intercalation/extraction of H^+, OH^-, Na^+ and SO_3^{2-} and Li^+ ions in $LiFePO_4$ lattices. On the other hand, $LiFePO_4$-based electrodes in a Li_2SO_4 electrolyte achieve lower specific capacitances than in a Na_2SO_3 electrolyte. Unlike Na_2SO_3, sulphate anions (SO_4^{2-}) in Li_2SO_4 do not provide pseudocapacitance, as needed in an energy storage system. Thus, the intercalation and extraction of lithium (Li^+) ions become the only predominant phenomenon responsible for the charge storage mechanism in a Li_2SO_4 electrolyte. A specific energy of 13 Wh/kg was attained for $LiFePO_4$-based electrodes in a Na_2SO_3 electrolyte at low specific power.

4) A simple approach has been developed to synthesize SnO_2-graphene nanocomposites by using graphite, $SnCl_2$ and glucose as precursors while ethanol and water as mixed solvent. This glucose-assisted solvothermal route is considered as a cost-effective, eco-friendly and scalable nanocomposite production as the starting materials are non-hazardous, coupling with the low-temperature solvothermal process (140^{o}C) that does not required high pressure or extreme synthetic condition. Glucose and ethanol were observed to play an

important role as reducing agent in fabrication of nanomaterials as well as the deposition of SnO_2 on the surface of graphene sheets. More importantly, the specific energy of SnO_2-graphene is 13.8 Wh/kg which is much higher than that of pure graphene (5.9 Wh/kg) at low specific power. Furthermore, the specific capacitance of SnO_2-graphene nanocomposites retains about 93 % of its original value after 1500 cycles of charging and discharging at a current density of 2 A/g.

5) As demonstrated in this study, a mild and facile solvothermal approach to synthesize MoO_3-graphene nanocomposites was developed. The synthesis strategy is based on the solvent exfoliation of raw graphite in ethanol-water mixtures followed by ethylene glycol-assisted solvothermal route to produce MoO_3-graphene nanocomposites. Additionally, this system employs mild and non-flammable aqueous electrolyte (neutral Na_2SO_3 solution) which is beneficial to the users, the environment and the cycle life of electrodes. The as-prepared MoO_3-graphene nanocomposites display enhanced capacitive performance due to the synergic effect of both components: (i) the anchoring of MoO_3 nanoparticles on exfoliated graphene sheets effectively prevents the latter from agglomeration, thus facilitating ion transport in the electrode material, and eventually improving the electric double-layer capacitance; (ii) MoO_3 nanoparticles deposited homogeneously on a conductive graphene sheet can promote both the electrochemical utilization of MoO_3 and the electrical conductivity of the electrode. A high average specific capacitance of 148 F/g could be achieved for MoO_3-graphene composites in neural 1 M Na_2SO_3 electrolyte at a scan rate of 10 mV/s with capacitive retention of 81 % after 1600 cycles.

Table 9.1 summarises the electrochemical performance of different types of composite electrodes reported in this thesis.

Table 9.1. Comparative table summarises different types of composite electrodes synthesized in relation to their electrochemical performance using neutral 1 M Na_2SO_3 electrolyte.

Composite Electrode	Electrode Form	Scan rate (mV/s)	Specific Capacitance (F/g)	Specific Energy (Wh/kg)	Cycle life
Fe_3O_4-AC	Dough	10	127	15	96 % (after 1000^{th})
TiO_2-AC	Dough	10	80	11	93 % (after 1000^{th})
ZnO-AC	Dough	10	116	17	95 % (after 1000^{th})
$LiFePO_4$-AC	Dough	10	112	13	95 % (after 1000^{th})
SnO_2-Grapehere	Paste	5	99	14	93 % (after 1500^{th})
MoO_3-Graphene	Paste	5	148	16	81 % (after 1600^{th})

9.2 Recommendations

Electrode materials are the key for realizing high-performance supercapacitors. Novel transition-metal-oxide-based and graphene-based materials as electrodes for energy storage devices will continue to attract research attention in the design of supercapacitors due to their unique properties. In this thesis, enhancement on the capacitive performance was achieved by the combination of both EDLC and pseudocapacitance. As following, a couple of recommendations for future research work and the perspective directions for the development of supercapacitors are discussed.

The results presented in this thesis suggest that the combination between a highly pseudocapacitive material and a carbon material with a good electrical conductivity is an effective approach to exploit the synergic effect of both components. Therefore, it can be expected that further improvement on energy storage and power capability is likely to be realized by designing ternary composite materials containing different metal oxides and carbon materials. Additionally, further research is still needed to optimize and correlate the content of pseudocapacitive materials in ternary composite materials with regard to performance, which will deepen our understanding of the remarkable capacitive properties of pseudocapacitive materials. Meanwhile, hybrid supercapacitor systems with asymmetric configuration that can be operated with different potentials for the cathode

and anode deserve a higher level of research and development. The asymmetric systems can combine both the merits of two electrodes, offering an attractive alternative to improve the cell voltage, energy and power densities. Pseudocapacitive metal-oxide based electrodes can be assembled into asymmetric configuration with electrochemical double-layer based graphene materials to afford a greatly enhanced specific capacitance with significant improvement in terms of energy density.

The configuration of a faradic battery-type electrode (such as lithium intercalated compound) with a highly conductive graphene is seen as another important research direction in supercapacitor application. This is motivated by the outstanding features attributed to the synergistic effect of a supercapacitor and a battery including fast charge capability, robust cycle life and high energy density. In comparison with the mature technologies of batteries and symmetric supercapacitors, the hybrid supercapacitor technology is still in infancy. However, with the rapidly growing demand, the development of novel hybrid supercapacitors is believed to grow substantially in the coming years.

With respect to the configuration of supercapacitor cells, utilizing ionic liquid with a large electrochemical stability window is another frontier research aspect for optimization potential range used on each electrode, in order to widen the overall cell voltage. The electrolytes that are stable at high operating voltages will receive continuously growing research interest for designing and fabrication of high-power and high-energy supercapacitor devices. New ionic liquids with high electrochemical stability windows will receive increasing research interests. Meanwhile, flexible, light and all-solid-state energy storage devices integrated solid polymer electrolyte with high energy and power densities will continue to gain increased research attention due to their promising applications to be integrated into stretchable and wearable electronics.

The precise control over the morphologic and structural parameters is crucial to maximize the utilization of electrode materials for supercapacitors. In particular, the nanocomposites with optimal 3D hierarchical structure, large surface area, or optimal pore size are promising to exhibit good capacitive performance. Graphene materials are easily suffered from agglomeration during materials processing and device fabrication process, which often results in low actual surface area. Porous 3D graphene with well-

defined and cross-linked structure would prevent the restacking of graphene sheets. Meanwhile, the continuously interconnected porous structures not only facilitate the diffusion of electrolyte ions through the network but also serve as robust matrix for accommodating metal oxide and conducting polymers for supercapacitor application.